Structural and Magnetic Characterisation of some Mixed Metal Oxides and Oxyhalides

by

Deborah Ann Stephens

A thesis Submitted to the
Faculty of Science of the
University of Birmingham
For the degree of
Doctor of Philosophy

School of Chemistry
University of Birmingham
Edgbaston
Birmingham
B15 2T, UK
October 2010

Abstract

This thesis investigates the structural and physical effects of changing the ratio of Mn:Ga in the anion deficient perovskite, $YSr_3Mn_{4-x}Ga_xO_{10.5}$. $YSr_3Mn_{4-x}Ga_xO_{10.5}$ crystallises in the tetragonal space group I4/*mmm,* with lattice parameters *a*~7.64 Å and *c*~15.66 Å. Magnetic characterisation indicates that the material is antiferromagnetic overall, with ferromagnetic ordering in the [001] direction of the unit cell. Earlier work on the structural analogue, $Y_{1.07}Sr_{2.93}Mn_{2.67}Ga_{1.33}O_{10.5}$, identified a magnetic peak in the neutron diffraction pattern that could not be fitted following refinement of NPD data. This work concluded that the extra peak was due to a small MnO impurity.

The effects of oxidation and fluorination on the structural and physical properties of $YSr_3Mn_{4-x}Ga_xO_{10.5}$ with various Mn:Ga ratios are investigated.

The physical and structural effects of substituting Mn^{3+} or Co^{3+} for Fe^{3+} in the perovskite related material, $Pb_4Fe_3O_8Cl$, have been investigated using XRPD, NPD and magnetic susceptibility measurements.

An earlier characterisation of $Pb_8WO_{10}Cl_2$ suggested a deficit on all atom sites within the unit cell. This work suggests a different structure with an intact cation and main oxygen sub-lattice. The site of an additional oxygen was established linked to tungsten. $Pb_8WO_{10}Cl_2$ crystallises in space group I4/*mmm*, with $a = 3.9846(2)$ and $c = 22.690(2)$ Å.

Acknowledgements

I would like to thank my supervisor, Professor Colin Greaves, who has never failed to provide inspiration, wisdom and advice throughout my PhD, it has been a great privilege to work with him.

I would also like to thank everyone on the fifth floor, both past and present for offering their help, advice, friendship and especially for being fun to work with.

A special thank you must go to my parents and family, without their support this work would not have been possible.

TABLE OF CONTENTS

Chapter 1 – Introduction

Chapter 2 – Experimental Techniques

Chapter 3- Structural and Magnetic Characterisation of the Brownmillerite Material $YSr_3Mn_{4-x}Ga_xO_{10.5}$

Chapter 4 – Magnetic and Structural Characterisation of $YSr_3Mn_{4-x}Ga_xO_{10.5}$ following Oxidation and Fluorination

Chapter 7 – Conclusions and Further Work

Abbreviations

AFM	Antiferromagnetic
BVS	Bond valence sum
CFSE	Crystal field stabilisation energy
CMR	Colossal magnetoresistance
FM	Ferromagnetic
MR	Magnetoresistance
NPD	Neutron powder diffraction
T_c	Curie temperature
TGA	Thermogravimetric analysis
T_N	Néel temperature
XRPD	X-ray powder diffraction

CHAPTER 1

Introduction

1.1 Background

Perovskite and perovskite related materials display many properties, which are of fundamental as well as technological importance. Properties of technological interest include: magnetoresistance, oxide ion conduction, ferroelectric behaviour and high temperature superconductivity. The brownmillerite and hematophanite type structures considered in this thesis can both be related to the perovskite structure.

1.2 Perovskite and Related Structures

1.2.1 Perovskite Structure

Perovskites of general formula AMX_3, where the A site is usually occupied by alkaline earth or lanthanide cations, the M site by transition metals and the X site by oxygen or fluorine, take their name from the mineral, $CaTiO_3$ [1]. The ideal perovskite structure has a cubic unit cell, with the larger A cation occupying the central twelve coordinate site at the centre of the unit cell. The M cation is located at the six coordinate cube corners and the X anion is situated halfway along each edge of the cube, as shown in *figure 1.1a.* Alternatively the structure can be described as a network of corner linked MO_6 octahedra, with the A cation occupying an interstitial site as shown in *figure 1.1b.*

The ideal perovskite structure is found when the value of the Goldschmidt tolerance factor, *t,* is one according to the following *equation 1.1* [2].

$$t = \frac{(r_A + r_x)}{\sqrt{2}(r_M + r_x)} \qquad (1.1)$$

where r_A , r_M and r_x are the ionic radii of ions A, M and X respectively. Almost all perovskites have a tolerance factor in the range 0.75- 1.00 [3].

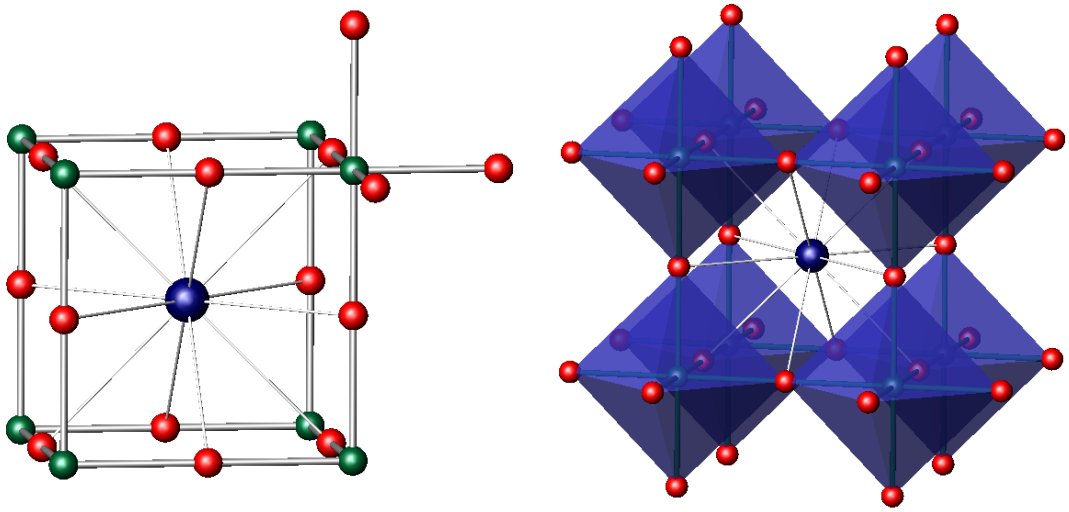

Figure 1.1a *Figure 1.1b*

Figure 1.1. Two views of the ideal cubic perovskite structure showing the A cation blue, M cation green and X anion red. *1.1a* shows the relationship between the cubic unit cell and the 6 coordinate M cation site. *1.1b*. shows the network of corner linked MO_6 octahedra with the central 12 coordinate A cation.

A large number of structures can be related to the perovskite structure due to its ability to tolerate: deviations from the ideal M-O or A-O bond lengths, intergrowth structures, anion or cation vacancies and Jahn Teller distortions. For values of $t < 1$ the radius of the M cation is larger than ideal compared to the radius of the A cation, resulting in compression of the M- X bonds and tension in the A-X bonds. These

stresses are relieved by tilting of the MX_6 octahedra, resulting in a lowering of the space group symmetry from cubic [4].

Double perovskites, $A_2MM'X_6$ are common, in which M and M' cations are ordered due to a charge difference and/or large size and electronegativity difference. A large cation in the octahedral site may be stabilised as a result of cation ordering. Perovskites in which the A site cations are ordered are also found.

Examples of intergrowth structures include the Ruddlesden-Popper phases $AX\cdot(AMX_3)_n$, which form as a result of a rocksalt type layer between the perovskite blocks, an example of a n=1 material is La_2CuO_4 [5].

Perovskite structures are found with vacancies on any of the ionic sites. The brownmillerite structure of $Ca_2Fe_2O_5$ is an example of an oxygen deficient perovskite in which vacancies have ordered to give 4-fold and 6-fold oxygen coordination for the M cation [6].

Jahn Teller (JT) effects also result in a lowering from cubic symmetry. For M site cations with d^4 or d^9 electron configuration elongation of the axial bond of the MO_6 octahedron removes the e_g orbital degeneracy and stabilises the structure. Cooperative JT distortions induce orbital ordering and crystallographic distortion as seen in $LaMnO_3$ [7,8].

1.2.2 Brownmillerite Structure

The structure of the material $YSr_3Mn_{4-x}Ga_xO_{10.5}$ investigated in Chapter 3, can be related to the brownmillerite structure. As will be discussed Chapter 3, the brownmillerite structure is an anion deficient perovskite, consists of alternating layers of octahedra and tetrahedra. Brownmillerite type materials crystallize in one of three space groups; *Ibm2, Pcmn* or *Icmm,* depending on the orientation of the tetrahedra,

which are corner linked along the [001] direction. Different displacement of the oxygen atoms within the tetrahedral layer lead to cooperative rotation of the tetrahedra, opposite rotations lead to the orientations labelled R or L in *figure 1.2* below, within a tetrahedral layer all orientations are either R or L. Adjacent tetrahedral layers have tetrahedral chains with the same orientation for space group *Ibm2,* whereas adjacent tetrahedral layers have chains with opposing orientations for space group *Pcmn* which is centrosymmetric. Space group *Icmm* has both rotations of tetrahedra, R and L within a given layer [9,10,11].

The brownmillerite related structure investigated in Chapters 3, $YSr_3Mn_{4-x}Ga_xO_{10.5}$, has an unusual arrangement of the tetrahedra. The tetrahedra form isolated squares along the [001] direction rather than corner linked chains, as shown in *figure 1.3* [12].

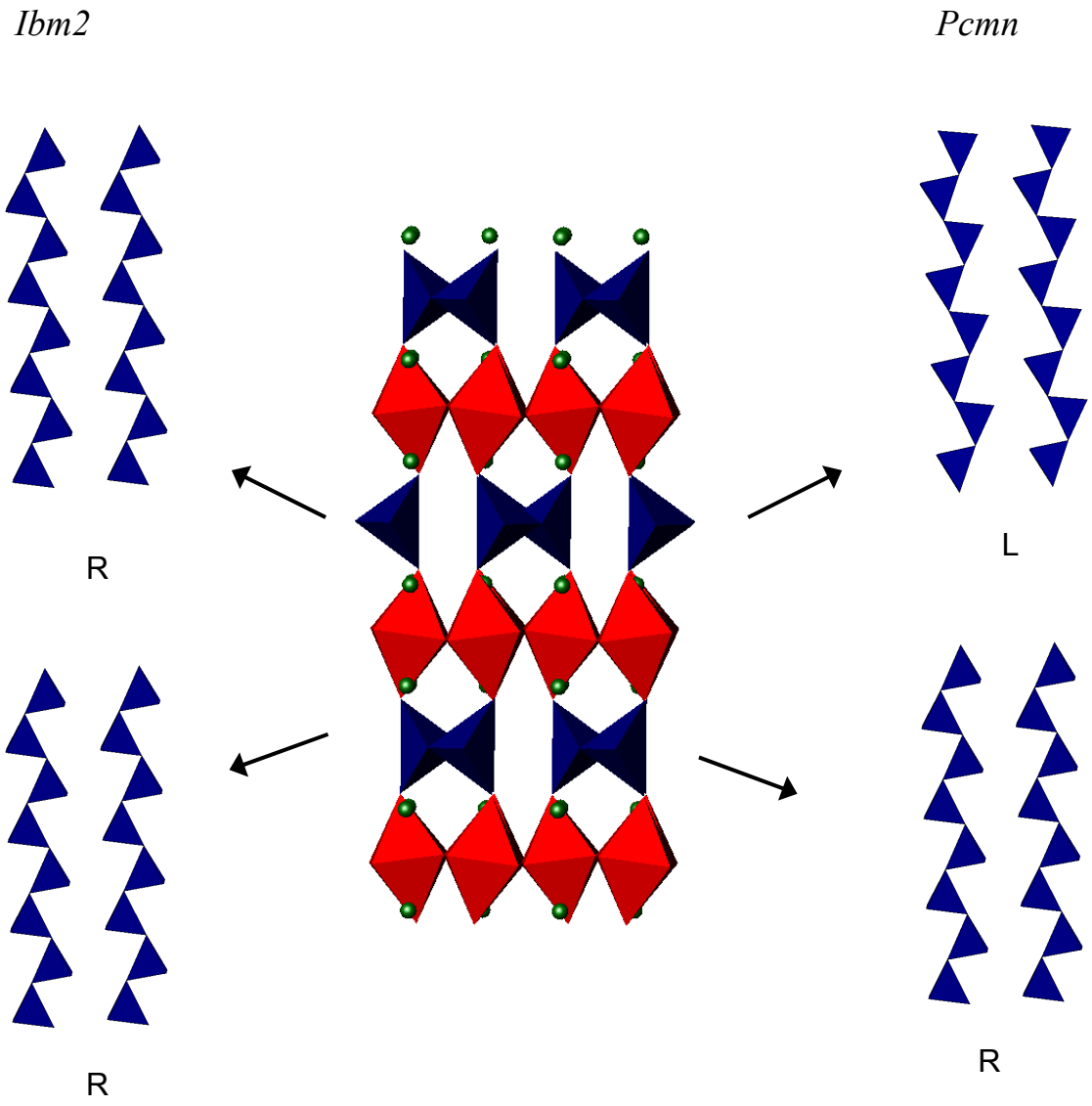

Figure 1.2. Diagram to show how the orientation of corner linked tetrahedral chains is related to space group for brownmillerite type structures.

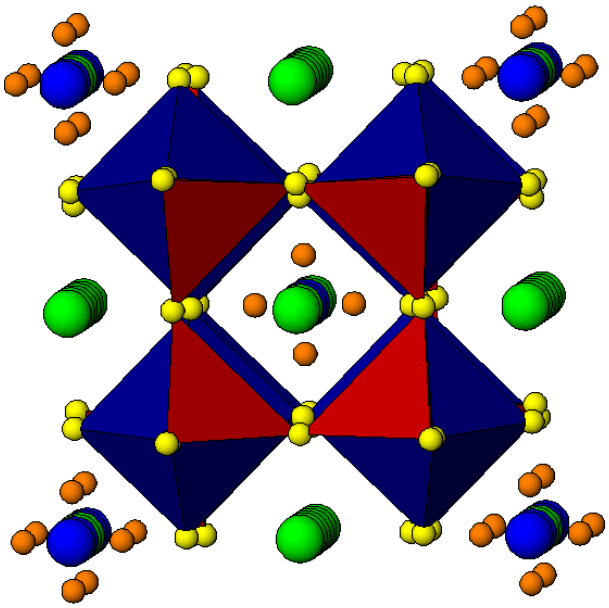

Figure 1.3. The tetrahedral layer in $YSr_3Mn_{4-x}Ga_xO_{10.5}$ viewed along [001] showing squares of corner-linked tetrahedra. MnO_6 are shown as blue polyhedra, Mn/GaO_4 as red polyhedra; yellow spheres are oxygen anions, orange spheres depict the ¼ occupied oxygen site, green spheres are $Sr(2)^{2+}$ cations and blue spheres are Y^{3+} cations.

1.2.3 Hematophanite Structure

The hematophanite structure is fully described in Chapter 5. The structure may be considered as an anion deficient perovskite, consisting of two FeO_5 square pyramids connected through a central FeO_6 octahedron, a Pb_2Cl intergrowth layer separates these triple perovskite blocks, as shown in *figure 1.4,* [13].

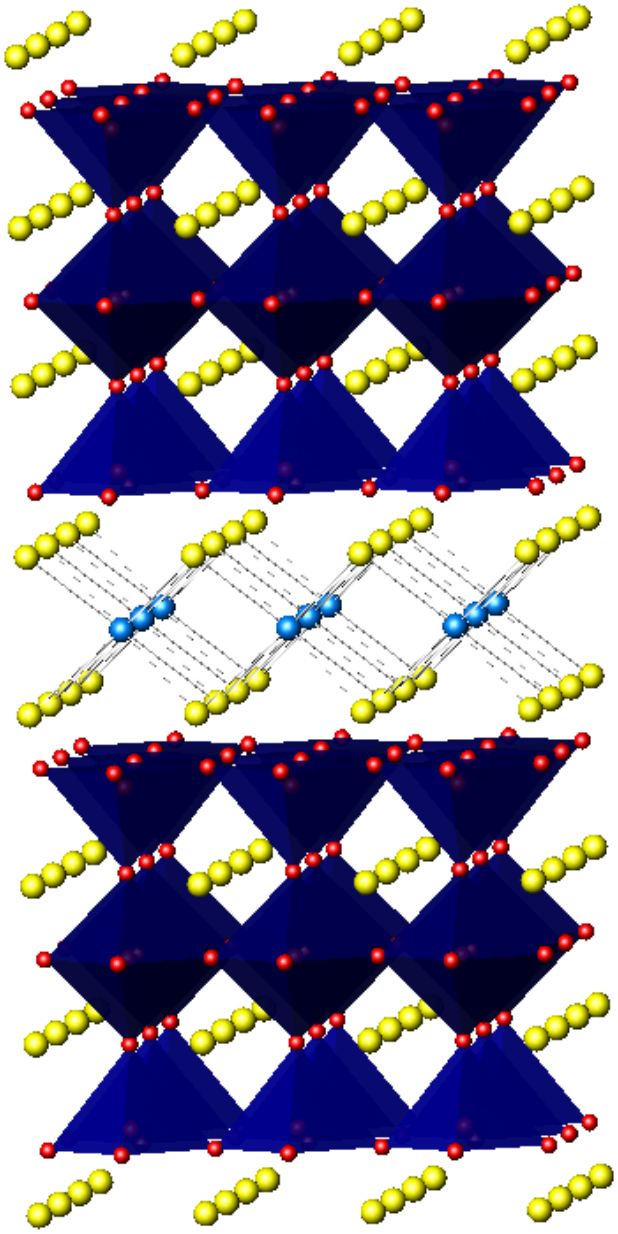

Figure 1.4. Crystallographic structure of $Pb_4Fe_3O_8Cl$. FeO_5 and FeO_6 are shown as blue polyhedra, red spheres are oxygen anions, yellow spheres are lead cations and light blue spheres are chloride anions.

1.3 Magnetoresitance and the Perovskite Structure

1.3.1 The Principles of Colossal Magnetoresistance

Magnetoresistance is defined as the change in electrical resistance induced by an external magnetic field and was first observed for iron samples by William Thomson, later to become Lord Kelvin, in 1857 [14]. Magnetoresistance (MR) is measured by one of the following *equations 1.2a or 1.2b.*

$$\mathrm{MR}(\%) = \frac{[\rho_H - \rho_0]}{\rho_H} \times 100 \qquad (1.2a)$$

$$\mathrm{MR}(\%) = \frac{[\rho_H - \rho_0]}{\rho_0} \times 100 \qquad (1.2b)$$

(where ρ_H = resistivity at applied field H and ρ_0 resistivity at applied field zero)

Although magnetoresistance is a phenomenon common to all metals and semiconductors to some degree, large negative magnetoresistance of greater than 50%, as defined by *equation 1.2b,* was discovered in a magnetic field strength of 2T at 4.2K for thin film multilayered Fe/ Cr/ Fe materials [15]. The multilayers consist of magnetic layers of iron separated by non-magnetic layers of chromium, coupling of Fe layers through non-magnetic Cr layers oscillates between antiferromagnetic (AFM) and ferromagnetic (FM) as the thickness of the Cr layers increases. When a magnetic field of 2T was applied to antiferromagnetically aligned multilayers the Fe spins aligned ferromagnetically and the resistivity of the material almost halved. The origin of this effect, termed giant magnetoresistance (GMR), is due to the fact that conduction electrons must have the same spin in order to hop between sites in the Fe layer via the

spacer (Cr) layer. When magnetic moments are aligned antiferromagnetically there is maximum resistivity, the application of a large magnetic field switches the magnetic alignment to ferromagnetic, enabling the conduction electrons to hop between sites and producing a large reduction in resistivity.

The development of GMR materials which operate at room temperature in reduced magnetic fields has led to commercial applications for these materials, for example as magnetic field sensors in the read heads of magnetic recording discs for computer information storage [16].

More recently the discovery of extremely large magnetoresistive effects, termed colossal magnetoresistance (CMR), in manganites with a perovkite or perovskite related structure have attracted considerable interest from a fundamental and technological point of view.

$La_{1-x}Ca_xMnO_3$ is the prototypical manganite that displays the CMR effect [17, 18, 19], as shown in *figure 1.5*. The end members of the series, $LaMnO_3$ and $CaMnO_3$ are antiferromagnetic insulators but in the doping range x ~ 0.2- 0.4, the ground state is ferromagnetic. As the temperature falls to T_c the paramagnetic to ferromagnetic transition is accompanied by a sharp drop in resistivity. A field induced insulator to metal transition is observed at temperatures above T_c on application of a magnetic field, the origin of this CMR effect can be partially explained by double exchange theory [20, 21].

The *3d* orbitals of Mn^{3+} in $LaMnO_3$ lose their degeneracy due to crystal field effects; Jahn Teller distortion further removes the degeneracy within the e_g and t_{2g} electronic energy levels, as illustrated in *figure 1.6.* In the parent material, $LaMnO_3$, the *3d* electrons are localised and the material is an insulator. Doping the material with Ca^{2+}

produces a material with mixed Mn^{3+} /Mn^{4+} valency, thereby creating electron vacancies or holes in the e_g orbitals, allowing the e_g electrons to become itinerant and act as conduction electrons; the t_{2g} electrons remain localized. Electron spins on each Mn site are aligned ferromagnetically by Hund's rule.

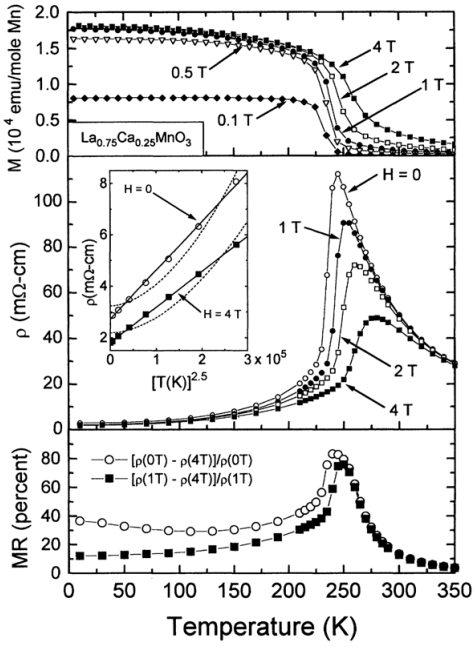

Figure 1.5. The magnetisation, resistivity and magnetoresistance of $La_{0.75}Ca_{0.25}MnO_3$ as a function of temperature at various fields. The inset shows ρ at low temperatures. Reproduced from [19].

The probability of the e_g electrons hopping between Mn^{3+} and Mn^{4+} sites, via the intervening O^{2-} anion, is proportional to $\cos\theta/2$ where θ is the angle between neighbouring Mn core spins and is therefore maximised when $\theta = 0$ [20]. Above T_c electron spins are disordered, the probability of hopping is reduced, as conduction electrons are strongly scattered by these misaligned spins and the material is an

insulator. Below T_c the e_g electron on Mn^{3+} can hop to the empty e_g orbital on Mn^{4+} if the spins on each of the two sites are ferromagnetically aligned. There is a kinetic energy saving if the hopping process is allowed and the overall energy of the system is reduced, hence it is energetically favourable for the material to be a ferromagnetic conductor below T_c.

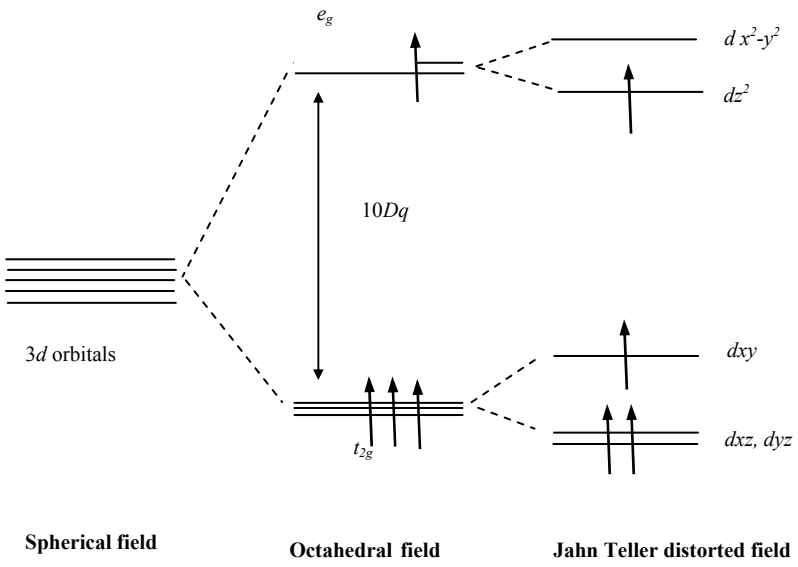

Figure 1.6. Crystal field splitting of five-fold degenerate *3d* into triply degenerate t_{2g} and doubly degenerate e_g energy levels, followed by Jahn Teller distortion of the MnO_6 octahedron further lifting the degeneracy as a result of elongation of the axial bonds.

Double exchange is not sufficient to explain the magnitude of the change in resistivity at the FM transition nor the very large resistivity above T_c, and research is on-going into other factors that influence the CMR effect [23]. By taking into consideration Electron- phonon coupling effects CMR can be explained more fully. Due to the Jahn Teller effect the transfer of an electron from Mn^{3+} to Mn^{4+} is accompanied

by a movement in the lattice distortion between sites, since Mn^{3+} would be Jahn Teller distorted and Mn^{4+} would not. The Mn^{3+} e_g electron is considered to be trapped in a potential well created by the lattice distortion; such a self- trapped electron is known as a polaron. These polarons are trapped in the lattice above T_c which explains the high resistivity of the paramagnetic state. As the temperature is decreased through T_c the ratio of electron itineracy to self-trapping energy increases to a point at which the polarons become itinerant and the material becomes metallic [23, 24].

1.3.2 Layered Perovskites and CMR

Although CMR of ~ 80%, based on *equation 1.2b,* has been reported for $La_{0.75}Ca_{0.25}MnO_3$ at temperatures of ~ 250K, high magnetic fields of ~ 4T are required to achieve these effects [19]. The aim of current research is to discover room temperature CMR materials that operate at lower field strengths, and the Ruddlesden-Popper series of compounds have received much interest in this respect. The n=2 Ruddlesden-Popper, $Sr_{1.8}La_{1.2}Mn_2O_7$, which comprises a double perovskite block separated by a rock salt Sr/LnO layer displays 200% MR in 0.3T at 126K, based on *equation 1.2a* [25]. As for simple perovskite CMR materials, the magnetoresistance effect in this material is associated with ferromagnetic ordering. The fall in magnetic ordering temperature for this layered material compared to the simple perovskite is due to weaker exchange interactions between the layers for this two dimensional material compared to the three dimensional perovskite.

1.4 Magnetic Ordering

Magnetic ordering in ionic solid such as $LaMnO_3$ or $CaMnO_3$ cannot be explained by direct exchange interactions since the magnetic cations are separated by O^{2-} anions. The indirect ordering of magnetic moments via a non-magnetic intermediary

is known as superexchange. The theory of superexchange was first developed by Kramers [26] and later expanded by Anderson [27]. The AFM ordering of magnetic spins below T_N in for example MnO is explained in *figure 1.7.*

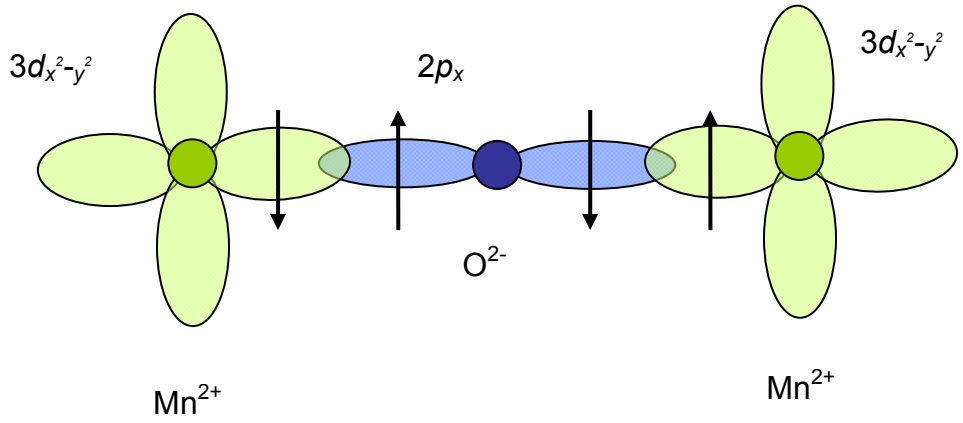

Figure 1.7a

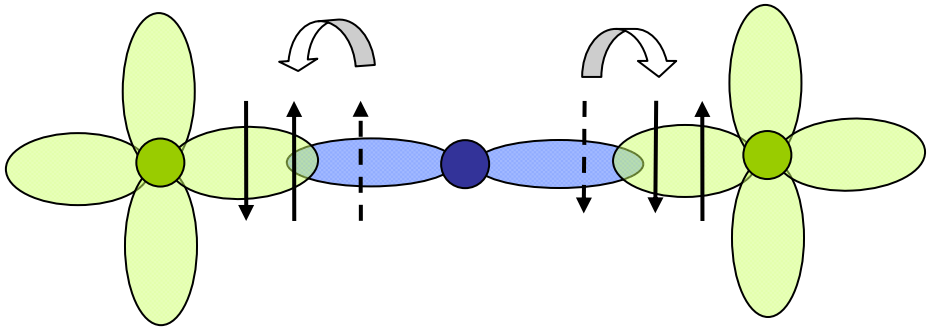

Figure 1.7b

Figure 1.7. Diagram to show the indirect interaction between Mn *3d* orbital known as superexchange. *1.7a.* Mn- O-Mn bond in the ground state with localised electron density. *1.7b.* Electron density is transferred from the O $2p_x$ to the Mn^{3+} $d_{x^2-y^2}$ orbital if aligned with opposite spin to existing Mn $d_{x^2-y^2}$ electron, by Pauli exclusion principle.

Where is there is sufficient overlap between O *2p* orbitals and Mn 3*d* orbitals covalency results and the overall energy of the system is lowered as O *2p* orbitals and Mn 3*d* become hybridised. This is only possible, by the Pauli exclusion principle if the spins on the magnetic ion are arranged antiferromagnetically when each of the overlapping magnetic ion orbitals is occupied.

Ferromagnetic exchange is predicted if an empty orbital of one magnetic ion is linked via an O *2p* orbital to the occupied orbital of another magnetic ion. Superexchange explains the magnetic ordering in $LaMnO_3$ which although ordered antiferromagnetically overall, the ordering between spins within *ab* planes is FM; these planes are then linked antiferromagnetically in the *c* direction. The MnO_6 octahedron in $LaMnO_3$ displays strong Jahn Teller distortion [30]. As a result of this Jahn Teller distortion orbitals are ordered so that the empty Mn^{3+} $d_{x^2-y^2}$ orbital is linked to a singly occupied Mn^{3+} d_{z^2} orbital via the interlinking O^{2-} *2p* orbital, within the *ab* plane as shown in *figure 1.8.* The overall energy of the system is lowered if oxygen *2p* electrons are able to transfer to the Mn e_g orbitals. The electron transferred to the occupied Mn orbital must be aligned with opposite spin to the electron in the d_{z^2} orbital, by the Pauli exclusion principle, whereas the electron transferred to the empty Mn orbital must be aligned with parallel spin to the electrons in occupied Mn orbitals, by Hund's rule. Therefore the interaction between a half-filled orbital and empty orbital is ferromagnetic. The extent of covalency between the anion and cation orbitals governs the strength of the superexhange interaction and hence the ordering temperature, T_N or T_c.

Goodenough and Kanamori [31] have further developed the theory to allow prediction of magnetic ordering for materials in which the cation-anion-cation bond

angle varies from the 180° shown in the *figures 1.7 and 1.8.* The Goodenough-Kanamori rules also take into consideration the weaker cation-anion-cation π bond interactions, although 180° σ bonding provides the strongest superexchange interaction.

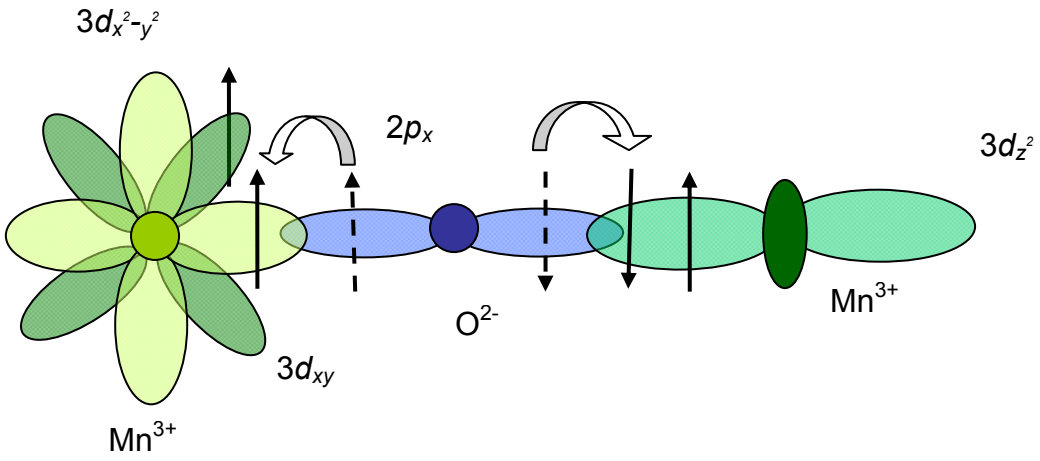

Figure 1.8. An unoccupied Mn^{3+} $3d_{x^2-y^2}$ is indirectly linked to an occupied $3d_{z^2}$ via a O^{2-} *2p* orbital. Electron density can move from the oxygen *2p* orbital if aligned with opposite spin to the electron in the occupied Mn $3d_{z^2}$, electron density can move from the oxygen *2p* orbital to the Mn $3d_{x^2-y^2}$ orbital if aligned with the same spin as electrons in other occupied Mn orbitals.

1.5 Aims of Project

The observation of CMR in low dimensional layered materials, such as the Ruddlesden-Popper material $Sr_{1.8}La_{1.2}Mn_2O_7$, has led to investigation of other layered perovskite-type materials with the potential for magnetoresistance. The brownmillerite-type material $YSr_3Mn_{4-x}Ga_xO_{10.5}$, studied in Chapters 3 and 4, is a layered anion deficient perovskite. It was proposed that changing the Mn:Ga ratio in this material

together with oxidation or fluorination would produce a layered perovskite-type material with the mixed Mn^{3+}/ Mn^{4+} valency. The structural and magnetic properties of this material would be of fundamental interest

Hematophanite, $Pb_4Fe_3O_8Cl$, is another layered perovskite material with interesting magnetic properties. Strong covalent Fe-O-Fe interactions result in a high AFM ordering temperature of ~ 602K. Substitution of Fe^{3+} by other magnetic cations such as Co^{3+} and Mn^{3+} offers the possibility of manipulating the electronic and magnetic properties of this material and its analogue $Pb_4Fe_3O_8Br$. The possibility of substitution on the Fe^{3+} sites is investigated in Chapter 5.

In Chapter 6 a more detailed structural characterisation of the lead oxychloride, $Pb_8WO_{10}Cl_2$ is made, following earlier single crystal x-ray powder diffraction by Aurivillius [32].

1.6 References

[1] S. Sasaki, C. T. Prewitt and J. D. Bass. *Acta Cryst.* **C43,** 1668, (1987)

[2] V.M. Goldschmidt. *Skrifer Norske Videnskaps-Akad. Oslo, I. Mat.-Nat*. Kl. 8 (1926).

[3] C. Li, K. Chi Kwan Soh and P. Wu. *Journal of Alloys and Compounds,* **372**, 40, (2004).

[4] J. B. Goodenough. *Rep. Prog. Phys.* **67,** 1915, (2004).

[5] S. N. Ruddlesden and P. Popper. *Acta Cryst.* **11**, 54, (1958).

[6] A. A. Colville and S. Geller. *Acta. Cryst.* **B27**,2311, (1971).

[7] P. Norby, E. K. Andersen and N. H. Andersen. *J. Solid State Chem.* **119**, 191, (1995)

[8] J. L. Garcia-Munoz, J. Rodriguez-Carvajal, P. Lacorre and J. B. Torrance. *Phys. Rev. B,* **46(8)**, 4414 (1992).

[9] A. J. Wright, H. M. Palmer, P. A. Anderson and C. Greaves. *J. Mater. Chem.* **12**, 978, (2002).

[10] P. D. Battle, A. M. T. Bell, S. J. Blundell, A. I. Coldea, D. J. Gallon, F. L. Pratt, M. J. Rosseinsky and C. A. Steer. *J. Solid State Chemistry*, **167**, 188, (2002).

[11] A. M. Abakumov, A. M. Alekseeva, M. G. Rozova, E. V. Antipov, O. I. Lebedev and G. Van Tendeloo. *J. Solid State Chemistry,* **174**, 319, (2003).

[12] L. J. Gillie, H. M. Palmer, A. J. Wright, J. Hadermann, G. Van Tendeloo, C Greaves. *Journal of Physics and Chemistry of Solids* 65, 87, (2004).

[13] C. S. Knee and M. T. Weller. *Journal of Materials Chemistry*, **11**, 2350, (2001).

[14] W. Thomson. *Proc. Royal Soc. (London)*, **A8**, 546 (1857).

[15] M. N. Baibich, J. M. Broto, A. Fert, F. Nguyen van Dau, F. Petroff, P. Eitenne, G. Creuzet, A. Friederich and J. Chazelas. *Phys. Rev. Lett.* **61**, 2472, (1988).

[16] G. A. Prinz. *Journal of Magnetism and Magnetic Materials,* **200**, 57, (1999).

[17] G. H. Jonker and J. H.Van Santen. *Physica,* **16**, 337, (1950).

[18] J. H.Van Santen and G. H. Jonker. *Physica,* **16**, 599, (1950).

[19] P. Schiffer, A. P. Ramirez, W. Boa and S-W. Cheong. *Phys. Rev. Lett.* **75**, 3336, (1995).

[20] C. Zener. *Phys. Rev.* **82**, 403, (1951).

[21] P. G. Gennes. *Phys. Rev.B*, **118**, 141 (1960).

[22] P. W. Anderson and H. Hasegawa. *Phys. Rev.* **100**, 675, (1955).

[23] A. J. Millis, B. I. Shraiman and R. Mueller. *Phys. Rev. Lett.***77**, 175, (1996).

[24] H. Röder, Jun Zang and A. R. Bishop. *Phys. Rev. Lett*. **76**, 1356, (1996).

[25] Y. Moritomo, A. Asamitsu, H. Kuwahara and Y. Tokura. *Nature*, **380**, 141, (1996).

[26] H. A. Kramers, *Physica* **1**, 182 (1934).

[27] P. W. Anderson, *Phys. Rev.* **79**, 350 (1950).

[28] P. W. Anderson, *Phys. Rev.* **79**, 705 (1950).

[29] J. B. Goodenough, *Magnetism and the Chemical Bond* (VCH-Wiley, New York, 1963).

[30] S. Satpathy, Z. S. Popović and F. R. Vukajlović. *Phys. Rev. Letters,* **76**, 6, 960, (1996).

[31] J. B. Goodenough. *Magnetism and the Chemical Bond.* John Wiley & Sons, (1963).

[32] B. Aurivillius. *Chemica Scripta,* **19**, 97 (1982).

CHAPTER 2

Experimental Techniques

2.1 Synthetic Techniques

2.1.1 Synthetic Methods

All materials were synthesised using standard ceramic methods. Stoichiometric quantities of high purity metal oxides and/ or carbonates were ground together with an agate pestle and mortar until a homogeneous mixture was produced. The reaction mixtures were heated to the appropriate temperature in an alumina crucible. The environment in the furnace could be controlled by excluding air and passing gases such as N_2 over the reaction vessel.

Following grinding and heating to the appropriate temperature, reaction takes place at the point of contact between the reaction grains; high temperatures are required to allow the diffusion of the ions to the points of contact. As the reaction proceeds, the product grains grow and the diffusion pathway increases. High temperature and repeat grindings are required to create new contact points between the grains until a homogeneous phase is produced [1].

2.1.2 Fluorination

Fluorination was carried out by heating the reaction mixture in a mixture of 10% $F_2(g)$/ 90% $N_2(g)$ in a nickel foil crucible using equipment designed to resist the corrosive effects of F_2 gas. The components were made from nickel, copper and PTFE (polytetrafluoroethylene), which are resistant to attack by F_2 and HF. Gases entering the equipment were initially passed through a vessel containing a desiccant and NaF pellets to remove any traces of moisture. The reaction mixture was placed in the foil crucible in a nickel furnace tube, and air and traces of moisture were flushed from the furnace by

N_2 gas before heating. The reaction mixture was then heated to the required temperature while exposed to a steady stream of 10% F_2(g)/ 90% N_2(g). The equipment remained sealed to the atmosphere during the heating process. N_2 gas was again used to purge the fluorine from the system before opening the furnace to the atmosphere.

2.2 Diffraction Techniques

2.2.1 Powder Diffraction

The polycrystalline materials synthesised in this thesis have been characterised initially by X-ray powder diffraction (XRPD) and subsequently by neutron powder diffraction (NPD) when a more detailed structural characterisation or magnetic characterisation was required.

Incident radiation is reflected from lattice planes in the crystal according to Bragg's law [2] as shown in *figure 2.1*. The powder sample is composed of many randomly orientated crystallites some of which will be aligned to allow constructive interference of the reflected radiation. *Figure 2.1* shows that the difference in the path lengths between adjacent planes, *d,* can be related to the angle of incidence by *equation 2.1*.

$$xy + yz = 2d\sin\theta \qquad (2.1)$$

The radiation reflected from the lower plane has travelled the extra distance xy + yz compared to that reflected from the upper plane, for constructive interference this distance must be an integer number of wavelengths.

$$xy + yz = n\lambda \qquad (2.2)$$

Therefore the Bragg equation is derived

$$2d \sin\theta = n\lambda \qquad (2.3)$$

Constructive interference from successive planes within the powder sample produce a diffraction pattern from which the unit cell size and symmetry of the material can be determined. Rietveld refinement [3] of diffraction data allows determination of atom coordinates from the position and relative intensity of the diffraction peaks. In order for diffraction to take place the wavelength of the incident radiation must be similar to the interatomic spacing.

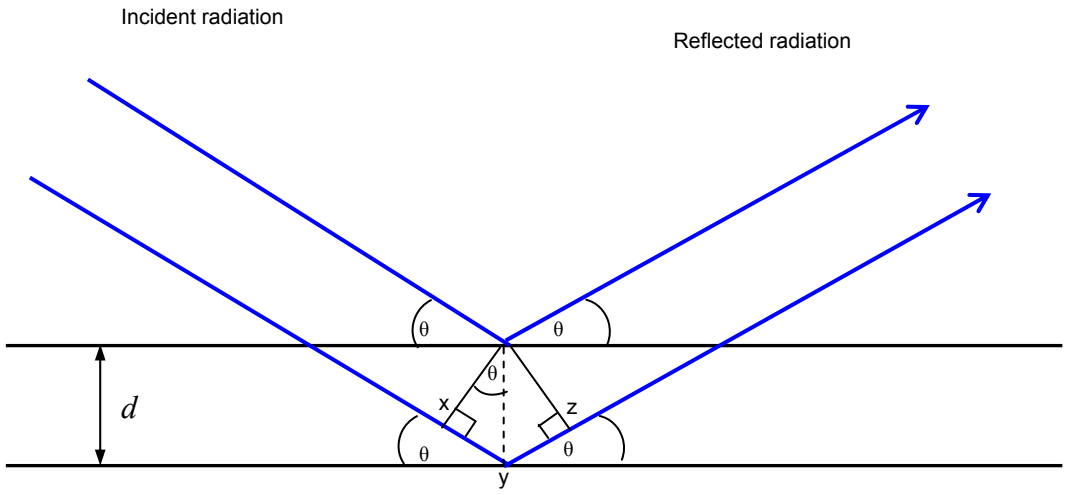

Figure 2.1. Diagram to illustrate the derivation of Bragg's law, showing incident radiation reflected from crystal lattice planes.

2.2.2 X-ray Powder Diffraction

The characterisation of crystalline solids is frequently achieved by X-ray powder diffraction (XRPD). Each crystalline solid has characteristic XRPD pattern, which can be compared to a database of known patterns, for example the JCPDS database [4], for identification. For unidentified materials computer programs 'Index', 'Dspace' and 'Cell'[5, 6, 7] were initially used to assign Miller indices and determine unit cell parameters. Rietveld refinement of the XRPD data of unidentified materials was used for further structural characterisation.

X-rays are produced when electrons are accelerated through a voltage of about 30000V and targeted at a metal such as copper. The X-ray spectra produced have two components: radiation with a broad spectrum of wavelengths or Bremstrahlung radiation produced as electrons decelerate and convert kinetic energy to electromagnetic radiation and a second component which consists of electromagnetic radiation of several well defined wavelengths or monochromatic X-rays. This monochromatic radiation is produced as a result of the incident electrons providing sufficient energy to ionise the copper 1*s* (*K* shell) electrons, as an electron in an outer orbital (2*p* or 3*p*) drops down to replace this electron energy is released. The energy released will have a quantified wavelength corresponding to the difference in energy between the outer orbital and the inner 1*s* orbital. The diffractometer used in this work uses X-rays of wavelength 1.5406Å or Cu $K\alpha_1$ which corresponds to the transition from the 2*p* shell to the 1*s* shell for copper. The $K\alpha_2$ transition is of slightly lower energy (1.54433 Å) and corresponds to the transition from the Cu 2*p* orbital with a different spin state to the 1*s* orbital. These two closely related transitions show as a doublet in the X-ray emission spectrum [8].

A Siemens D5000 diffractometer operating in transmission mode was used to collect XRPD profiles in this work. A Ge crystal monochromator selected purely $K\alpha_1$ radiation and focused the X-ray beam. A moveable 2θ position sensitive detector (PSD) with a step size of 0.02^o and angular range 8 degrees recorded the transmitted x-rays.

2.2.2.1 Structural determination from XRPD

The 2θ peak positions from the X-ray diffraction pattern can be used to determine the interplanar *d*-spacing and hence allow determination of the lattice parameters. Not all lattice planes, denoted by the Miller indices *h k l*, give rise to a peak in the diffraction pattern; these systematic absences can distinguish between primative, body centred and face centred unit cell symmetry and help identify the space group.

The intensity, I_{hkl}, of diffracted X- ray radiation can be related to the type of atoms on the atomic planes and the fractional coordinates of the atoms on these planes by the *equation 2.4*.

$$\sqrt{I_{hkl}} \propto F_{hkl} = \sum_{j=1}^{m} N_j f_j \, exp\,[\,2\,\pi i\,(hx_j + ky_j + lz_j) \qquad (2.4)$$

The structure factor, F_{hkl}, quantifies the amplitude of X-ray radiation scattered by the crystal. F_{hkl} is the sum of the scattering from all of the atoms in the unit cell to form a diffraction peak from the *hkl* planes of atoms. F_{hkl} depends on where the atoms are in the unit cell, i.e. their fractional coordinates, *x y z,* and what type of atom is in a site.

The scattering factor, *f,* in *equation 2.4* quantifies the efficiency of scattering from the electrons around an atom. X-rays interact with the electrons of an atom. Atoms with a greater number of electrons scatter X-rays more strongly therefore atoms with a higher atomic number produce more intense diffraction peaks and light atoms such as hydrogen are difficult to locate by XRPD. The scattering factor, *f,* also depends on the

interference effects between the radiation scattered from different electrons around an atom. This interference effect varies as function of sinθ/ λ, hence the atomic scattering factor decreases with sinθ/ λ resulting in a gradual decrease in peak intensity at high angles. N_j in *equation 2.4* is the fraction of every equivalent position that is occupied by atom j. The scattering factor is quantified in *equation 2.5*.

$$|f|^2 = \left(f_0 \exp\left[\frac{-B \sin 2\theta}{\lambda} \right] + \Delta f' \right)^2 + (\Delta f'')^2 \qquad (2.5)$$

Referring to *equation 2.5,* f_0 is equal to the number of electrons for a specific atom, B is the Debye-Waller temperature factor, f' and f'' are anomalous scattering factors. The Debye-Waller temperature factor, B, quantifies the reduction in scattering due to the vibration of the atom about its lattice site. B can be related to the thermal parameter used in refinements, U, by *equation 2.6*. Where U is the mean squared displacement of the atom with respect to its equilibrium position in $Å^2$. The anomalous scattering factors, f' and f'', are greatest when the incident X-ray energy approaches the ionisation energy of the atom and account for the change in phase of some of the scattered photons compared to the majority [9, 10, 11].

$$B = 8\pi^2 U \qquad (2.6)$$

2.2.3 Neutron Powder Diffraction

Although neutron powder diffraction (NPD) is an expensive technique and can be only be accessed at national laboratories, it can provide additional information to

XRPD. The interaction of neutrons with the atomic nucleus is weaker than the interaction between X-rays and the atomic electrons, therefore larger samples are required to obtain sufficiently intense diffraction peaks from NPD. The intensity of NPD peaks does not increase with atomic number as for X-rays but varies with isotope in a non-systematic way. Therefore some lighter elements such as hydrogen are relatively strong scatterers of neutrons and can be detected by NPD. It is also possible to distinguish between elements with similar atomic numbers. The size of atomic nuclei are considerably smaller than the wavelength of the incident neutrons therefore the nuclei act as 'point scatterers' and interference effects do not increase with $\sin\theta/\lambda$. As a result the intensity of scattered neutrons does not fall off with $\sin\theta/\lambda$. Neutrons have a magnetic moment that enables them to interact with the unpaired electrons in a material, hence extra Bragg peaks are evident in the diffraction pattern when data is collected below the ordering temperature of the material. These additional peaks allow determination of the magnetic structure of a material. NPD facilities use nuclear reactors or the spallation process as a source of neutrons [12, 13]

2.2.3.1 Neutron Powder Diffraction Techniques

The nuclear reactor source at Institut Laue- Langevin (ILL), Grenoble, France and the spallation sources at; ISIS, Rutherford Appleton Laboratory, Oxford, UK and SINQ at Paul Scherrer Institut, Switzerland were used in this work.

Neutrons are generated at ILL as a result nuclear fission of U^{235}. The wavelength of the neutrons is moderated by D_2O in order to produce the wavelengths comparable to interatomic distances required for diffraction techniques. The constant wavelength used at nuclear facilities is selected using a crystal monochromator. At ILL instrument D2B

was used, a wavelength of 1.59432 Å was selected with a Ge crystal monochromator. The intensity of the diffracted beam was measured as a function of 2θ.

Neutrons at ISIS are produced as a result of spallation, a process in which a heavy metal target is bombarded by accelerated high energy protons. This process produces pulsed neutrons with a range of wavelengths. In contrast to X-ray techniques and neutron sources using fixed wavelengths, the sample is irradiated by neutrons with a range of wavelengths and the detector is fixed at an angle 2θ to the incident radiation. The velocity of the incident neutrons can be calculated from the path length to the sample, *L*, hence the wavelength of the incident neutrons can be calculated from the de Broglie relationship, *equation 2.7.*

$$\lambda = \frac{h}{mv} \qquad (2.7)$$

by combining Bragg's Law we get *equation 2.8,*

$$\lambda = 2d\sin\theta = \frac{h}{mv} = \frac{ht}{mL} \qquad (2.8)$$

Where t= time of flight of neutron along pathlength and L = distance of path, hence the interplanar distance, *d,* is recorded as a function of the time of flight, *t*, in spallation source instruments such as POLARIS, used in this work. POLARIS uses a number of detectors arranged in a series of banks, each with a specific *d*-spacing range [13, 14, 15]

2.2.3.2 Stuctural Determination using NPD

The intensity of diffracted neutron radiation, I_{hkl}, can be related to the position and type of atom in the unit cell, as for X-ray techniques. As for XRPD the intensity of a Bragg peak is proportional to the square of the structure factor F_{hkl}. The structure

factor is related to the positions, x_j, y_j ,z_j, of all the j atoms in the unit cell by *equation 2.9*.

$$F_{hkl} = \sum_j n_j f_j \exp\left(2\pi i\left(hx_j + ky_j + lz_j\right)\right) \times \exp\left(-\frac{B_j \sin^2\theta}{\lambda^2}\right) \qquad (2.9)$$

The atomic scattering factor, f_j, is different for NPD compared to XRPD and is not related to atomic number, the scattering power of a particular atom is related to the properties of the nucleus, hence as mentioned earlier there is no systematic increase in scattering power with atomic number. B_j in *equation 2.9* is the Debye- Waller temperature factor that, as in XRPD, accounts for the reduction in intensity due to the vibration of atoms about their mean position. The intensity of the Bragg peaks is also influenced by other factors such as absorption, extinction and preferred orientation.

A neutron is a spin ½ particle as a result of which magnetic scattering occurs from the dipole-dipole interaction between the magnetic moment of a neutron and the magnetic moment of an atom during NPD [16]. Due to destructive interference between scattering from different parts of the electron cloud the intensity of magnetic Bragg peaks decreases with 2θ as observed for XRPD. Additional Bragg peaks due to magnetic interactions are evident below the ordering temperature of a material. The structure factor, F_{mag} is given by equation *2.10*, where q_j is the magnetic interaction vector and p is the magnetic scattering length.

$$F_{mag} = \sum_j q_j p_j \exp\left(2\pi i h x_j\right) \qquad (2.10)$$

The magnetic scattering length, *p,* is calculated from the magnitude of the magnetic moment on an atom, *S,* and the magnetic form factor, f_m according to *equation 2.11* [13, 14, 15]

$$p = Sf_{m\times} 0.54 \times 10^{-12}\, cm \qquad (2.11)$$

2.4 Rietveld Refinement

The Rietveld method is a technique widely used in the characterisation of polycrystalline materials. The diffraction pattern consists of a series of peaks with a position, shape and integrated area that can be related to lattice parameters, atom type and atom position as described above. Due to overlap between the peaks it is not always possibly to fully resolve these peaks. The Rietveld method overcomes difficulties due to peak overlap by calculating the expected intensity for each individual point in the diffraction pattern. With an understanding of the effects of the diffractometer parameters on the peak shape and width and a knowledge of the effects of the sample parameters on the peak position and intensity, a model of the diffraction profile can be produced. This model is then refined until the fit between the observed profile and the modelled profile is optimum. The least squared method is used to determine the best fit between the model and experimental profile. The quantity minimised is the residual S_y *equation 2.12.*

$$S_y = \sum_i w_i \left(y_i - y_{ci}\right)^2 \qquad (2.12)$$

Where y_i is the observed intensity, y_{ci} is the calculated intensity and $w_i = y_i^{-1}$ is a weighting factor for the i^{th} data point. The quality of fit between the observed and calculated model is assessed using reliability factors R_{wp} (R weighted pattern) and R_p (R pattern) *equations 2.13* and *2.14.*

$$R_{wp} = \left\{ \frac{\sum w_i \left(y_i - y_{ci} \right)^2}{\sum w_i y_i^2} \right\}^{1/2} \qquad (2.13)$$

$$R_p = \frac{\sum \left| y_i - y_{ci} \right|}{\sum y_i} \qquad (2.14)$$

The value χ^2, *equation 2.15*, is used to assess the fit of the refinement taking into consideration the number of parameters used and the quality of the data.

$$\chi^2 = \left(\frac{R_{wp}}{\mathrm{R_e}} \right)^2 \qquad (2.15)$$

where

$$\mathrm{R_e} = \left\{ \frac{\left(n - p + c \right)}{\sum w_i y_i^2} \right\}^{1/2} \qquad (2.16)$$

and n = number of points; p = number of variables and c = number of constraints applied.

2.3 Magnetic Measurements

DC magnetic measurements were used to measure the magnetisation of samples as a function of temperature, using a Quantum Design Model 6000 Physical Properties Measurement System (PPMS). The method known as extraction magnetometry was used in which the sample is moved relative to an external magnetic field provided by a superconducting magnet, a voltage is induced in the pickup coils. The amplitude of this induced voltage is proportional to the magnetic moment of the sample and the speed of extraction. Zero field cooled (ZFC) and field cooled (FC) measurements were made. The sample is cooled in the absence of a magnetic field for ZFC measurements, with measurements taken and a field applied on warming. FC samples are cooled in a magnetic field, which remains as measurements are taken on warming.

2.4 References

[1] A. K. Cheetham and P. Day. *Solid State Chemistry,* Oxford University Press, (1990).

[2] W. L. Bragg. *Proc. Camb. Phil. Soc.* **17,** 43 (1913).

[3] H. M. Rietveld. *Acta Cryst.* **22,** 157 (1967).

[4] International Centre for Diffraction Data, Powder Diffraction File, PDF-2 (sets 1-14)

[5] D. Louer and M. Louer. *Journal Appl. Cryst.* **5,** 271, (1972).

[6] Computer program written by C. Greaves. *University of Birmingham,* (1982).

[7] Computer program written by M. F. Pye. *Inorganic Chemistry Laboratory, Oxford.*

[8] A. R. West. *Basic Solid State Chemistry,* John Wiley & Sons, (1991).

[9] J. M. Cowley. *Diffraction Physics,* North- Holland Physics Publishing (1981).

[10] D. T. Cromer and J. Mann. *Acta Cryst.* **A24**, (1968).

[11] M. F. C. Ladd and R. A. Palmer. *Structure Determination by X-ray Crystallography.* Plenum Press, (1985).

[12] Y. A. Izyumov, V. E. Naish, and R. P. Ozerov. *Neutron Diffraction of Magnetic Materials* (Plenum Publishing Corp., New York, 1991).

[13] R. I. Smith. *Neutron Training Course Manual,* Chapter 1,3. ISIS, Rutherford Appleton Laboratory.

[14] C. G. Windsor. *Pulsed Neutron Scattering,* Taylor and Francis, London, (1981)

[15] S. W. Lovesay. *Theory of Neutron Scattering from Condensed Matter,* Oxford University Press, (1986).

[16] O. Halpern and M. H. Johnson. *Phys. Rev.* **55**, 898, (1939).

[17] R. A. Young. *The Rietveld Method*, Oxford University Press, (1996).

CHAPTER 3

Structural and Magnetic Characterisation of the Brownmillerite related material $YSr_3Mn_{4-x}Ga_xO_{10.5}$

3.1 Background

The structure of brownmillerite (Ca_2FeAlO_5), a major constituent of Portland cement, has been extensively studied [1- 7]. As shown in *figure 3.1*, it consists of alternating oxygen deficient perovskite layers of corner sharing octahedra and layers of tetrahedra. Aluminium preferentially occupies the tetrahedral site to give the following site occupancies, $Ca_2[Fe_{0.76}Al_{0.24}]_{oct}[Al_{0.76}Fe_{0.24}]_{tet}O_5$ [7]. Brownmillerite crystallises in space group *Ibm2*, with lattice parameters a = 5.584(5), b = 14.60(1) and c = 5.374(5) Å [7].

The manganese containing brownmillerite Sr_2MnGaO_5 [8, 9] crystallises in space group *Icmm* and differs from Ca_2FeAlO_5 in the ordering of the corner-linked tetrahedral chains that run along the [001] direction of the unit cell. Differences in the ordering of the oxygen atoms within the tetrahedral layer result in two different orientations for the tetrahedral chains within the same tetrahedral layer for Sr_2MnGaO_5 with space group *Icmm* therefore giving the best fit following rietveld refinement of NPD (neutron powder diffraction) data [9]. A full description of the relationship between tetrahedral chain orientation and space group for brownmillerites is given in Chapter 1. Sr_2MnGaO_5 consists of alternate layers of MnO_6 and GaO_4 tetrahedra. The apical bonds of the octahedra are elongated due to Jahn-Teller distortion.

Brownmillerite type materials with a double octahedral layer separated by a single tetrahedral layer have been reported, for example $Ca_2AFe_2TiO_8$ (A= Ca, Sr or Ba)

[10] and $Ca_3Mn_{1.35}Fe_{1.65}O_{8.02}$ [11]. In the former Ti^{4+} is found in the octahedral site only, Fe^{3+} is found in both octahedral and tetrahedral sites. Manganese and iron are found in both tetrahedral and octahedral sites in $Ca_3Mn_{1.35}Fe_{1.65}O_{8.02}$, with Mn^{3+} found in square pyramidal coordination in some of the 'tetrahedral' sites as a result of excess oxygen in this layer.

Layered manganite materials, such as the n= 2 Ruddlesden-Popper phase $La_{2-2x}Sr_{1+2x}Mn_2O_7$ show colossal magnetoresistance (CMR) at values of x = 0.3- 0.4 [12]. Brownmillerite type materials offer an alternative low dimensional structure with the possibility of displaying CMR at appropriate levels of doping. $Ca_{2.5}Sr_{0.5}GaMn_2O_8$ is an example of a brownmillerite type material that exhibits mangentoresistance. $Ca_{2.5}Sr_{0.5}GaMn_2O_8$ consists of two layers of MnO_6 octahedra, separated by a single layer of GaO_4 tetrahedra. It exhibits ~ 50% magnetoresistance in an applied field of 8T at 110K [13]. This material contains mixed valence Mn^{3+}/ Mn^{4+} within in the octahedral layer.

The brownmillerite related material, $Y_{0.8}Sr_{2.2}Mn_2GaO_{8-\delta}$, was synthesised, with a view to producing a material with Mn^{3+} in a double layer of MnO_6 octahedra separated by a diamagnetic layer of GaO_4 tetrahedra [14]. The material synthesised unexpectedly consisted of a single octahedral layer separated by a tetrahedral layer.

The material $Sr_{0.7}Y_{0.3}\ CoO_{2.62}$ ($Sr_{2.1}Y_{0.9}Co_3O_{7.9}$), which is iso-structural with $Y_{0.8}Sr_{2.2}Mn_2GaO_{8-\delta}$, consists of single layers of CoO_6 octahedra separated by oxygen deficient layers of CoO_4 tetrahedra/ CoO_5 square pyramids [15]. The square pyramidal coordination is disordered and occurs as a result of bonding to a 25% occupied oxygen site within the tetrahedral layer. The lattice parameters are related to the perovskite unit cell, a_p, by $2a_p \times 2a_p \times 4a_p$. The structure is very sensitive to yttrium content. Yttrium

contents of $0.15 \leq x \leq 0.25$ for $Sr_{1-x}Y_xCoO_{2.62}$ lead to distortion of the tetragonal unit cell, space group I4/*mmm*, to the orthorhombic unit cell, *Cmma*, with lattice parameters $2\sqrt{2}a_p \times 2\sqrt{2}a_p \times 4a_p$. $Sr_{0.7}Y_{0.3}CoO_{2.62}$ exhibits G-type antiferromagnetic (AFM) ordering with an ordering temperature of ~ 320K [15, 16,17].

Substitution of Co^{3+} by Fe^{3+} was possible for $Sr_{0.75}Y_{0.25}CoO_{2.62}$. Substitution levels up to $x \leq 0.625$ were achieved for $Sr_{0.75}Y_{0.25}Co_{1-x}Fe_xO_{2.625+\delta}$ ($Sr_{2.25}Y_{0.75}Co_{3-3x}Fe_{3x}O_{7.875+3\delta}$), resulting in a material that is iso-structural with $Y_{0.8}Sr_{2.2}Mn_2GaO_{8-\delta}$. $Sr_{0.75}Y_{0.25}Co_{0.5}Fe_{0.5}O_{2.625+\delta}$ displays G-type AFM ordering at room temperature [18, 19].

The material investigated in this chapter, $YSr_3Mn_{2.67}Ga_{1.33}O_{10.5}$, is iso-structural with the brownmillerite related material $Y_{0.8}Sr_{2.2}Mn_2GaO_{7.9}$, fully characterised by Gillie *et al* [14]. $Y_{0.8}Sr_{2.2}Mn_2GaO_{7.9}$ may be considered as a brownmillerite-type structure with the formula $Y_{0.53}Sr_{1.47}Mn^{oct}Mn_{0.33}{}^{tet}Ga_{0.67}{}^{tet}O_{5.27}$, as shown in *figure 3.2*. The extra oxygen is required to balance the trivalent A cation, Y. $Y_{1.07}Sr_{2.93}Mn_{2.67}Ga_{1.33}O_{10.53}$ / $Y_{0.8}Sr_{2.2}Mn_2GaO_{7.9}$ crystallises with body centred tetragonal symmetry, in space group I4/*mmm*. The material consists of alternating layers of octahedral and tetrahedral polyhedra. The octahedral layers are preferentially occupied by manganese and the tetrahedral layers comprise 67% Ga and 33% Mn cations. The A cations (Y/Sr) are located in an ordered array in the interstices between the octahedral and tetrahedral layers. $YSr_3Mn_{2.67}Ga_{1.33}O_{10.5}$ has an unusual arrangement of the tetrahedra, which are arranged in isolated squares in the [001] direction rather than the corner linked chains of tetrahedra that are more common for the brownmillerite-type structure, as described fully in Chapter1 and *figure 1.3*. The extra oxygen, compared to the generic brownmillerite, was considered to be associated with

Mn^{3+} in the tetrahedral layers leading to a square pyramidal coordination for these cations. Mn^{3+}, a d^4 cation, is often stabilised in an oxide environment by square pyramidal coordination as a result of Jahn-Teller distortion. $Y_{0.8}Sr_{2.2}Mn_2GaO_{7.9}$ / $Y_{1.07}Sr_{2.93}Mn_{2.67}Ga_{1.33}O_{10.53}$ is antiferromagnetic (AFM), with a Néel temperature of ~ 100K [14].

It was proposed that changing the ratio of manganese to gallium followed by subsequent oxidation or fluorination, resulting in materials with a mix of Mn^{3+} and Mn^{4+} may offer a means of manipulating the magnetic properties of the material.

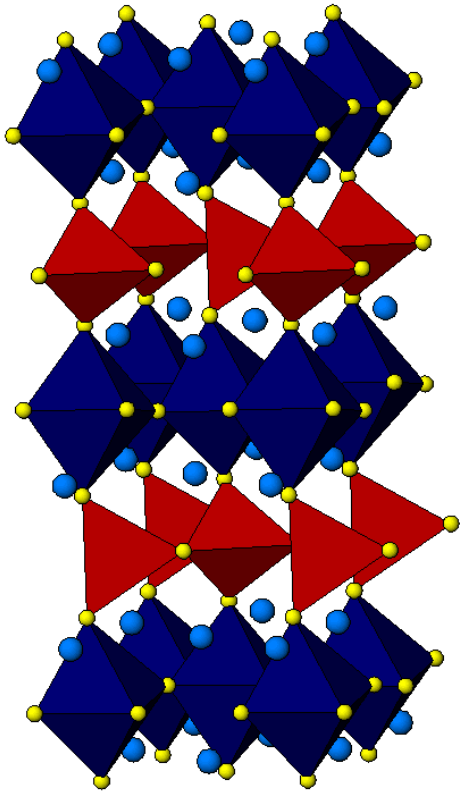

Figure 3.1. Crystallographic structure of brownmillerite, Ca_2FeAlO_5. Showing Fe/AlO_6 as blue polyhedra, Fe/AlO_4 as red polyhedra, yellow spheres are oxygen anions, blue spheres are Ca^{2+} ions.

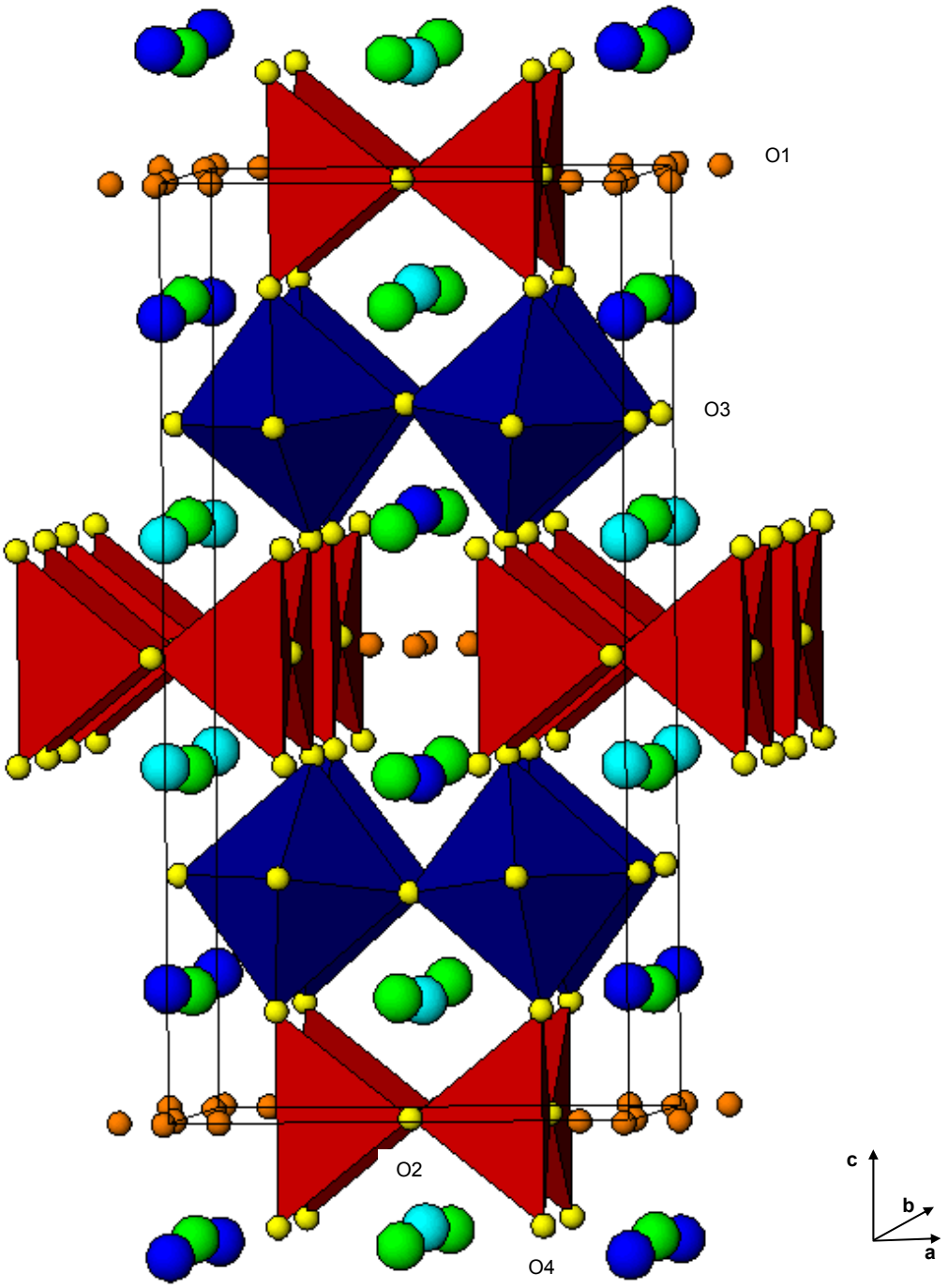

Figure 3.2. Crystallographic structure of $YSr_3Mn_{2.67}Ga_{1.33}O_{10.5.}$ Showing MnO_6 as blue polyhedra, Mn/GaO_4 as red polyhedra, yellow spheres are oxygen anions, orange spheres depict the ¼ occupied oxygen site, turquoise spheres are $Sr1^{2+}$, green spheres are $Sr2^{2+}$ cations and blue spheres are Y^{3+} cations. Axes of unit cell shown.

3.2 Synthesis of $YSr_3Mn_{4-x}Ga_xO_{10.5}$

Samples with various ratios of Mn: Ga were synthesised using standard ceramic methods. Stoichiometric quantities of Y_2O_3, $SrCO_3$, Ga_2O_3 and Mn_2O_3 were ground to produce a homogeneous mixture. The samples were fired in flowing nitrogen at 1250^oC for several periods of 12 hours, with intermediate grindings, to achieve phase purity. Sample purity was monitored by X-ray powder diffraction (XRPD, Siemens D5000, PSD, Ge monochromator, $CuK_{\alpha 1}$ radiation).

3.3 Structural Characterisation of $YSr_3Mn_{4-x}Ga_xO_{10.5}$

XRPD indicated that single phase samples could be produced with a maximum Mn: Ga ratio of 3.1:0.9 and a minimum ration of 2.23:1.77. *Table 3.1* lists the samples synthesised together with the theoretical occupancy of the octahedral and tetrahedral sites, assuming preference of manganese for octahedral sites.

Table 3.1. Single phase materials synthesised, together with theoretical octahedral and tetrahedral site occupancy.

Sample	**Theoretical octahedral site occupancy**	**Theoretical tetrahedral site occupancy**
$YSr_3Mn_{3.1}Ga_{0.9}O_{10.5}$	Mn^{3+} 1	Mn^{3+} 0.55, Ga^{3+} 0.45
$YSr_3Mn_{2.67}Ga_{1.33}O_{10.5}$	Mn^{3+} 1	Mn^{3+} 0.335, Ga^{3+} 0.665
$YSr_3Mn_{2.3}Ga_{1.7}O_{10.5}$	Mn^{3+} 1	Mn^{3+} 0.15, Ga^{3+} 0.85
$YSr_3Mn_{2.23}Ga_{1.77}O_{10.5}$	Mn^{3+} 1	Mn^{3+} 0.115, Ga^{3+} 0.885

Room temperature and 2K time of flight neutron powder diffraction (NPD) data were collected at POLARIS, ISIS, UK, for the samples listed in *table 3.1*. NPD allows the distribution of the Mn and Ga cations to be determined precisely due to the constrasting scattering lengths of the nuclei, Mn -3.73×10^{-15} m, Ga 7.88×10^{-15} m [20]. NPD also provides a more reliable determination of the oxygen sublattice compared to XRPD. Refinement of NPD data using the GSAS suite of programs [21] was carried out, with background parameters, lattice parameters, thermal parameters, histogram scale factors, diffractometer zero point, peak shape (pseudo-Voigt), atomic coordinates and fractional occupancies of the octahedral, tetrahedral and partially occupied oxygen site refined. The Rietveld plots for samples $YSr_3Mn_{3.1}Ga_{0.9}O_{10.4}$, $YSr_3Mn_{2.67}Ga_{1.33}O_{10.5}$, $YSr_3Mn_{2.3}Ga_{1.7}O_{10.5}$ and $YSr_3Mn_{2.23}Ga_{1.77}O_{10.5}$ are shown in *figures 3.3- 3.6*, and the refined structural parameters are given in *tables 3.2- 3.5*. Oxygen contents are calculated following refinement of the fractional occupancy of the partially occupied oxygen site, O1. The thermal factors for Mn and Ga cations were constrained to be equal in order to eliminate correlation effects.

3.3a.

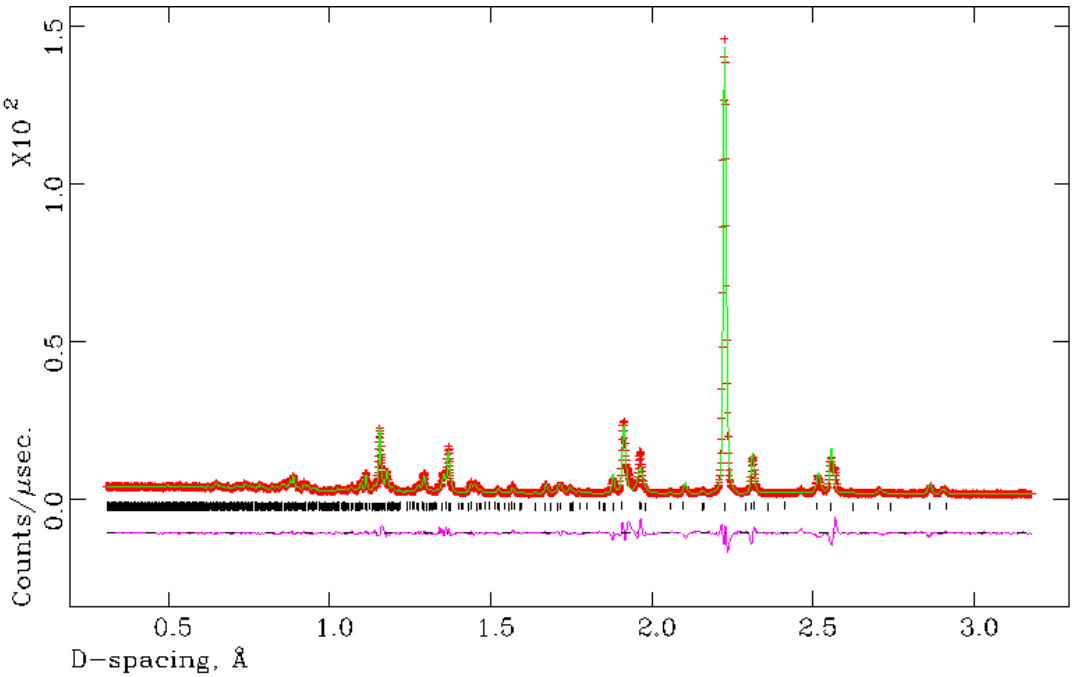

3.3b.

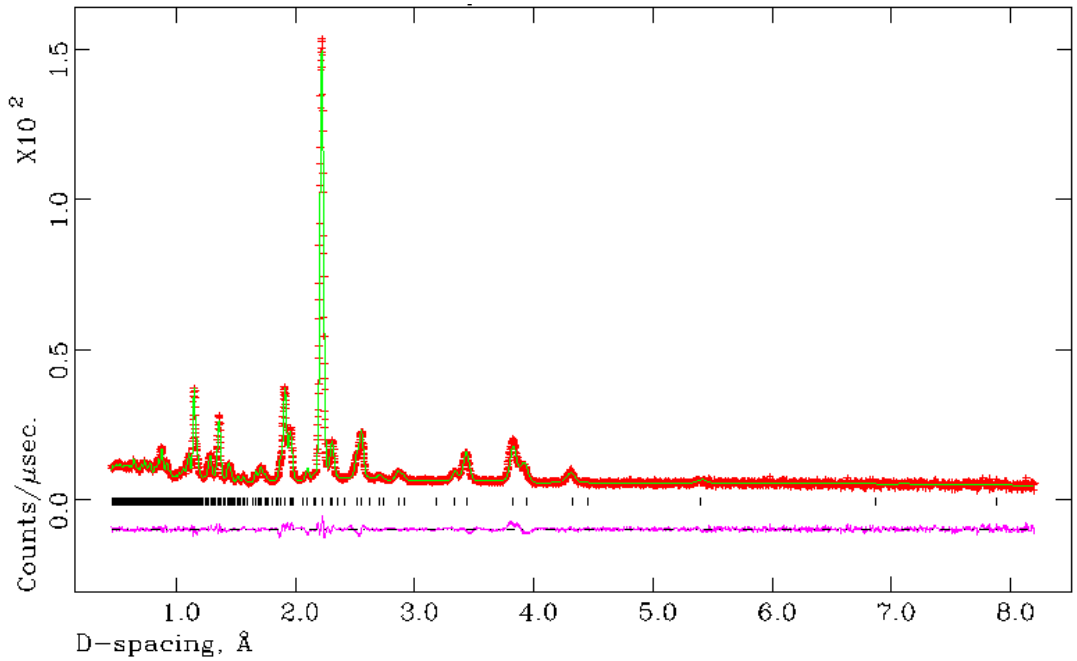

Figure 3.3. Observed (+), calculated (-) and difference (-) profiles from refinement using room temperature NPD data for $YSr_3Mn_{3.1}Ga_{0.9}O_{10.4}$ in space group I4/*mmm*, *a*) C bank, $2\theta = 145^{o}$ *b*) A bank $2\theta = 35^{o}$.$\chi^2 = 11.12$, R_{wp} =4.21% and R_p = 5.91%.

Table 3.2a. Refinement results from room temperature NPD data for $YSr_3Mn_{3.1}Ga_{0.9}O_{10.42(2)}$

Atom	Position	x	y	z	Frac.	U_{iso} x 100/Å^2
Mn1	8*f*	0.25	0.25	0.25	0.982(3)	0.62(6)
Ga1	8*f*	0.25	0.25	0.25	0.018(3)	0.62(6)
Mn2	8*h*	0.276(1)	0.276(1)	0	0.568(3)	0.62(6)
Ga2	8*h*	0.276(1)	0.276(1)	0	0.432(3)	0.62(6)
Y	4*e*	0	0	0.1432(1)	1	0.25(5)
Sr1	4*e*	0	0	0.6265(3)	1	1.17(1)
Sr2	8*g*	0.5	0	0.1300(1)	1	0.33(4)
O1	8*i*	0	0.105(1)	0	0.21(1)	1.2(3)
O2	8*j*	0.5	0.2291(7)	0	1	2.70*
O3	16*n*	0	0.2450(3)	0.2584(1)	1	0.654(3)
O4	16*m*	0.2169(2)	0.2169(2)	0.1143(2)	1	2.37*

* anisotropic thermal parameters given below

a = 7.6566(3) Å, *c* = 15.790(5) Å, χ^2 = 11.12, R_{wp} = 4.21% and R_p = 5.91%.

space group I4/*mmm*.

Table 3.2b. Anisotropic thermal parameters

Atom	U_{11} x 100/Å^2	U_{22} x 100/Å^2	U_{33} x 100/Å^2	U_{12} x 100/Å^2	U_{13} x 100/Å^2
O2	0.16(1)	6.3(3)	1.6(2)		
O4	2.50(8)	2.50(9)	2.1(1)	0.66(8)	1.23(7)

*Table 3.2c.*Selected bond lengths for $YSr_3Mn_{3.1}Ga_{0.9}O_{10.42(2)}$

Mn/Ga– O bond lengths,	**Å**	**BVS**
Mn/Ga1- O3 (x4)	1.9191(2)	Mn1- 3.26
Mn/Ga1- O4 (x2)	2.172(3)	
Mn/Ga2 – O1	2.47(1)	
Mn/Ga2 – O2 (x2)	1.763(7)	
Mn/Ga2 – O4 (x2)	1.909(5)	

Table 3.2d. Selected bond angles for $YSr_3Mn_{3.1}Ga_{0.9}O_{10.42(2)}$

Mn/Ga – O angles,	**degrees**
O3 - Mn/Ga1- O3 (x2)	87.4(1)
O3 - Mn/Ga1- O3 (x2)	92.6(1)
O3 - Mn/Ga1 – O4 (x4)	87.11(8)
O3 - Mn/Ga1 – O4 (x4)	92.89(8)
O2 - Mn/Ga2 – O2 (x1)	112.6(8)
O2 – Mn/Ga2 – O4 (x4)	100.4(1)
O4 – Mn/Ga2 – O4 (x1)	142.0(7)

3.4a.

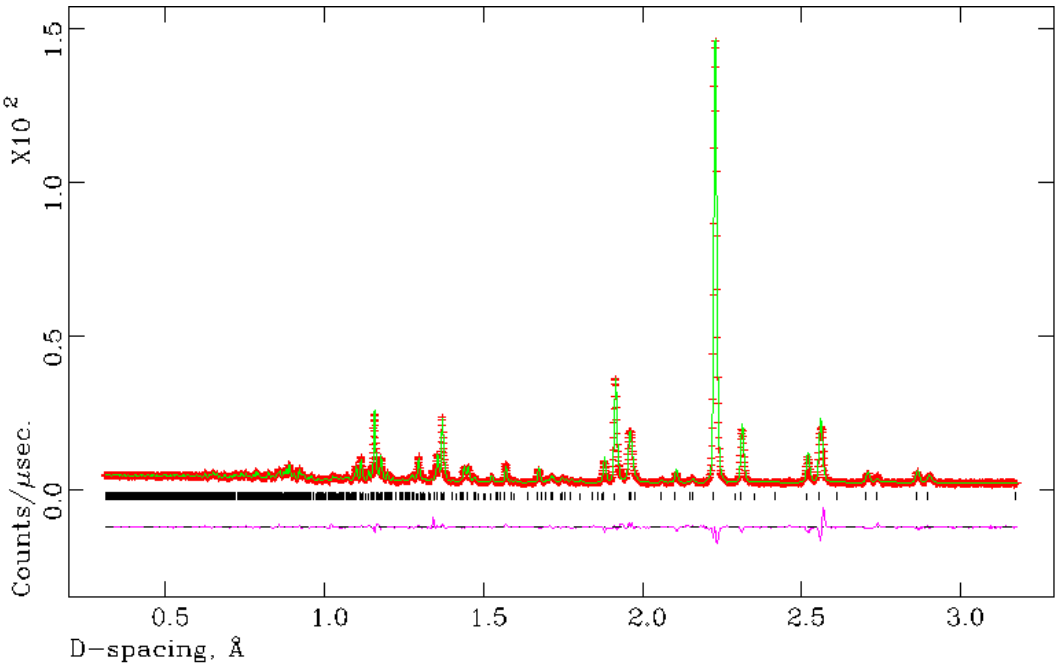

3.4b.

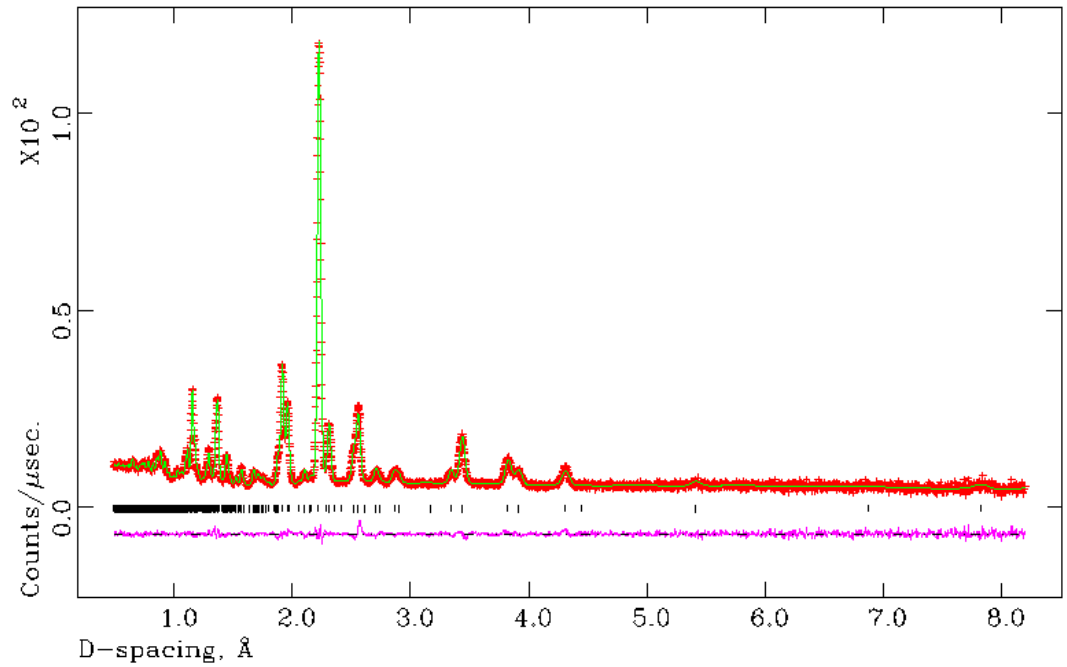

Figure 3.4. Observed (+), calculated (-) and difference (-) profiles from refinement using room temperature NPD data for $YSr_3Mn_{2.67}Ga_{1.33}O_{10.5}$ in space group I4/*mmm*, *a*) C bank, $2\theta = 145^{o}$ *b*) A bank $2\theta = 35^{o}$.$\chi^2 = 5.722$, R_{wp} =3.21% and R_p = 4.77%.

Table 3.3a. Refinement results from room temperature NPD data for $YSr_3Mn_{2.67}Ga_{1.33}O_{10.52(2)}$

Atom	Position	x	y	z	Frac.	U_{iso} x 100/Å^2
Mn1	8*f*	0.25	0.25	0.25	0.899(2)	0.35(4)
Ga1	8*f*	0.25	0.25	0.25	0.101(2)	0.35(4)
Mn2	8*h*	0.2670(3)	0.2670(3)	0	0.436(2)	0.35(4)
Ga2	8*h*	0.2670(3)	0.2670(3)	0	0.564(2)	0.35(4)
Y	4*e*	0	0	0.1439(1)	1	0.59(3)
Sr1	4*e*	0	0	0.6245(2)	1	1.92*
Sr2	8*g*	0.5	0	0.1303(1)	1	0.63(3)
O1	8*i*	0	0.1050(8)	0	0.259(7)	1.3(1)
O2	8*j*	0.5	0.2220(4)	0	1	2.77*
O3	16*n*	0	0.2455(2)	0.25912(9)	1	0.68(2)
O4	16*m*	0.2130(1)	0.2130(1)	0.1133(1)	1	2.29*

* anisotropic thermal parameters given below

a = 7.6546(2) Å, *c* = 15.680(2) Å, χ^2 = 5.722, R_{wp} = 3.21% and R_p = 4.77%. Space group I4/*mmm*.

Table 3.3b. Anisotropic thermal parameters

Atom	U_{11} x 100/Å^2	U_{22} x 100/Å^2	U_{33} x 100/Å^2	U_{12} x 100/Å^2	U_{13} x 100/Å^2
Sr1	2.4(1)	2.4(1)	1.0(1)		
O2	0.90(7)	6.4(2)	0.9(1)		
O4	2.44(4)	2.44(5)	2.01(7)	0.41(5)	1.40(4)

Table 3.3c. Selected bond lengths for $YSr_3Mn_{2.67}Ga_{1.33}O_{10.52(2)}$

Mn/Ga–O bond lengths,	**Å**	**BVS**
Mn/Ga1- O3 (x4)	1.9193(1)	Mn1- 3.24
Mn/Ga1- O4 (x2)	2.180(1)	
Mn/Ga2 – O1	2.391(4)	
Mn/Ga2 – O2 (x2)	1.816(1)	
Mn/Ga2 – O4 (x2)	1.871(1)	

Table 3.3d. Selected bond angles for $YSr_3Mn_{2.67}Ga_{1.33}O_{10.52(2)}$

Mn/Ga – O angles,	**degrees**
O3 - Mn/Ga1- O3 (x2)	87.63(9)
O3 - Mn/Ga1- O3 (x2)	92.37(9)
O3 - Mn/Ga1 – O4 (x4)	86.63(5)
O3 - Mn/Ga1 – O4 (x4)	93.37(5)
O2 - Mn/Ga2 – O2 (x1)	111.8(3)
O2 – Mn/Ga2 – O4 (x4)	100.09(5)
O4 – Mn/Ga2 – O4 (x1)	143.6(2)

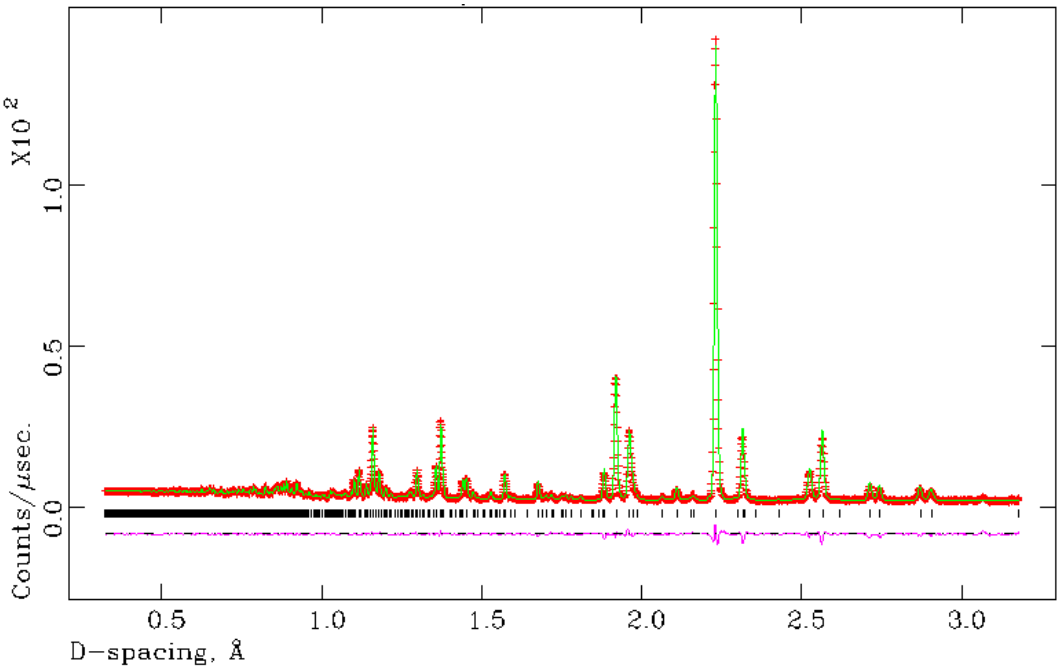

Figure 3.5a.

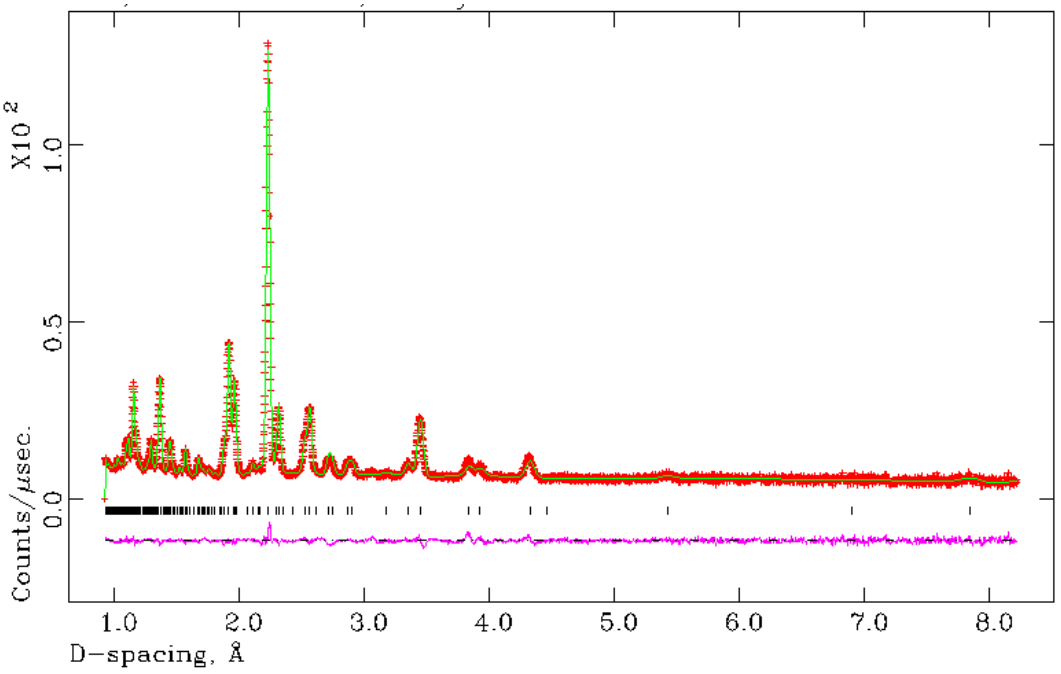

Figure 3.5b.

Figure 3.5. Observed (+), calculated (-) and difference (-) profiles from refinement using room temperature NPD data for $YSr_3Mn_{2.3}Ga_{1.7}O_{10.5}$ in space group I4/*mmm*, *a*) C bank, 2 θ = 145° *b*) A bank 2 θ = 35° .χ^2 = 3.049, R_{wp} =2.02% and R_p = 4.43%.

Table 3.4a. Refinement results from room temperature NPD data for $YSr_3Mn_{2.3}Ga_{1.7}O_{10.47(1)}$

Atom	Position	x	y	z	Frac.	U_{iso} x 100/Å^2
Mn1	8*f*	0.25	0.25	0.25	0.821(1)	0.20(2)
Ga1	8*f*	0.25	0.25	0.25	0.179(1)	0.20(2)
Mn2	8*h*	0.2695(1)	0.2695(1)	0	0.329(1)	0.20(2)
Ga2	8*h*	0.2695(1)	0.2695(1)	0	0.671(1)	0.20(2)
Y	4*e*	0	0	0.14489(7)	1	0.71(2)
Sr1	4*e*	0	0	0.6240(1)	1	2.31*
Sr2	8*g*	0.5	0	0.1315(7)	1	0.63(2)
O1	8*i*	0	0.1195(5)	0	0.235(5)	0.87(1)
O2	8*j*	0.5	0.2220(3)	0	1	2.60*
O3	16*n*	0	0.2464(1)	0.25943(6)	1	0.80(1)
O4	16*m*	0.21152(9)	0.21152(9)	0.11266(7)	1	2.36*

* anisotropic thermal parameters given below

a = 7.6881(6) Å, *c* = 15.717(1) Å, χ^2 = 3.049, R_{wp} = 2.02% and R_p = 4.43%. Space group I4/*mmm*.

Table 3.4b. Anisotropic thermal parameters

Atom	U_{11} x 100/Å^2	U_{22} x 100/Å^2	U_{33} x 100/Å^2	U_{12} x 100/Å^2	U_{13} x 100/Å^2
Sr1	2.73(7)	2.73(7)	1.48(9)		
O2	0.79(5)	6.3(1)	0.71(6)		
O4	2.39(3)	2.39(3)	2.30(5)	0.68(3)	1.60(3)

Table 3.4c. Selected bond lengths for $YSr_3Mn_{2.3}Ga_{1.7}O_{10.47(1)}$.

Mn/Ga–O bond lengths,	**Å**	**BVS**
Mn/Ga1- O3 (x4)	1.9279(2)	Mn1 – 3.15
Mn/Ga1- O4 (x2)	2.198(1)	
Mn/Ga2 – O1	2.372(2)	
Mn/Ga2 – O2 (x2)	1.8093(8)	
Mn/Ga2 – O4 (x2)	1.879(1)	

Table 3.4d. Selected bond angles for $YSr_3Mn_{2.3}Ga_{1.7}O_{10.47(1)}$.

Mn/Ga – O angles,	**degrees**
O3 - Mn/Ga1- O3 (x2)	88.02(6)
O3 - Mn/Ga1- O3 (x2)	91.98(6)
O3 - Mn/Ga1 – O4 (x4)	86.53(3)
O3 - Mn/Ga1 – O4 (x4)	93.47(3)
O2 - Mn/Ga2 – O2 (x1)	113.3(2)
O2 – Mn/Ga2 – O4 (x4)	100.63(3)
O4 – Mn/Ga2 – O4 (x1)	140.8(1)

Figure 3.6a.

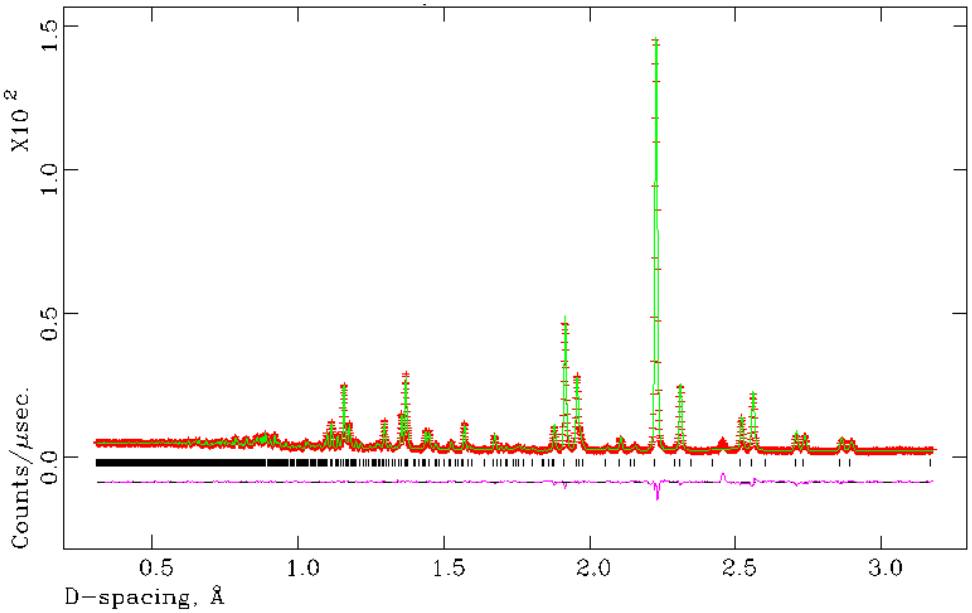

Figure 3.6b

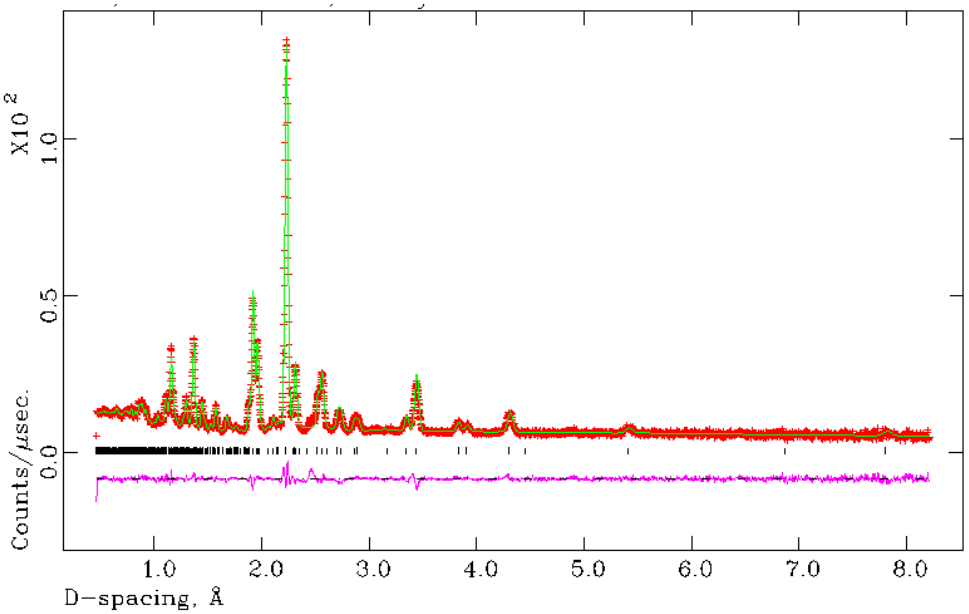

Figure 3.6. Observed (+), calculated (-) and difference (-) profiles from refinement using room temperature NPD data for $YSr_3Mn_{2.23}Ga_{1.77}O_{10.5}$ in space group I4/*mmm*, *a*) C bank, 2 θ = 145° *b*) A bank 2 θ = 35° .χ^2 = 3.561, R_{wp} =2.19% and R_p = 4.43%.

Table 3.5a. Refinement results from room temperature NPD data for $YSr_3Mn_{2.23}Ga_{1.77}O_{10.53(1)}$

Atom	Position	x	y	z	Frac.	U_{iso} x100/Å^2
Mn1	8*f*	0.25	0.25	0.25	0.782(1)	0.18(2)
Ga1	8*f*	0.25	0.25	0.25	0.218(1)	0.18(2)
Mn2	8*h*	0.2677(1)	0.2677(1)	0	0.333(1)	0.18(2)
Ga2	8*h*	0.2677(1)	0.2677(1)	0	0.667(1)	0.18(2)
Y	4*e*	0	0	0.14512(7)	1	0.74(2)
Sr1	4*e*	0	0	0.6240(1)	1	2.28*
Sr2	8*g*	0.5	0	0.13148(7)	1	0.58(2)
O1	8*i*	0	0.1177(5)	0	0.265(5)	1.2(1)
O2	8*j*	0.5	0.2239(2)	0	1	2.13*
O3	16*n*	0	0.2457(1)	0.25941(5)	1	0.71(1)
O4	16*m*	0.21133(9)	0.21133(9)	0.11338(7)	1	2.19*

* anisotropic thermal parameters given below

a = 7.6595(1) Å, *c* = 15.6444(2) Å, χ^2 = 3.561, R_{wp} = 2.19% and R_p = 4.37%. Space group I4/*mmm*.

Table 3.5b. Anisotropic thermal parameters

Atom	U_{11} x 100/Å^2	U_{22} x 100/Å^2	U_{33} x 100/Å^2	U_{12} x 100/Å^2	U_{13} x 100/Å^2
Sr1	2.82(7)	2.82(7)	1.21(8)		
O2	0.66(4)	5.0(1)	0.64(6)		
O4	2.09(2)	2.09(2)	2.40(4)	0.77(3)	1.58(3)

*Table 3.5c.*Selected bond lengths for $YSr_3Mn_{2.23}Ga_{1.77}O_{10.53(1)}$.

Mn/Ga–O bond lengths,	**Å**	**BVS**
Mn/Ga1- O3 (x4)	1.92108(8)	Mn1- 3.21
Mn/Ga1- O4 (x2)	2.176(1)	
Mn/Ga2 – O1	2.352(2)	
Mn/Ga2 – O2 (x2)	1.8129(9)	
Mn/Ga2 – O4 (x2)	1.877(1)	

Table 3.5d. Selected bond angles for $YSr_3Mn_{2.23}Ga_{1.77}O_{10.53(1)}$.

Mn/Ga – O angles,	**degrees**
O3 - Mn/Ga1- O3 (x2)	87.39(6)
O3 - Mn/Ga1- O3 (x2)	92.61(6)
O3 - Mn/Ga1 – O4 (x4)	86.47(3)
O3 - Mn/Ga1 – O4 (x4)	93.53(3)
O2 - Mn/Ga2 – O2 (x1)	111.8(1)
O2 – Mn/Ga2 – O4 (x4)	100.46(3)
O4 – Mn/Ga2 – O4 (x1)	142.2(1)

3.3.1 Results and Discussion

Rietveld refinement of all four samples, in the body- centred tetragonal space group I4/*mmm*, converged to give χ^2 = 11.12 for $YSr_3Mn_{3.1}Ga_{0.9}O_{10.4}$, χ^2 = 5.722 for $YSr_3Mn_{2.67}Ga_{1.33}O_{10.5}$, χ^2 = 3.049 for $YSr_3Mn_{2.3}Ga_{1.7}O_{10.5}$ and χ^2 = 3.561 for $YSr_3Mn_{2.23}Ga_{1.77}O_{10.5}$. The best fit between observed and calculated profiles was obtained by allowing the Mn and Ga cations to adopt a disordered arrangement over the tetrahedral and octahedral sites. As manganese content falls there is greater mixing between the octahedral and tetrahedral sites, leading to a greater proportion of gallium occupying the octahedral site at lower manganese contents, as shown in *figure 3.7*. The O1 anions can be viewed as being coordinated to Mn^{3+} ions in the tetrahedral sites, resulting in a Jahn-Teller distorted square pyramid with an elongated bond to O1. Increased cation mixing at lower Mn content may be because it is energetically favourable to maintain the Mn content of the tetrahedral site if the bond to O1 results in greater stability for the structure. *Figure 3.8* shows that the Mn2 – O1 bond length increases with the manganese content of the tetrahedral site. The refined bond length Mn2 – O1 is an average value depending on whether Mn^{3+} or Ga^{3+} occupy the tetrahedral site, as manganese content increases the refined value represents the true Jahn-Teller distorted Mn2 – O1 bond length more accurately.

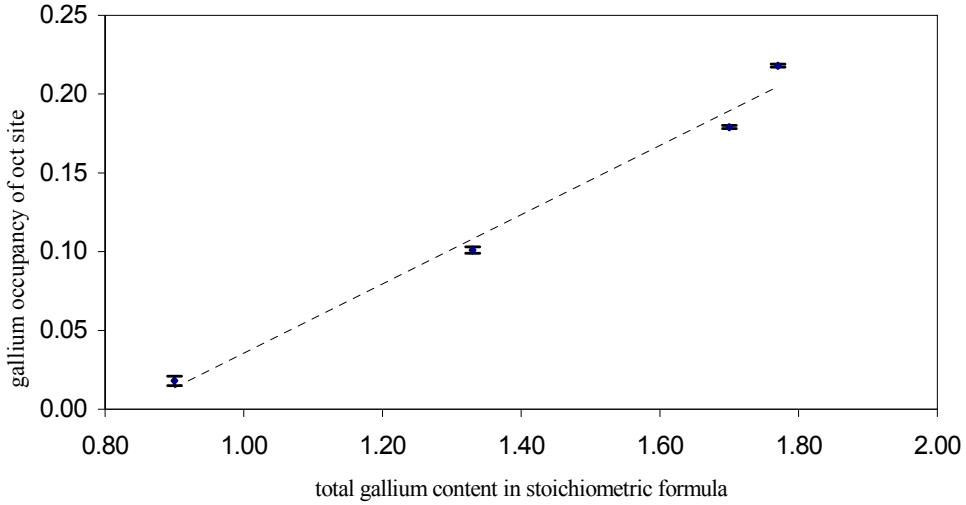

Figure 3.7. Plot to show the increased gallium occupancy of the octahedral site as total gallium content increases.

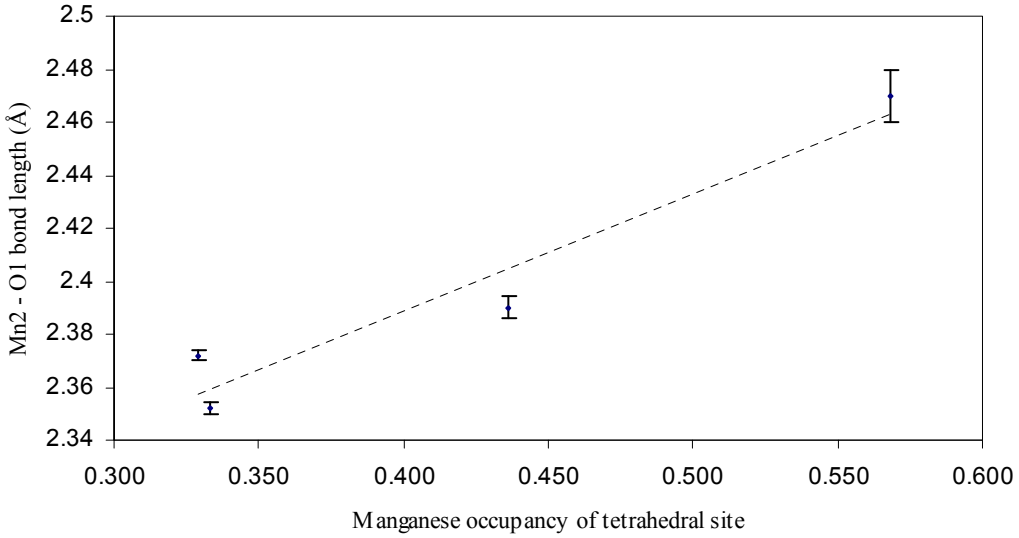

Figure 3.8. Plot to show increased apical bond length of Jahn-Teller distorted square pyramid with increasing Mn^{3+} occupancy of tetrahedral site.

Refinement of the fractional occupancy of the partially occupied O1 site resulted in a better fit between observed and calculated profiles. Differences between the oxygen stoichiometry were found between the samples resulting in a valency of $Mn^{2.9+}$ for $YSr_3Mn_{3.1}Ga_{0.9}O_{10.4}$. Manganese cations had a valency of 3+ for the remaining samples.

These results are consistent with those of Gillie [22] in which $Y_{0.8}Sr_{2.2}Mn_2GaO_{7.9}$ with a Mn valency of 3+ and $Y_{0.8}Sr_{2.2}Mn_2GaO_{7.8}$ with a Mn valency of 2.9+ were synthesised.

Temperature factors were high for oxygen anions O2 and O4, anisotropic refinement of these thermal parameters resulted in an improved fit between observed and calculated profiles. Oxygen atoms O2 and O4 are bonded to the cation in the tetrahedral site, which may be Ga^{3+} or Mn^{3+}, bond lengths between this tetrahedrally coordinated cation and oxygen will vary depending on which cation occupies the site. Therefore the positions of O2 and O4 are average positions, this disorder results in high temperature factors for O2 and O4. The temperature factor for the strontium cation $Sr1^{2+}$ was also high. Sr1 is bonded to the oxygen atom in the partially occupied site, O1. The occupancy of this site is disordered, so that some Sr1 cations will be bonded to an additional oxygen, O1, and others will not. The position of Sr1 will vary depending on whether or not the O1 site is occupied, hence the temperature factor is high for Sr1.

The possibility that there may be mixing between the Y^{3+} site and the $Sr1^{2+}$ site was investigated by refinement, allowing both sites to be fractionally occupied by Y and Sr cations. Y^{3+} shows a strong preference for its original position and the fit between observed and calculated profiles was optimal when there was no mixing between the two sites.

Bond valence sum calculations *tables 3.2c, 3.3c, 3.4c* and *3.5c,* give values ranging from 3.15- 3.26 for the octahedral site slightly higher than expected for a manganese valency of 3. It was not possible to determine bond valence sums for the tetrahedral site due to disordered occupancy of this site.

3.4 Magnetic Characterisation of $YSr_3Mn_xGa_yO_{10.5}$

3.4.1 Magnetic Susceptibility Studies

Magnetic susceptibility measurements were taken using a Quantum Design Physical Properties Measurement System (PPMS). DC magnetisation measurements were made for $YSr_3Mn_{3.1}Ga_{0.9}O_{10.4}$, $YSr_3Mn_{2.67}Ga_{1.33}O_{10.5}$, $YSr_3Mn_{2.3}Ga_{1.7}O_{10.5}$ and $YSr_3Mn_{2.23}Ga_{1.77}O_{10.5}$, with an applied field of 1000 Gauss. Both zero field cooled and field cooled data were collected. *Figures 3.9 – 3.12* show the susceptibility versus temperature plots for all four samples.

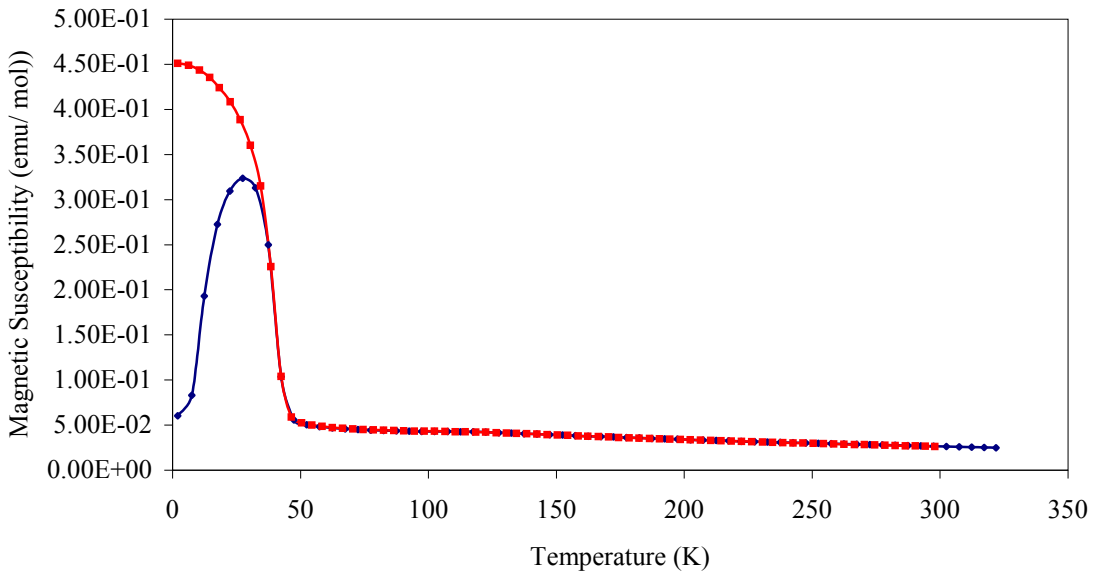

Figure 3.9. Magnetic susceptibility versus temperature plot for $YSr_3Mn_{3.1}Ga_{0.9}O_{10.4}$ (DC magnetisation performed in an applied field of 1000 Gauss. Zero-field cooled is shown blue and field cooled data in red.)

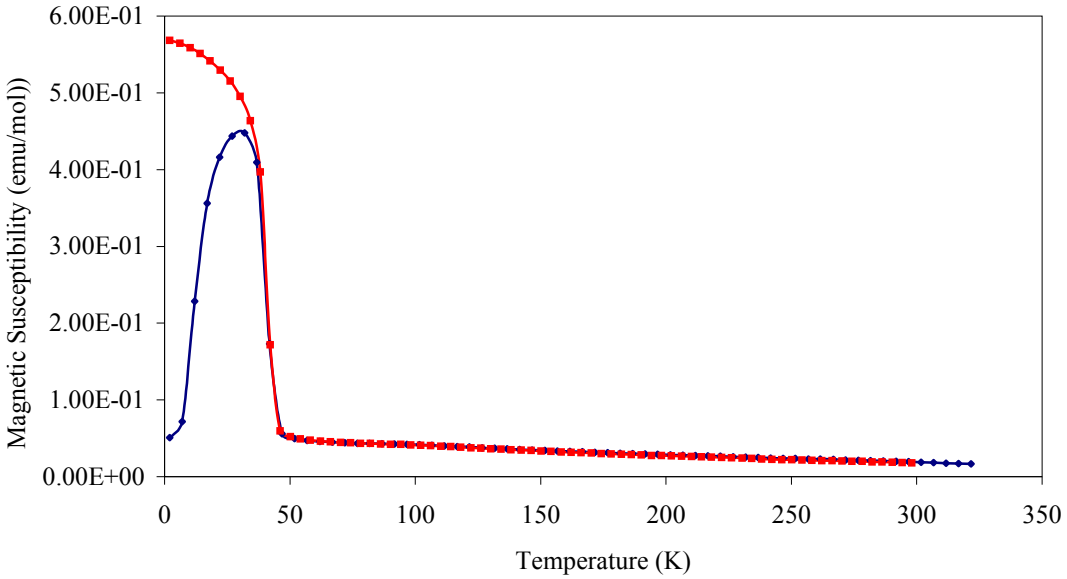

Figure 3.10. Magnetic susceptibility versus temperature plot for $YSr_3Mn_{2.67}Ga_{1.33}O_{10.5}$ (DC magnetisation performed in an applied field of 1000 Gauss. Zero-field cooled is shown blue and field cooled data in red.)

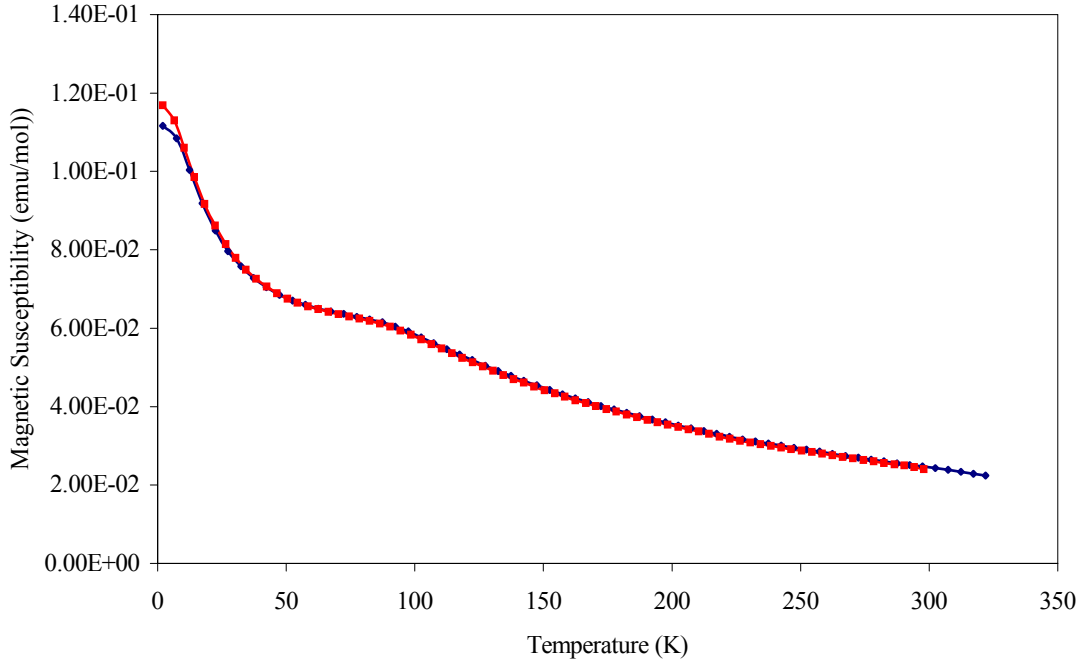

Figure 3.11. Magnetic susceptibility versus temperature plot for $YSr_3Mn_{2.3}Ga_{1.7}O_{10.5}$ (DC magnetisation performed in an applied field of 1000 Gauss. Zero-field cooled is shown blue and field cooled data in red.)

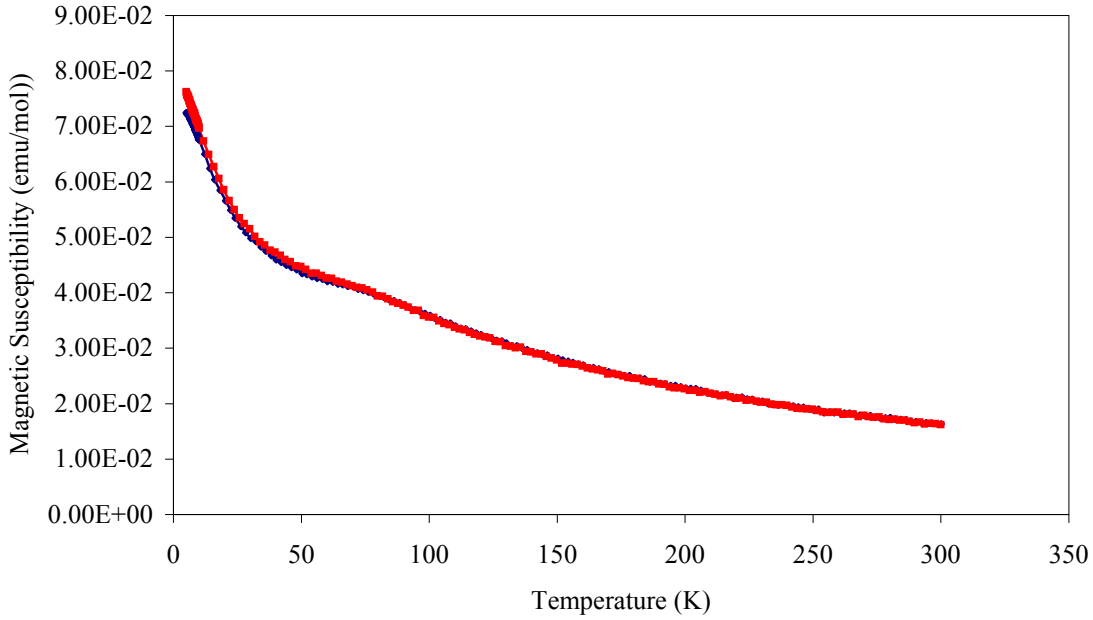

Figure 3.12. Magnetic susceptibility versus temperature plot for $YSr_3Mn_{2.23}Ga_{1.77}O_{10.5}$ (DC magnetisation performed in an applied field of 1000 Gauss. Zero-field cooled is shown blue and field cooled data in red.)

Magnetic susceptibility plots for $YSr_3Mn_{3.1}Ga_{0.9}O_{10.4}$, $YSr_3Mn_{2.67}Ga_{1.33}O_{10.5}$, $YSr_3Mn_{2.3}Ga_{1.7}O_{10.5}$ and $YSr_3Mn_{2.23}Ga_{1.77}O_{10.5}$ indicate antiferromagnetic ordering, with Néel temperatures of ~ 47K, 50K, 86K and 73K respectively. Zero field cooled and field cooled data diverge after ordering for $YSr_3Mn_{3.1}Ga_{0.9}O_{10.4}$ and $YSr_3Mn_{2.67}Ga_{1.33}O_{10.5}$ suggesting that there is a ferromagnetic component to the magnetic properties. Although the plots of inverse susceptibility against temperature, *figures 3.13-3.16*, show some deviations from linear behaviour above the ordering temperature the Curie- Weiss paramagnetic moments were calculated. Deviations from the Curie- Weiss behaviour above the ordering temperature would be predicted for

tetrahedrally coordinated Mn^{3+} cations. Mn^{3+} a d^4 cation, has T_2 ground state electronic energy level. When tetrahedrally coordinated, spin orbit coupling further splits the T_2 into energy level with different J values, the magnetic moment of the cation will depend on the occupancy of these J energy levels, which in turn varies with temperature. Hence the magnetic moment of the cation varies with temperature and the Curie- Weiss law is not obeyed.

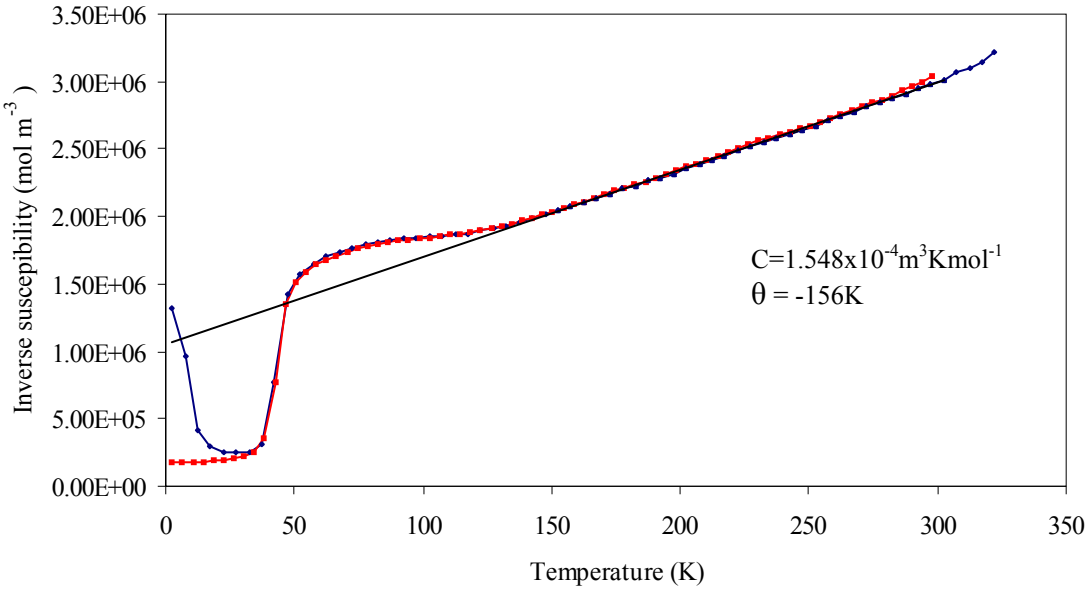

Figure 3.13. Inverse susceptibility versus temperature plot for $YSr_3Mn_{3.1}Ga_{0.9}O_{10.4}$ (DC magnetisation performed in an applied field of 1000 Gauss. Zero-field cooled is shown blue and field cooled data in red.)

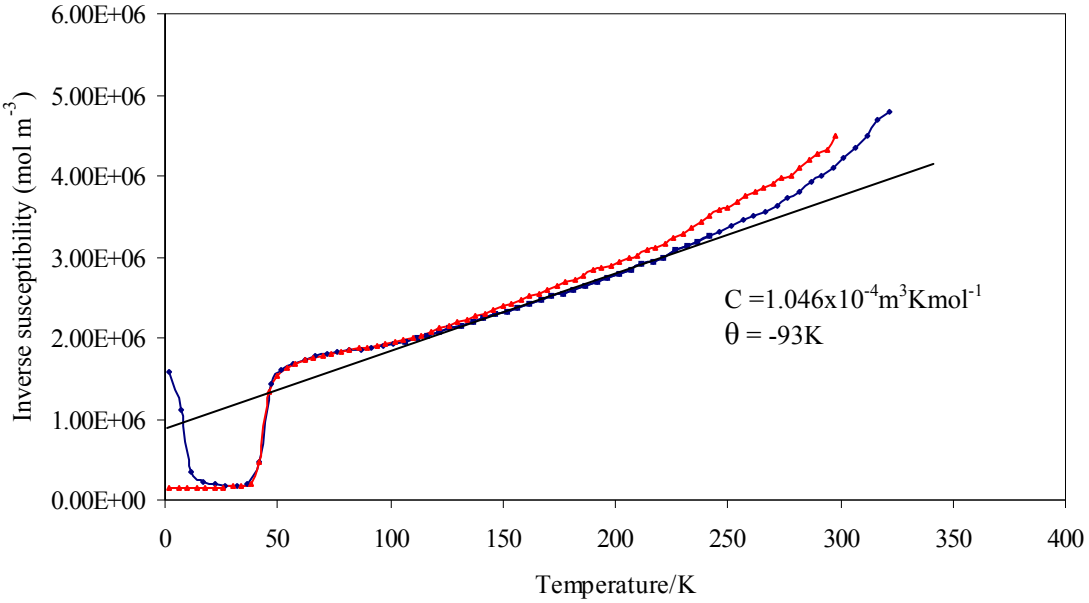

Figure 3.14. Inverse susceptibility versus temperature plot for $YSr_3Mn_{2.67}Ga_{1.33}O_{10.5}$ (DC magnetisation performed in an applied field of 1000 Gauss. Zero-field cooled is shown blue and field cooled data in red.)

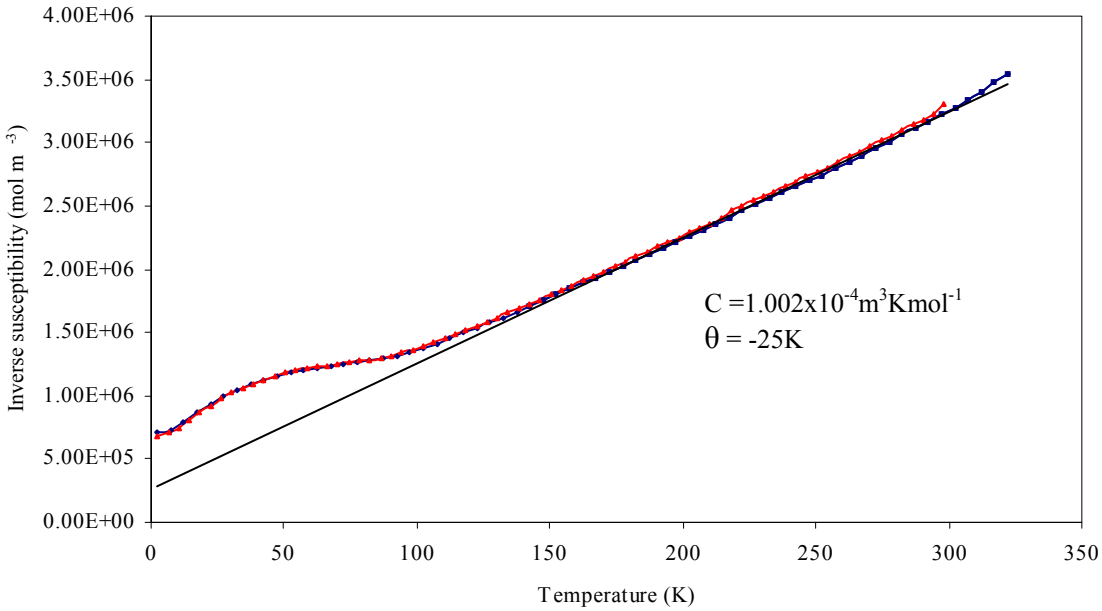

Figure 3.15. Inverse susceptibility versus temperature plot for $YSr_3Mn_{2.3}Ga_{1.7}O_{10.5}$ (DC magnetisation performed in an applied field of 1000 Gauss. Zero-field cooled is shown blue and field cooled data in red.)

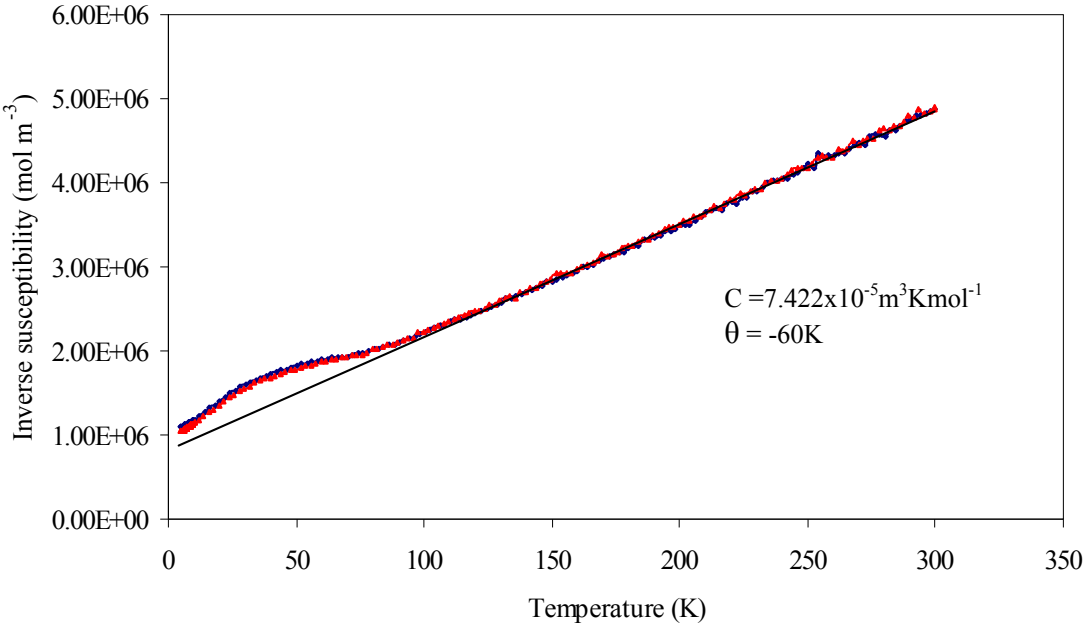

Figure 3.16. Inverse susceptibility versus temperature plot for $YSr_3Mn_{2.23}Ga_{1.77}O_{10.5}$ (DC magnetisation performed in an applied field of 1000 Gauss. Zero-field cooled is shown blue and field cooled data in red.)

Although there was some deviation from linear behaviour above the ordering temperature, a reasonable estimate of the paramagnetic moments could be calculated from the gradient of the paramagnetic region of the inverse susceptibility versus temperature plots. The results were as follows, $YSr_3Mn_{3.1}Ga_{0.9}O_{10.4}$ = 5.64 μ_B per Mn ion, $YSr_3Mn_{2.67}Ga_{1.33}O_{10.5}$ = 5.00 μ_B per Mn ion, $YSr_3Mn_{2.3}Ga_{1.7}O_{10.5}$ = 5.27 μ_B per Mn ion and $YSr_3Mn_{2.23}Ga_{1.77}O_{10.5}$ = 4.50 μ_B per Mn ion. The expected value for a d^4 cation with an electronic spin only contribution would be 4.89 μ_B. Higher than predicted values for the magnetic moment may be due to an orbital contribution to the magnetic moment for tetrahedrally coordinated Mn^{3+}.

3.4.2 Low Temperature Neutron Powder Diffraction Studies

Neutron powder diffraction (NPD) data were collected at POLARIS, ISIS, UK at 2K, for samples $YSr_3Mn_{3.1}Ga_{0.9}O_{10.4}$, $YSr_3Mn_{2.67}Ga_{1.33}O_{10.5}$ and $YSr_3Mn_{2.3}Ga_{1.7}O_{10.5}$. NPD data were collected at 4K on D2B at ILL, Grenoble, France for $YSr_3Mn_{2.23}Ga_{1.77}O_{10.5}$. Previous study by Gillie [22] of $Y_{0.8}$ $Sr_{2.2}Mn_2GaO_{7.8}$ (equivalent to $Y_{1.07}Sr_{2.93}Mn_{2.67}Ga_{1.33}O_{10.4}$) identified an 'incommensurate' magnetic peak. The magnetic moments of the Mn^{3+} cations in the polyhedra which are corner linked in the [001] direction are aligned ferromagnetically parallel to the [001] direction of the unit cell, as shown in *figure 3.17*. Antiferromagnetic exchange occurs within the octahedral and tetrahedral layers in both the [100] and [010] directions [22].

The following study aims to identify the nature of this peak in addition to investigating the magnetic behaviour of samples with various Mn:Ga ratios as listed in *table 3.1*.NPD profiles collected at high d-spacing, are shown in *figures 3.18-3.21*.

The best agreement between calculated and experimental profiles, for $YSr_3Mn_{3.1}Ga_{0.9}O_{10.4}$, $YSr_3Mn_{2.67}Ga_{1.33}O_{10.5}$, $YSr_3Mn_{2.3}Ga_{1.7}O_{10.5}$ and $YSr_3Mn_{2.23}Ga_{1.77}O_{10.5}$ was obtained when the magnetic moments were ordered antiferromagnetically. The unit cell and symmetry of the magnetic model were equivalent to the crystallographic unit cell. Ferromagnetic ordering in the [001] direction can be predicted from superexchange interactions. Mn^{3+} cations usually exist in higher geometry than tetrahedral, therefore it is likely that Mn^{3+} in the 'tetrahedral' layer is associated with the partially occupied O1 site, leading to a 5-coordinate square pyramidal arrangement for Mn in this site. The partially occupied O1 site is split from the ideal 2*a* position at (0, 0, 0) to the 8*i* position at (0, *x,* 0) allowing Mn^{3+} to associate with O1. The Mn-O1 bond is the apical bond of the MnO_5 square pyramid. Interaction

of an empty $d_{x^2-y^2}$ orbital from the 5-coordinate Mn^{3+} with the half filled d_{z^2} orbital from the Jahn-Teller distorted octahedral Mn^{3+} would lead to ferromagnetic exchange along the [001] direction of the unit cell.

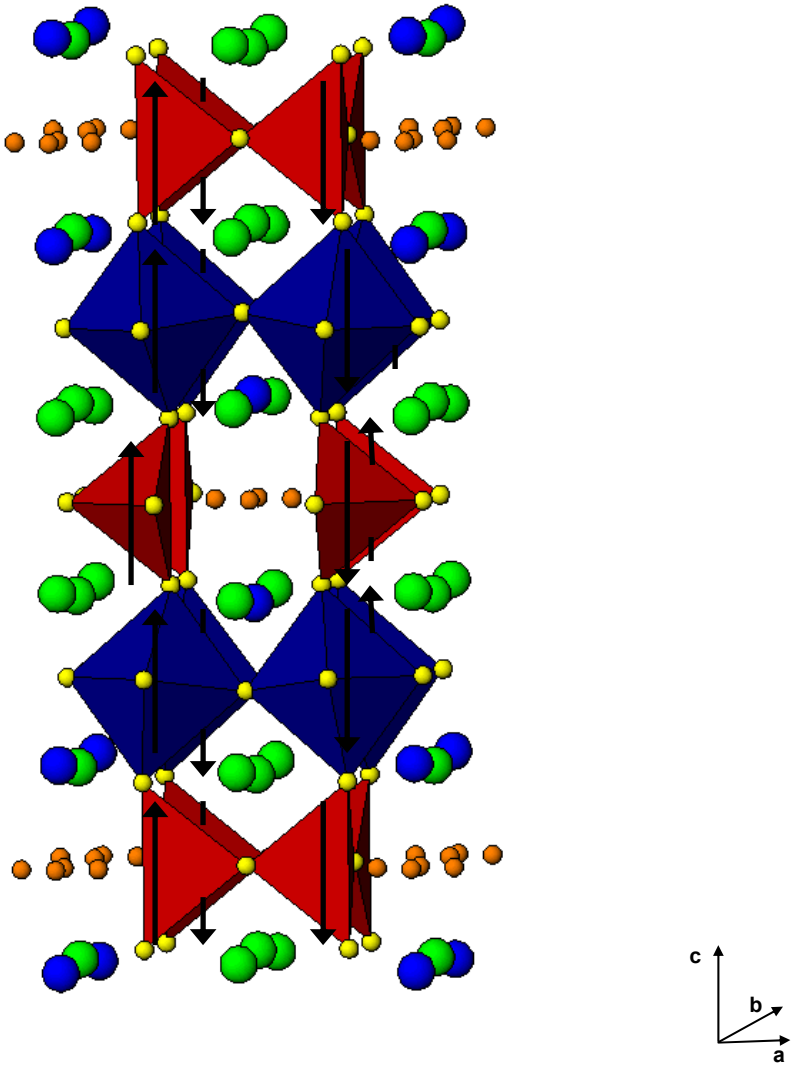

Figure 3.17. Magnetic structure of $YSr_3Mn_{2.67}Ga_{1.33}O_{10.5}$. Showing MnO_6 as blue polyhedra, Mn/GaO_4 as red polyhedra, yellow spheres are oxygen anions, orange spheres depict the ¼ occupied oxygen site, green spheres are Sr^{2+} cations and blue spheres are Y^{3+} cations.

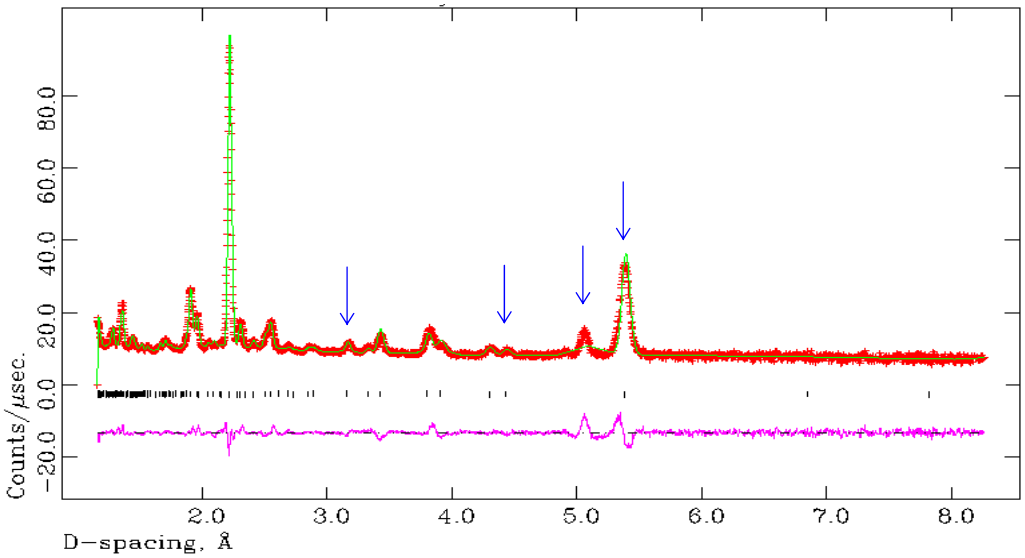

Figure 3.18. Observed (+), calculated(-) and difference (-) profiles from refinement using 2K NPD data for $YSr_3Mn_{3.1}Ga_{0.9}O_{10.4}$ in space group I4/*mmm*, χ^2 = 6.638, R_{wp} = 2.65% and R_p = 4.79%. Peaks primarily due to magnetic scattering are marked with a blue arrow.

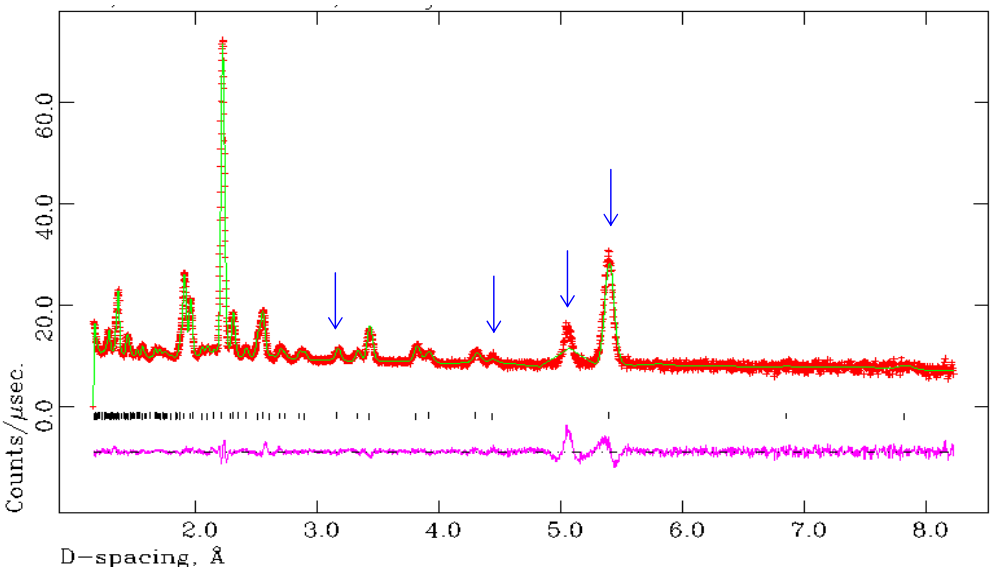

Figure 3.19. Observed (+), calculated (-) and difference (-) profiles from refinement using 2K NPD data for $YSr_3Mn_{2.67}Ga_{1.33}O_{10.5}$ in space group I4/*mmm*. χ^2 = 3.942, R_{wp} =1.97% and R_p = 3.82%. Peaks primarily due to magnetic scattering are marked with a blue arrow.

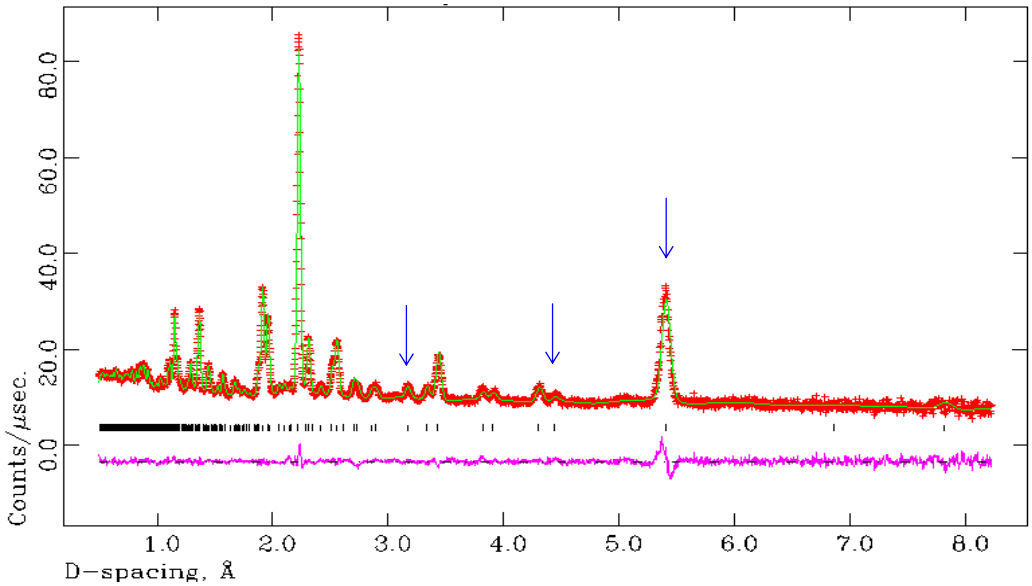

Figure 3.20. Observed (+), calculated (-) and difference (-) profiles from refinement using 2K NPD data for $YSr_3Mn_{2.3}Ga_{1.7}O_{10.5}$ in space group I4/*mmm*, $\chi^2 = 2.491$, $R_{wp} = 1.65\%$ and $R_p = 3.22\%$. Peaks primarily due to magnetic scattering are marked with a blue arrow.

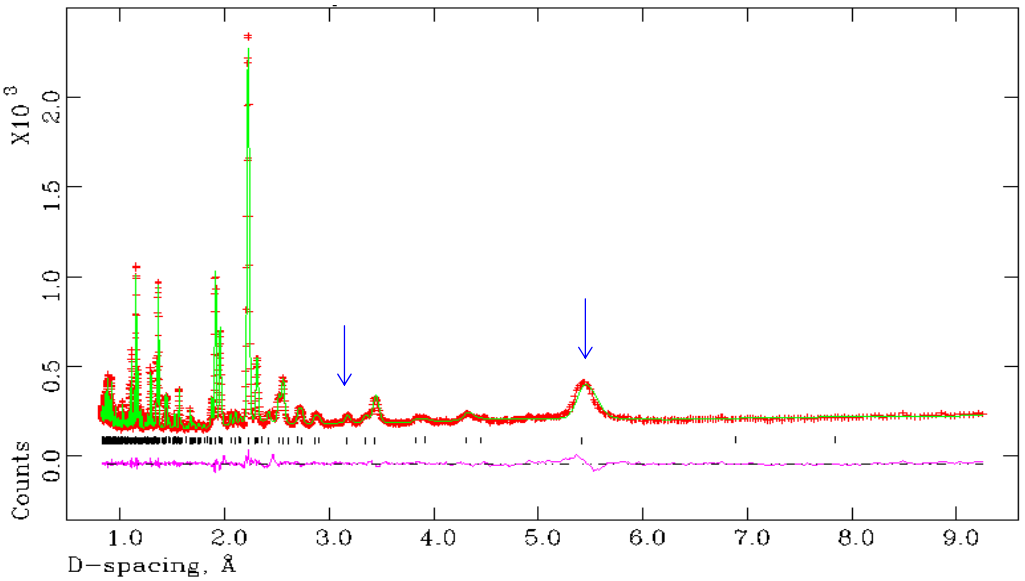

Figure 3.21. Observed (+), calculated (-) and difference (-) profiles from refinement using 4K NPD data for $YSr_3Mn_{2.23}Ga_{1.77}O_{10.5}$ in space group I4/*mmm*, $\chi^2 = 3.217$, $R_{wp} = 3.67\%$ and $R_p = 2.73\%$. Peaks primarily due to magnetic scattering are marked with a blue arrow.

3.4.3 The Incommensurate Magnetic Peak

Peaks due to magnetic scattering were identified at d-spacings of 5.4Å, 5.05Å, 4.4Å and 3.2 Å for samples $YSr_3Mn_{3.1}Ga_{0.9}O_{10.4}$ and $YSr_3Mn_{2.67}Ga_{1.33}O_{10.5}$ (*figures3.18 and 3.19*) . Equivalent magnetic peaks were identified by Gillie [22] in her previous study for the material $Y_{1.07}Sr_{2.93}Mn_{2.67}Ga_{1.33}O_{10.4}$ ($Y_{0.8}Sr_{2.2}Mn_2GaO_{7.8}$), including the 'incommensurate' magnetic peak at 5.05Å. Rietveld refinement of NPD data did not show evidence of this additional magnetic peak for $YSr_3Mn_{2.3}Ga_{1.7}O_{10.5}$ and $YSr_3Mn_{2.23}Ga_{1.77}O_{10.5}$ (*figures 3.20and 3.21*).

It was proposed that the additional magnetic peak may be a magnetic reflection due to a MnO impurity in the manganese-rich samples, which was insufficient to show during refinement of room temperature data, where only nuclear scattering would be observed. This proposal was supported by the fact that the additional magnetic peak was evident for the reduced sample $Y_{0.8}Sr_{2.2}Mn_2GaO_{7.8}$ ($Y_{1.07}Sr_{2.93}Mn_{2.67}Ga_{1.33}O_{10.4}$) but not for the sample with slightly higher oxygen content, $Y_{0.8}Sr_{2.2}Mn_2GaO_{7.9}$ ($Y_{1.07}Sr_{2.93}Mn_{2.67}Ga_{1.33}O_{10.5}$) in Gillie's previous study.

Refinement of low temperature NPD data was carried out for $YSr_3Mn_{3.1}Ga_{0.9}O_{10.4}$ and $YSr_3Mn_{2.67}Ga_{1.33}O_{10.5}$ with a second phase of MnO included, the resultant profiles are shown in *figures 3.23 and 3.24*. The MnO phase was refined in the face centred cubic space group Fm3m, with lattice parameter a = 4.395Å. The magnetic MnO phase was refined in space group P-1, with the magnetic unit cell lattice parameters related to MnO lattice parameter by $\sqrt{2}a \times \sqrt{2}a \times 2a$. Inclusion of MnO as a second phase improved the fit for both $YSr_3Mn_{3.1}Ga_{0.9}O_{10.4}$ (χ^2 reduced from 6.638 to 5.616) and $YSr_3Mn_{2.67}Ga_{1.33}O_{10.5}$ (χ^2 reduced from 3.942 to 3.294). The amount of the MnO phase was low for both samples, $YSr_3Mn_{3.1}Ga_{0.9}O_{10.4}$ 1.0(4)% and

$YSr_3Mn_{2.67}Ga_{1.33}O_{10.5}$ 1.59(4)% by weight. It can be seen from *figures 3.23 and 3.24* that the 'incommensurate' magnetic peak at 5.05Å can be attributed to a magnetic MnO reflection.

Following allowance for a MnO impurity in the manganese-rich samples NPD profiles shown in *figures 3.23, 3.24, 3.20* and *3.21* together with the associated results in *tables3.7- 3.10* give the best agreement between calculated and experimental profiles.

The refined magnetic moments of the Mn^{3+} ion are lower than the expected value of 4 μ_B for all four samples, with a larger magnetic moment on the tetrahedral site, as shown in *table 3.6*. Refined magnetic moments may be low due to magnetic interactions becoming more 2-dimensional as diamagnetic Ga^{3+} cations interrupt the Mn-O-Mn superexhange pathway both between the octahedral and tetrahedral layers and within the tetrahedral layer. Refined magnetic moments would also be reduced by covalency between Mn^{3+} and O^{2-}.

Magnetic moments are lower than expected on the octahedral site for all samples (*table 3.6)*. The magnetic model used assumes that the octahedral moments are aligned in the x direction only. A slight canting of these moments would result in a component of the octahedral moment not being included in the overall moment and an under estimate of the magnetic moment.

The magnetic moments on the tetrahedral site may be greater than those on the octahedral site due to an orbital contribution to the moment. An orbital contribution would not be predicted for an octahedrally coordinated Mn^{3+} d^4 cation The magnetic moments on the tetrahedral site increase as the proportion of 5 coordinate Mn^{3+} increases, as shown in *table 3.6* and *figure 3.22*. This increase may be due to a greater

orbital contribution to the magnetic moment for square pyramidal Mn^{3+} compared to tetrahedrally coordinated Mn^{3+}.

Table 3.6. Summary of magnetic properties

Sample	Proportion of Mn^{3+} on 'tet.' site that is 5-coordinate	Refined magnetic moment 'tet.' site. (μ_B)	Refined magnetic moment 'oct.' site (μ_B)	T_N (K)
$YSr_3Mn_{3.1}Ga_{0.9}O_{10.4}$	38%	2.6(1)	2.13(5)	47
$YSr_3Mn_{2.67}Ga_{1.33}O_{10.5}$	63%	3.3(1)	2.26(6)	50
$YSr_3Mn_{2.3}Ga_{1.7}O_{10.5}$	74%	3.8(1)	2.21(4)	86
$YSr_3Mn_{2.23}Ga_{1.77}O_{10.5}$	88%	3.8(2)	2.2(1)	73

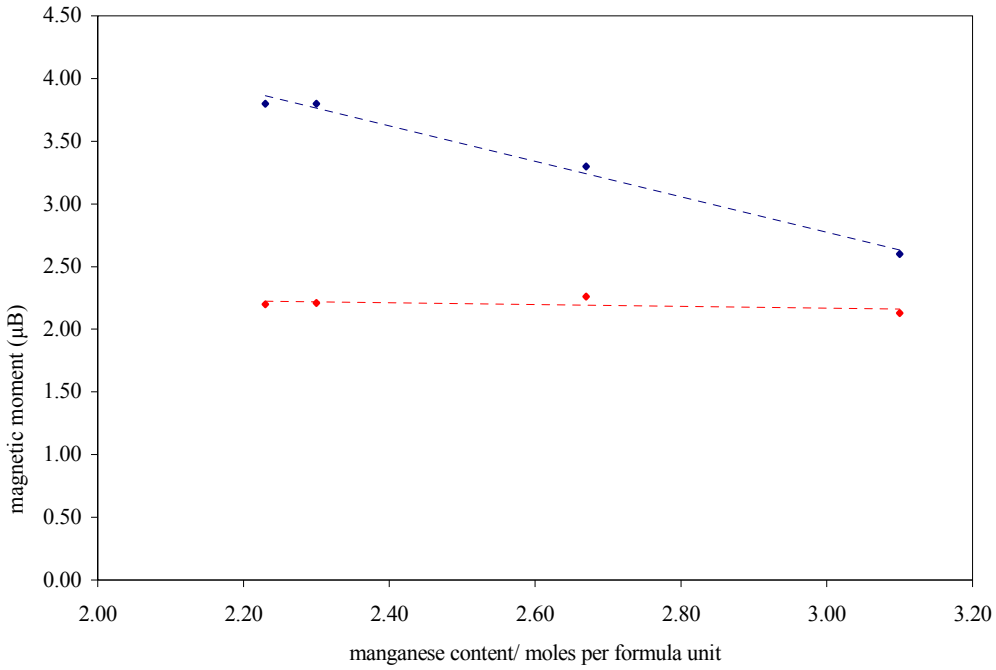

Figure 3.22. Plot to show variation in ordered magnetic moment with manganese content. Magnetic moment of tetrahedral site shown in blue and octahedral site red.

Figure 3.23a.

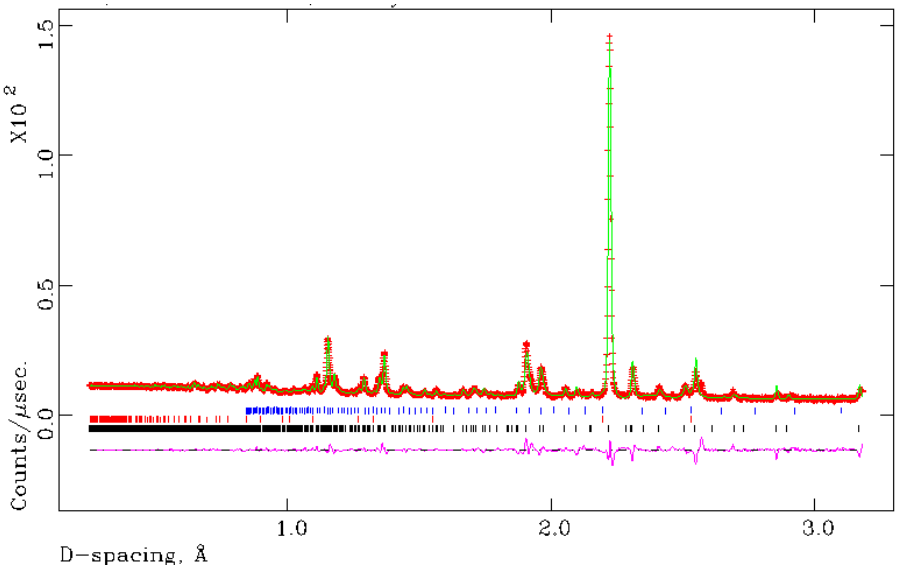

Figure 3.23b.

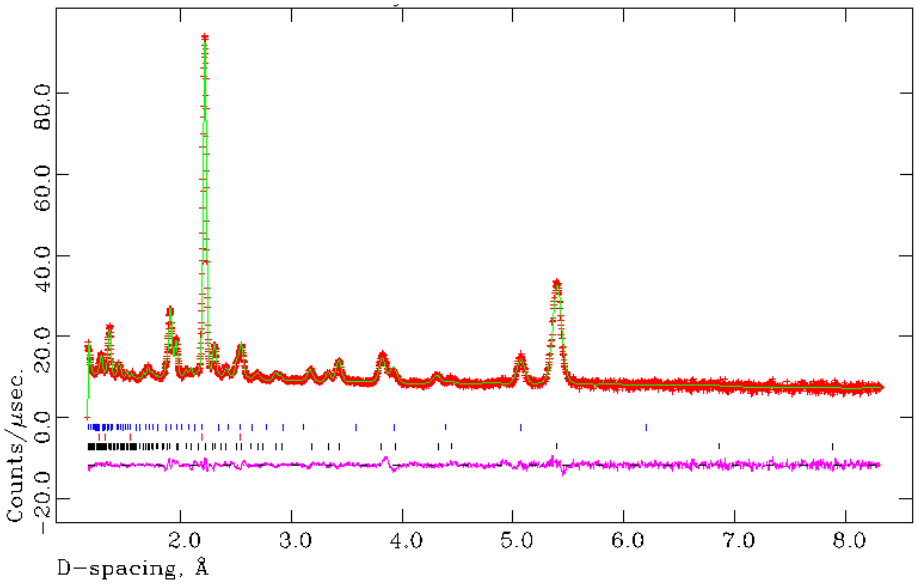

*Figure 3.23.*Observed (+), calculated (-) and difference(-) profiles from refinement using 2K NPD data for $YSr_3Mn_{3.1}Ga_{0.9}O_{10.4}$ *a*) C bank, 2 θ = 145° *b*) A bank, 2 θ = 35° $\chi^2 = 5.616$, R_{wp} =2.34% and R_p = 4.15%. Reflection positions are marked: main phase (|); MnO (|), 1.0(4)% by weight; MnO magnetic phase (|).

Figure 3.24a

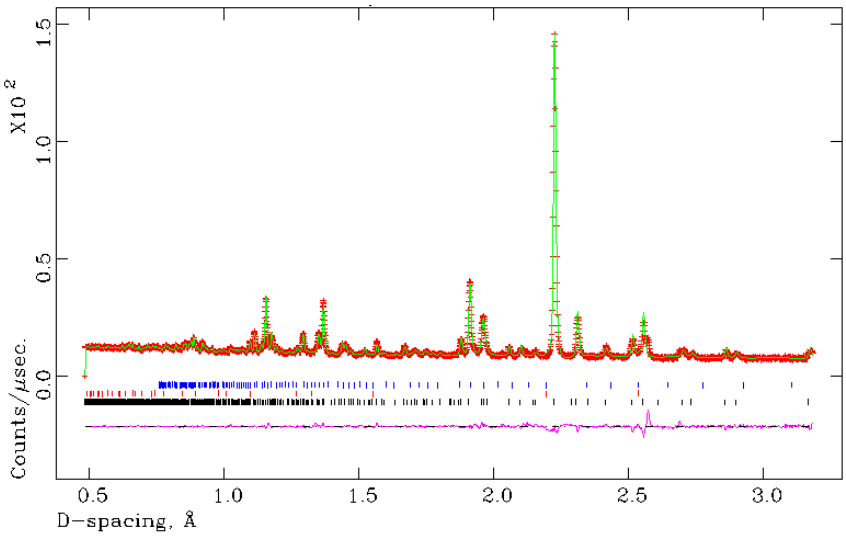

Figure 3.24b

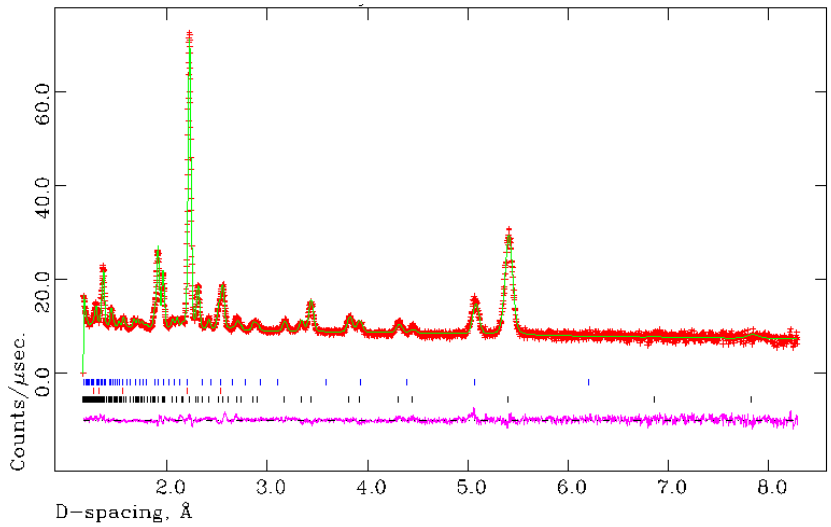

Figure 3.24. Observed (+), calculated (-) and difference (-) profiles from refinement using 2K NPD data for $YSr_3Mn_{2.67}Ga_{1.33}O_{10.5}$ *a*) C bank, 2 θ = 145° *b*) A bank, 2 θ = 35° .χ^2 = 3.294, R_{wp} =1.93% and R_p = 3.36%. Reflection positions are marked: main phase (|); MnO (|), 1.59(4)% by weight; MnO magnetic phase (|).

Tables 3.7–3.10 show the refinement results for $YSr_3Mn_{3.1}Ga_{0.9}O_{10.4}$, $YSr_3Mn_{2.67}Ga_{1.33}O_{10.5}$, $YSr_3Mn_{2.3}Ga_{1.7}O_{10.5}$ and $YSr_3Mn_{2.23}Ga_{1.77}O_{10.5}$. Associated profiles are shown in *figures 3.23, 3.24, 3.20* and *3.21* respectively.

Table 3.7a. Refinement results from 2K NPD data for $YSr_3Mn_{3.1}Ga_{0.9}O_{10.43(2)}$.

Atom	Position	x	y	z	Frac.	U_{iso} x100/Å^2
Mn1	8*f*	0.25	0.25	0.25	0.979(2)	1*
Ga1	8*f*	0.25	0.25	0.25	0.021(2)	1*
Mn2	8*h*	0.276(1)	0.276(1)	0	0.571(2)	1*
Ga2	8*h*	0.276(1)	0.276(1)	0	0.429(2)	1*
Y	4*e*	0	0	0.1440(2)	1	0.35(4)
Sr1	4*e*	0	0	0.6257(3)	1	1.32(9)
Sr2	8*g*	0.5	0	0.1300(1)	1	0.044(7)
O1	8*i*	0	0.095(1)	0	0.217(9)	1*
O2	8*j*	0.5	0.2286(4)	0	1	0.94(5)
O3	16*n*	0	0.2449(3)	0.2571(1)	1	0.32(2)
O4	16*m*	0.2185(2)	0.2185(2)	0.1132(1)	1	2.21(5)

a = 7.6288(2) Å, c = 15.6823(8) Å, χ^2 = 5.616, R_{wp} = 2.34% and R_p = 4.15%.

Magnetic moments: Mn1=2.13(5)μ_B ; Mn2 = 2.6(1) μ_B. Space group I4/*mmm*.

* denotes where thermal parameters fixed to a sensible value

Table 3.8a. Refinement results from 2K NPD data for $YSr_3Mn_{2.67}Ga_{1.33}O_{10.53(2)}$.

Atom	Position	x	y	z	Frac.	U_{iso} x100/Å^2
Mn1	8*f*	0.25	0.25	0.25	0.912(2)	1[#]
Ga1	8*f*	0.25	0.25	0.25	0.088(2)	1[#]
Mn2	8*h*	0.2656(4)	0.2656(4)	0	0.423(2)	1[#]
Ga2	8*h*	0.2656(4)	0.2656(4)	0	0.577(2)	1[#]
Y	4*e*	0	0	0.1431(1)	1	0.23(4)
Sr1	4*e*	0	0	0.6242(2)	1	2.0[*]
Sr2	8*g*	0.5	0	0.1300(1)	1	0.05(3)
O1	8*i*	0	0.102(1)	0	0.266(9)	1.5(2)
O2	8*j*	0.5	0.2197(4)	0	1	1.74(7)
O3	16*n*	0	0.2462(2)	0.2602(1)	1	0.43(2)
O4	16*m*	0.2129(1)	0.2129(1)	0.1134(1)	1	2.21[*]

[*] anisotropic thermal parameters given below. [#] denotes where thermal parameters fixed to a sensible value

a = 7.6409(1) Å, *c* = 15.6711(5) Å, χ^2 = 3.294, R_{wp} = 1.93% and R_p = 3.36%.

Magnetic moments: Mn1=2.26(6)μ_B; Mn2 = 3.3(1) μ_B. Space group I4/*mmm*.

Table 3.8b. Anisotropic thermal parameters

Atom	U_{11} x 100/Å^2	U_{22} x 100/Å^2	U_{33} x 100/Å^2	U_{12} x 100/Å^2	U_{13} x 100/Å^2
Sr1	2.87(1)	2.87(1)	0.27(1)		
O4	2.23(6)	2.23(6)	2.17(9)	0.88(6)	1.71(5)

Table 3.9a. Refinement results from 2K NPD data for $YSr_3Mn_{2.3}Ga_{1.7}O_{10.46(1)}$.

Atom	Position	x	y	z	Frac.	U_{iso} x100/Å^2
Mn1	8*f*	0.25	0.25	0.25	0.841(2)	1[#]
Ga1	8*f*	0.25	0.25	0.25	0.159(2)	1[#]
Mn2	8*h*	0.2687(1)	0.2687(1)	0	0.309(2)	1[#]
Ga2	8*h*	0.2687(1)	0.2687(1)	0	0.691(2)	1[#]
Y	4*e*	0	0	0.1447(1)	1	0.38(2)
Sr1	4*e*	0	0	0.6237(1)	1	2.22[*]
Sr2	8*g*	0.5	0	0.1312(8)	1	0.10(1)
O1	8*i*	0	0.1153(6)	0	0.228(6)	0.1(1)
O2	8*j*	0.5	0.2181(2)	0	1	1.56(4)
O3	16*n*	0	0.2466(1)	0.2602(7)	1	0.54(1)
O4	16*m*	0.2121(1)	0.2121(1)	0.1131(1)	1	2.42[*]

[*] anisotropic thermal parameters given below. [#]denotes where thermal parameters fixed to a sensible value.

a = 7.6423(1) Å, *c* = 15.6464(4) Å, χ^2 = 2.491, R_{wp} = 1.65% and R_p = 3.22%.

Magnetic moments: Mn1=2.21(4) μ_B; Mn2 = 3.8(1)μ_B. Space group I4/*mmm*.

Table 3.9b. Anisotropic thermal parameters

Atom	U_{11} x 100/Å^2	U_{22} x 100/Å^2	U_{33} x 100/Å^2	U_{12} x 100/Å^2	U_{13} x 100/Å^2
Sr1	3.02(1)	3.02(1)	0.61(9)		
O4	2.48(4)	2.48(4)	2.30(6)	0.97(5)	1.97(4)

Table 3.10a. Refinement results from 2K NPD data for $YSr_3Mn_{2.23}Ga_{1.67}O_{10.59(2)}$.

Atom	Position	x	y	z	Frac.	U_{iso} x100/Å^2
Mn1	8*f*	0.25	0.25	0.25	0.781(3)	1$^{\#}$
Ga1	8*f*	0.25	0.25	0.25	0.219(3)	1$^{\#}$
Mn2	8*h*	0.2683(4)	0.2683(4)	0	0.334(3)	1$^{\#}$
Ga2	8*h*	0.2683(4)	0.2683(4)	0	0.666(3)	1$^{\#}$
Y	4*e*	0	0	0.1454(2)	1	0.6(1)
Sr1	4*e*	0	0	0.6217(3)	1	1.81*
Sr2	8*g*	0.5	0	0.1313(2)	1	0.36(6)
O1	8*i*	0	0.120(1)	0	0.295(9)	1$^{\#}$
O2	8*j*	0.5	0.2234(6)	0	1	2.73*
O3	16*n*	0	0.2450(3)	0.2600(1)	1	0.41(6)
O4	16*m*	0.2112(2)	0.2112(2)	0.1131(1)	1	1.93*

* anisotropic thermal parameters given below. $^{\#}$ denotes where thermal parameters fixed to a sensible value

a = 7.6462(2) Å, *c* = 15.6355(5) Å, χ^2 = 3.217, R_{wp} = 3.67% and R_p = 2.73%.

Magnetic moments: Mn1=2.2(1) μ_B ; Mn2 = 3.8(2) μ_B. Space group I4/*mmm*.

Table 3.10b. Anisotropic thermal parameters

Atom	U_{11} x 100/Å^2	U_{22} x 100/Å^2	U_{33} x 100/Å^2	U_{12} x 100/Å^2	U_{13} x 100/Å^2
Sr1	2.6(2)	2.6(2)	0.2(2)		
O2	1.1(1)	4.9(3)	2.2(3)		
O4	1.85(8)	1.85(8)	2.1(1)	0.61(9)	1.22(8)

3.5 References

[1] W. C. Hansen and L. T. Brownmiller, *Amer. J. Sci*. 15**,** 244, (1928).

[2] W. Büssem, *Fortschr. Min.* 22**,** 31, (1937).

[3] W. Büssem, *Proc. Symposium on the Chemistry of Cement (Stockholm)* **,** 153 (1938).

[4] E. F. Bertaut, P. Blum, and A. Sagnières, C.R. *Acad. Sci. (Paris)* 244**,** 2944, (1957).

[5] E. F. Bertaut, P. Blum, and A. Sagnières, *Acta Cryst.* 12**,** 149, (1959).

[6] D. K. Smith, *Acta Cryst.* 15**,** 1146, (1962).

[7] A. A. Colville and S. Geller, *Acta Cryst.* B27, 2311, (1971).

[8] A. J. Wright, H. M. Palmer, P. A. Anderson and C. Greaves. *J. Mater. Chem.* **11**, 1324-1326, (2001).

[9] A. J. Wright, H. M. Palmer, P. A. Anderson and C. Greaves. *J. Mater. Chem.* **12**, 978-982, (2002).

[10] J.-C. Grenier, F. Menil, M. Pouchard, and P. Hagenmuller, Mat. Res. Bull. 13**,** 329, (1978).

[11] N. Nguyen, Y. Calage, F. Varret, and G. Ferey, *J. Solid State Chem.* 53, 398 (1984).

[12] Y. Moritomo, A. Asamitsu, H. Kuwahara and Y. Tokura, *Nature* 380, 141, (1996)

[13] P. D. Battle, S. J. Blundell, P. N. Santhosh, M. J. Rosseinsky and C. Steer. *J. Phys*. *Condens. Matter* 14, 13569, (2002).

[14] L. J. Gillie, H. M. Palmer, A. J. Wright, J. Hadermann, G. Van Tendeloo, C Greaves. *Journal of Physics and Chemistry of Solids* 65, 87, (2004).

[15] S.Ya Istomin, J. Grins, G. Swensson, O.A. Drozhzhin, V. L. Kozhevnikov

, E. V. Antipov, J.P. Attfield. *Chem. Mater*. **15**,4012, (2003).

[16] M. James, M. Avdeev, P. Barnes, L. Morales, K. Wallwork, R. Withers *J Solid State Chem* **180**, 2233, (2007).

[17] S. Kimura, Y. Maeda, T. Kashiwagi, H. Yamaguchi, M. Hagiwara, S. Yoshida, I. Terasaki, K. Kindo. *Phys Rev B,* **78**,180403(R) (2008).

[18] I. O. Troyanchuk, D. V. Karpinsky, A. P. Sazonov, V. Sikolenko, V. Efimov and A. Senyshyn. *J. Mater. Sci*. 44, 5900, (2009).

[19] F. Lindberg, O. A. Drozhzhin, S. Ya Istomin, G. Svensson, F.B. Kaynak, P.Svedlinh, P. Warnicke, A. Wannberg, A. Mellergard, E. V. Antipov. *J. Solid State Chemistry*, 179, 1434, (2006).

[20] A. Munter. *Neutron News* 3, 29, (1992).

[21] A. C. Larson, R. B. Von Dreele, General Structure Analysis System, Los Alamos National Laboratory, Los Alamos, NM, (1994).

[22] L. J. Gillie, PhD University of Birmingham 2003.

CHAPTER 4

Magnetic and Structural Characterisation of $YSr_3Mn_{4-x}Ga_xO_{10.5}$ following Oxidation or Fluorination.

4.1 Introduction

The material $Y_{0.8}Sr_{2.2}Mn_2GaO_{7.9}$, as described in the previous chapter, was oxidised to $Y_{0.8}Sr_{2.2}Mn_2GaO_9$ by Gillie [1]. Oxidation resulted in a structure in which the vacancies in the tetrahedral layer were filled, giving octahedral coordination for manganese and gallium cations. Oxidation of samples $YSr_3Mn_{3.1}Ga_{0.9}O_{10.4}$, $YSr_3Mn_{2.67}Ga_{1.33}O_{10.5}$, $YSr_3Mn_{2.3}Ga_{1.7}O_{10.5}$ and $YSr_3Mn_{2.23}Ga_{1.77}O_{10.5}$, would allow partial filling of the vacancies in the tetrahedral layer up to the maximum when Mn^{3+} has been fully oxidised to Mn^{4+}.

It was proposed that fluorination of the samples would result in a material with mixed Mn^{3+}/ Mn^{4+} oxidation states. $Y_{0.8}Sr_{2.2}Mn_2GaO_8$ ($Y_{1.07}Sr_{2.93}Mn_{2.67}Ga_{1.33}O_{10.6}$) was successfully fluorinated by Gillie [1], using copper fluoride as the fluorinating agent. CuF_2 was thoroughly ground with the sample, the resulting homogeneous mixture was heated at 300^{o}C for several periods of 24 hours until phase purity was reached. Subsequent XRPD detected peaks due to a CuO impurity. It was proposed that fluorination with 10% F_2 / 90% N_2 would result in samples without the CuO impurities associated with CuF_2 fluorination.

Gillie synthesised a sample in which all of the vacancies in the tetrahedral layer of the parent oxide were fully occupied, resulting in a sample with stoichiometric formula $Y_{0.8}Sr_{2.2}Mn_2GaO_8F$.

4.2 Synthesis of Oxidised Samples

Oxidation of the four samples, $YSr_3Mn_{3.1}Ga_{0.9}O_{10.4}$, $YSr_3Mn_{2.67}Ga_{1.33}O_{10.5}$, $YSr_3Mn_{2.3}Ga_{1.7}O_{10.5}$ and $YSr_3Mn_{2.23}Ga_{1.77}O_{10.5}$, was carried out by heating in air at 400^{o}C for 12 hours.

4.3 Structural Characterisation

Neutron Powder Diffraction (NPD) data were collected at room temperature and 4K on D2B at ILL, Grenoble, France. Full occupancy of the oxygen O1 site would result in filling of the vacancies in the tetrahedral layer resulting in octahedral coordination for Mn and Ga cations, as shown in *figure 4.2* for $YSr_3Mn_{3.1}Ga_{0.9}O_{12.}$ Refinement of NPD data using the GSAS suite of programs [2] was carried out. The Rietveld plots (room temperature) for the oxidised samples $YSr_3Mn_{3.1}Ga_{0.9}O_{12}$, $YSr_3Mn_{2.67}Ga_{1.33}O_{11.835}$, $YSr_3Mn_{2.3}Ga_{1.7}O_{11.65}$ and $YSr_3Mn_{2.23}Ga_{1.77}O_{11.615}$ are shown in *figures 4.3-4.6.* Oxygen contents assume that all of the manganese has been oxidised to Mn^{4+}. Refined structural parameters are given in *tables 4.1-4.4.* The refinement of room temperature samples $YSr_3Mn_{3.1}Ga_{0.9}O_{12}$, $YSr_3Mn_{2.67}Ga_{1.33}O_{11.835,}$ $YSr_3Mn_{2.3}Ga_{1.7}O_{11.65}$ and $YSr_3Mn_{2.23}Ga_{1.77}O_{11.615}$ converged with χ^2 = 7.431, 17.48, 1.531, and 2.971 respectively.

The oxygen content of samples $YSr_3Mn_{2.67}Ga_{1.33}O_{11.835}$, $YSr_3Mn_{2.3}Ga_{1.7}O_{11.65}$ and $YSr_3Mn_{2.23}Ga_{1.77}O_{11.615}$ is restricted by Mn^{4+} content resulting in a structure with the possibility of octahedral, square pyramidal and tetrahedral coordination for Ga^{3+}/ Mn^{4+} ions in the former tetrahedral layer.

There is a tendency for greater mixing of Mn^{3+} and Ga^{3+} between the octahedral and 'tetrahedral' layers for the oxidised samples compared to the reduced samples as shown in *figure 4.1* and by comparison of *tables 3.2a, 3.3a, 3.4a* and *3.5a* (Chapter 3)

with *tables 4.1a, 4.2a, 4.3a* and *4.4a* (Chapter 4). Some migration of Mn^{3+} from the octahedral site is to be expected as the predominate coordination in the former tetrahedral layer changes to octahedral and the preferences of manganese for octahedral coordination and gallium for tetrahedral found in the reduced samples are no longer relevant. The temperature at which oxidation takes place i.e. 400^{o}C would limit mixing of Mn^{3+} and Ga^{3+} between the layers

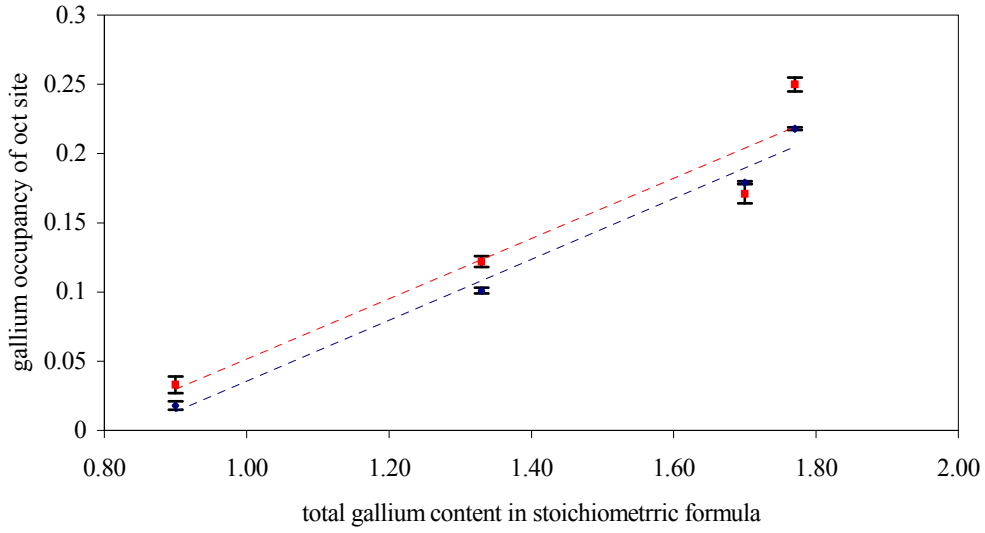

Figure 4.1. Plot to show gallium content of the octahedral site versus total gallium content. Red markers represent oxidised samples and blue markers reduced samples.

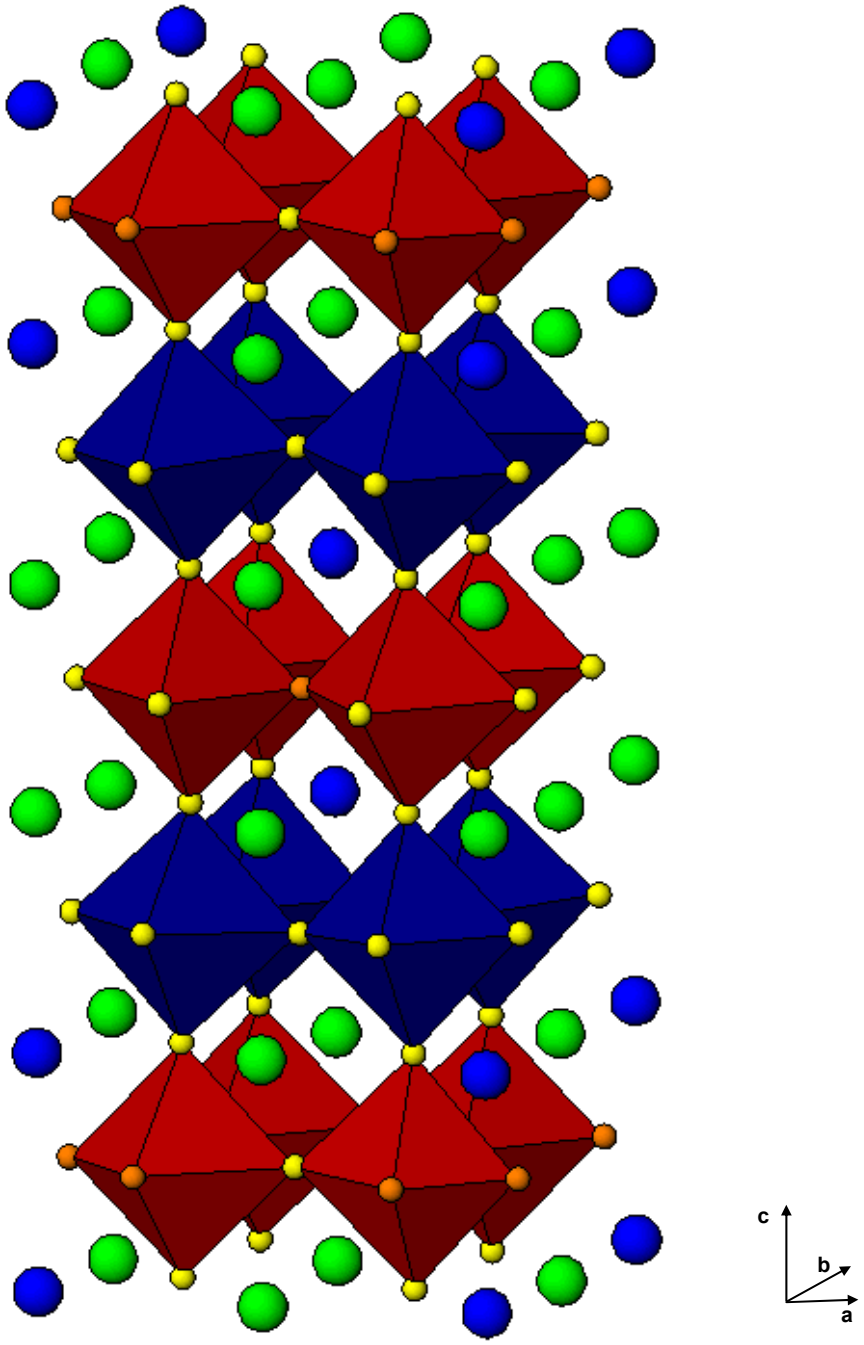

Figure 4.2. Crystallographic structure of $YSr_3Mn_{3.1}Ga_{0.9}O_{12.}$ Showing MnO_6 as blue polyhedra, Mn/GaO_6 as red polyhedra, yellow spheres are oxygen anions, orange spheres are oxygen anions (partially occupied prior to oxidation), green spheres are Sr^{2+} cations and blue spheres are Y^{3+} cations.

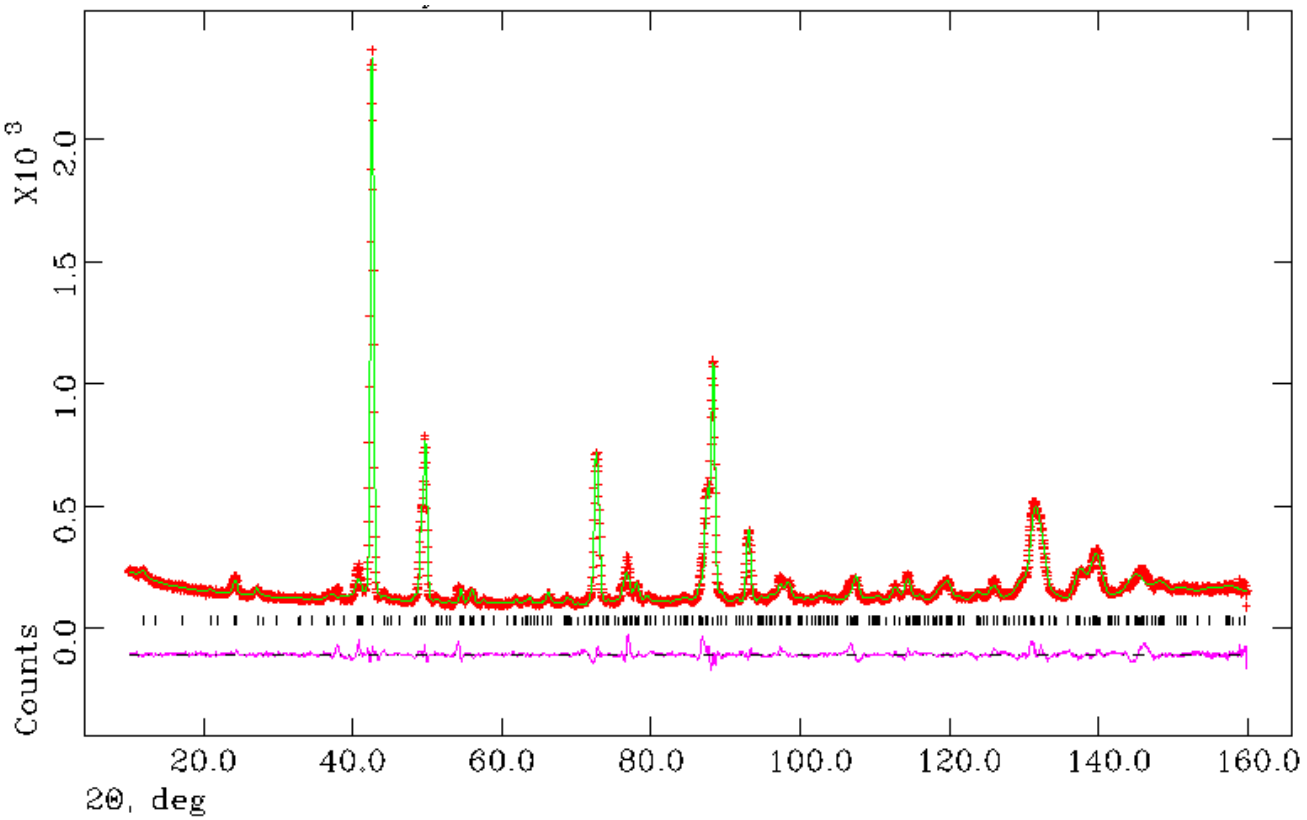

Figure 4.3. Observed (+), calculated (-) and difference (-) profiles from refinement using room temperature NPD data for $YSr_3Mn_{3.1}Ga_{0.9}O_{12}$ in space group I4/*mmm*, $\chi^2 = 7.431$, $R_{wp} = 6.90\%$ and $R_p = 4.79\%$.

Table 4.1a. Refinement results from room temperature NPD data for $YSr_3Mn_{3.1}Ga_{0.9}O_{12}$

Atom	Position	x	y	z	Frac.	U_{iso} x100/Å^2
Mn1	8*f*	0.25	0.25	0.25	0.967(6)	0.60*
Ga1	8*f*	0.25	0.25	0.25	0.033(6)	0.60*
Mn2	8*h*	0.211(4)	0.211(4)	0	0.583(6)	0.60*
Ga2	8*h*	0.211(4)	0.211(4)	0	0.417(6)	0.60*
Y	4*e*	0	0	0.1273(9)	1	0.60*
Sr1	4*e*	0	0	0.633(1)	1	0.60*
Sr2	8*g*	0.5	0	0.1188(5)	1	0.60*
O1	8*i*	0	0.241(2)	0	1	0.97(5)
O2	8*j*	0.5	0.283(2)	0	1	0.97(5)
O3	16*n*	0	0.272(1)	0.2437(7)	1	0.97(5)
O4	16*m*	0.2626(8)	0.2626(8)	0.1280(5)	1	0.97(5)

a = 7.5963(6) Å, c = 15.339(1) Å, χ^2 = 7.431, R_{wp} = 6.90% and R_p = 4.79%. Space group I4/*mmm*.

* denotes where thermal parameters were fixed to a sensible value based on that for the reduced sample, $YSr_3Mn_{3.1}Ga_{0.9}O_{10.4}$.

*Table 4.1b.*Selected bond lengths for $YSr_3Mn_{3.1}Ga_{0.9}O_{12.}$

Mn/Ga – O bond lengths	**Å**	**BVS**
Mn/Ga1- O3 (x4)	1.909(1)	Mn1 - 4.05
Mn/Ga1- O4 (x2)	1.876(8)	
Mn/Ga2 – O1 (x2)	1.62(2)	Mn2 – 4.29
Mn/Ga2 – O2 (x2)	2.26(4)	
Mn/Ga2 – O4 (x2)	2.04(1)	

Table 4.1c. Selected bond angles for $YSr_3Mn_{3.1}Ga_{0.9}O_{12}$.

Mn/Ga – O angles,	**degrees**
O3 - Mn/Ga1- O3 (x2)	99.7(7)
O3 - Mn/Ga1- O3 (x2)	80.3(7)
O3 - Mn/Ga1 – O4 (x4)	89.8(4)
O3 - Mn/Ga1 – O4 (x4)	90.2(4)
O2 - Mn/Ga2 – O2 (x1)	62(1)
O2 – Mn/Ga2 – O4 (x4)	76.6(1)
O4 – Mn/Ga2 – O4 (x1)	148.5(2)
O1 – Mn/Ga2 – O1 (x1)	96.0(3)

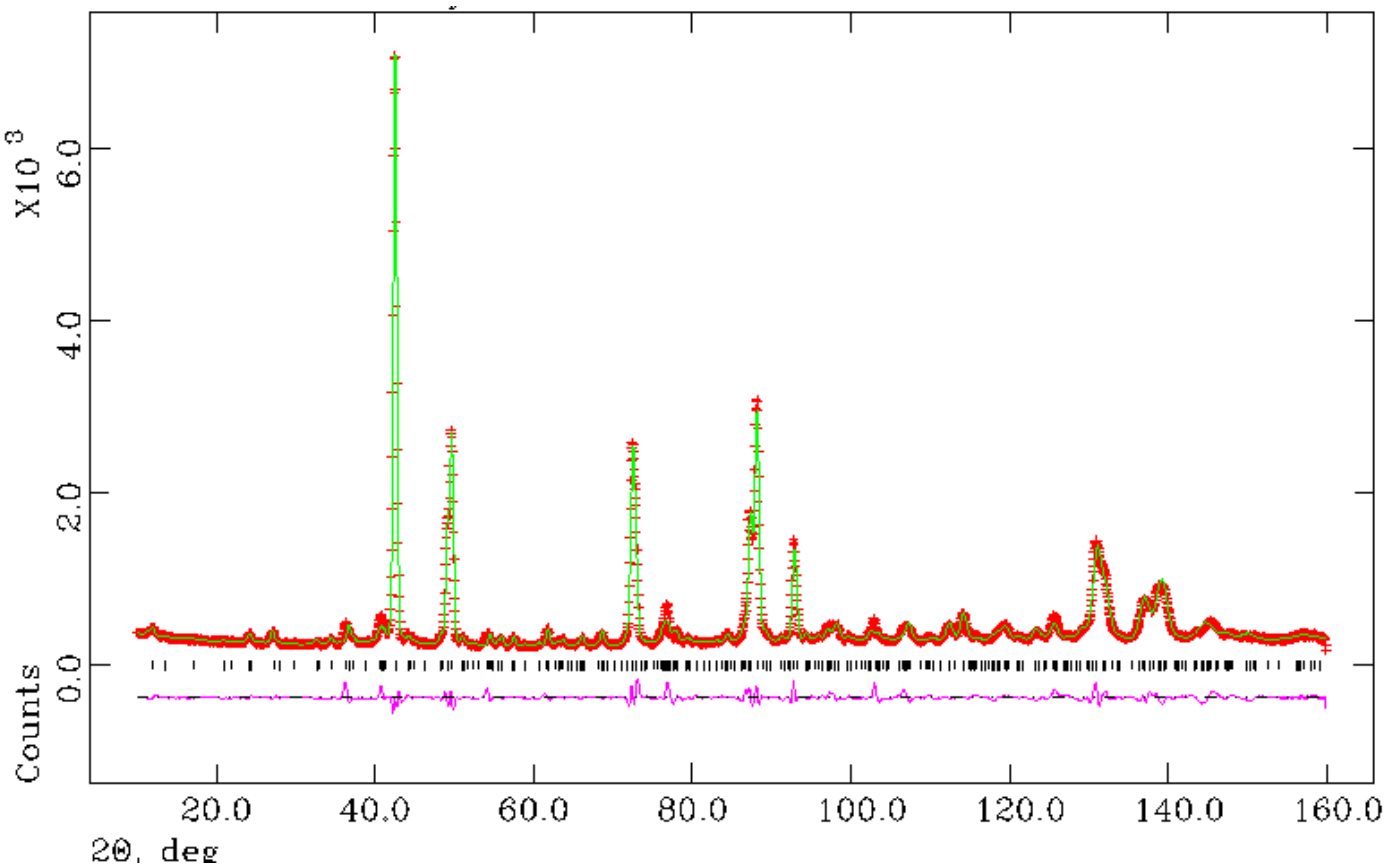

Figure 4.4. Observed (+), calculated (-) and difference (-) profiles from refinement using room temperature NPD data for $YSr_{2.67}Mn_{1.33}Ga_{0.9}O_{11.835}$ in space group I4/*mmm*, χ^2=17.48, R_{wp}=6.59% and R_p = 4.76%.

Table 4.2a. Refinement results from room temperature NPD data for $YSr_3Mn_{2.67}Ga_{1.33}O_{11.835}$

Atom	Position	x	y	z	Frac.	U_{iso} x100/Å^2
Mn1	8*f*	0.25	0.25	0.25	0.878(4)	0.35*
Ga1	8*f*	0.25	0.25	0.25	0.122(4)	0.35*
Mn2	8*h*	0.2680(9)	0.2680(9)	0	0.457(4)	0.35*
Ga2	8*h*	0.2680(9)	0.2680(9)	0	0.543(4)	0.35*
Y	4*e*	0	0	0.1323(5)	1	0.60*
Sr1	4*e*	0	0	0.6273(5)	1	0.60*
Sr2	8*g*	0.5	0	0.1197(2)	1	0.60*
O1	8*i*	0	0.2171(9)	0	0.9175	1.2(1)
O2	8*j*	0.5	0.257(1)	0	1	1.0*
O3	16*n*	0	0.261(6)	0.2568(4)	1	0.06(7)
O4	16*m*	0.2286(6)	0.2286(6)	0.1250(4)	1	3.5(1)

a = 7.6067(4) Å, *c* = 15.3666(9) Å, χ^2 = 17.48, R_{wp} = 6.59% and R_p = 4.76%. Space group I4/*mmm*.

* denotes where thermal parameters were fixed to a sensible value based on that for the reduced sample, $YSr_3Mn_{2.67}Ga_{1.33}O_{10.5}$

*Table 4.2b.*Selected bond lengths for $YSr_3Mn_{2.67}Ga_{1.33}O_{11.66}$.

Mn/Ga – O bond length	**Å**	**BVS**
Mn/Ga1- O3 (x4)	1.9062(3)	Mn1 – 3.87
Mn/Ga1- O4 (x2)	1.934(6)	
Mn/Ga2 – O1	2.075(8)	Mn2 – 3.82
Mn/Ga2 – O2 (x2)	1.767(7)	
Mn/Ga2 – O4 (x2)	1.967(6)	

Table 4.2c. Selected bond angles for $YSr_3Mn_{2.67}Ga_{1.33}O_{11.66}$.

Mn/Ga – O angles,	**degrees**
O3 - Mn/Ga1- O3 (x2)	94.6(3)
O3 - Mn/Ga1- O3 (x2)	85.3(3)
O3 - Mn/Ga1 – O4 (x4)	88.5(2)
O3 - Mn/Ga1 – O4 (x4)	91.5(2)
O2 - Mn/Ga2 – O2 (x1)	95.6(7)
O2 – Mn/Ga2 – O4 (x4)	98.3(2)
O4 – Mn/Ga2 – O4 (x1)	155.1(6)
O1 – Mn/Ga2 – O1 (x1)	68.5(5)

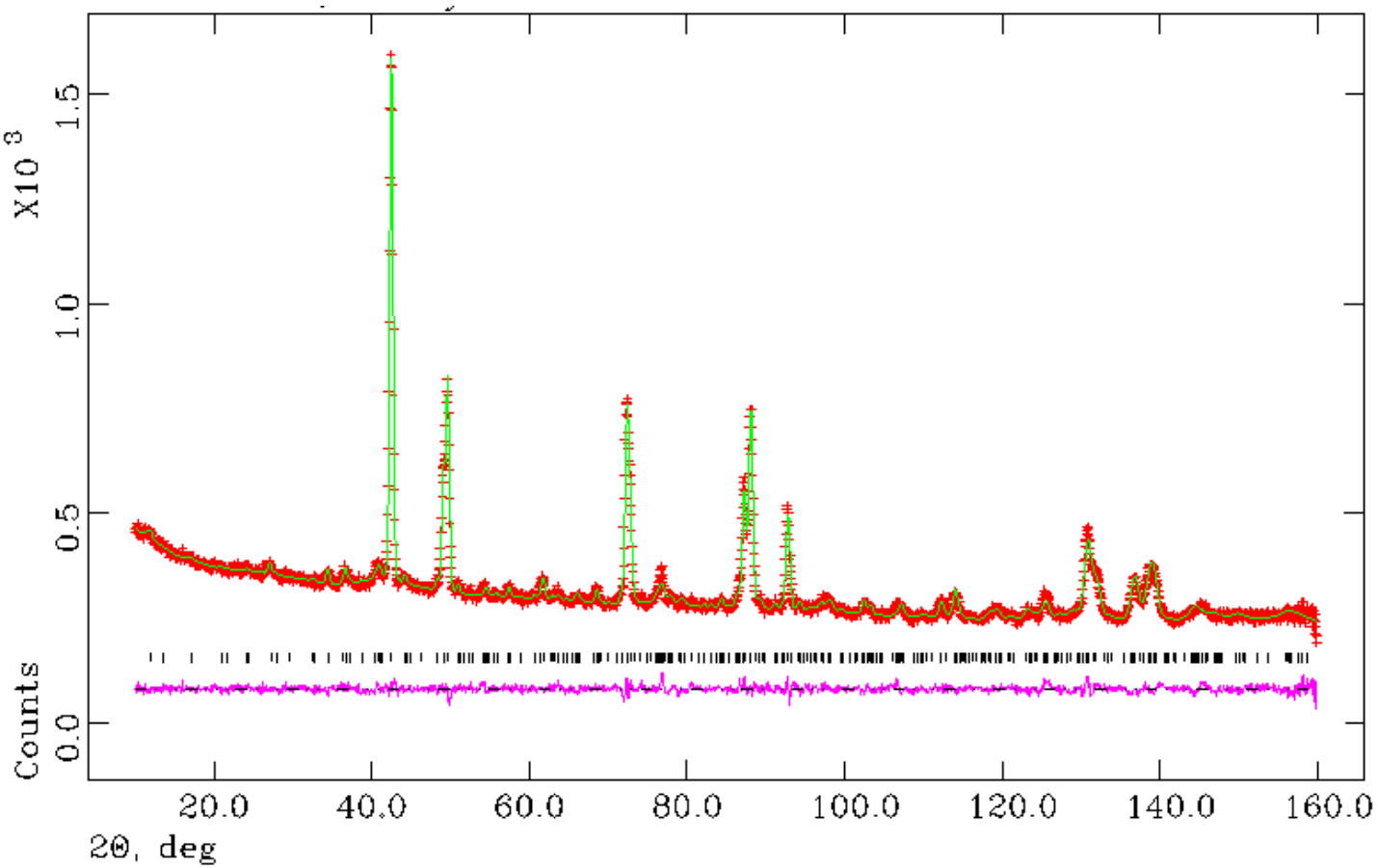

Figure 4.5. Observed (+), calculated (-) and difference (-) profiles from refinement using room temperature NPD data for $YSr_{2.3}Mn_{1.7}Ga_{0.9}O_{11.65}$ in space group I4/*mmm*, $\chi^2 = 1.531$, $R_{wp} = 2.21\%$ and $R_p = 1.75\%$.

Table 4.3a. Refinement results from room temperature NPD data for $YSr_3Mn_{2.3}Ga_{1.7}O_{11.65}$

Atom	Position	x	y	z	Frac.	U_{iso} x100/Å^2
Mn1	8*f*	0.25	0.25	0.25	0.829(7)	3.5(5)*
Ga1	8*f*	0.25	0.25	0.25	0.171(7)	3.5(5)*
Mn2	8*h*	0.265(1)	0.265(1)	0	0.321(7)	3.5(5)*
Ga2	8*h*	0.265(1)	0.265(1)	0	0.679(7)	3.5(5)*
Y	4*e*	0	0	0.1309(7)	1	0.8(2)
Sr1	4*e*	0	0	0.6241(7)	1	0.6(2)
Sr2	8*g*	0.5	0	0.1211(4)	1	0.1(1)
O1	8*i*	0	0.204(1)	0	0.825	1.9(2)
O2	8*j*	0.5	0.261(1)	0	1	1.2(2)
O3	16*n*	0	0.2580(8)	0.2575(5)	1	1.0(1)
O4	16*m*	0.2320(8)	0.2320(8)	0.1278(5)	1	2.6(1)

a = 7.6115(4) Å, *c* = 15.3797(8) Å, χ^2 = 1.531, R_{wp} = 2.21% and R_p = 1.75%. Space group I4/*mmm*.

* thermal parameters constrained to avoid correlation effects.

*Table 4.3b.*Selected bond lengths for $YSr_3Mn_{2.3}Ga_{1.7}O_{11.65.}$

Mn/Ga – O bond lengths,	**Å**	**BVS**
Mn/Ga1- O3 (x4)	1.9070(4)	Mn1 – 3.99
Mn/Ga1- O4 (x2)	1.899(7)	
Mn/Ga2 – O1	2.092(8)	Mn2 – 3.63
Mn/Ga2 – O2 (x2)	1.771(6)	
Mn/Ga2 – O4 (x2)	1.988(7)	

Table 4.3c. Selected bond angles for $YSr_3Mn_{2.3}Ga_{1.7}O_{11.65}$.

Mn/Ga – O angles,	**degrees**
O3 - Mn/Ga1- O3 (x2)	93.2(4)
O3 - Mn/Ga1- O3 (x2)	86.8(4)
O3 - Mn/Ga1 – O4 (x4)	89.6(2)
O3 - Mn/Ga1 – O4 (x4)	90.3(2)
O2 - Mn/Ga2 – O2 (x1)	93.6(7)
O2 – Mn/Ga2 – O4 (x4)	97.3(2)
O4 – Mn/Ga2 – O4 (x1)	158.7(6)
O1 – Mn/Ga2 – O1 (x1)	63.3(7)

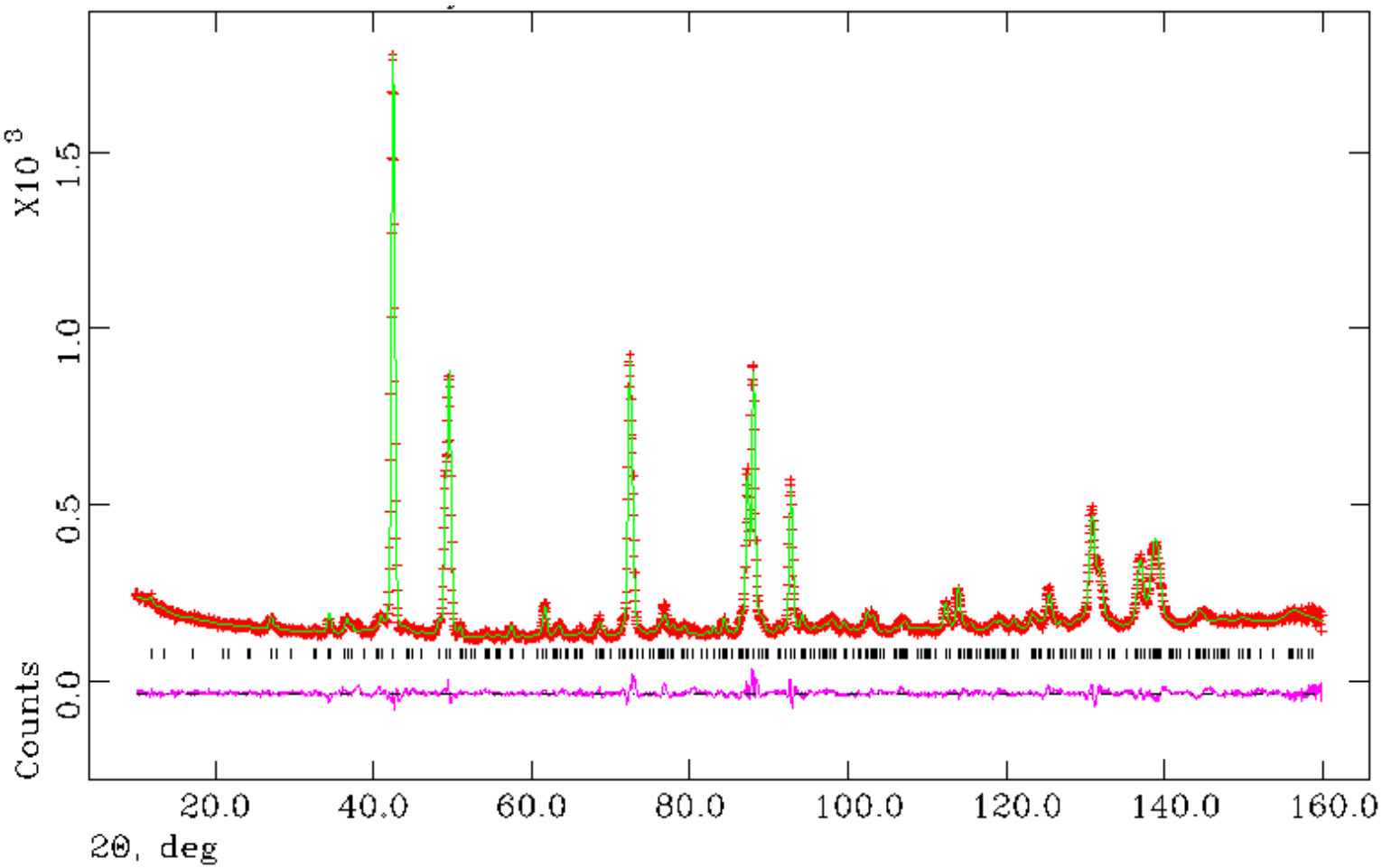

Figure 4.6. Observed (+), calculated (-) and difference (-) profiles from refinement using room temperature NPD data for $YSr_3Mn_{2.23}Ga_{1.77}O_{11.615}$ in space group I4/*mmm*, $\chi^2 = 2.971$, $R_{wp} = 4.16\%$ and $R_p = 3.24\%$.

Table 4.4a. Refinement results from room temperature NPD data for $YSr_3Mn_{2.23}Ga_{1.77}O_{11.615}$

Atom	Position	x	y	z	Frac.	U_{iso} x100/Å^2
Mn1	8*f*	0.25	0.25	0.25	0.750(5)	2.23(2)*
Ga1	8*f*	0.25	0.25	0.25	0.250(5)	2.23(2)*
Mn2	8*h*	0.255(1)	0.255(1)	0	0.365(5)	2.23(2)*
Ga2	8*h*	0.255(1)	0.255(1)	0	0.635(5)	2.23(2)*
Y	4*e*	0	0	0.1258(4)	1	0.17(4)#
Sr1	4*e*	0	0	0.6202(5)	1	0.17(4)#
Sr2	8*g*	0.5	0	0.1303(3)	1	0.17(4)#
O1	8*i*	0	0.212(1)	0	0.8075	2.2(2)
O2	8*j*	0.5	0.223(1)	0	1	0.7(1)
O3	16*n*	0	0.2376(7)	0.2566(3)	1	0.62(8)
O4	16*m*	0.2414(7)	0.2414(7)	0.1241(3)	1	2.7(1)

a = 7.6149(3) Å, *c* = 15.3705(7) Å, χ^2 = 2.971, R_{wp} = 4.16% and R_p = 3.24%.
* Thermal parameters constrained to avoid correlation effects
# Thermal parameters constrained to avoid negative values. Space group I4/*mmm.*

*Table 4.4b.*Selected bond lengths for $YSr_3Mn_{2.23}Ga_{1.77}O_{11.615.}$

Mn/Ga – O bond lengths,	**Å**	**BVS**
Mn/Ga1- O3 (x4)	1.9087(4)	Mn1 – 3.85
Mn/Ga1- O4 (x2)	1.937(6)	
Mn/Ga2 – O1	1.967(10)	Mn2 – 3.61
Mn/Ga2 – O2 (x2)	1.883(7)	
Mn/Ga2 – O4 (x2)	1.913(6)	

Table 4.4c. Selected bond angles for $YSr_3Mn_{2.23}Ga_{1.77}O_{11.615}$.

	Mn/Ga – O angles,	**degrees**
O3 - Mn/Ga1- O3 (x2)		84.2(3)
O3 - Mn/Ga1- O3 (x2)		95.8 (3)
O3 - Mn/Ga1 – O4 (x4)		91.0(2)
O3 - Mn/Ga1 – O4 (x4)		89.0(2)
O2 - Mn/Ga2 – O2 (x1)		104.6(6)
O2 – Mn/Ga2 – O4 (x4)		92.6(2)
O4 – Mn/Ga2 – O4 (x1)		171.4(8)
O1 – Mn/Ga2 – O1 (x1)		71.0(7)

4.3.1 Discussion

The occupancy of the O1 site, which was approximately 25% occupied in the reduced samples, was fixed to a level assuming complete oxidation of Mn^{3+} to Mn^{4+}. Refinement of the fractional occupancy of the O1 site did not improve the agreement between experimental and calculated profiles.

In contrast to the Jahn-Teller distorted polyhedra evident for the reduced samples, the apical bond length for the octahedra is not substantially different to that of the equatorial bond length. There is no evidence of the long bond from Mn2 to the partially occupied O1 site as found for the Jahn- Teller distorted square pyramid in the reduced samples, the bonds of the square pyramid/ octahedra within the former tetarhedral layer are of similar length for the oxidised samples, as shown in *figure 4.7*.

These results are consistent with an oxidation state of IV for manganese, a d^3 cation that would not display Jahn- Teller distortion.

Bond valence sum calculations [3] (*tables 4.1b, 4.2b, 4.3b and 4.4b)*, give a valency for manganese in the octahedral site close to the expected value of 4. As the gallium content of the octahedral site increases there is greater deviation from the predicted valency, as expected since the refined Mn – O bond distances represent an average of Ga – O and Mn – O bond distances where sites are occupied by Mn^{4+} or Ga^{3+} in a disordered fashion. There is greater deviation from the predicted valency for the former tetrahedral layer since the gallium occupancy of this site is greater.

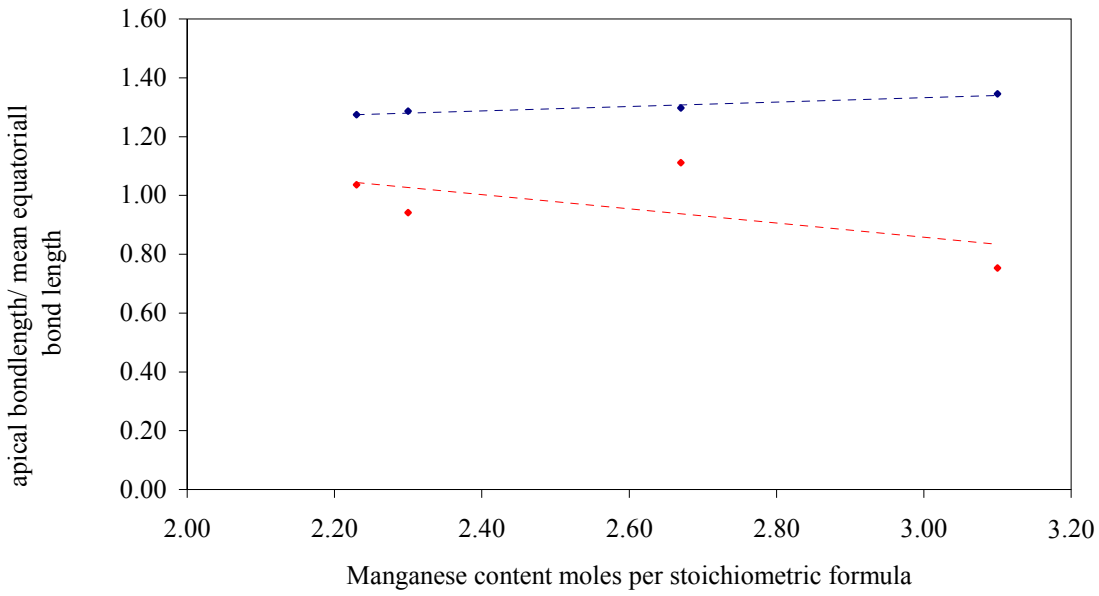

Figure 4.7. Plot to show apical bond length compared to the mean equatorial bond length for reduced samples, blue markers and oxidised samples, red markers.

4.4 Magnetic Characterisation of Oxidised Samples

4.4.1 Magnetic Susceptibility Studies

Magnetic susceptibility measurements were taken using a Quantum Design Physical Properties Measurement System (PPMS). DC magnetisation measurements were made for $YSr_3Mn_{3.1}Ga_{0.9}O_{12}$, $YSr_3Mn_{2.67}Ga_{1.33}O_{11.835}$, $YSr_3Mn_{2.3}Ga_{1.7}O_{11.65}$ and $YSr_3Mn_{2.23}Ga_{1.77}O_{11.615}$, with an applied field of 1000 Gauss. Both zero field cooled and field cooled data were collected. *Figures 4.8 – 4.11* show the susceptibility versus temperature plots for all four samples. $YSr_3Mn_{3.1}Ga_{0.9}O_{12}$, $YSr_3Mn_{2.67}Ga_{1.33}O_{11.835}$, $YSr_3Mn_{2.3}Ga_{1.7}O_{11.65}$ order antiferromagnetically, although it is not possible to identify a maximum in the susceptibility for $YSr_3Mn_{2.23}Ga_{1.77}O_{11.615}$ a negative Weiss temperature, θ, for the inverse susceptibility plot indicates antiferromagnetic behaviour, as detailed later.

The Néel temperature is similar to that for the equivalent reduced samples for $YSr_3Mn_{3.1}Ga_{0.9}O_{12}$ and $YSr_3Mn_{2.67}Ga_{1.33}O_{11.835}$. Compared to the reduced samples the Néel temperature reduces from ~ 86K to 45K for $YSr_3Mn_{2.3}Ga_{1.7}O_{11.65}$. Divergence of field cooled and zero field data after ordering suggest that there is a ferromagnetic component to the magnetic properties for $YSr_3Mn_{3.1}Ga_{0.9}O_{12}$, $YSr_3Mn_{2.67}Ga_{1.33}O_{11.835}$ and $YSr_3Mn_{2.3}Ga_{1.7}O_{11.65.}$ Although there is some deviation from linear behaviour above the ordering temperature in the plots of inverse susceptibility against temperature *figures 4.12-4.15*, the Curie-Weiss law was used to estimate the paramagnetic moments.

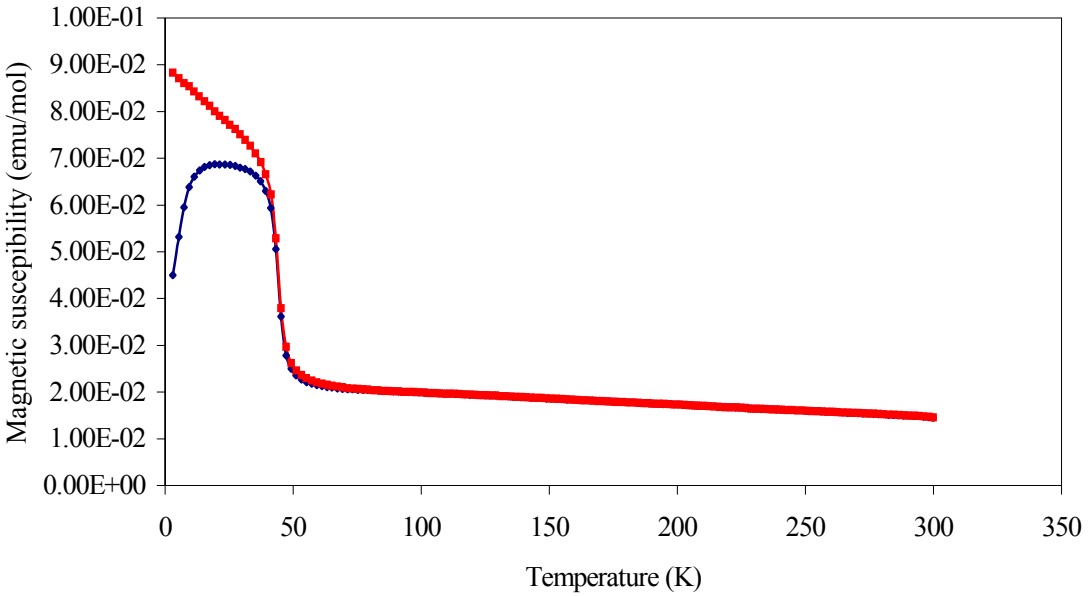

Figure 4.8. Magnetic susceptibility versus temperature plot for $YSr_3Mn_{3.1}Ga_{0.9}O_{12}$ (DC magnetisation performed in an applied field of 1000 Gauss. Zero-field cooled is shown blue and field cooled data in red.)

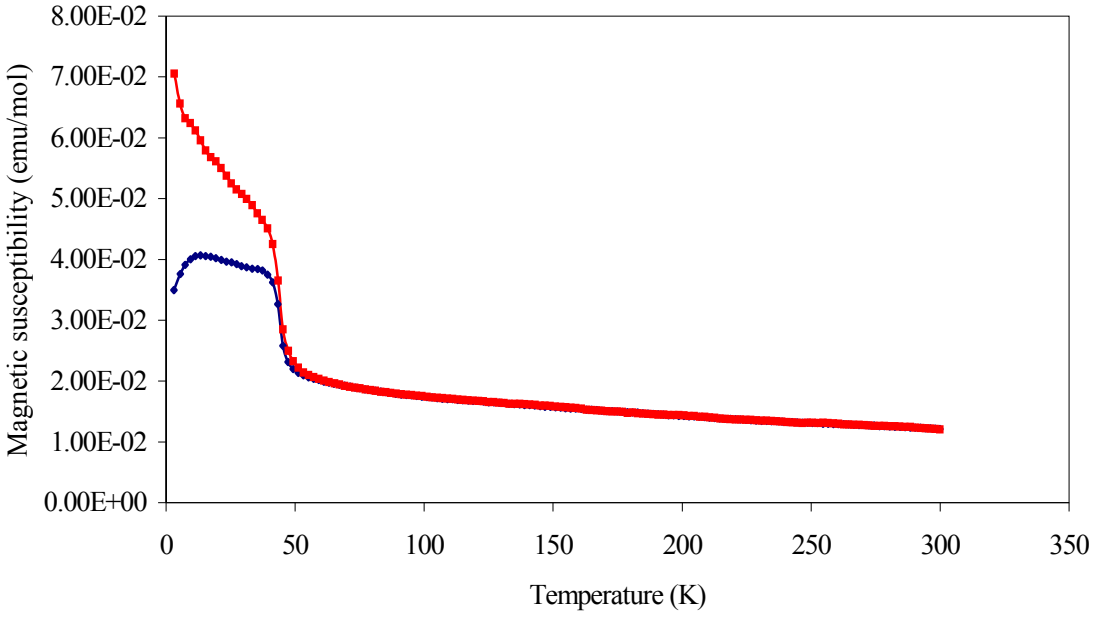

Figure 4.9. Magnetic susceptibility versus temperature plot for $YSr_3Mn_{2.67}Ga_{1.33}O_{11.835}$ (DC magnetisation performed in an applied field of 1000 Gauss. Zero-field cooled is shown blue and field cooled data in red.)

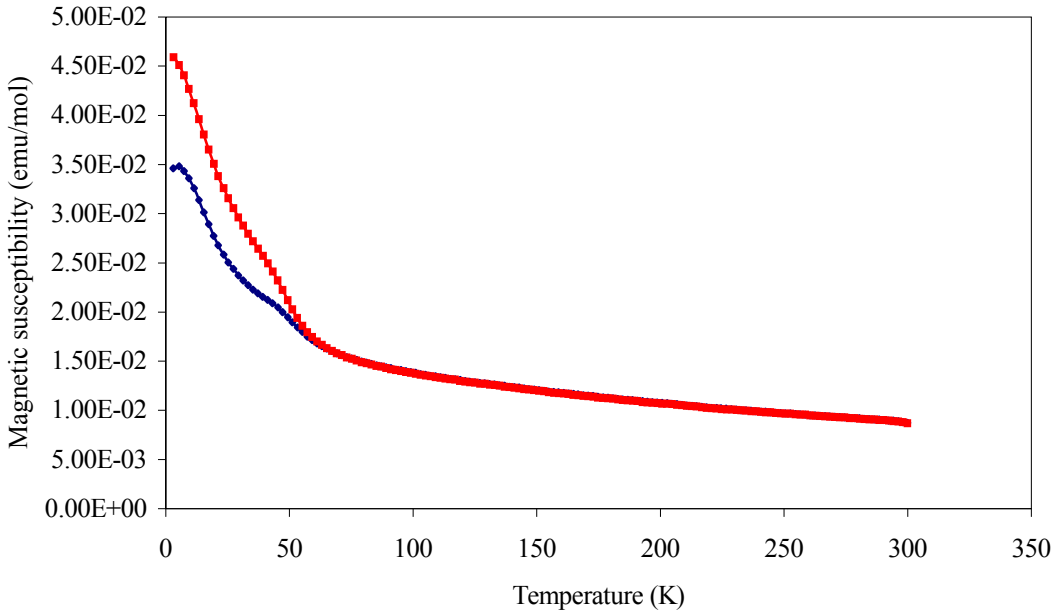

Figure 4.10. Magnetic susceptibility versus temperature plot for $YSr_3Mn_{2.3}Ga_{1.7}O_{11.65}$ (DC magnetisation performed in an applied field of 1000 Gauss. Zero-field cooled is shown blue and field cooled data in red.)

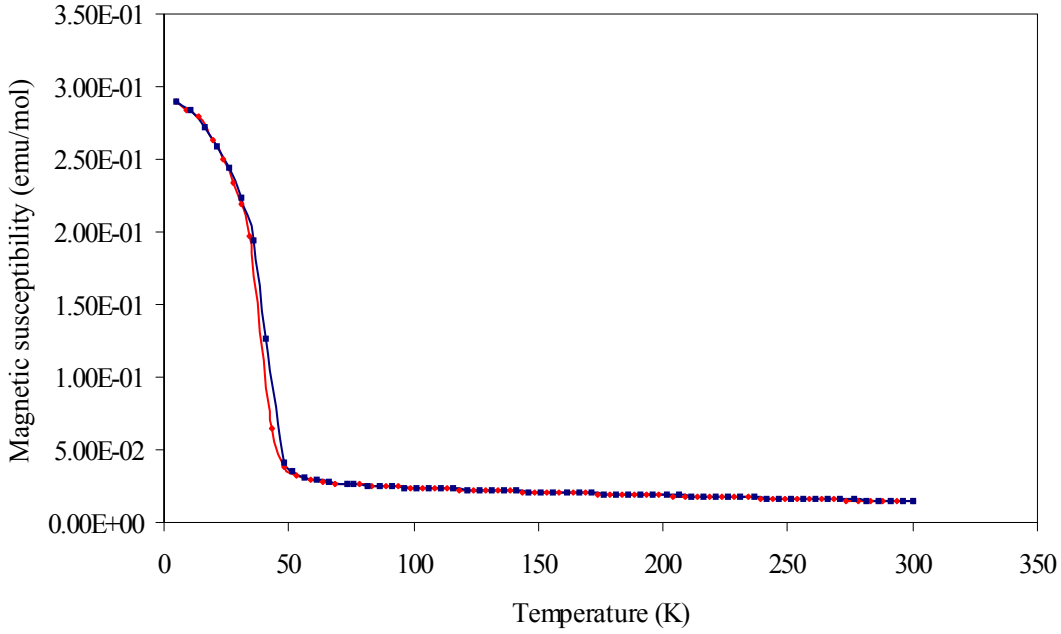

Figure 4.11. Magnetic susceptibility versus temperature plot for $YSr_3Mn_{2.23}Ga_{1.77}O_{11.615}$ (DC magnetisation performed in an applied field of 1000 Gauss. Zero-field cooled is shown blue and field cooled data in red.)

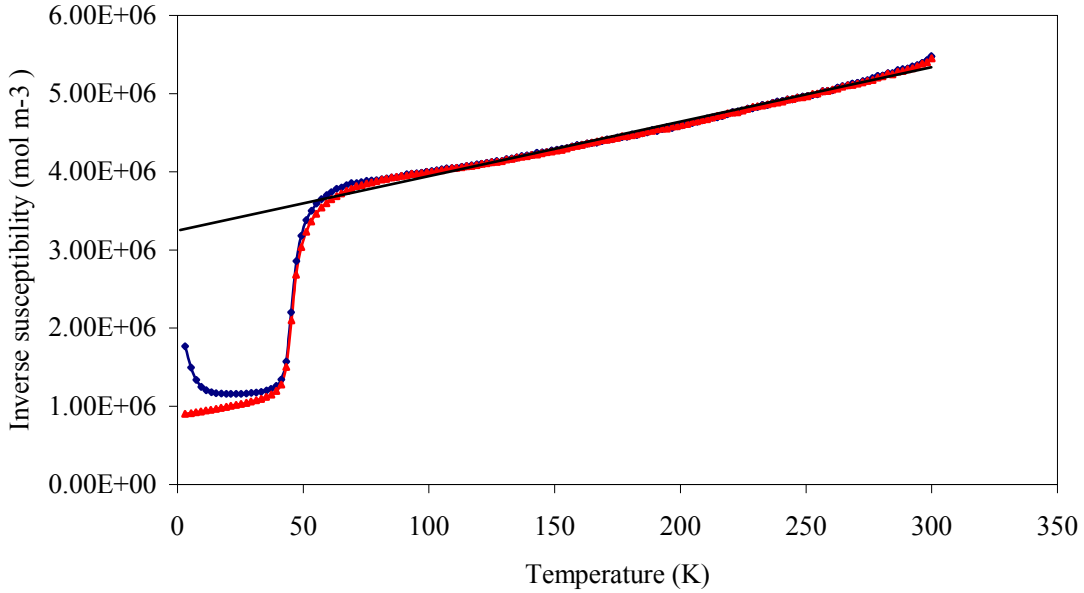

Figure 4.12. Inverse susceptibility versus temperature plot for $YSr_3Mn_{3.1}Ga_{0.9}O_{12}$ (DC magnetisation performed in an applied field of 1000 Gauss. Zero-field cooled is shown blue and field cooled data in red. Black line is linear fit to paramagnetic data.)

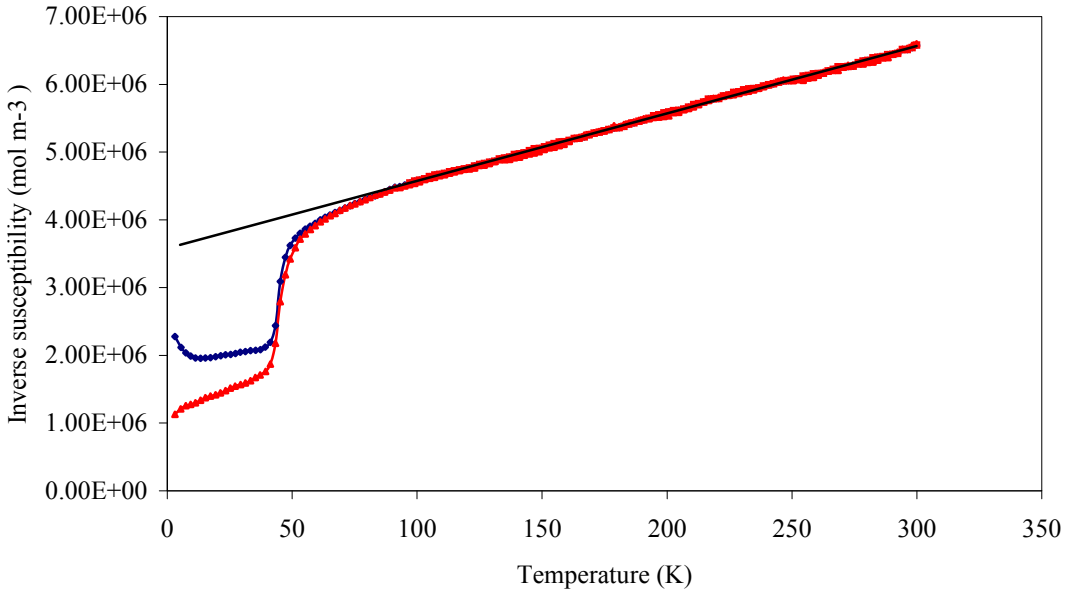

Figure 4.13. Inverse susceptibility versus temperature plot for $YSr_3Mn_{2.67}Ga_{1.33}O_{11.835}$ (DC magnetisation performed in an applied field of 1000 Gauss. Zero-field cooled is shown blue and field cooled data in red. Black line is linear fit to paramagnetic data.)

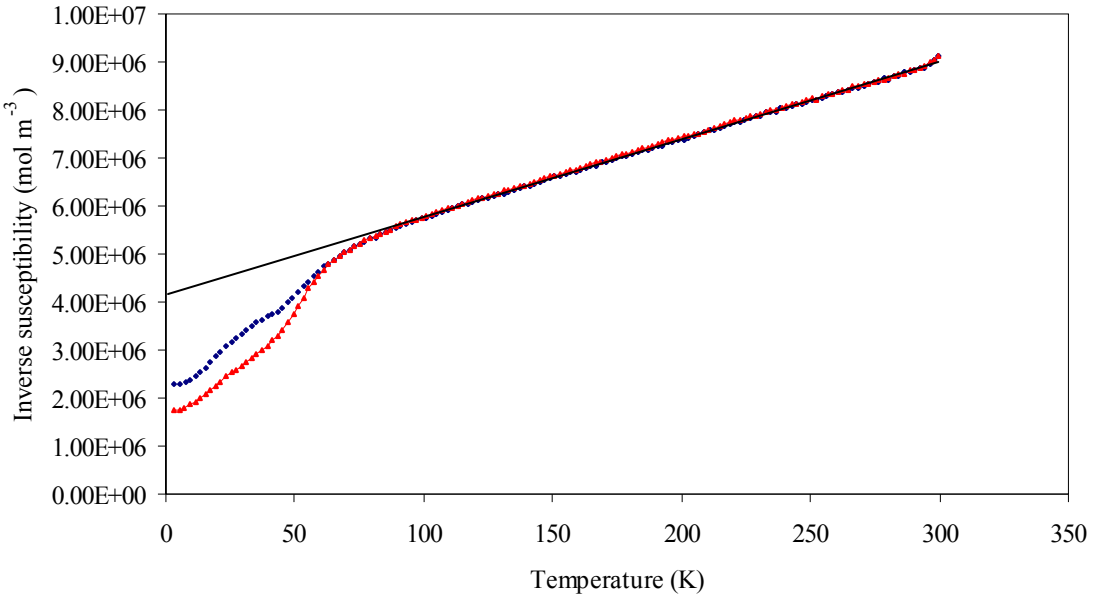

Figure 4.14. Inverse susceptibility versus temperature plot for $YSr_3Mn_{2.3}Ga_{1.7}O_{11.65}$ (DC magnetisation performed in an applied field of 1000 Gauss. Zero-field cooled is shown blue and field cooled data in red. Black line is linear fit to paramagnetic data.)

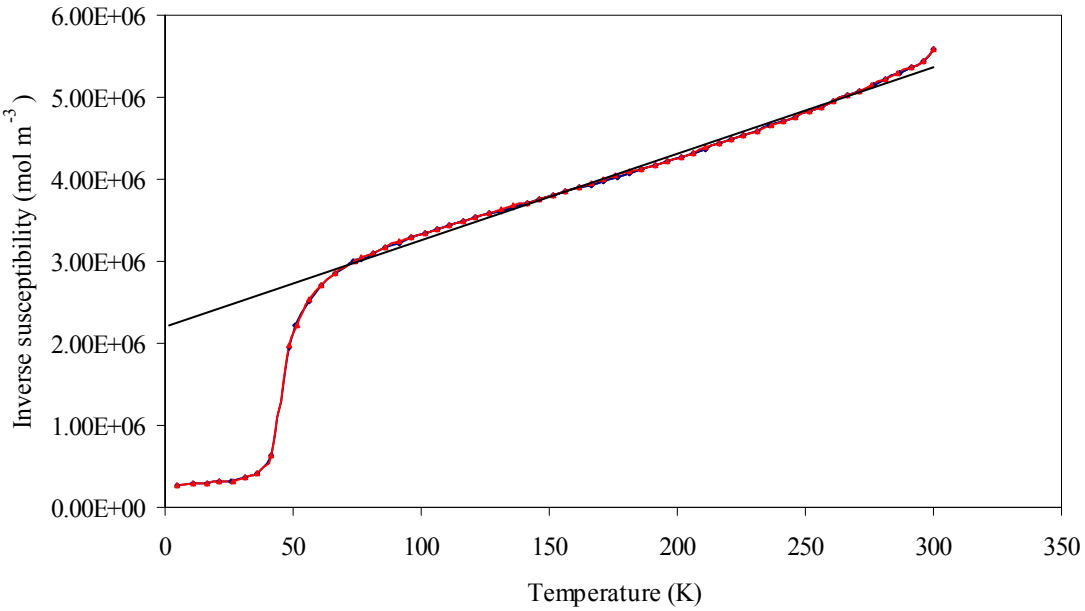

Figure 4.15. Inverse susceptibility versus temperature plot for $YSr_3Mn_{2.23}Ga_{1.77}O_{11.615}$ (DC magnetisation performed in an applied field of 1000 Gauss. Zero-field cooled is shown blue and field cooled data in red. Black line is linear fit to paramagnetic data.)

The Weiss temperature, θ, is negative for all four samples based on extrapolation of the paramagnetic region of the inverse susceptibility plot. θ = -465.3K for $YSr_3Mn_{3.1}Ga_{0.9}O_{12}$, -359.3K for $YSr_3Mn_{2.67}Ga_{1.33}O_{11.835,}$ -258.6K for $YSr_3Mn_{2.3}Ga_{1.7}O_{11.65}$ and –209.9K for $YSr_3Mn_{2.23}Ga_{1.77}O_{11.615}$ again indicating antiferromagnetic behaviour.

The paramagnetic moments were estimated from the gradient of the paramagnetic region of the inverse susceptibility versus temperature plots. The results were as follows, $YSr_3Mn_{3.1}Ga_{0.9}O_{12}$ = 5.43μ_B per Mn ion, $YSr_3Mn_{2.67}Ga_{1.33}O_{11.835}$ = 4.89μ_B per Mn ion, $YSr_3Mn_{2.3}Ga_{1.7}O_{11.65}$ = 4.15μ_B per Mn ion and $YSr_3Mn_{2.23}Ga_{1.77}O_{11.615}$ = 5.21μ_B per Mn ion. The expected spin only value for Mn^{4+}, a d^3 ion, would be 3.87 μ_B. The high magnetic moment could be due to clusters of manganese ions in which moments are aligned ferromagnetically. Divergence of the field cooled and zero field plots below the ordering temperature for samples $YSr_3Mn_{3.1}Ga_{0.9}O_{12,}$ $YSr_3Mn_{2.67}Ga_{1.33}O_{11.835}$ and $YSr_3Mn_{2.3}Ga_{1.7}O_{11.65}$ suggest that there may be a ferromagnetic component to the magnetic behaviour for these samples at low temperature.

4.4.2 Low Temperature Neutron Powder Diffraction Studies

NPD data were collected on D2B at 4K at ILL, Grenoble, France for $YSr_3Mn_{2.3}Ga_{1.7}O_{11.65}$ and $YSr_3Mn_{2.23}Ga_{1.77}O_{11.615}$ and at POLARIS, ISIS, UK, for $YSr_3Mn_{3.1}Ga_{0.9}O_{12.}$ Rietveld refinement was carried out on the data using the same magnetic model as for the reduced samples, in which the unit cell and symmetry of the magnetic model were equivalent to the crystallographic unit cell. Magnetic form factors for Mn^{4+} were used [4]. For $YSr_3Mn_{3.1}Ga_{0.9}O_{12}$ the magnetic moments in all directions of the unit cell were antiferromagnetic, compared to ferromagnetic alignment in the

[001] direction and antiferromagnetic ordering in the [100] and [010] directions for the reduced samples. Antiferromagnetic exchange would be predicted from superexchange interactions in which empty e_g orbitals from octahedrally coordinated Mn^{4+} [$(t_{2g})^3$ $(e_g)^0$] interact via oxygen *2p* orbitals. *Figure 4.16* shows the magnetic structure of $YSr_3Mn_{3.1}Ga_{0.9}O_{12.}$ Refined magnetic moments were low on both the octahedral (2.35(7)μ_B) and former tetrahedral sites (0.05(1)μ_B) for $YSr_3Mn_{3.1}Ga_{0.9}O_{12}$; a value of 3 μ_B would be expected. In contrast to the reduced sample, refined magnetic moments were lower on the 'tetrahedral' site. Gillie reported low refined magnetic moments of 1.8(1) μ_B and 1.1(1) μ_B on the octahedral and 'tetrahedral' sites respectively for $Y_{0.8}Sr_{2.2}Mn_2GaO_9$ ($Y_{1.07}Sr_{2.93}Mn_{2.67}Ga_{1.33}O_{12}$) [1].

Reitveld plots following refinement of low temperature NPD data for $YSr_3Mn_{2.3}Ga_{1.7}O_{11.65}$ and $YSr_3Mn_{2.23}Ga_{1.77}O_{11.615}$ did not clearly show additional intensity due to magnetic reflections. Rietveld plots for $YSr_3Mn_{2.3}Ga_{1.7}O_{11.65,}$ $YSr_3Mn_{2.23}Ga_{1.77}O_{11.615}$ and $YSr_3Mn_{3.1}Ga_{0.9}O_{12}$ are shown in *figures 4.17-4.19* and refined structural parameters are given in *tables 4.5-4.7.*

The gallium content of the layers appears to suppress magnetic ordering in these samples, with ordering only evident in the octahedral layer for the sample with the highest manganese content, $YSr_3Mn_{3.1}Ga_{0.9}O_{12,}$ which has a negligible gallium content in this layer. The former tetrahedral layer of $YSr_3Mn_{3.1}Ga_{0.9}O_{12}$ and both layers in all of the other samples have a gallium content greater than 23%. The presence of diamagnetic Ga^{3+} would interrupt the Mn^{4+}- O- Mn^{4+} superexchange pathway, both within the layers and between layers. This effect is more pronounced for oxidised samples compared to the reduced samples because there is poorer Mn-O orbital overlap for the more contracted Mn^{4+} *d* orbitals compared to the Mn^{3+} *d* orbitals.

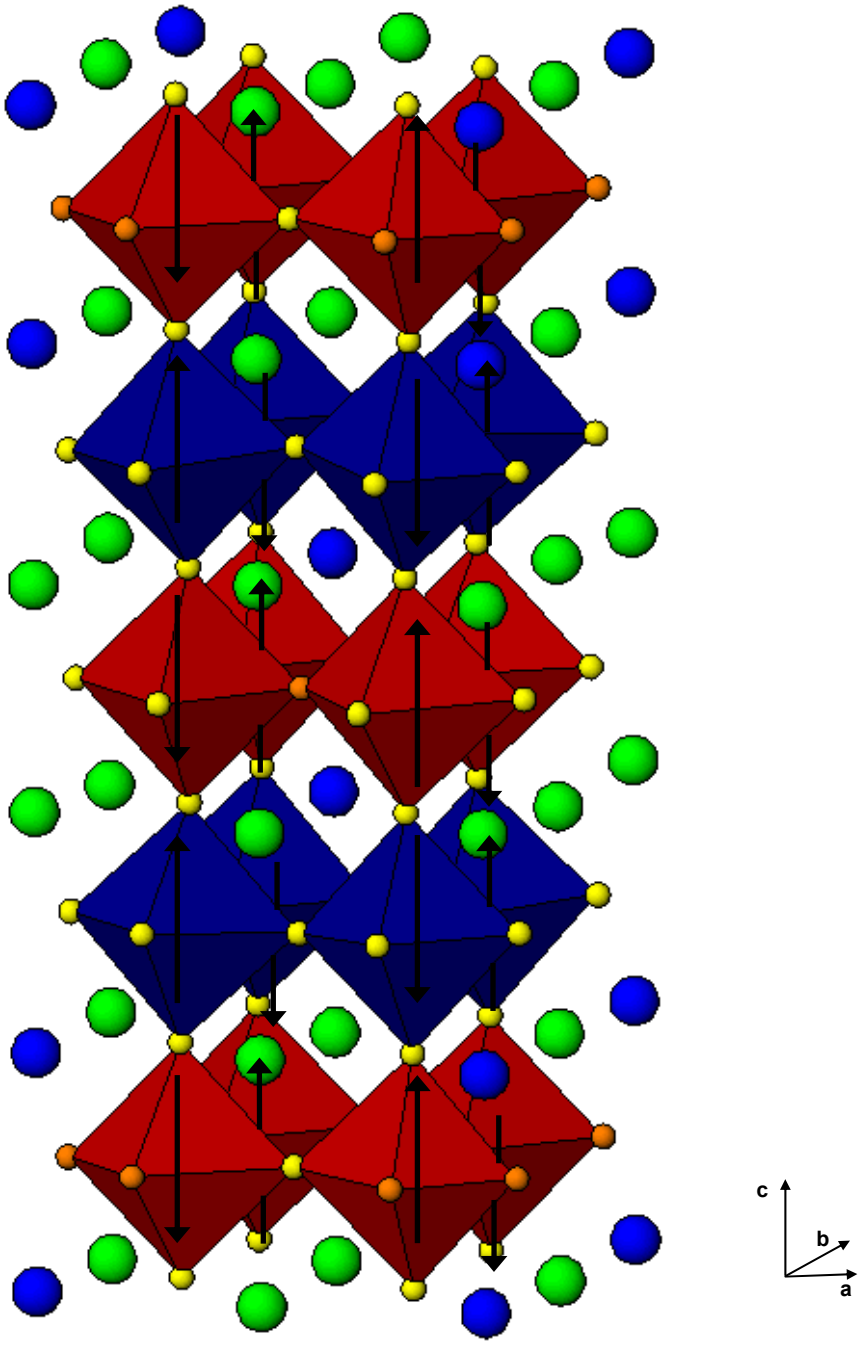

Figure 4.16. Magnetic structure of $YSr_3Mn_{3.1}Ga_{0.9}O_{12.}$ Showing MnO_6 as blue polyhedra, Mn/GaO_6 as red polyhedra, yellow spheres are oxygen anions, orange spheres are oxygen anions (partially occupied prior to oxidation), green spheres are Sr^{2+} cations and blue spheres are Y^{3+} cations.

Figure 4.17a

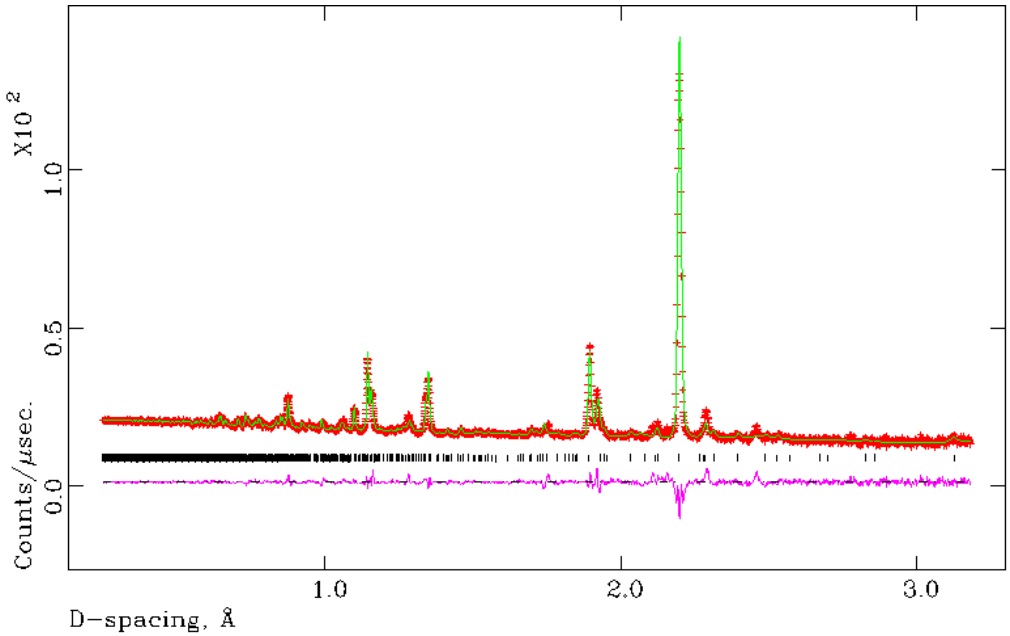

Figure 4.17b.

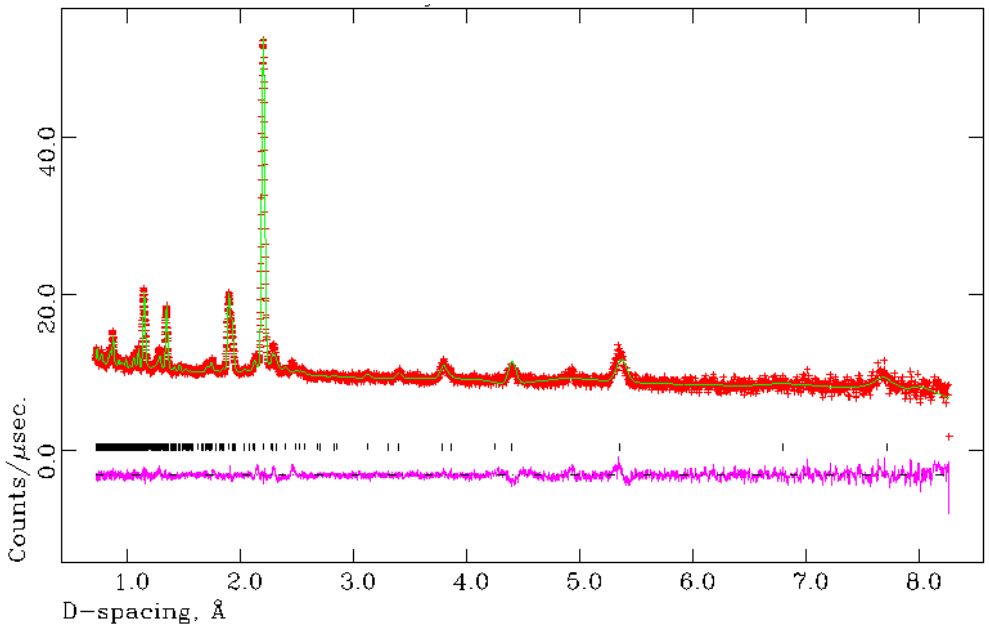

Figure 4.17. Observed (+), calculated (-) and difference (-) profiles from refinement using 4K NPD data for $YSr_3Mn_{3.1}Ga_{0.9}O_{12}$ *a*) C bank, 2 θ = 145° *b*) A bank, 2 θ = 35° .χ^2 = 2.960 , R_{wp} = 1.67% and R_p = 2.99 %.

Table 4.5. Refinement results from 4K NPD data for $YSr_3Mn_{3.1}Ga_{0.9}O_{12}$

Atom	Position	x	y	z	Frac.	U_{iso} x100/Å^2
Mn1	8*f*	0.25	0.25	0.25	0.994(7)	1.0*
Ga1	8*f*	0.25	0.25	0.25	0.006(7)	1.0*
Mn2	8*h*	0.205(1)	0.205(1)	0	0.556(7)	1.0*
Ga2	8*h*	0.205(1)	0.205(1)	0	0.444(7)	1.0*
Y	4*e*	0	0	0.1273(5)	1	0.50*
Sr1	4*e*	0	0	0.6292(5)	1	0.50*
Sr2	8*g*	0.5	0	0.1168(3)	1	0.50*
O1	8*i*	0	0.249(7)	0	1	0.47(7)
O2	8*j*	0.5	0.277(8)	0	1	0.20(8)
O3	16*n*	0	0.280(4)	0.2453(2)	1	0.06(4)
O4	16*m*	0.2677(5)	0.2677(5)	0.1317(3)	1	1.69(1)

a = 7.5757(6) Å, c = 15.446(5) Å, χ^2 = 2.960, R_{wp} = 1.67% and R_p = 2.99%. Space group I4/*mmm*.

Magnetic moments: Mn1=2.31(7)μ_B ; Mn2 = 0.05(1) μ_B

* denotes where thermal parameters fixed to sensible values.

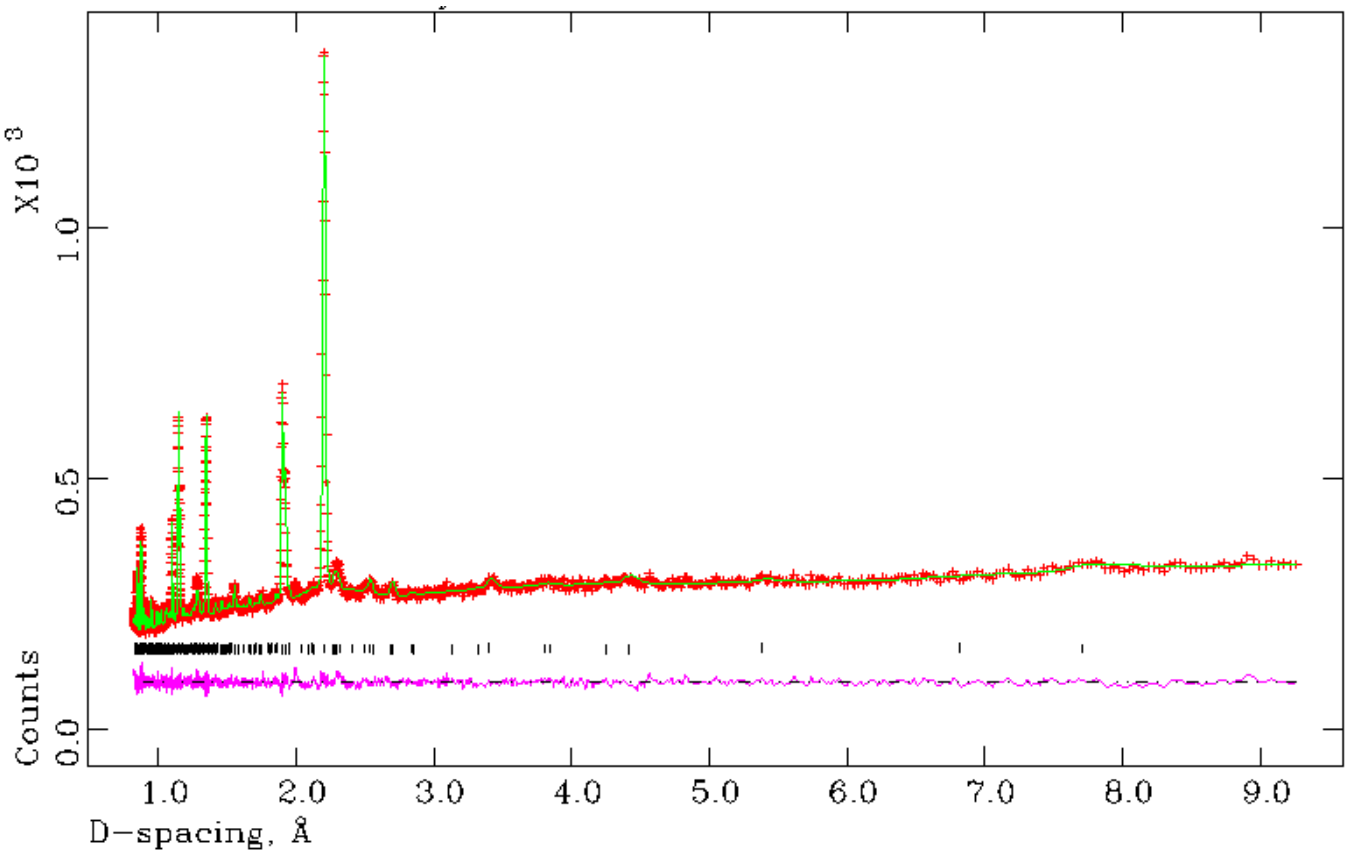

Figure 4.18. Observed (+), calculated (-) and difference (-) profiles from refinement using 4K NPD data for $YSr_3Mn_{2.3}Ga_{1.7}O_{11.65}$. $\chi^2 = 1.776$, $R_{wp} = 2.65\%$ and $R_p = 2.05$ %.

Table 4.6. Refinement results from 4K NPD data for $YSr_3Mn_{2.3}Ga_{1.7}O_{11.65}$

Atom	Position	x	y	z	Frac.	U_{iso} x100/Å^2
Mn1	8*f*	0.25	0.25	0.25	0.770(8)	1.0*
Ga1	8*f*	0.25	0.25	0.25	0.230(8)	1.0*
Mn2	8*h*	0.2742(9)	0.2742(9)	0	0..380(8)	1.0*
Ga2	8*h*	0.2742(9)	0.2742(9)	0	0.620(8)	1.0*
Y	4*e*	0	0	0.1360(8)	1	0.18(7)
Sr1	4*e*	0	0	0.6247(8)	1	0.18(7)
Sr2	8*g*	0.5	0	0.1212(4)	1	0.18(7)
O1	8*i*	0	0.201(2)	0	0.825	2.6(3)
O2	8*j*	0.5	0.263(1)	0	1	0.7(2)
O3	16*n*	0	0.2588(10)	0.2554 (7)	1	0.6(1)
O4	16*m*	0.2311(9)	0.2311(9)	0.1231(6)	1	3.0(2)

a = 7.5958(4) Å, *c* = 15.3581(8) Å, χ^2 = 1.776, R_{wp} = 2.65% and R_p = 2.05%. Space group I4/*mmm*.

*denotes where thermal parameters fixed to sensible values

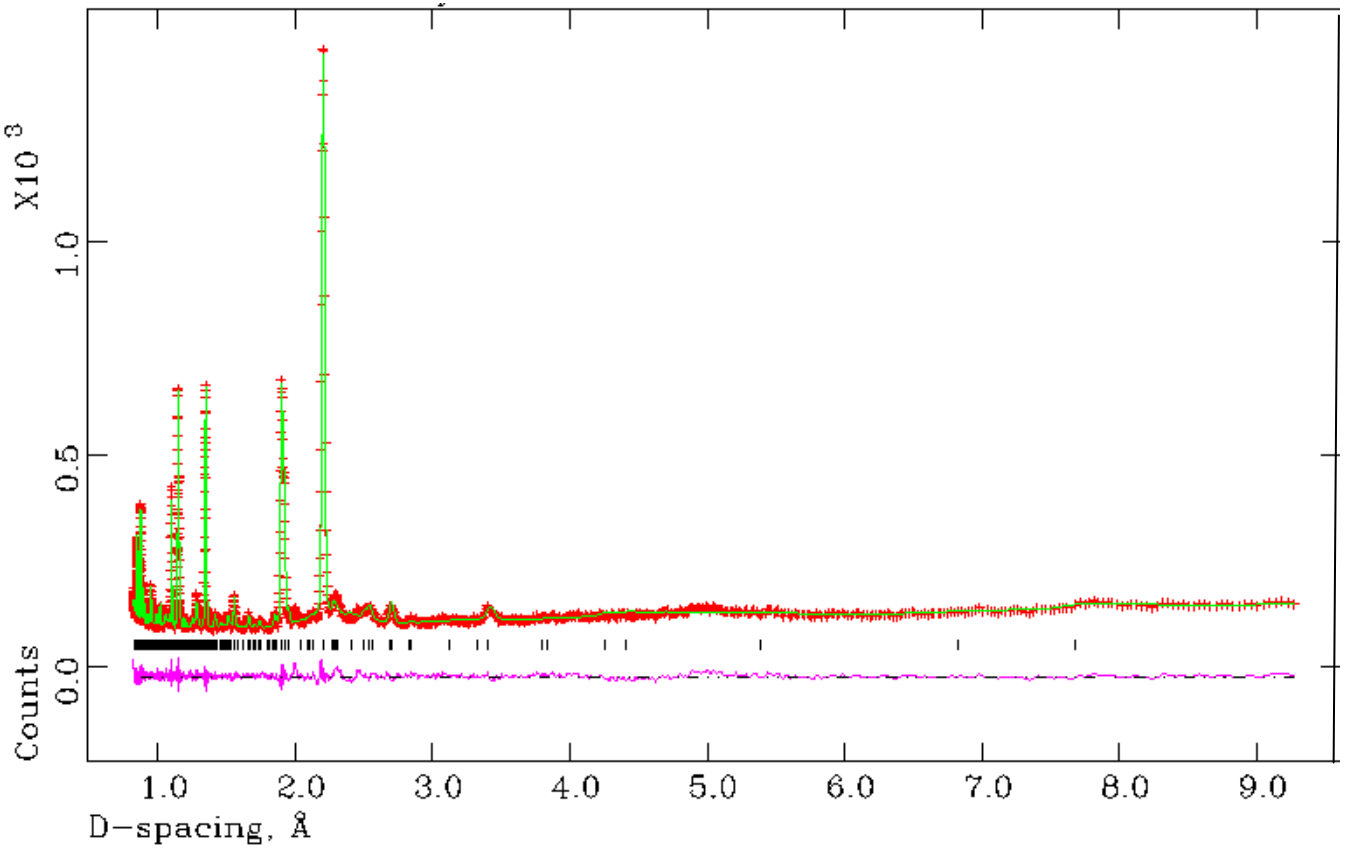

Figure 4.19. Observed (+), calculated (-) and difference (-) profiles from refinement using 4K NPD data for $YSr_3Mn_{2.23}Ga_{1.77}O_{11.615}$. $\chi^2 = 2.934$, $R_{wp} = 4.73\%$ and $R_p = 3.65$ %.

Table 4.7. Refinement results from 4K NPD data for $YSr_3Mn_{2.23}Ga_{1.77}O_{11.615}$

Atom	Position	x	y	z	Frac.	U_{iso} x100/Å^2
Mn1	8*f*	0.25	0.25	0.25	0.752(6)	1.0*
Ga1	8*f*	0.25	0.25	0.25	0.248(6)	1.0*
Mn2	8*h*	0.2610(9)	0.2610(9)	0	0.363(6)	1.0*
Ga2	8*h*	0.2610(9)	0.2610(9)	0	0.637(6)	1.0*
Y	4*e*	0	0	0.1393(5)	1	0.03(5)
Sr1	4*e*	0	0	0.6226(6)	1	0.03(5)
Sr2	8*g*	0.5	0	0.1231(4)	1	0.03(5)
O1	8*i*	0	0.215(1)	0	0.8075	1.4(2)
O2	8*j*	0.5	0.236(1)	0	1	0.8(1)
O3	16*n*	0	0.2638(8)	0.2522 (4)	1	0.7(1)
O4	16*m*	0.2338(8)	0.2338(8)	0.1235(5)	1	3.0(2)

a = 7.6018(2) Å, c = 15.3515(6) Å, χ^2 = 2.934, R_{wp} = 4.73% and R_p = 3.65%.

Space group I4/*mmm*.

* denotes where thermal parameters fixed to sensible values

4.5 Synthesis of Fluorinated Samples

Fluorination was carried out using 10% F_2 / 90% N_2 as the fluorinating agent. It proved difficult to determine the ideal conditions for fluorination. The samples ($YSr_3Mn_{3.1}Ga_{0.9}O_{10.4}$, $YSr_3Mn_{2.3}Ga_{1.7}O_{10.5}$ and $YSr_3Mn_{2.23}Ga_{1.77}O_{10.5}$) were heated to 280^{o}C for 20 minutes in flowing 10% F_2, using the apparatus described in chapter 2. Thermogravimetric analysis was carried out in order to verify the presence of fluorine. Samples were reduced at high temperature (900^{o}C) for 15 minutes in 10% H_2 / 90% N_2,

the products SrF_2, MnO, Ga, Y_2O_3 and SrO were confirmed by XRPD. It was not possible to determine F_2 content by this method due to the loss of Ga metal at high temperatures.

4.6 Structural Characterisation

NPD data were collected at room temperature at POLARIS, ISIS, UK for samples $YSr_3Mn_{3.1}Ga_{0.9}O_{10.4}$+F, and $YSr_3Mn_{2.23}Ga_{1.77}O_{10.5}$+F and at ILL, Grenoble, France for $YSr_3Mn_{2.3}Ga_{1.7}O_{10.5}$+F. The Rietveld plots (room temperature) for the fluorinated samples $YSr_3Mn_{3.1}Ga_{0.9}O_{10.4}F_{0.3}$, $YSr_3Mn_{2.3}Ga_{1.7}O_{10.5}F_{0.1}$ and $YSr_3Mn_{2.23}Ga_{1.77}O_{10.5}F_{0.1}$ are shown in *figures 4.20-4.22.* Refined structural parameters are given in *tables 4.8-4.10.* The refinement of room temperature samples $YSr_3Mn_{3.1}Ga_{0.9}O_{10.4}F_{0.3}$, $YSr_3Mn_{2.3}Ga_{1.7}O_{10.5}F_{0.1}$ and $YSr_3Mn_{2.23}Ga_{1.77}O_{10.5}F_{0.1}$ converged with $\chi^2 = 6.043$, 2.756 and 1.497 respectively. Although it was not possible to determine the ordering of oxygen and fluorine within the tetrahedral layer due to the similar scattering lengths of fluorine (5.564×10^{-15}m) and oxygen (5.803×10^{-15}m) [5], the fluorine content could be calculated following deduction of the fractional oxygen occupancy of site O1/ F1 from the total fractional occupancy. Oxygen occupancy of the site for the reduced samples can be obtained from *tables 3.2a, 3.4a and 3.5a* in the Chapter 3. The results of refinement show that the tetrahedral layer, which is a quarter occupied by oxygen in the parent material, is additionally occupied by fluorine in the fluorinated samples. The tetrahedral layer remains only partially occupied in these samples.

Fluorination results in oxidation of some of the manganese cations in the tetrahedral layer from Mn^{3+} to Mn^{4+}, with octahedral coordination for the Mn^{4+} at these

sites. Although it was not possible to determine accurate bond valence sums for manganese on the 'tetrahedral' site due the mixed Ga/Mn occupancy of this site, it can be seen that the average manganese to oxygen bond length within the 'tetrahedral' layer decreases (*tables 4.8b, 4.9b* and *4.10b*). This decrease is especially evident for the sample with highest fluorine content. A decrease in bond length would be predicted as a proportion Mn^{3+} is oxidised to Mn^{4+} on fluorination.

There is less evidence of the mixing of gallium and manganese between the octahedral and tetrahedral layers for the fluorinated samples compared to the oxidised samples, which is consistent with the lower temperature used for fluorination, 280^{o}C, compared to the temperature used for oxidation, 400^{o}C.

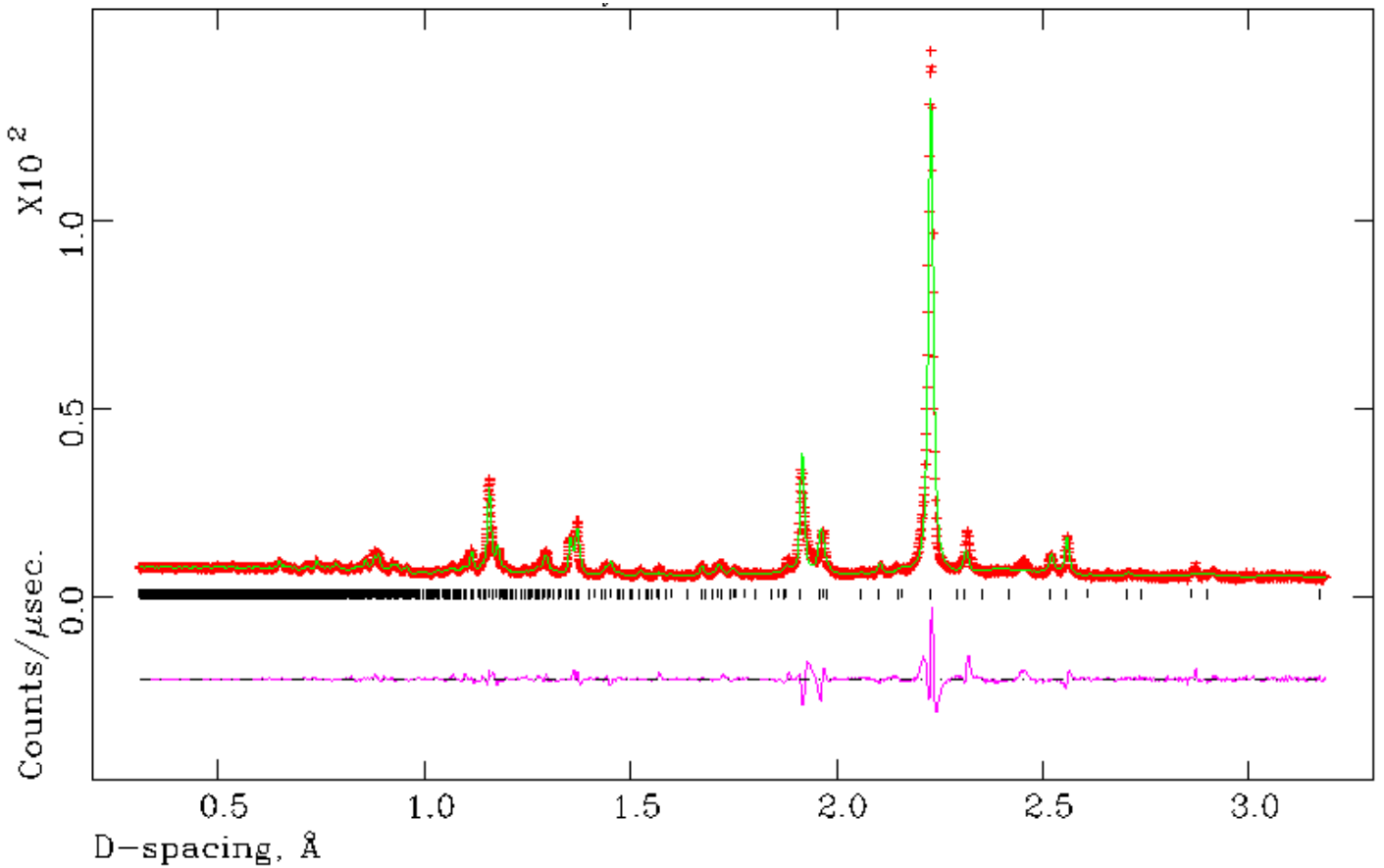

Figure 4.20. Observed (+), calculated (-) and difference (-) profiles from refinement using room temperature NPD data for $YSr_3Mn_{3.1}Ga_{0.9}O_{10.4}F_{0.3}$ in space group I4/*mmm*, $\chi^2 = 6.035$, $R_{wp} = 3.60\%$ and $R_p = 5.72$

Table 4.8a. Refinement results from room temperature NPD data for $YSr_3Mn_{3.1}Ga_{0.9}O_{10.4}F_{0.3}$

Atom	Position	x	y	z	Frac.	U_{iso} x100/Å^2
Mn1	8*f*	0.25	0.25	0.25	0.972(3)	0.10(6)*
Ga1	8*f*	0.25	0.25	0.25	0.028(3)	0.10(6)*
Mn2	8*h*	0.283(1)	0.283(1)	0	0.578(3)	0.10(6)*
Ga2	8*h*	0.283(1)	0.283(1)	0	0.422(3)	0.10(6)*
Y	4*e*	0	0	0.1444(2)	1	0.20(6)
Sr1	4*e*	0	0	0.6179(5)	1	1.14(1)
Sr2	8*g*	0.5	0	0.1294(2)	1	0.18(4)
O1/F1	8*i*	0	0.257(2)	0	0.35(1)	1.13(3)
O2	8*j*	0.5	0.2360(6)	0	1	1.13(3)
O3	16*n*	0	0.2483(6)	0.2539(2)	1	1.13(3)
O4	16*m*	0.2224(2)	0.2224(2)	0.1095(1)	1	1.13(3)

a = 7.6590(5) Å, *c* = 15.682(1) Å, χ^2 = 6.035, R_{wp} = 3.60% and R_p = 5.72%.

Space group I4/*mmm*.

*denotes where thermal parameters constrained to avoid correlation effects

*Table 4.8b.*Selected bond lengths for $YSr_3Mn_{3.1}Ga_{0.9}O_{10.4}F_{0.3}$.

Mn/Ga–O bond lengths,	**Å**	**BVS**
Mn/Ga1- O3 (x4)	1.9159(1)	Mn1- 3.19
Mn/Ga1- O4 (x2)	2.228(2)	
Mn/Ga2 – O1/ F1	2.17(1)	
Mn/Ga2 – O2 (x2)	1.703(9)	
Mn/Ga2 – O4 (x2)	1.834(6)	

Table 4.8c. Selected bond angles for $YSr_3Mn_{3.1}Ga_{0.9}O_{10.4}F_{0.3}$.

Mn/Ga – O angles,	**degrees**
O3 - Mn/Ga1- O3 (x2)	89.1(3)
O3 - Mn/Ga1- O3 (x2)	90.8(3)
O3 - Mn/Ga1 – O4 (x4)	86.3(1)
O3 - Mn/Ga1 – O4 (x4)	93.6(1)
O2 - Mn/Ga2 – O2 (x1)	114.4(1)
O2 – Mn/Ga2 – O4 (x4)	101.2(1)
O4 – Mn/Ga2 – O4 (x1)	138.1(9)
O1/F1-Mn/Ga2-O1/F1 (x1)	79.8(1)

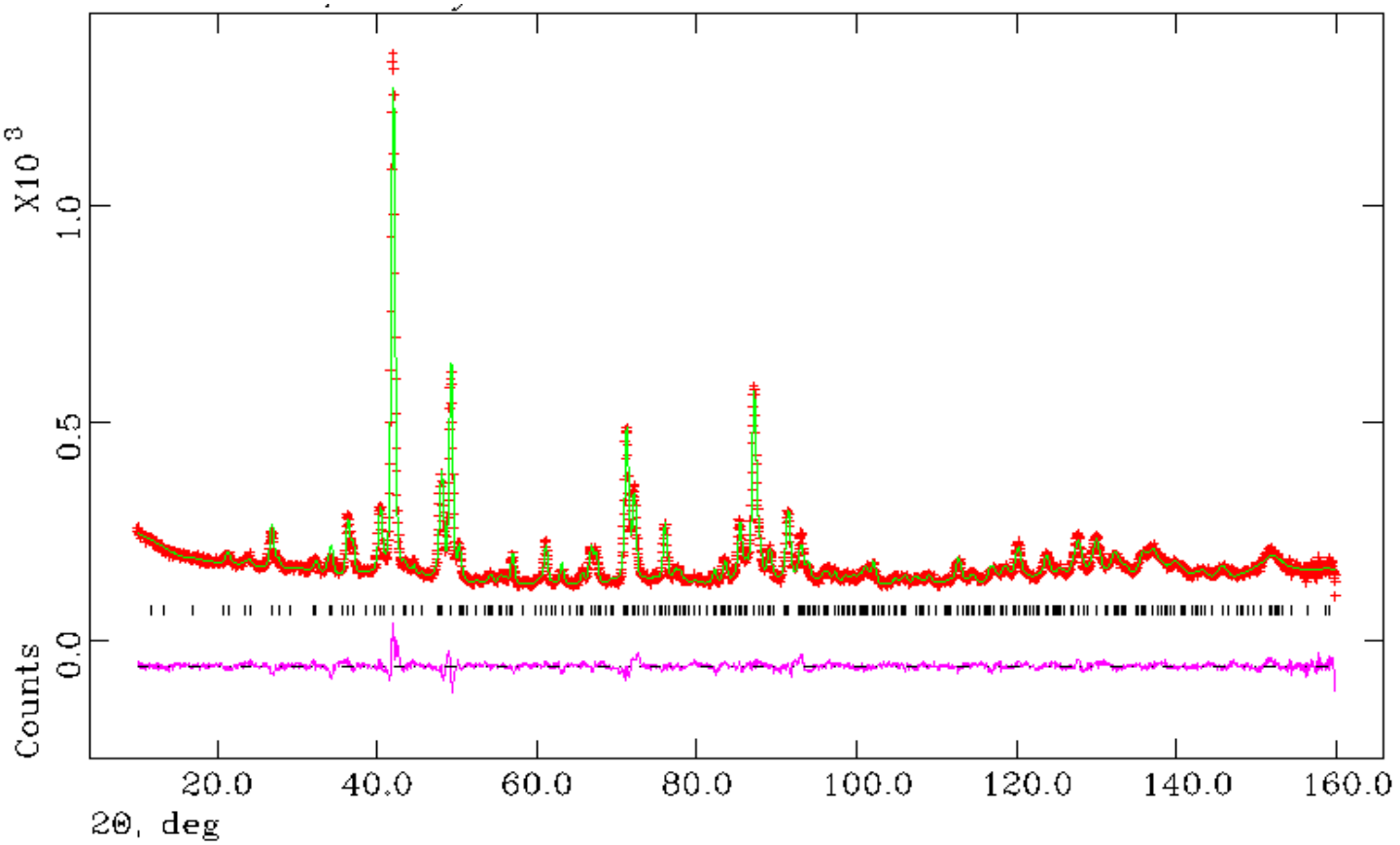

Figure 4.21. Observed (+), calculated (-) and difference (-) profiles from refinement using room temperature NPD data for $YSr_3Mn_{2.3}Ga1.7O_{10.5}F_{0.1}$ in space group I4/*mmm*, $\chi^2 = 2.756$, $R_{wp} = 4.03\%$ and $R_p = 3.15\%$.

Table 4.9a. Refinement results from room temperature NPD data for $YSr_3Mn_{2.3}Ga_{1.7}O_{10.5}F_{0.1}$

Atom	Position	x	y	z	Frac.	U_{iso} x100/Å^2
Mn1	8*f*	0.25	0.25	0.25	0.803(4)	1.2(1)
Ga1	8*f*	0.25	0.25	0.25	0.197(4)	1.2(1)
Mn2	8*h*	0.2648(6)	0.2648(6)	0	0.347(4)	1.2(1)
Ga2	8*h*	0.2648(6)	0.2648(6)	0	0.653(4)	1.2(1)
Y	4*e*	0	0	0.1474(4)	1	0.88(6)
Sr1	4*e*	0	0	0.6185(5)	1	0.88(6)
Sr2	8*g*	0.5	0	0.1327(3)	1	0.88(6)
O1/F1	8*i*	0	0.134(2)	0	0.29(1)	2.69(6)
O2	8*j*	0.5	0.222(1)	0	1	2.69(6)
O3	16*n*	0	0.2476(9)	0.2545(3)	1	2.69(6)
O4	16*m*	0.2189(3)	0.2189(3)	0.1130(2)	1	2.69(6)

a = 7.6659(2) Å, c = 15.6776(8) Å, χ^2 = 2.756, R_{wp} = 4.03% and R_p = 3.15%. Space group I4/*mmm*.

*Table 4.9b.*Selected bond lengths for $YSr_3Mn_{2.3}Ga_{1.7}O_{10.5}F_{0.1}$.

Mn/Ga–O bond lengths,	**Å**	**BVS**
Mn/Ga1- O3 (x4)	1.9178(2)	Mn1- 3.26
Mn/Ga1- O4 (x2)	2.175(4)	
Mn/Ga2 – O1/ F1	2.26(1)	
Mn/Ga2 – O2 (x2)	1.832 (4)	
Mn/Ga2 – O4 (x2)	1.840(4)	

Table 4.9c. Selected bond angles for $YSr_3Mn_{2.3}Ga_{1.7}O_{10.5}F_{0.1}$.

Mn/Ga – O angles,	**degrees**
O3 - Mn/Ga1- O3 (x2)	88.8(4)
O3 - Mn/Ga1- O3 (x2)	91.2(4)
O3 - Mn/Ga1 – O4 (x4)	85.7(1)
O3 - Mn/Ga1 – O4 (x4)	94.3(1)
O2 - Mn/Ga2 – O2 (x1)	110.6(6)
O2 – Mn/Ga2 – O4 (x4)	98.87(1)
O4 – Mn/Ga2 – O4 (x1)	148.6(5)
O1/F1-Mn/Ga2-O1/F1 (x1)	37.5(9)

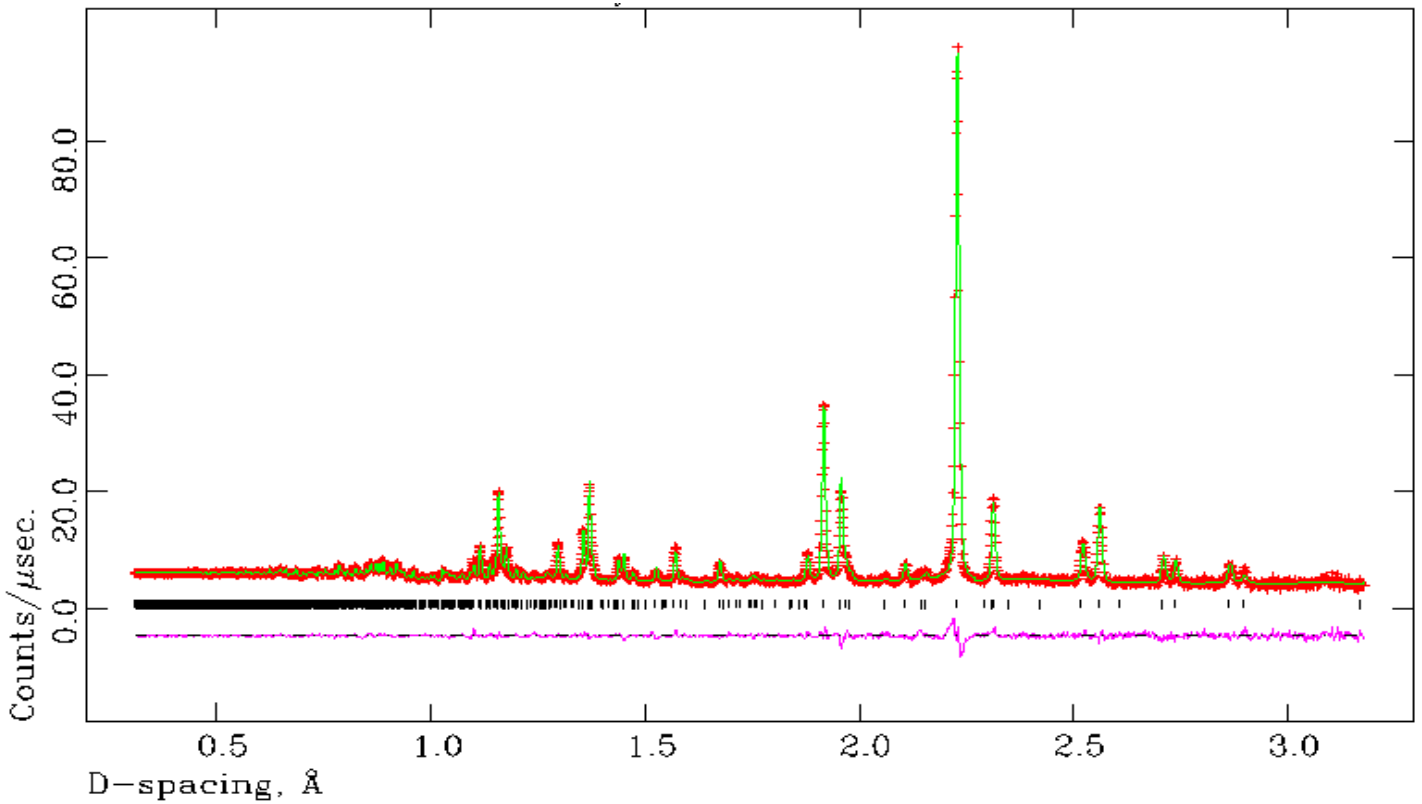

Figure 4.22. Observed (+), calculated (-) and difference (-) profiles from refinement using room temperature NPD data for $YSr_3Mn_{2.23}Ga_{1.77}O_{10.5}F_{0.1}$ in space group I4/*mmm*, $\chi^2 = 1.497$, $R_{wp} = 2.46\%$ and $R_p = 4.85\%$.

Table 4.10a. Refinement results from room temperature NPD data for $YSr_3Mn_{2.23}Ga_{1.77}O_{10.5}F_{0.1}$

Atom	Position	x	y	z	Frac.	U_{iso} x100/Å^2
Mn1	8*f*	0.25	0.25	0.25	0.797(2)	0.08(5)
Ga1	8*f*	0.25	0.25	0.25	0.203(2)	0.08(5)
Mn2	8*h*	0.2644(2)	0.2644(2)	0	0.318(2)	0.08(5)
Ga2	8*h*	0.2644(2)	0.2644(2)	0	0.682(2)	0.08(5)
Y	4*e*	0	0	0.1449(1)	1	0.64(5)
Sr1	4*e*	0	0	0.6222(3)	1	1.48(7)
Sr2	8*g*	0.5	0	0.1301(1)	1	0.42(3)
O1/F1	8*i*	0	0.1233(9)	0	0.312(7)	1.23(2)
O2	8*j*	0.5	0.2321(3)	0	1	1.23(2)
O3	16*n*	0	0.2466(3)	0.2567(1)	1	1.23(2)
O4	16*m*	0.2138(1)	0.2138(1)	0.1118(1)	1	1.23(2)

a = 7.6649(2) Å, c = 15.6579(5) Å, χ^2 = 2.756, R_{wp} = 2.46% and R_p = 4.85%. Space group I4/*mmm*.

*Table 4.10b.*Selected bond lengths for $YSr_3Mn_{2.23}Ga_{1.77}O_{10.5}F_{0.1}$.

Mn/Ga–O bond lengths,	**Å**	**BVS**
Mn/Ga1- O3 (x4)	1.9193(1)	3.21
Mn/Ga1- O4 (x2)	2.199(1)	
Mn/Ga2 – O1/ F1	2.297(4)	
Mn/Ga2 – O2 (x2)	1.823 (1)	
Mn/Ga2 – O4 (x2)	1.835(2)	

Table 4.10c. Selected bond angles for $YSr_3Mn_{2.23}Ga_{1.77}O_{10.5}F_{0.1}$.

Mn/Ga – O angles,	degrees
O3 - Mn/Ga1- O3 (x2)	88.3(1)
O3 - Mn/Ga1- O3 (x2)	91.7(1)
O3 - Mn/Ga1 – O4 (x4)	85.8(7)
O3 - Mn/Ga1 – O4 (x4)	94.22(7)
O2 - Mn/Ga2 – O2 (x1)	105.6(2)
O2 – Mn/Ga2 – O4 (x4)	100.41(5)
O4 – Mn/Ga2 – O4 (x1)	145.2(1)
O1/F1-Mn/Ga2-O1/F1 (x1)	33.82(3)

4.7 Magnetic Characterisation of Fluorinated Samples

4.7.1 Magnetic Susceptibility Studies

Magnetic susceptibility measurements were taken using a Quantum Design Physical Properties Measurement System (PPMS). DC magnetisation measurements were made for $YSr_3Mn_{3.1}Ga_{0.9}O_{10.4}F_{0.3}$, $YSr_3Mn_{2.3}Ga_{1.7}O_{10.5}F_{0.1}$ and $YSr_3Mn_{2.23}Ga_{1.77}O_{10.5}F_{0.1}$, with an applied field of 1000 Gauss. Both zero field cooled and field cooled data were collected. *Figures 4.23 – 4.25* show the susceptibility versus temperature plots for all three samples. Inverse susceptibility plots are shown in *figures 4.26-4.28.* The plots suggest antiferromagnetic ordering for $YSr_3Mn_{3.1}Ga_{0.9}O_{10.4}F_{0.3}$ and $YSr_3Mn_{2.23}Ga_{1.77}O_{10.5}F_{0.1.}$ Divergence of field cooled and zero field data after ordering suggest that there is a ferromagnetic component to the magnetic properties for

$YSr_3Mn_{3.1}Ga_{0.9}O_{10.4}F_{0.3.}$ Although there is no maximum in the susceptibility plot for $YSr_3Mn_{2.3}Ga_{1.7}O_{10.5}F_{0.1,}$ the inverse susceptibility versus temperature plot (*figure 4.27*) gives a negative Weiss temperature, θ, of –40.6K, indicating antiferromagnetic exchange.

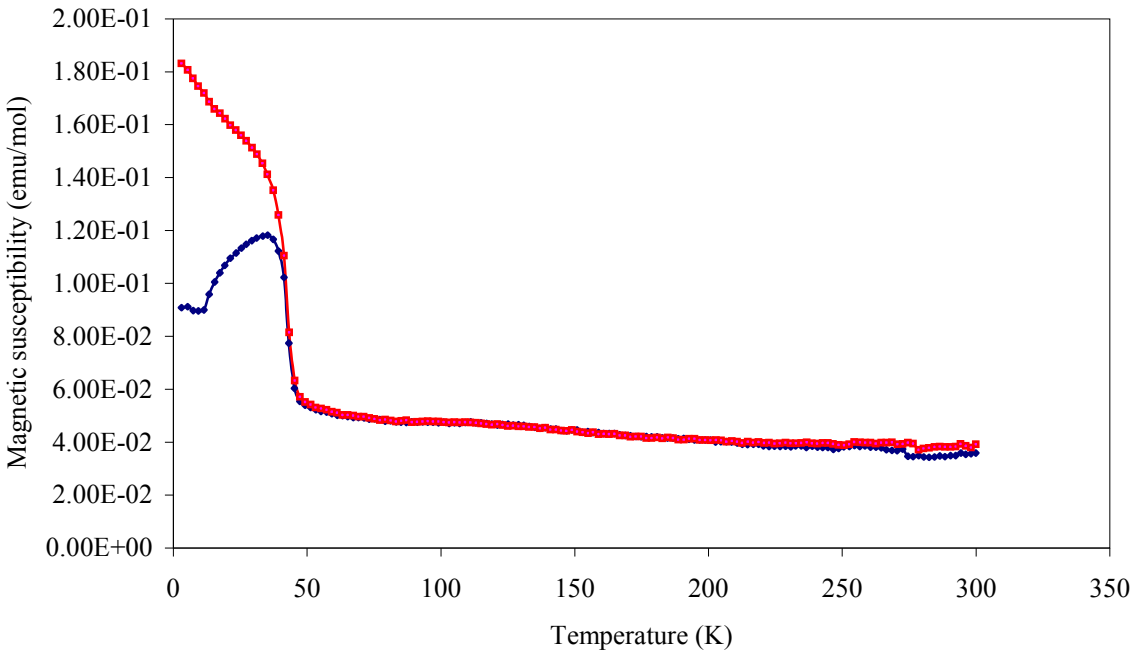

Figure 4.23. Magnetic susceptibility versus temperature plot for $YSr_3Mn_{3.1}Ga_{0.9}O_{10.4}F_{0.3}$ (DC magnetisation performed in an applied field of 1000 Gauss. Zero-field cooled is shown blue and field cooled data in red.)

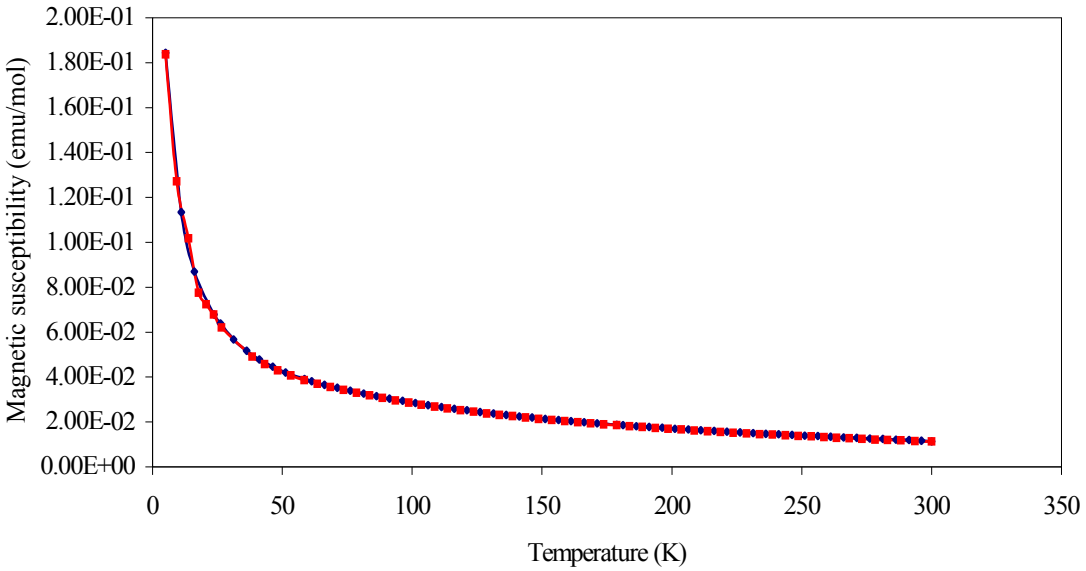

Figure 4.24. Magnetic susceptibility versus temperature plot for $YSr_3Mn_{2.3}Ga_{1.7}O_{10.5}F_{0.1}$ (DC magnetisation performed in an applied field of 1000 Gauss. Zero-field cooled is shown blue and field cooled data in red.)

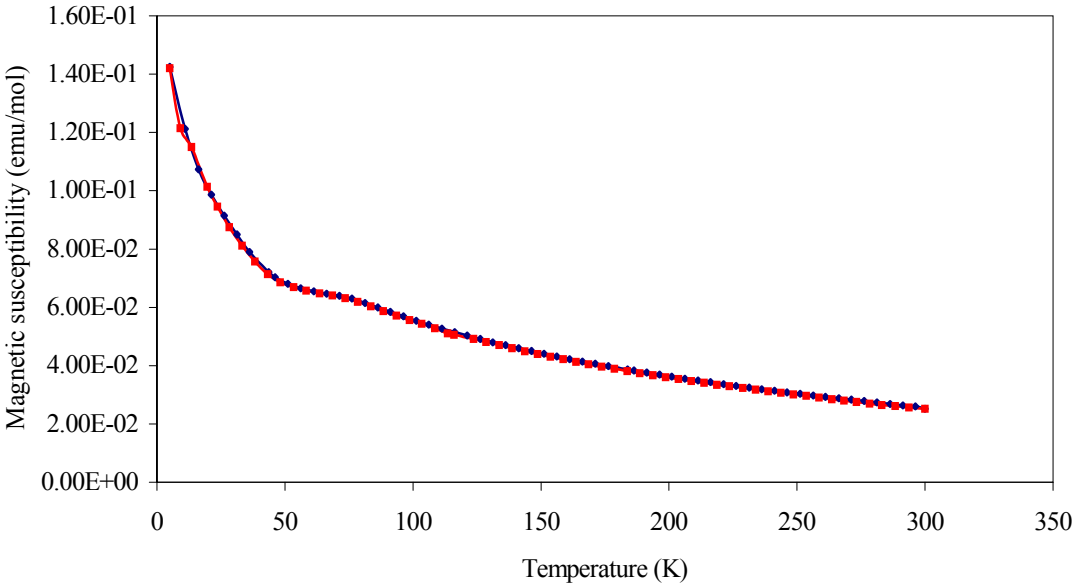

Figure 4.25. Magnetic susceptibility versus temperature plot for $YSr_3Mn_{2.23}Ga_{1.77}O_{10.5}F_{0.1}$ (DC magnetisation performed in an applied field of 1000 Gauss. Zero-field cooled is shown blue and field cooled data in red.)

The plots of inverse susceptibility against temperature are shown in *figures 4.26-4.28.*

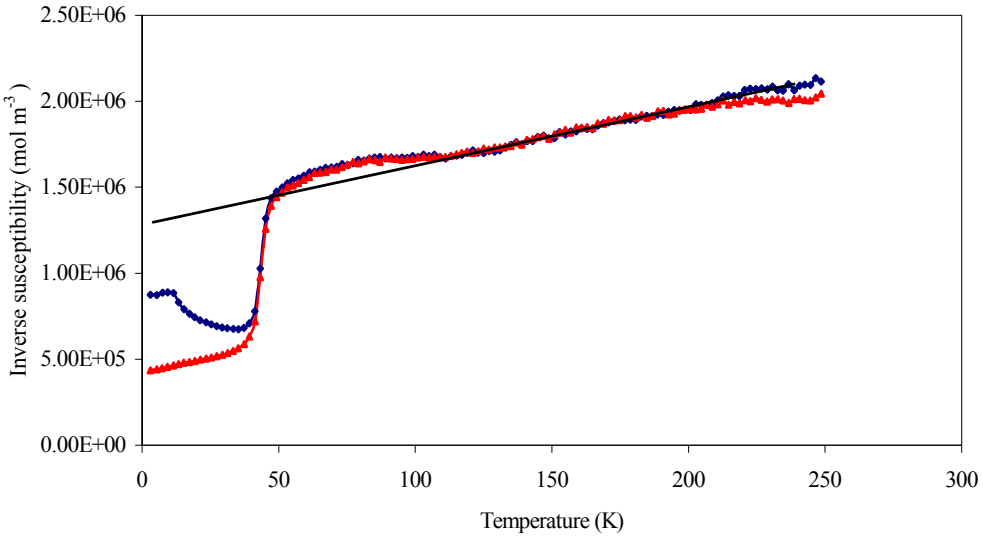

Figure 4.26. Inverse susceptibility versus temperature plot for $YSr_3Mn_{3.1}Ga_{0.9}O_{10.4}F_{0.3}$ (DC magnetisation performed in an applied field of 1000 Gauss. Zero-field cooled is shown blue and field cooled data in red. Black line is linear fit to paramagnetic region.)

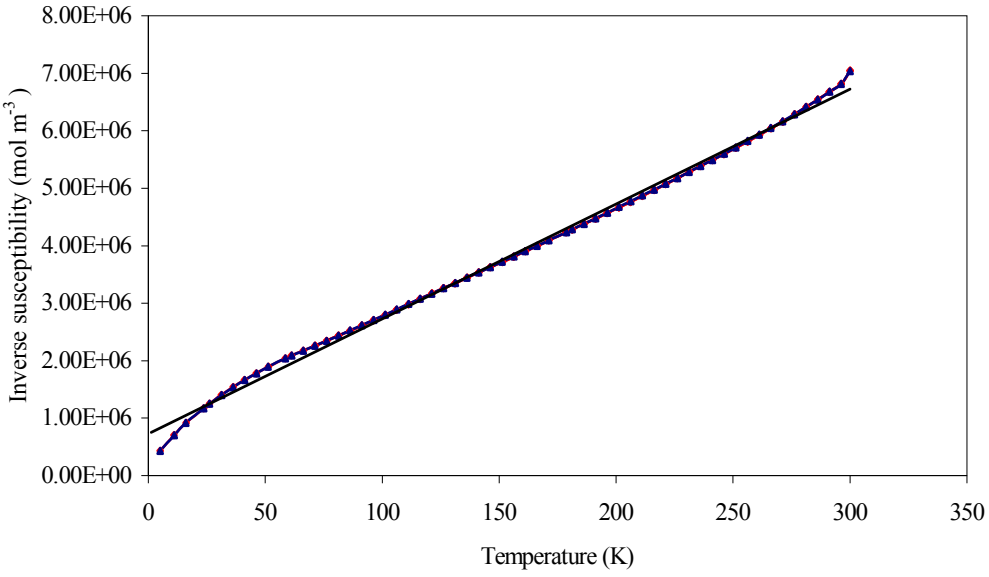

Figure 4.27. Inverse susceptibility versus temperature plot for $YSr_3Mn_{2.3}Ga_{1.7}O_{10.5}F_{0.1}$ (DC magnetisation performed in an applied field of 1000 Gauss. Zero-field cooled is shown blue and field cooled data in red. Black line is linear fit to paramagnetic region.)

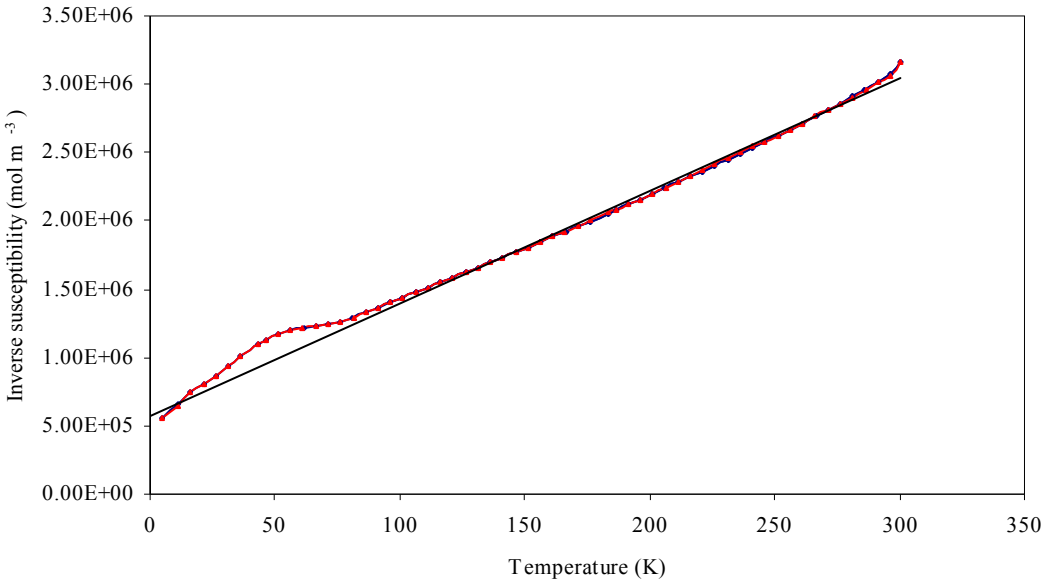

Figure 4.28. Inverse susceptibility versus temperature plot for $YSr_3Mn_{2.23}Ga_{1.77}O_{10.5}F_{0.1}$ (DC magnetisation performed in an applied field of 1000 Gauss. Zero-field cooled is shown blue and field cooled data in red. Black line is linear fit to paramagnetic region.)

The magnetic susceptibility plots, *figures 4.23-4.25* are similar to the equivalent plots for the reduced samples, reflecting small changes in the magnetic behaviour at these low fluorine contents.

The Curie-Weiss law is obeyed above the ordering temperature for $YSr_3Mn_{2.3}Ga_{1.7}O_{10.5}F_{0.1}$ and $YSr_3Mn_{2.23}Ga_{1.77}O_{10.5}F_{0.1}$. The inverse susceptibility plot is not linear over the complete temperature range above the ordering temperature for $YSr_3Mn_{3.1}Ga_{0.9}O_{10.4}F_{0.3}$. The paramagnetic moments were estimated from the gradient of the paramagnetic region of the inverse susceptibility versus temperature plots. The results were as follows, $YSr_3Mn_{3.1}Ga_{0.9}O_{10.4}F_{0.3}$ = 7.74μ_B per Mn ion, $YSr_3Mn_{2.3}Ga_{1.7}O_{10.5}F_{0.1}$ = 3.72 μ_B per Mn ion and $YSr_3Mn_{2.23}Ga_{1.77}O_{10.5}F_{0.1}$ = 5.87μ_B per

Mn ion. The expected value for a d^4 cation (Mn^{3+}) with an electronic spin only contribution would be 4.89 μ_B and 3.87 μ_B for a d^3 cation (Mn^{4+}). The value for $YSr_3Mn_{3.1}Ga_{0.9}O_{10.4}F_{0.3}$ was estimated from the linear section, 117K- 238K, of the inverse susceptibility plot above the ordering temperature, and is unreliable due to deviation from Curie-Weiss behaviour. Higher than predicted paramagnetic moments may be due to an orbital contribution for tetrahedrally coordinated Mn^{3+} (d^4). Clusters of manganese ions in which moments are arranged ferromagnetically could also lead to higher than predicted paramagnetic moments.

4.7.2 Low Temperature Neutron Powder Diffraction Studies

NPD data were collected at 4K at POLARIS, ISIS, UK. Rietveld refinement was carried out on the data using the same magnetic model as for the reduced samples, in which the unit cell and symmetry of the magnetic model were equivalent to the crystallographic unit cell. The low temperature Rietveld plots for the fluorinated samples $YSr_3Mn_{3.1}Ga_{0.9}O_{10.4}F_{0.3}$, $YSr_3Mn_{2.3}Ga_{1.7}O_{10.5}F_{0.1}$ and $YSr_3Mn_{2.23}Ga_{1.77}O_{10.5}F_{0.1}$ are shown in *figures 4.29-4.31.* Refined structural parameters are given in *tables 4.11-4.13.* The refinement of low temperature samples $YSr_3Mn_{3.1}Ga_{0.9}O_{10.4}F_{0.3}$, $YSr_3Mn_{2.3}Ga_{1.7}O_{10.5}F_{0.1}$ and $YSr_3Mn_{2.23}Ga_{1.77}O_{10.5}F_{0.1}$ converged with χ^2 = 4.212, 1.487 and 2.408 respectively. The magnetic exchange interactions are the same as the parent material, as shown in *Figure 3.17*, Chapter 3. The magnetic moments of the Mn^{3+} cations in the polyhedra which are corner linked in the [001] direction are aligned ferromagnetically parallel to the [001] direction of the unit cell, Antiferromagnetic exchange occurs within the octahedral and tetrahedral layers in both the [100] and [010]

directions. The refined magnetic moments, as shown in *table 4.14*, are lower than expected for Mn^{4+} (3 μ_B) or Mn^{3+} (4 μ_B). Low refined magnetic moments could be due to reduced dimensionality as diamagnetic Ga^{3+} or magnetic Mn^{3+}/ Mn^{4+} occupy the tetrahedral layer in a disordered fashion leading to disruption of Mn – O – Mn superexchange. In comparison to the reduced samples it can be seen that refined magnetic moments are lower in the tetrahedral layer (*table 4.14*). Lower magnetic moments would be expected for the fluorinated samples due to the presence of Mn^{4+}, with a predicted refined magnetic moment of 3 μ_B, on some sites within the in the tetrahedral layer associated with F, compared to Mn^{3+} only for the reduced sample, with a predicted refined magnetic moment of 4 μ_B. $YSr_3Mn_{3.1}Ga_{0.9}O_{10.4}F_{0.3,}$ which has the highest fluorine content and hence the highest Mn^{4+} concentration, has the lowest refined magnetic moment on the tetrahedral site (1.2(1) μ_B). Poorer orbital overlap between Mn^{4+} and O^{2-} *p* orbitals may also contribute to the reduced ordered magnetic moments on the tetrahedral site for the fluorinated samples compared to the reduced samples.

In comparison with the oxidised samples, for which only the sample $YSr_3Mn_{3.1}Ga_{0.9}O_{10.4}$ showed evidence of magnetic ordering, all of the fluorinated samples had extra peaks in the low temperature NPD profiles associated with magnetic ordering. The fluorinated samples contain less than 5% Mn^{4+} so that the loss of magnetic ordering due to contraction of the Mn^{4+} *d* orbitals is not evident for the fluorinated samples.

Figure 4.29a

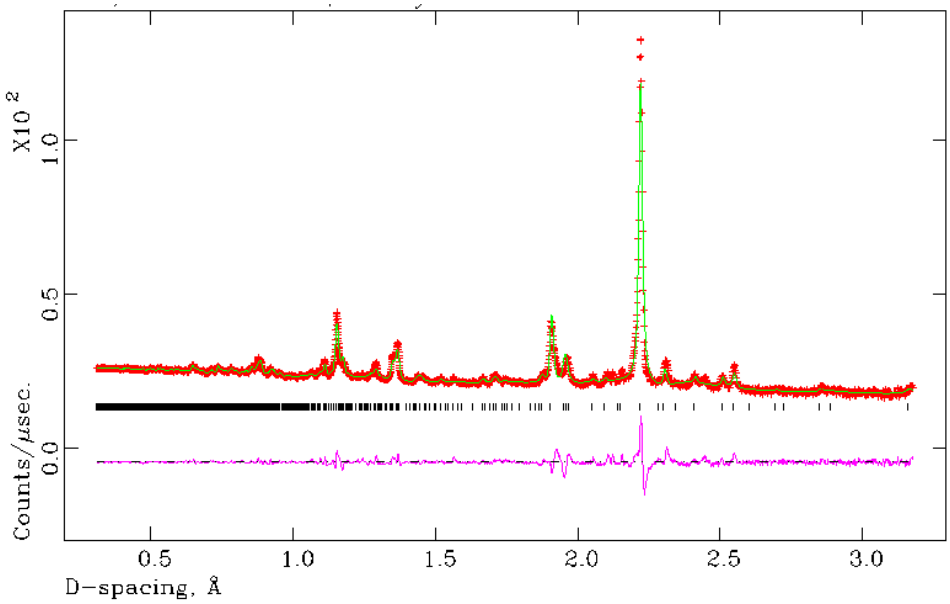

Figure 4.29b

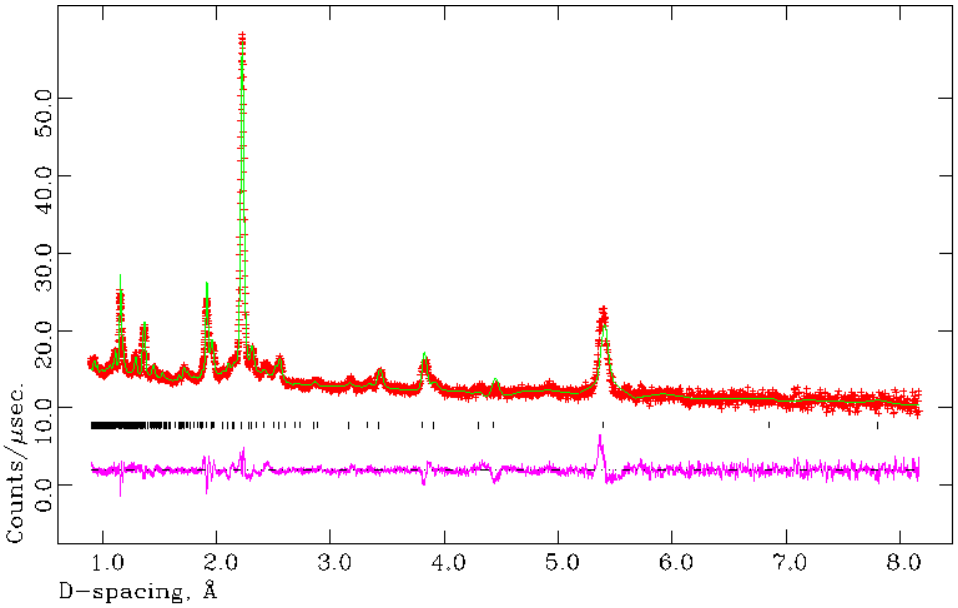

Figure 4.29. Observed (+), calculated (-) and difference (-) profiles from refinement using 4K NPD data for $YSr_3Mn_{3.1}Ga_{0.9}O_{10.4}F_{0.3}$ *a*) C bank, $2\theta = 145^{o}$ *b*) A bank, $2\theta = 35^{o}$.$\chi^2 = 4.212$, $R_{wp} = 1.58\%$ and $R_p = 2.71\%$.

Table 4.11. Refinement results from 4K NPD data for $YSr_3Mn_{3.1}Ga_{0.9}O_{10.4}F_{0.3}$

Atom	Position	x	y	z	Frac.	U_{iso} x100/Å^2
Mn1	8*f*	0.25	0.25	0.25	0.998(5)	1.0*
Ga1	8*f*	0.25	0.25	0.25	0.002(5)	1.0*
Mn2	8*h*	0.291(1)	0.291(1)	0	0.575(3)	1.0*
Ga2	8*h*	0.291(1)	0.291(1)	0	0.425(3)	1.0*
Y	4*e*	0	0	0.1469(4)	1	0.09(3)#
Sr1	4*e*	0	0	0.6176(5)	1	0.09(3)#
Sr2	8*g*	0.5	0	0.1294(2)	1	0.09(3)#
O1/F1	8*i*	0	0.228(4)	0	0.35(1)	1.25(5)#
O2	8*j*	0.5	0.237(2)	0	1	1.25(5)#
O3	16*n*	0	0.253(1)	0.254(5)	1	1.25(5)#
O4	16*m*	0.2254(5)	0.2254(5)	0.1184(4)	1	1.25(5)#

a = 7.6287(2) Å, *c* = 15.631(1) Å, χ^2 = 4.212, R_{wp} = 1.58% and R_p = 2.71%. Space group I4/*mmm*

Magnetic moments: Mn1=2.28(7)μ_B ; Mn2 = 1.2(1) μ_B

*denotes thermal parameters fixed to sensible values.

#denotes thermal parameters constrained to avoid negative values

Figure 4.30a

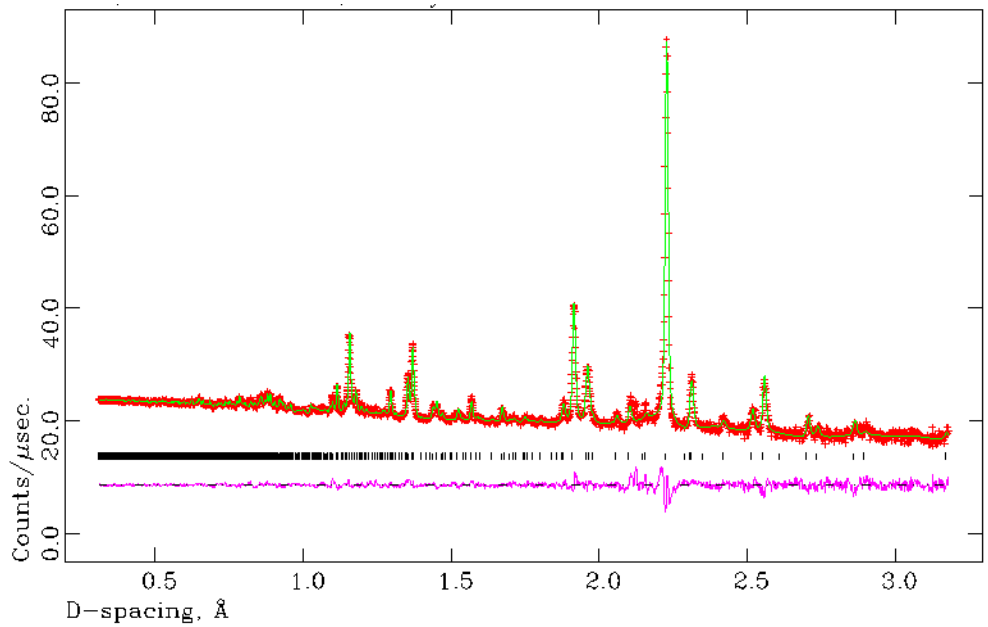

Figure 4.30 b

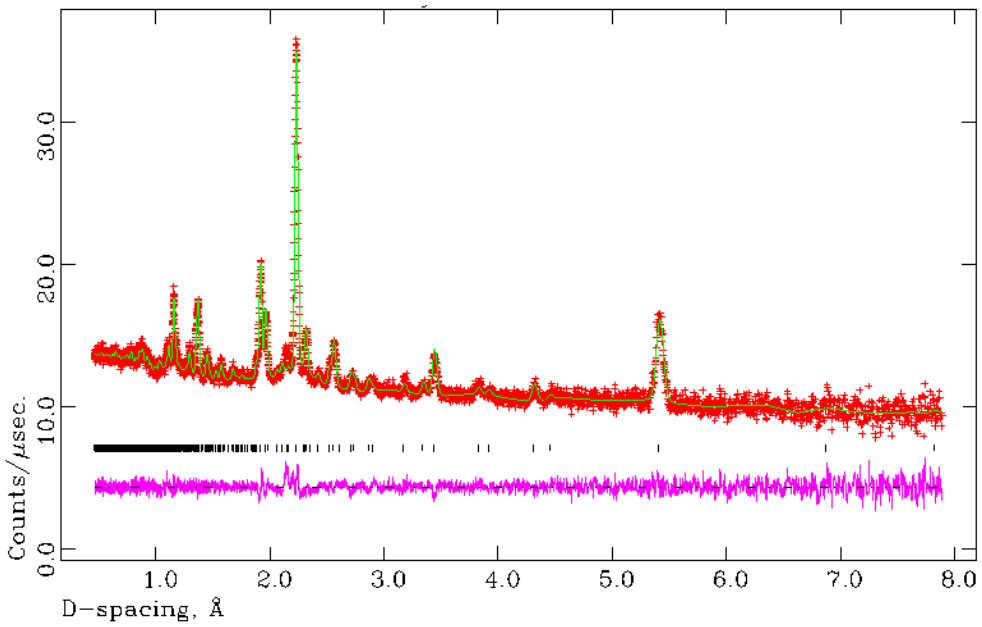

Figure 4.30. Observed (+), calculated (-) and difference (-) profiles from refinement using 4K NPD data for $YSr_3Mn_{2.3}Ga_{1.7}O_{10.5}F_{0.1}$ *a*) C bank, $2\theta = 145^{o}$ *b*) A bank, $2\theta = 35^{o}$.$\chi^2 = 1.487$, $R_{wp} = 1.07\%$ and $R_p = 2.05\%$.

Table 4.12. Refinement results from 4K NPD data for $YSr_3Mn_{2.3}Ga_{1.7}O_{10.5}F_{0.1}$

Atom	Position	x	y	z	Frac.	U_{iso} x100/Å^2
Mn1	8*f*	0.25	0.25	0.25	0.799(3)	1.0*
Ga1	8*f*	0.25	0.25	0.25	0.201(3)	1.0*
Mn2	8*h*	0.2631(4)	0.2631(4)	0	0.351(3)	1.0*
Ga2	8*h*	0.2631(4)	0.2631(4)	0	0.649(3)	1.0*
Y	4*e*	0	0	0.1453(2)	1	0.43(7)
Sr1	4*e*	0	0	0.6234(4)	1	0.9(1)
Sr2	8*g*	0.5	0	0.1307(2)	1	0.08(4)
O1/F1	8*i*	0	0.108(1)	0	0.29(1)	1.03(3)#
O2	8*j*	0.5	0.2333(6)	0	1	1.03(3)#
O3	16*n*	0	0.2470(6)	0.2556(2)	1	1.03(3)#
O4	16*m*	0.2167(2)	0.2167(2)	0.1111(2)	1	1.03(3)*

a = 7.6509(2) Å, *c* = 15.6700(7) Å, χ^2 = 1.487, R_{wp} = 1.07% and R_p = 2.05%. Space group I4/*mmm*.

Magnetic moments: Mn1=2.13(9)μ_B ; Mn2 = 2.7(2) μ_B

*denotes thermal parameters fixed to sensible values.

#denotes thermal parameters constrained to avoid negative values.

Figure 4.31a

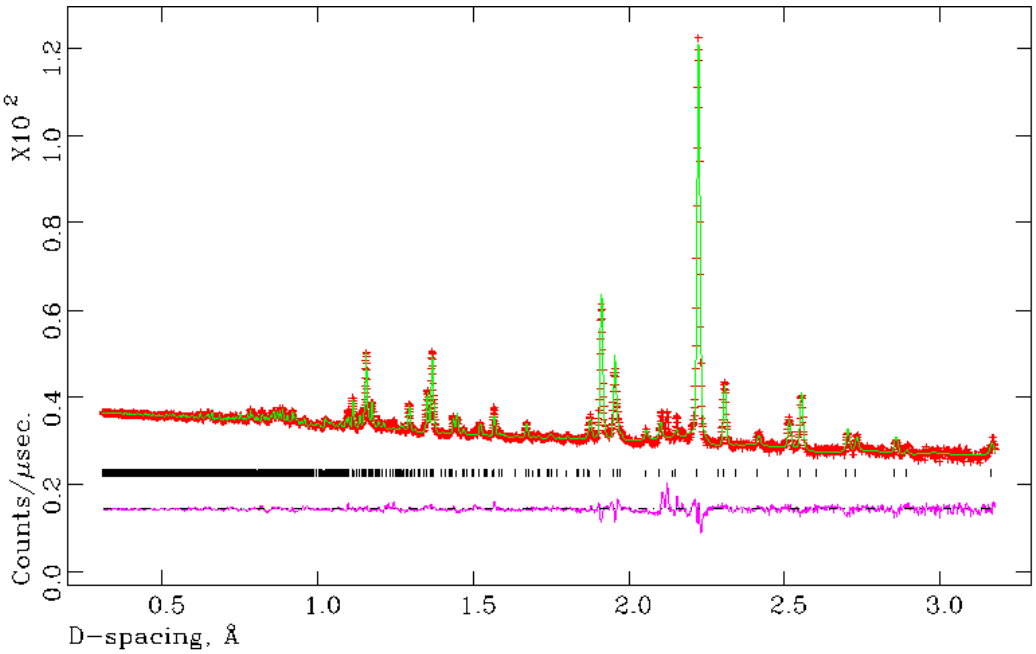

Figure 4.31b

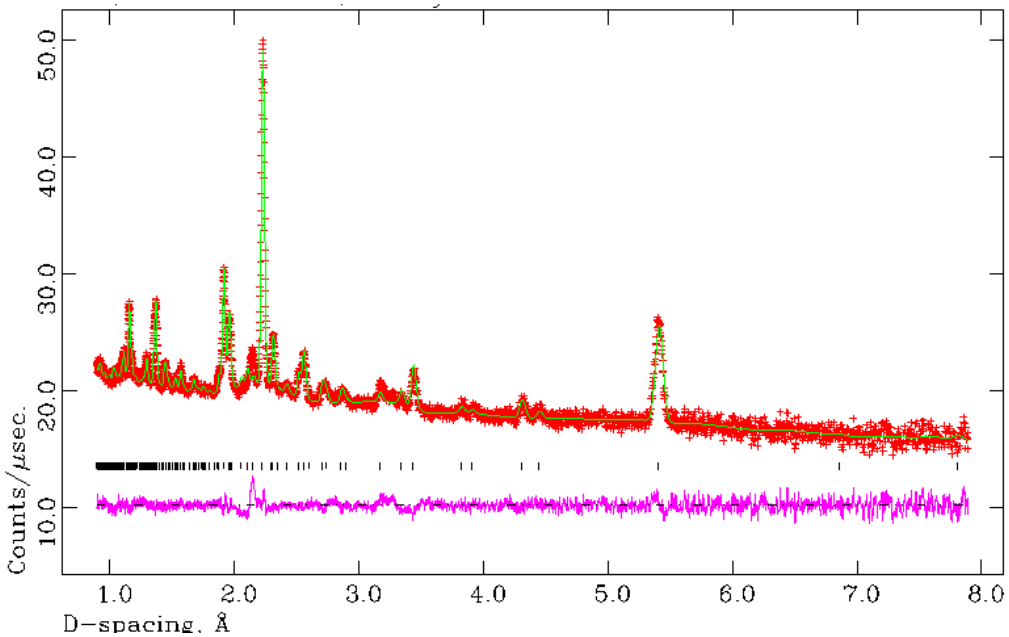

Figure 4.31. Observed (+), calculated (-) and difference (-) profiles from refinement using 4K NPD data for $YSr_3Mn_{2.23}Ga_{1.77}O_{10.5}F_{0.1}$ in space group I4/*mmm*, *a*) C bank, 2θ = 145° *b*) A bank, 2θ = 35° . $\chi^2 = 2.408$, $R_{wp} = 0.85\%$ and $R_p = 1.47\%$.

Table 4.13. Refinement results from 4K NPD data for $YSr_3Mn_{2.23}Ga_{1.77}O_{10.5}F_{0.1}$

Atom	Position	x	y	z	Frac.	U_{iso} x100/Å^2
Mn1	8*f*	0.25	0.25	0.25	0.774(3)	1.0*
Ga1	8*f*	0.25	0.25	0.25	0.226(3)	1.0*
Mn2	8*h*	0.2632(4)	0.2632(4)	0	0.341(3)	1.0*
Ga2	8*h*	0.2632(4)	0.2632(4)	0	0.659(3)	1.0*
Y	4*e*	0	0	0.1453(2)	1	0.48(8)
Sr1	4*e*	0	0	0.6221(4)	1	1.2(1)
Sr2	8*g*	0.5	0	0.1313(2)	1	0.19(4)
O1/F1	8*i*	0	0.106(1)	0	0.32(1)	0.86(2)#
O2	8*j*	0.5	0.2317(5)	0	1	0.86(2)#
O3	16*n*	0	0.2476(5)	0.2558(2)	1	0.86(2)#
O4	16*m*	0.2142(2)	0.2142(2)	0.1116(1)	1	0.86(2)#

a = 7.6431(1) Å, c = 15.6302(4) Å, χ^2 = 2.408, R_{wp} = 0.85% and R_p = 1.93%. Space group I4/*mmm*.

Magnetic moments: Mn1=2.41(9)μ_B ; Mn2 = 2.8(2) μ_B

*denotes thermal parameters fixed to sensible values.

#denotes thermal parameters constrained to avoid negative values.

Table 4.14. Comparison of refined magnetic moments for reduced samples to fluorinated samples.

	Standard sample refined magnetic moment (μ_B)	Fluorinated sample refined magnetic moment (μ_B)
$YSr_3Mn_{3.1}Ga_{0.9}O_{10.4}$	Mn1 - 2.13(5) Mn2 - 2.6(1)	Mn1 - 2.28(7) Mn2 - 1.2(1)
$YSr_3Mn_{2.67}Ga_{1.33}O_{10.5}$	Mn1 - 2.26(6) Mn2 - 3.3(1)	
$YSr_3Mn_{2.3}Ga_{1.7}O_{10.5}$	Mn1 - 2.21(4) Mn2 - 3.78(1)	Mn1 - 2.13(9) Mn2 - 2.7(2)
$YSr_3Mn_{2.23}Ga_{1.77}O_{10.5}$	Mn1 - 2.21(1) Mn2 – 3.8(2)	Mn1 - 2.41(9) Mn2 – 2.8(2)

4.8 References

[1] L. J. Gillie PhD, University of Birmingham 2003.

[2] A. C. Larson, R. B. Von Dreele, General Structure Analysis System, Los Alamos National Laboratory, Los Alamos, NM, 1994.

[3] I. D. Brown and D. Altermatt. *Acta Cryst.* **B41**, 244, 1985.

[4] P. J. Brown, *Magnetic form factors*, chapter 4.4.5, International tables for crystallography vol. C (A. J. C. Wilson, ed.), 391.

[5] A.Munter. *Neutron News*, **Vol. 3**, No. 3, 1992, 29.

CHAPTER 5

Structural and Magnetic Characterisation of Chemically Modified Hematophanite

5.1 Background

The structure of the naturally occurring mineral hematophanite, $Pb_4Fe_3O_8Cl$, was first investigated by Rouse, who concluded that it crystallised in the non-centrosymmetric space group *P4mm* [1]. A subsequent study using single crystal X-ray diffraction data assigned the mineral to the centrosymmetric space group P4/*mmm* [2]. Following a M□ssbauer study the mineral was found to order antiferromagnetically at ~ 602K [3]. $Pb_4Fe_3O_8Cl$ and its analogue $Pb_4Fe_3O_8Br$ have been fully characterised by Weller *et al*. [4]. The material, which crystallises in the centrosymmetric space group P4/*mmm*, comprises two FeO_5 square pyramids connected through a central FeO_6 octahedron. A CsCl-type Pb_2Cl layer separates the perovskite blocks. The structure is shown *figure 5.1*. Horizontal displacement of the equatorial oxygen (O3) of the central FeO_6 octahedron results in rotation of the Fe-octahedra about the *c*-axis by $12.8(2)^o$ for both compounds, at 10K. The degree of rotation decreases with heating to 10.9^o for $Pb_4Fe_3O_8Br$ and 10.3^o for $Pb_4Fe_3O_8Cl$ at 650K. It was proposed that extended regions exist in which neighbouring octahedra rotate in opposing directions. Lattice parameters are a = 3.91476(7) and c = 15.3088(3) for $Pb_4Fe_3O_8Cl$ and a = 3.92347(4) and c = 15.5687(2) for $Pb_4Fe_3O_8Br$[4].

Both $Pb_4Fe_3O_8Cl$ and $Pb_4Fe_3O_8Br$ order antiferromagnetically, in the *ab* plane, with Néel temperatures, T_N, of 610(5)K and 600(5)K respectively. The magnetic cell is related to the nuclear structure by $a_{magnetic} = \sqrt{2}a_{nuclear}$ and $c_{magnetic} = 2c_{nuclear}$, with

magnetic reflections consistent with space group I*mm'm*. Refined magnetic moments of 3.94(3) μ_B for $Pb_4Fe_3O_8Cl$ and 4.10(3) μ_B for $Pb_4Fe_3O_8Br$ at 10K are consistent with high spin Fe^{3+} [4].

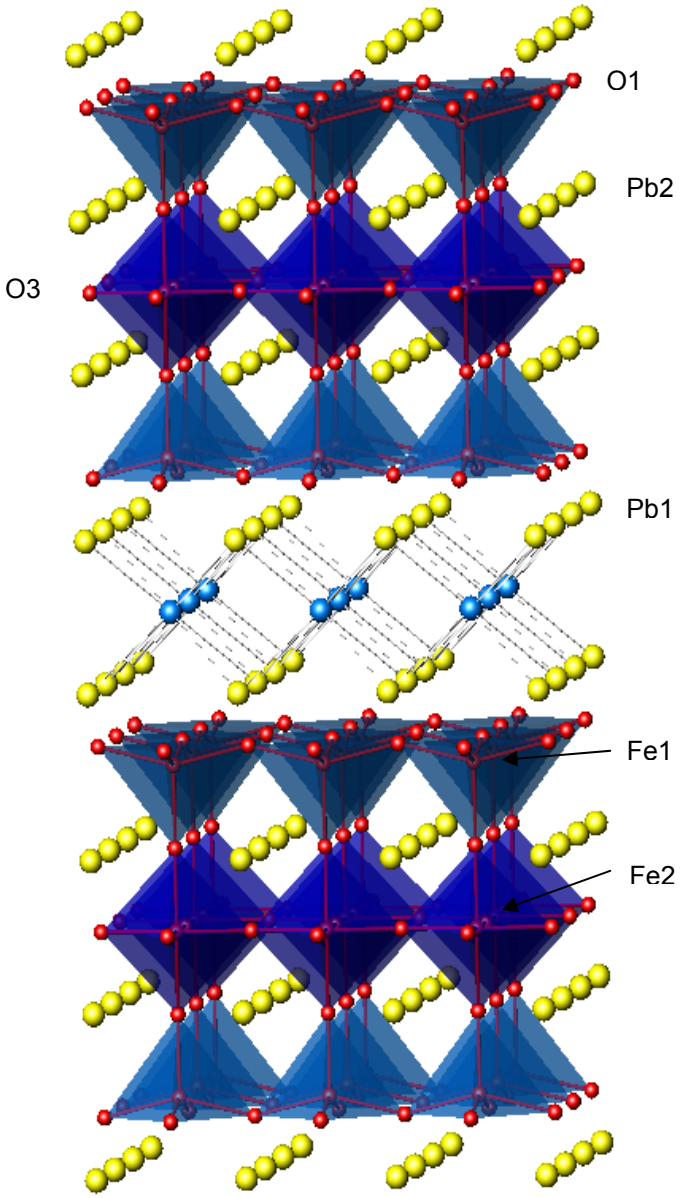

Figure 5.1. Crystallographic structure of $Pb_4Fe_3O_8Cl$. Showing FeO_5 and FeO_6 as blue polyhedra, red spheres are oxygen anions, yellow spheres are lead cations and light blue spheres are chloride anions.

Materials that are iso-structural with hematophanite, in which the FeO_5 polyhedra are replaced by CuO_5 and the FeO_6 octahedra by TaO_6, NbO_6 or SbO_6 have been extensively studied [5, 6, 7], with a view to producing layered cuprates with copper in square pyramidal coordination as found in high T_c superconductors.

This study will investigate the feasibility of replacing Fe^{3+} in $Pb_4Fe_3O_8Cl$ and its Br analogue with Co^{3+} or Mn^{3+} with a view to manipulating the electronic-magnetic properties of the material.

5.2 Synthesis of Modified Hematophanite

Attempts were made to completely substitute Fe^{3+} in $Pb_4Fe_3O_8X$, X=Cl/ Br, with Mn^{3+} or Co^{3+}. Stoiochiometric quantities of $PbCl_2$, PbO and Mn_2O_3 / Co_3O_4 were thoroughly ground and fired at 550^{o}C for 12 hours. The precursor powder was reground and heated to 680^{o}C for subsequent periods of 12 hours in an attempt to achieve phase purity. Phase purity was monitored between firings by X-ray powder diffraction (XRPD) using a Siemens D5000, PSD, Ge monochromator, $CuK_{\alpha 1}$ radiation.

It proved impossible to produce single phase samples of $Pb_4Mn_3O_8X$ or $Pb_4Co_3O_8X$, in all cases multiphase samples were produced. Further attempts to produce a single phase sample were made by partially replacing Pb^{2+} with Ba^{2+} or Sr^{2+} in efforts to synthesise the following samples; $Pb_2Ba_2M_3O_8X$, $Pb_3BaM_3O_8X$, $Pb_2Sr_2M_3O_8X$ and $Pb_3SrM_3O_8X$ where M = Mn or Co, X=Cl or Br. Multiphase samples were again produced.

By partial substitution of Fe^{3+} with Mn^{3+} or Co^{3+} it was possible to synthesise single phase samples of $Pb_4Fe_{2.4}Co_{0.6}O_8Cl$, $Pb_4Fe_{2.6}Co_{0.4}O_8Cl$, $Pb_4Fe_{2.6}Mn_{0.4}O_8Cl$ and $Pb_4Fe_{2.6}Mn_{0.4}O_8Br$. NPD data were collected at ambient temperature on instrument D2B at ILL, Grenoble, France.

5.3 Structural Characterisation of $Pb_4Fe_{2.4}Co_{0.6}O_8Cl$, $Pb_4Fe_{2.6}Co_{0.4}O_8Cl$ $Pb_4Fe_{2.6}Mn_{0.4}O_8Cl$ and $Pb_4Fe_{2.6}Mn_{0.4}O_8Br$

NPD allows a more accurate determination of the crystal structure than XRPD due to a less pronounced difference in the scattering power of lead compared to the lighter elements for NPD compared to XRPD.

Rietveld refinement of NPD data was carried out using the GSAS suite of programs [8], with background parameters, lattice parameters, thermal parameters, histogram scale factor, diffractometer zero point, peak shape (pseudo-voigt) and atomic coordinates refined. Reflections due to magnetic intensity were evident for room temperature scans, as anticipated due to the high ordering temperature of the parent material, $Pb_4Fe_3O_8Cl$, which is antiferromagnetic T_N = 600(5)K [4]. Starting atomic positions were based on those reported by Knee and Weller [4]. The magnetic cell could be related to the nuclear structure by $a_{magnetic} = b_{magnetic} = \sqrt{2}a_{nuclear}$ and $c_{magnetic} = 2c_{nuclear.}$ The Rietveld plots are shown in *figures 2-5,* and the refined structural parameters are given in *tables 5.1-5.4.*

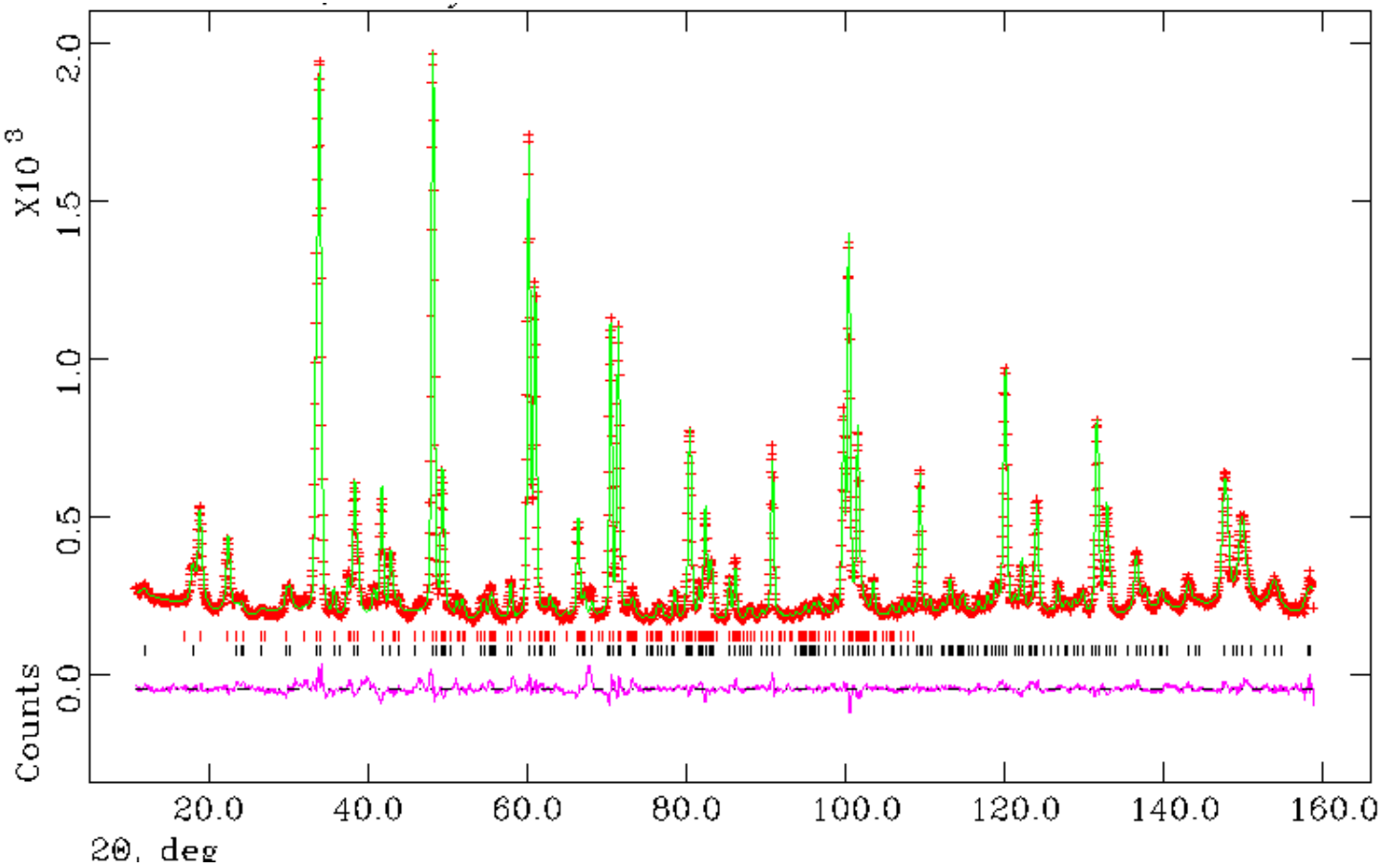

Figure 5.2. Observed (+), calculated (-) and difference (-) profiles from refinement using room temperature NPD data for $Pb_4Fe_{2.4}Co_{0.6}O_8Cl$ in space group P4/ *mmm*. Magnetic unit cell space group I*mm'm*. Reflection positions are marked (|) main phase and (|) magnetic phase.

Table 5.1a. Refinement results from room temperature NPD data for $Pb_4Fe_{2.4}Co_{0.6}O_8Cl$

Atom	Position	x	y	z	U_{iso} x100/ Å^2	Frac.
Pb1	2*h*	0.5	0.5	0.1194(1)	1.40(5)	1
Pb2	2*h*	0.5	0.5	0.3803(1)	1.70(6)	1
Fe1	2*g*	0	0	0.2437(1)	0.29(4)*	0.799(4)
Co1	2*g*	0	0	0.2437(1)	0.29(4)*	0.201(4)
Fe2	1*b*	0	0	0.5	0.29(4)*	0.802(9)
Co2	1*b*	0	0	0.5	0.29(4)*	0.198(9)
O1	4*i*	0	0.5	0.2112(1)	1.44(5)	1
O2	2*g*	0	0	0.3672(2)	2.08(7)	1
O3	4*o*	0.107(1)	0.5	0.5	1.55(9)	0.5
Cl	1*a*	0	0	0	2.20(8)	1

Space group P4/*mmm*; *a* = 3.91072(8) Å; *c* = 15.2901(4) Å. χ^2 =4.319, R_{wp} = 4.18 %, R_p = 3.1%. Magnetic unit cell space group I*mm'm*, Fe/ Co = 3.74(6) μ_B. * constrained to avoid correlation effects between temperature factors and fractional occupancy

*Table 5.1b.*Selected bond lengths for $Pb_4Fe_{2.4}Co_{0.6}O_8Cl$.

Fe/Co - O bond lengths,	Å
Fe1/ Co1 – O1 (x4)	2.0177(8)
Fe1/ Co1 – O2 (x1)	1.889(5)
Fe2/ Co2 – O2 (x2)	2.030(4)
Fe2/ Co2 – O3 (x4)	2.0000(8)

Table 5.1c. Selected bond angles for $Pb_4Fe_{2.4}Co_{0.6}O_8Cl$

	Fe/Co – O angles,	degrees
O1 – Fe1/Co1 – O1		151.4(1)
O1 – Fe1/Co1– O2		104.28(9)
O2 – Fe2/Co2 – O3		90.00
O3 – Fe2/Co2 – O3		180.00

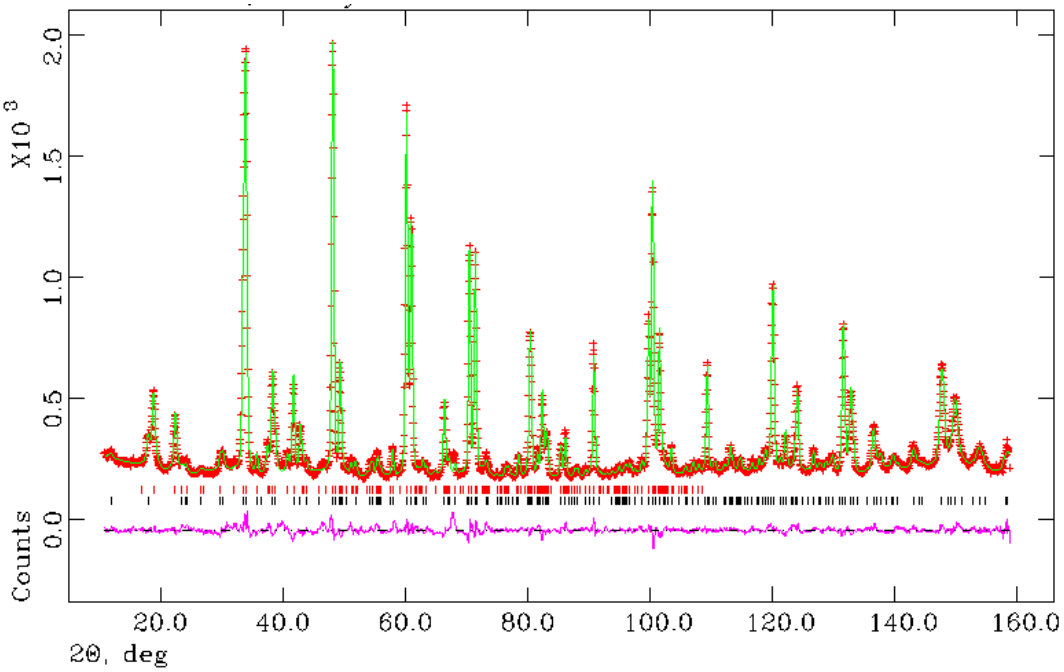

Figure 5.3. Observed (+), calculated (-) and difference (-) profiles from refinement using room temperature NPD data for $Pb_4Fe_{2.6}Co_{0.4}O_8Cl$ in space group P4/ *mmm*. Magnetic unit cell space group I*mm'm*. Reflection positions are marked (|) main phase and (|) magnetic phase.

Table 5.2a. Refinement results from room temperature NPD data for $Pb_4Fe_{2.6}Co_{0.4}O_8Cl$

Atom	Position	x	y	z	U_{iso} x100/ Å^2	Frac.
Pb1	2*h*	0.5	0.5	0.1197(1)	0.51(4)	1
Pb2	2*h*	0.5	0.5	0.3795(1)	1.05(4)	1
Fe1	2*g*	0	0	0.2439(1)	0.30(4)*	0.869(4)
Co1	2*g*	0	0	0.2439(1)	0.30(4)*	0.131(4)
Fe2	1*b*	0	0	0.5	0.30(4)*	0.862(8)
Co2	1*b*	0	0	0.5	0.30(4)*	0.138(8)
O1	4*i*	0	0.5	0.2112(1)	0.86(5)	1
O2	2*g*	0	0	0.3672(2)	1.22(5)	1
O3	4*o*	0.1090(8)	0.5	0.5	0.95(7)	0.5
Cl	1*a*	0	0	0	1.51(6)	1

Space group P4/*mmm*; *a* = 3.91102(7) Å; *c* = 15.2927(3) Å. χ^2 =6.366, R_{wp} = 3.75 %, R_p = 2.9%. Magnetic unit cell space group I*mm'm*, Fe/ Co = 3.56(4) μ_B. * constrained to avoid correlation effects between temperature factors and fractional occupancy

*Table 5.2b.*Selected bond lengths for $Pb_4Fe_{2.6}Co_{0.4}O_8Cl$.

Fe/Co - O bond lengths,	Å
Fe1/ Co1 – O1 (x4)	2.0183(7)
Fe1/ Co1 – O2 (x1)	1.886(4)
Fe2/ Co2 – O2 (x2)	2.031(3)
Fe2/ Co2 – O3 (x4)	2.0017(7)

Table 5.2c. Selected bond angles for $Pb_4Fe_{2.6}Co_{0.4}O_8Cl$

	Fe/Co – O angles,	degrees
O1 – Fe1/Co1 – O1		151.3(1)
O1 – Fe1/Co1– O2		104.33(7)
O2 – Fe2/Co2 – O3		90.00
O3 – Fe2/Co2 – O3		180.00

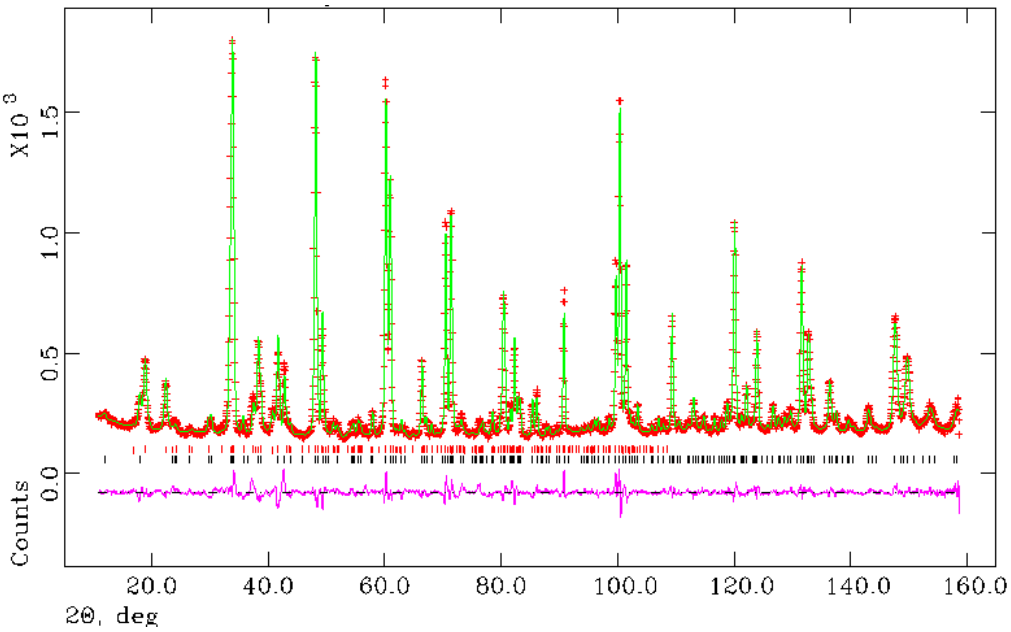

Figure 5.4. Observed (+), calculated (-) and difference (-) profiles from refinement using room temperature NPD data for $Pb_4Fe_{2.6}Mn_{0.4}O_8Cl$ in space group P4/ *mmm*. Magnetic unit cell space group I*mm'm*. Reflection positions are marked (|) main phase and (|) magnetic phase.

Table 5.3a. Refinement results from room temperature NPD data for $Pb_4Fe_{2.6}Mn_{0.4}O_8Cl$

Atom	Position	x	y	z	U_{iso} x100/ Å^2	Frac.
Pb1	2*h*	0.5	0.5	0.1190(1)	1.16(5)	1
Pb2	2*h*	0.5	0.5	0.3790(1)	1.38(5)	1
Fe1	2*g*	0	0	0.2436(1)	0.34(4)*	0.859(2)
Mn1	2*g*	0	0	0.2436(1)	0.34(4)*	0.141(2)
Fe2	1*b*	0	0	0.5	0.34(4)*	0.881(5)
Mn2	1*b*	0	0	0.5	0.34(4)*	0.119(5)
O1	4*i*	0	0.5	0.2111(1)	1.50(5)	1
O2	2*g*	0	0	0.3661(2)	1.97(7)	1
O3	4*o*	0.1170(1)	0.5	0.5	1.22(8)	0.5
Cl	1*a*	0	0	0	2.31(8)	1

Space group P4/*mmm*; *a* = 3.91061(7) Å; *c* = 15.2998(3) Å. χ^2 =5.480, R_{wp} = 4.96 %, R_p = 3.75%. Magnetic unit cell space group I*mm'm*, Fe/ Mn = 3.72(6) $\mu_{B.}$

* constrained to avoid correlation effects between temperature factors and fractional occupancy

*Table 5.3b.*Selected bond lengths for $Pb_4Fe_{2.6}Mn_{0.4}O_8Cl$.

Fe/Co - O bond lengths,	Å
Fe1/ Mn1 – O1 (x4)	2.0174(9)
Fe1/ Mn1 – O2 (x1)	1.874(5)
Fe2/ Mn2 – O2 (x2)	2.049(4)
Fe2/ Mn2 – O3 (x4)	2.0081(9)

Table 5.3c. Selected bond angles for $Pb_4Fe_{2.6}Mn_{0.4}O_8Cl$

	Fe/Co – O angles,	degrees
O1 – Fe1/Mn1 – O1		151.5(1)
O1 – Fe1/Mn1– O2		104.26(1)
O2 – Fe2/Mn2 – O3		90.00
O3 – Fe2/Mn2 – O3		180.00

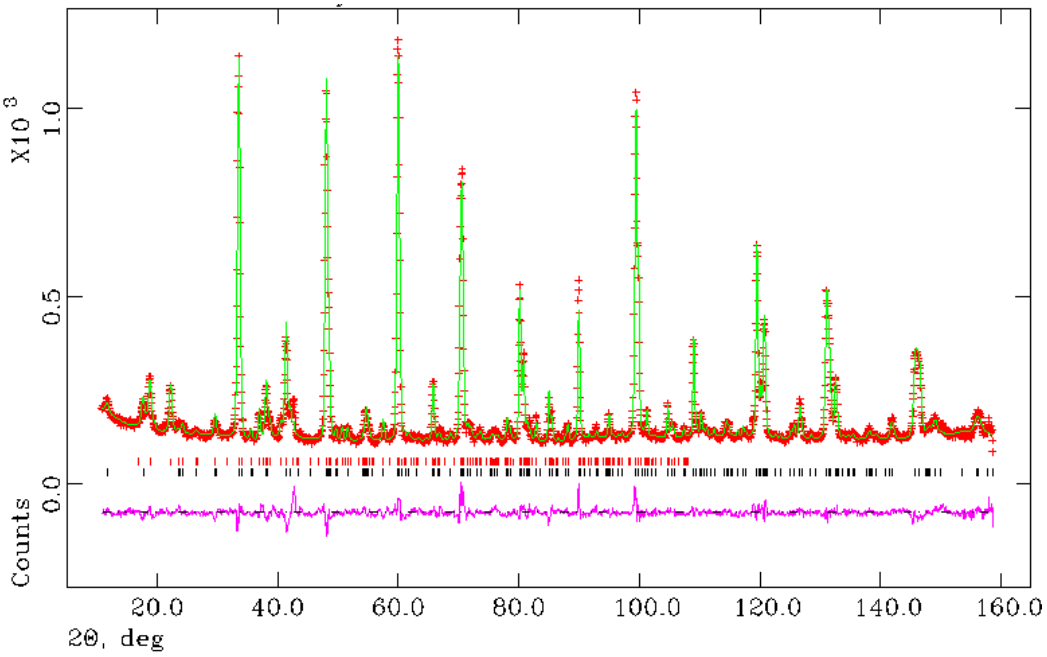

Figure 5.5. Observed (+), calculated (-) and difference (-) profiles from refinement using room temperature NPD data for $Pb_4Fe_{2.6}Mn_{0.4}O_8Br$ in space group P4/ *mmm*. Magnetic unit cell space group I*mm'm*. Reflection positions are marked (|) main phase and (|) magnetic phase.

Table 5.4a. Refinement results from room temperature NPD data for $Pb_4Fe_{2.6}Mn_{0.4}O_8Br$

Atom	Position	x	y	z	U_{iso} x100/ Å^2	Frac.
Pb1	2*h*	0.5	0.5	0.1262(2)	1.05(5)	1
Pb2	2*h*	0.5	0.5	0.3822(1)	1.31(6)	1
Fe1	2*g*	0	0	0.2483(2)	0.41(5)*	0.856(3)
Mn1	2*g*	0	0	0.2483(2)	0.41(5)*	0.144(3)
Fe2	1*b*	0	0	0.5	0.41(5)*	0.888(6)
Mn2	1*b*	0	0	0.5	0.41(5)*	0.112(6)
O1	4*i*	0	0.5	0.2158(1)	1.39(6)	1
O2	2*g*	0	0	0.3694(3)	1.88(8)	1
O3	4*o*	0.106(1)	0.5	0.5	1.3(1)	0.5
Cl	1*a*	0	0	0	1.5(1)	1

Space group P4/*mmm*; *a* = 3.9185(1) Å; *c* = 15.5608(5) Å. χ^2 =3.848, R_{wp} = 5.19 %, R_p = 3.95%. Magnetic unit cell space group I*mm'm*, Fe/ Mn = 3.67(7) $\mu_{B.}$ * constrained to avoid correlation effects between temperature factors and fractional occupancy

*Table 5.4b.*Selected bond lengths for $Pb_4Fe_{2.6}Mn_{0.4}O_8Br$.

Fe/Mn - O bond lengths,	Å
Fe1/ Mn1 – O1 (x4)	2.024(1)
Fe1/ Mn1 – O2 (x1)	1.884(8)
Fe2/ Mn2 – O2 (x2)	2.033(6)
Fe2/ Mn2 – O3 (x4)	2.003(1)

Table 5.4c. Selected bond angles for $Pb_4Fe_{2.6}Mn_{0.4}O_8Br$

	Fe/Co – O angles,	degrees
O1 – Fe1/Mn1 – O1		151.0(2)
O1 – Fe1/Mn1– O2		104.5(1)
O2 – Fe2/Mn2 – O3		90.00
O3 – Fe2/Mn2 – O3		180.00

Refinement proceeded smoothly for all four samples to give a good fit between calculated and observed profiles: $Pb_4Fe_{2.4}Co_{0.6}O_8Cl$ χ^2=4.319, $Pb_4Fe_{2.6}Co_{0.4}O_8Cl$ χ^2 =6.366, $Pb_4Fe_{2.6}Mn_{0.4}O_8Cl$ χ^2 =5.480 and $Pb_4Fe_{2.6}Mn_{0.4}O_8Br$ χ^2 =3.848. Indicating that cobalt and manganese can be substituted into hematophanite, $Pb_4Fe_3O_8Cl$, up to the levels specified.

Co^{3+} substitutes for Fe^{3+} on both octahedral and square pyramidal sites with no evidence for a preference for either site. Comparable results were found for the structurally related material $YBa_2Fe_3O_8$. $YBa_2Fe_3O_8$ comprises two FeO_5 square pyramids separated by a FeO_6 octahedron, a yittrium ion separates these perovskite blocks in $YBa_2Fe_3O_8$ instead of the Pb_2Cl layer found in $Pb_4Fe_3O_8Cl$ [9]. Substitution of Co^{3+} into $YBa_2Fe_3O_8$ was possible to a maximum level of $YBa_2Fe_{2.53}Co_{0.47}O_8$, with Co^{3+} distributed evenly over both square pyramidal and octahedral [10].

Mn^{3+} occupies both sites with some evidence for a preference for the square pyramidal site to give the following compositions: $Pb_4(Fe_{1.72}Mn_{0.28})_{sq.\ pyramid}(Fe_{0.88}Mn_{0.12})_{oct}O_8Cl$ and $Pb_4(Fe_{1.71}Mn_{0.29})_{sq.\ pyramid}(Fe_{0.89}Mn_{0.11})_{oct}O_8Br$.

Lattice parameters are less than the parent material, $Pb_4Fe_3O_8Cl$ (a=3.91476(7), c=15.3088(3)) for both cobalt substituted samples; $Pb_4Fe_{2.4}Co_{0.6}O_8Cl$ (a = 3.91072(8), c = 15.2901(4)), $Pb_4Fe_{2.6}Co_{0.4}O_8Cl$ (a =3.91102(7), c = 15.2927(3)). The ionic radius of octahedrally coordinated Co^{3+} (0.61 Å high spin and 0.545 Å low spin [8]) is less than that for octahedrally coordinated Fe^{3+} (0.645 Å high spin and 0.55 Å low spin), which may explain the slight decrease in lattice parameters on substitution with Co^{3+}. Substitution of cobalt into the structurally related material $YBa_2Fe_3O_8$ also results in a contraction in unit cell dimensions [10].

Lattice parameters are also less than the parent material, $Pb_4Fe_3O_8Cl$ (a=3.91476(7), c=15.3088(3)) and $Pb_4Fe_3O_8Br$ (a=3.92347(4), c=15.5687(2)), for manganese substituted samples $Pb_4Fe_{2.6}Mn_{0.4}O_8Cl$ (a=3.91061(7), c=15.2998(3)) and $Pb_4Fe_{2.6}Mn_{0.4}O_8Br$ (a=3.9185(1), c=15.5608(5)). Differences in ionic radius cannot explain reduced lattice parameters for Mn^{3+} substituted samples since the ionic radius of Mn^{3+} is the same as Fe^{3+} for both five coordinate (0.58 Å) and octahedral (0.645 Å high spin Å) coordination. On substitution with Mn^{3+}, a d^4, cation one would expect some evidence of Jahn-Teller distortion such as an increase or decrease in apical bond length relative to the equatorial bond length, resulting in an increase or decrease in lattice parameter c relative to lattice parameter a. There is no evidence of Jahn-Teller distortion for the Mn^{3+} substituted samples.

5.4 Low temperature studies of $Pb_4Fe_{2.4}Co_{0.6}O_8Cl$, $Pb_4Fe_{2.6}Co_{0.4}O_8Cl$ $Pb_4Fe_{2.6}Mn_{0.4}O_8Cl$ and $Pb_4Fe_{2.6}Mn_{0.4}O_8Br$

NPD data were collected at 5K on instrument D2B at ILL, Grenoble, France. Rietveld refinement was carried using the GSAS program [8], in space group *P4/mmm* for the nuclear phase and in orthorhombic space group I*mm'm* for the magnetic phase,

with the magnetic unit cell related to the nuclear structure by $a_{magnetic} = b_{magnetic} = \sqrt{2}a_{nuclear}$ and $c_{magnetic} = 2c_{nuclear}$ using a magnetic model based on that for $Pb_4Fe_3O_8Cl$ [4]. The Rietveld plots are shown in *figures 5.6-5.9,* and the refined structural parameters are given in *tables 5.6-5.9.* The best fit between observed and calculated profiles was obtained when magnetic moments were aligned antiferromagnetically along the [100] direction of the unit cell as illustrated in *figure 5.10.*

Initially the magnetic moments for Fe/Co or Fe/Mn on the octahedral and square pyramidal sites were refined individually but following an unrealistic value of 6.7(1) μ_B on the octahedral site in $Pb_4Fe_{2.6}Mn_{0.4}O_8Cl$, the moments on the two sites were constrained to be equal for all samples. Following a Mössbauer study of $Pb_4Fe_3O_8Cl$ it was concluded that the magnetic moments on the two sites are slightly different [3], but it was not possible to detect this difference by refinement of NPD data.

The possibility of a canted magnetic moment was investigated by refining moments in the x [100] and y [010] directions simultaneously or the x [100] and z [100] directions simultaneously. There was a slight improvement in the fit between observed and calculated profiles when moments were refined in both the x and y direction but this was not significant.

Ordered magnetic moments for the substituted samples are similar to those for hematophanite, $Pb_4Fe_3O_8Cl$. Ordered magnetic moments are lower than the expected value of 5 for Fe^{3+} (d^5), due to the strong covalent interaction between Fe and O. This strong interaction results in the high antiferromagnetic ordering temperatures of 610(5)K and 600(5)K for $Pb_4Fe_3O_8Cl$ and $Pb_4Fe_3O_8Br$ respectively [4]. The substitution

of Fe^{3+} by Mn^{3+} or Co^{3+} does not appear to affect these strong superexchange interactions.

Table 5.5. Summary of ordered magnetic moments for doped samples compared to parent samples.

Sample	Room temperature refined magnetic moments (μ_B)	Low temperature refined magnetic moments (μ_B)
$Pb_4Fe_3O_8Cl$ [4]	3.55(3)	3.94(3) at 10K
$Pb_4Fe_{2.4}Co_{0.6}O_8Cl$	3.74(6)	4.31(8) at 5K
$Pb_4Fe_{2.6}Co_{0.4}O_8Cl$	3.56(4)	3.93(6) at 5K
$Pb_4Fe_{2.4}Mn_{0.6}O_8Cl$	3.72(6)	3.93(5) at 5K
$Pb_4Fe_3O_8Br$ [4]	3.52(3)	4.10(3) at 10K
$Pb_4Fe_{2.4}Mn_{0.6}O_8Br$	3.67(7)	4.25(6) at 5K

Refined magnetic moments are higher for the sample doped with greater amounts of cobalt ($Pb_4Fe_{2.4}Co_{0.6}O_8Cl$) compared to the undoped parent sample, as shown in *table 5.5*. The increase in magnetic moment may be due to an orbital contribution to the magnetic moment for octahedrally coordinated high spin Co^{3+}, a d^6 cation with a T_{2g} electronic ground state. Refined magnetic moments are also higher for the bromine analogue when doped with manganese ($Pb_4Fe_{2.4}Mn_{0.6}O_8Br$), compared to the parent sample ($Pb_4Fe_3O_8Br$), this increase in magnetic moment may be due to an orbital contribution to the magnetic moment for Mn^{3+} in square pyramidal coordination.

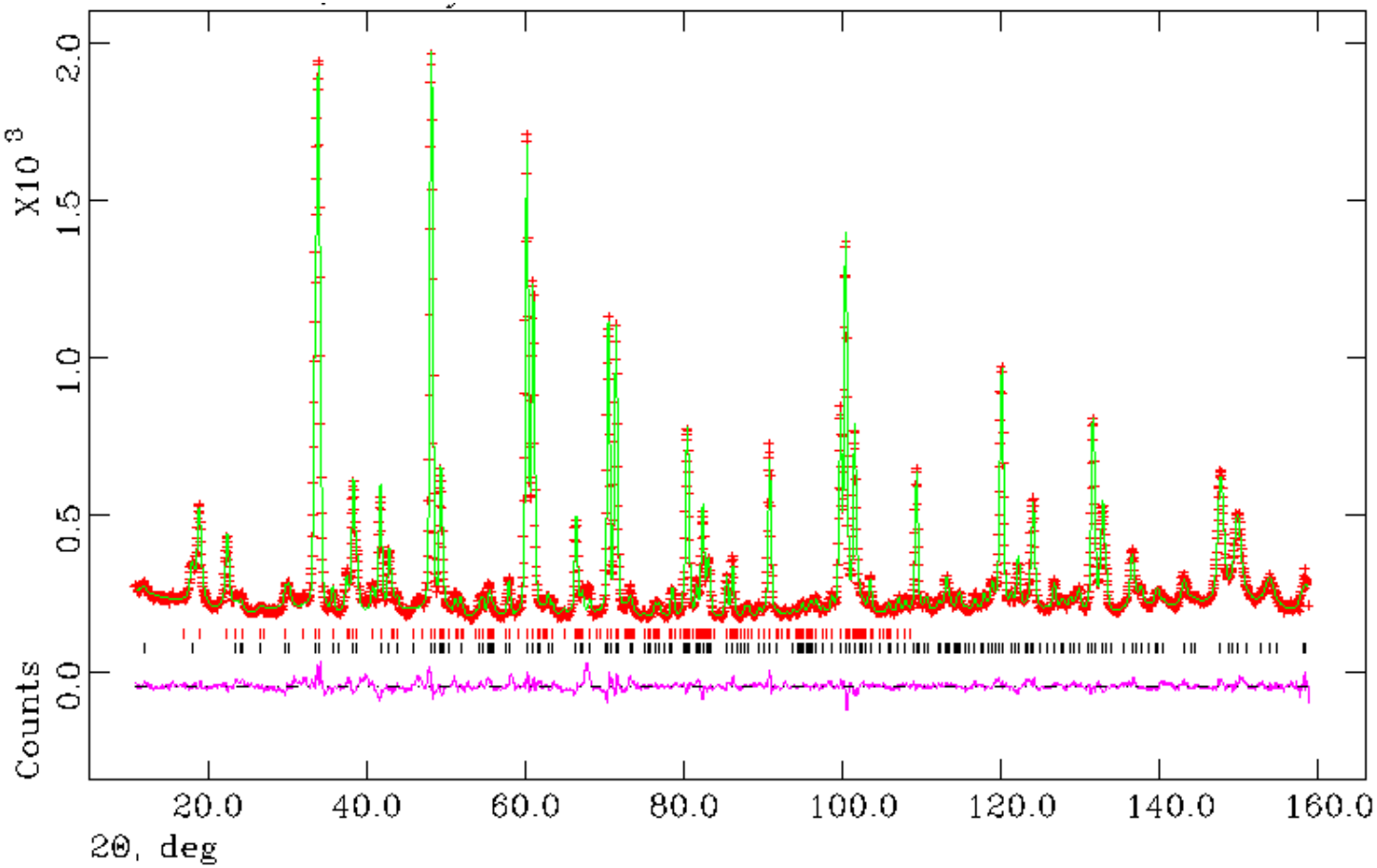

Figure 5.6. Observed (+), calculated (-) and difference (-) profiles from refinement using 5K NPD data for $Pb_4Fe_{2.4}Co_{0.6}O_8Cl$ in space group P4/ *mmm*. Magnetic unit cell space group I*mm'm*. Reflection positions are marked (|) main phase and (|) magnetic phase.

Table 5.6. Refinement results from 5K NPD data for $Pb_4Fe_{2.4}Co_{0.6}O_8Cl$

Atom	Position	x	y	z	U_{iso} x100/ Å^2	Frac.
Pb1	2*h*	0.5	0.5	0.1189(1)	0.54(5)	1
Pb2	2*h*	0.5	0.5	0.3788(1)	0.22(5)	1
Fe1	2*g*	0	0	0.2441(2)	0.3*	0.806(5)
Co1	2*g*	0	0	0.2441(2)	0.3*	0.194(5)
Fe2	1*b*	0	0	0.5	0.3*	0.788(11)
Co2	1*b*	0	0	0.5	0.3*	0.212(11)
O1	4*i*	0	0.5	0.2106(1)	0.83(5)	1
O2	2*g*	0	0	0.3673(2)	0.85(7)	1
O3	4*o*	0.119(1)	0.5	0.5	0.49(9)	0.5
Cl	1*a*	0	0	0	0.29(7)	1

Space group P4/*mmm*; *a* = 3.90013(1) Å; *c* = 15.2321(5) Å. χ^2 =4.940, R_{wp} = 5.35 %, R_p = 4.1%. Magnetic unit cell space group I*mm'm*, Fe/ Co = 4.31(8) μ_B.

* fixed to avoid negative temperature factors.

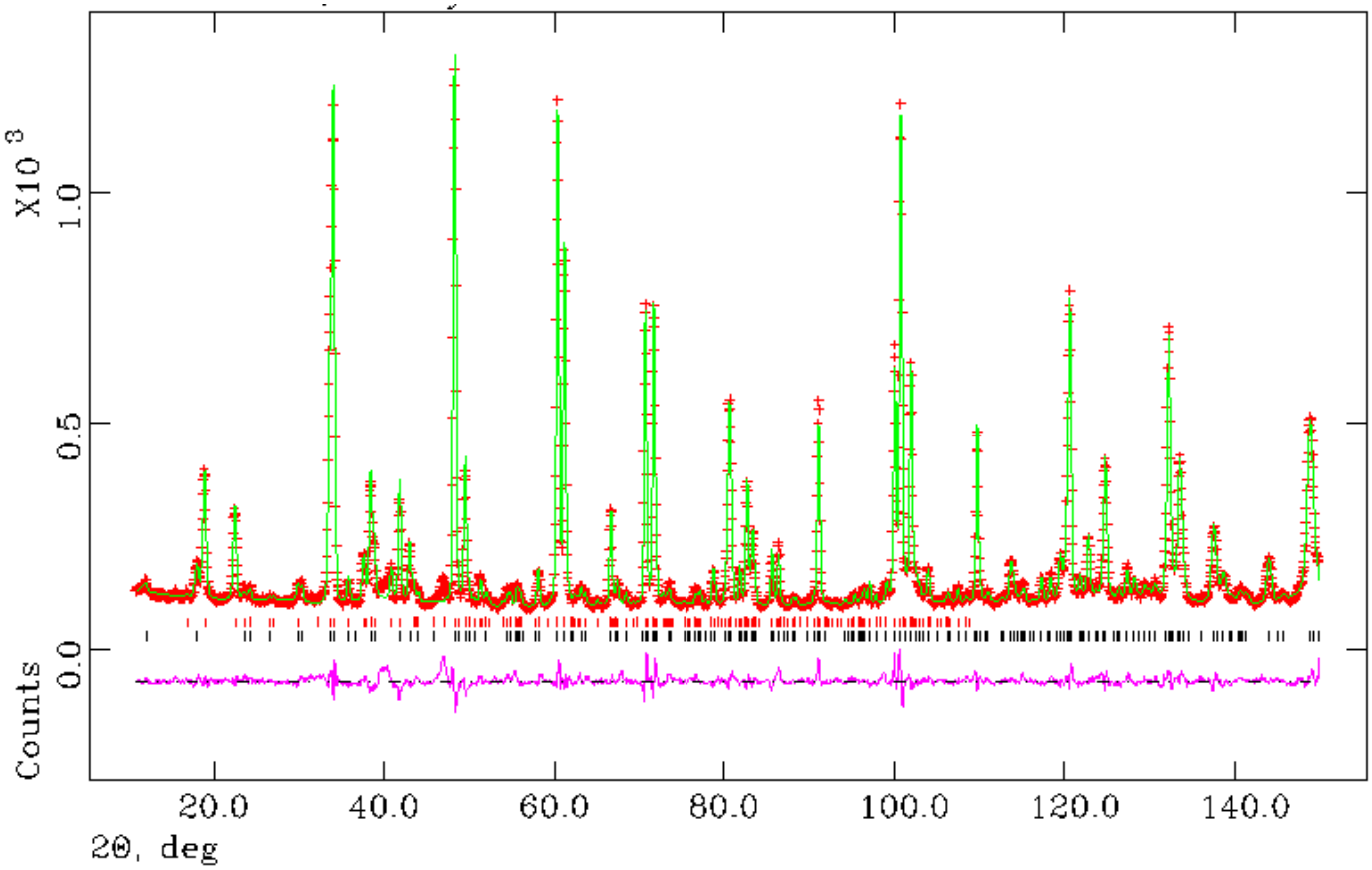

Figure 5.7. Observed (+), calculated (-) and difference (-) profiles from refinement using 5K NPD data for $Pb_4Fe_{2.6}Co_{0.4}O_8Cl$ in space group P4/ *mmm*. Magnetic unit cell space group I*mm'm*. Reflection positions are marked (|) main phase and (|) magnetic phase.

Table 5.7. Refinement results from 5K NPD data for $Pb_4Fe_{2.6}Co_{0.4}O_8Cl$

Atom	Position	x	y	z	U_{iso} x100/ Å^2	Frac.
Pb1	2*h*	0.5	0.5	0.1191(1)	0.04(4)	1
Pb2	2*h*	0.5	0.5	0.3788(1)	0.06(1)	1
Fe1	2*g*	0	0	0.2441(2)	0.3*	0.869(5)
Co1	2*g*	0	0	0.2441(2)	0.3*	0.131(5)
Fe2	1*b*	0	0	0.5	0.3*	0.863(1)
Co2	1*b*	0	0	0.5	0.3*	0.137(1)
O1	4*i*	0	0.5	0.2110(1)	0.55(4)	1
O2	2*g*	0	0	0.3671(2)	0.61(6)	1
O3	4*o*	0.117(1)	0.5	0.5	0.63(9)	0.5
Cl	1*a*	0	0	0	0.09(6)	1

Space group P4/*mmm*; *a* = 3.90018(7) Å; *c* = 15.2331(3) Å. χ^2 =8.440, R_{wp} = 5.25 %, R_p = 3.99%. Magnetic unit cell space group I*mm'm*, Fe/ Co = 3.93(6) μ_B.

* fixed to avoid negative temperature factors.

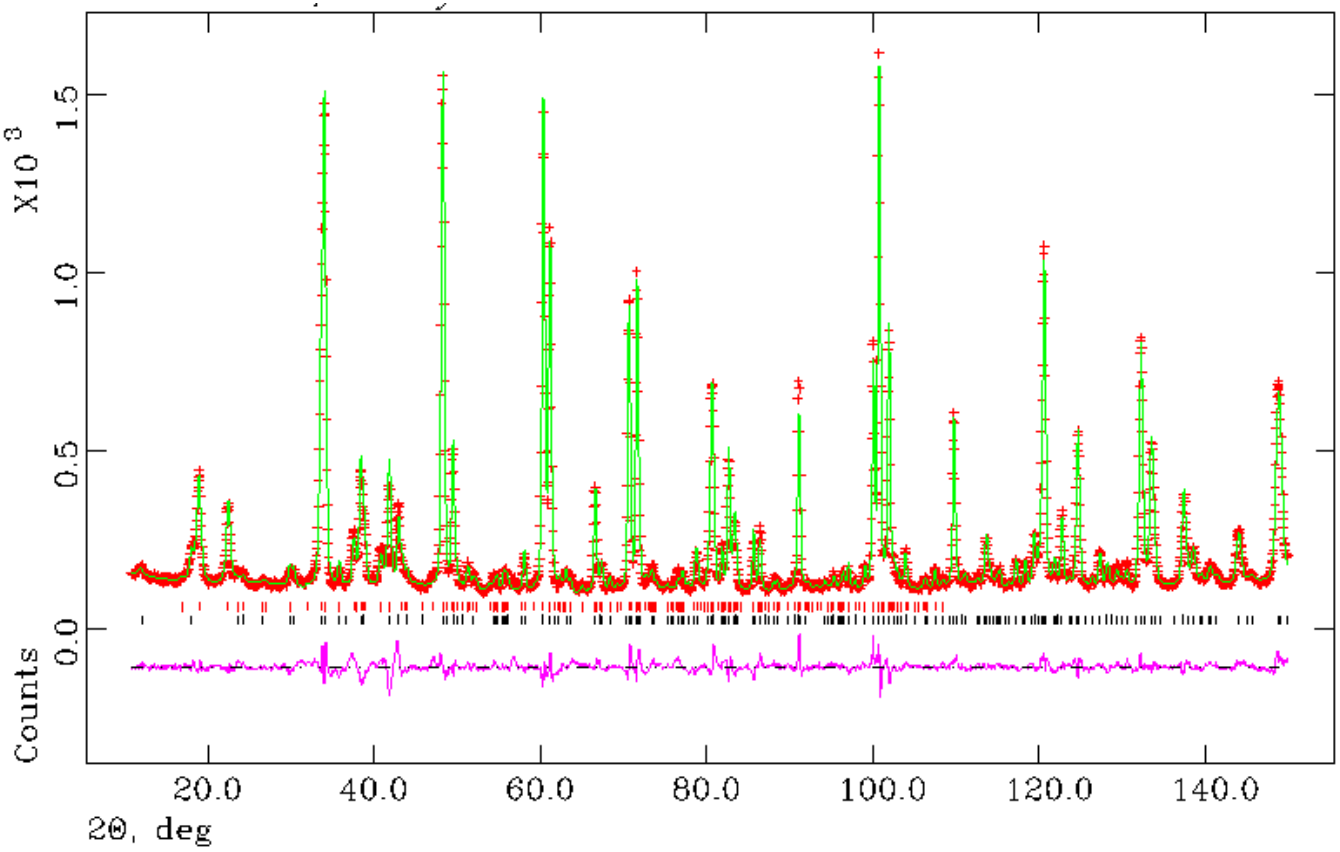

Figure 5.8. Observed (+), calculated (-) and difference (-) profiles from refinement using 5K NPD data for $Pb_4Fe_{2.6}Mn_{0.4}O_8Cl$ in space group P4/ *mmm*. Magnetic unit cell space group I*mm'm*. Reflection positions are marked (|) main phase and (|) magnetic phase.

Table 5.8. Refinement results from 5K NPD data for $Pb_4Fe_{2.6}Mn_{0.4}O_8Cl$

Atom	Position	x	y	z	U_{iso} x100/ Å^2	Frac.
Pb1	2*h*	0.5	0.5	0.1191(1)	0.68(4)	1
Pb2	2*h*	0.5	0.5	0.3784(1)	0.48(4)	1
Fe1	2*g*	0	0	0.2437(2)	0.3*	0.866(3)
Mn1	2*g*	0	0	0.2437(2)	0.3*	0.134(3)
Fe2	1*b*	0	0	0.5	0.3*	0.867(5)
Mn2	1*b*	0	0	0.5	0.3*	0.133(5)
O1	4*i*	0	0.5	0.2106(1)	1.08(4)	1
O2	2*g*	0	0	0.3662(2)	1.11(7)	1
O3	4*o*	0.121(1)	0.5	0.5	0.47(7)	0.5
Cl	1*a*	0	0	0	0.83(6)	1

Space group P4/*mmm*; *a* = 3.89916(8) Å; *c* = 15.2372(4) Å. χ^2 =6.081, R_{wp} = 5.85 %, R_p = 4.48%. Magnetic unit cell space group I*mm'm*, Mn/ Co = 3.93(5) μ_B.

* fixed to avoid negative temperature factors.

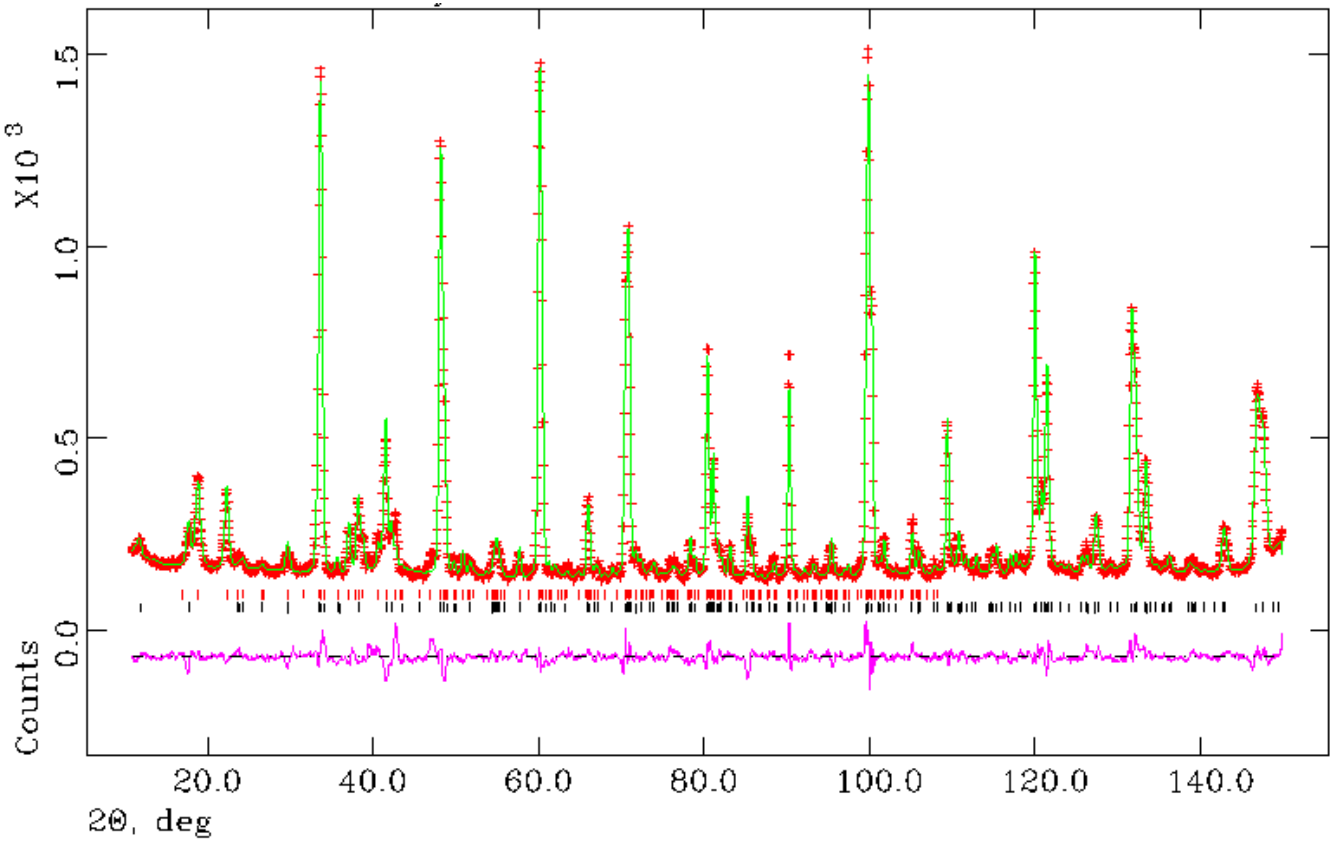

Figure 5.9. Observed (+), calculated (-) and difference (-) profiles from refinement using 5K NPD data for $Pb_4Fe_{2.6}Mn_{0.4}O_8Br$ in space group P4/ *mmm*. Magnetic unit cell space group I*mm'm*. Reflection positions are marked (|) main phase and (|) magnetic phase.

Table 5.9. Refinement results from 5K NPD data for $Pb_4Fe_{2.6}Mn_{0.4}O_8Br$

Atom	Position	x	y	z	U_{iso} x100/ Å^2	Frac.
Pb1	2*h*	0.5	0.5	0.1256(2)	0.06(5)	1
Pb2	2*h*	0.5	0.5	0.3815(1)	0.08(4)	1
Fe1	2*g*	0	0	0.2480(2)	0.3*	0.853(3)
Mn1	2*g*	0	0	0.2480(2)	0.3*	0.147(3)
Fe2	1*b*	0	0	0.5	0.3*	0.893(7)
Mn2	1*b*	0	0	0.5	0.3*	0.107(7)
O1	4*i*	0	0.5	0.2154(2)	1.08(6)	1
O2	2*g*	0	0	0.3688(3)	0.69(7)	1
O3		0.118(10	0.5	0.5	0.8(1)	0.5
Cl	1*a*	0	0	0	0. 3(1)	1

Space group P4/*mmm*; *a* = 3.9087(1) Å; *c* = 15.5029(4) Å. χ^2 =6.36, R_{wp} = 5.56 %, R_p = 4.25%. Magnetic unit cell space group I*mm'm*, Fe/ Mn = 4.25(6) μ_B.

* fixed to avoid negative temperature factors.

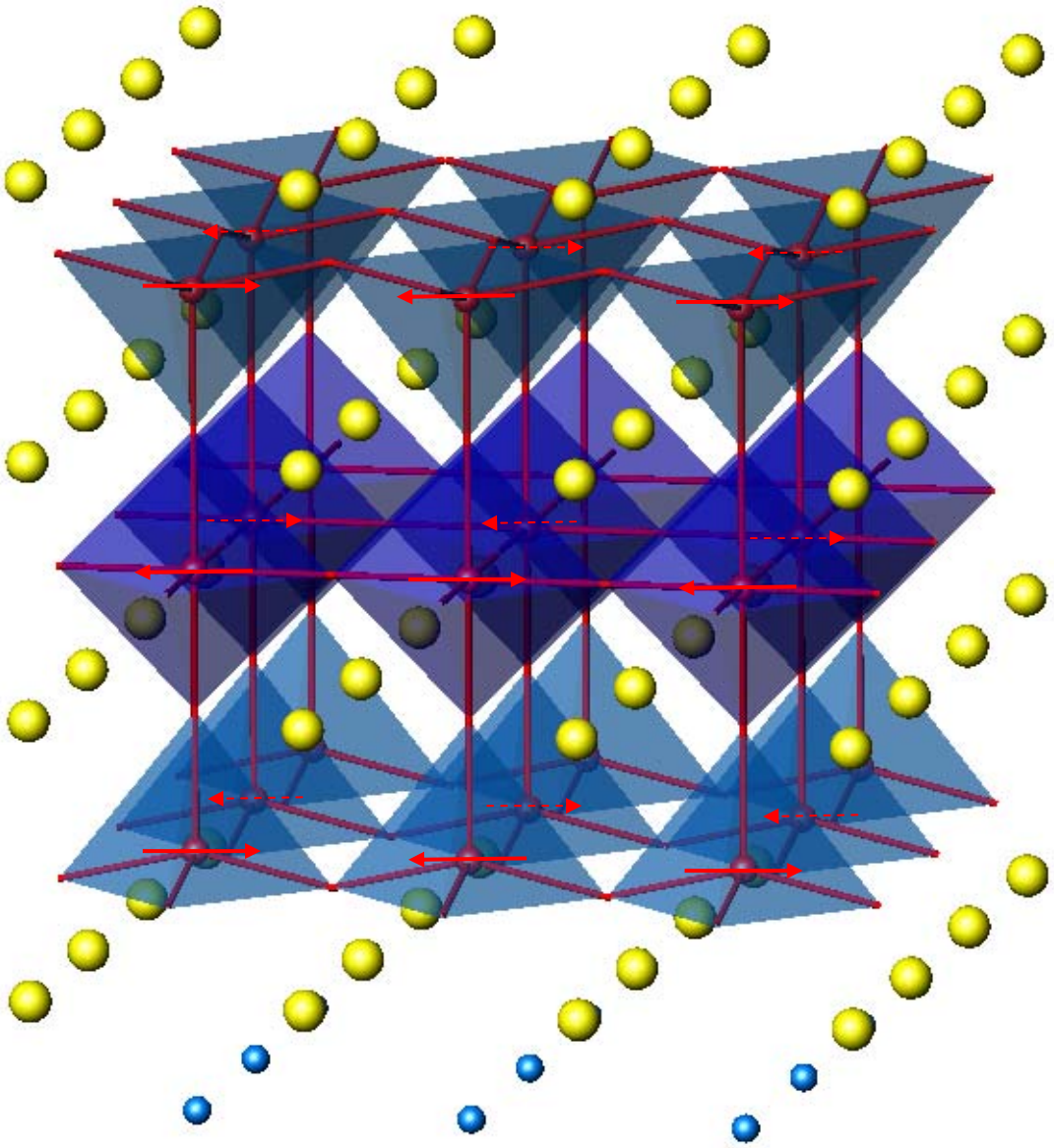

Figure 5.10. Magnetic structure of $Pb_4Fe_{3-x}M_xO_8Cl$, (M=Co/Mn). Showing Fe/MO_6 dark blue polyhedra, Fe/MO_5 light blue polyhedra, yellow spheres lead ions and blue spheres are chloride ions.

5.4.1 Magnetic Susceptibility Studies

Magnetic susceptibility measurements were taken using a Quantum Design Physical Properties Measurement System (PPMS). DC magnetisation measurements were made for $Pb_4Fe_3O_8Cl$, $Pb_4Fe_{2.4}Co_{0.6}O_8Cl$, $Pb_4Fe_{2.6}Co_{0.4}O_8Cl$ $Pb_4Fe_{2.6}Mn_{0.4}O_8Cl$ and $Pb_4Fe_{2.6}Mn_{0.4}O_8Br$, with an applied field of 1000 Guass. Both zero field cooled and field cooled data were collected. *Figures 5.11- 5.15* show the susceptibility versus temperature plots.

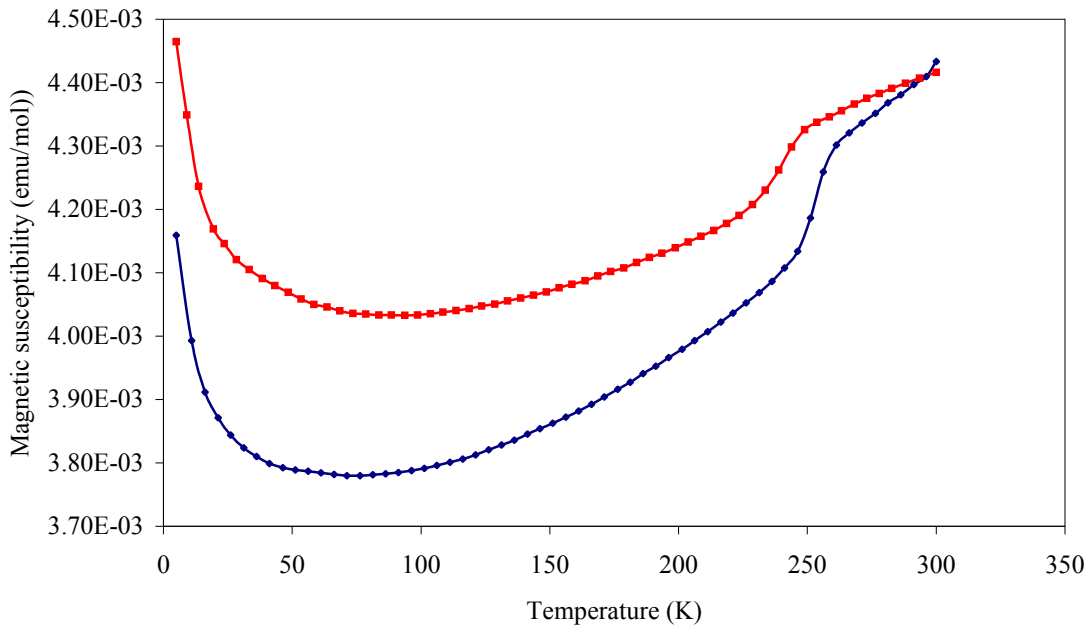

Figure 5.11. Magnetic susceptibility versus temperature plot for $Pb_4Fe_3O_8Cl$ performed in an applied field of 1000 Gauss. Zero-field cooled is shown in blue and field cooled data in red.

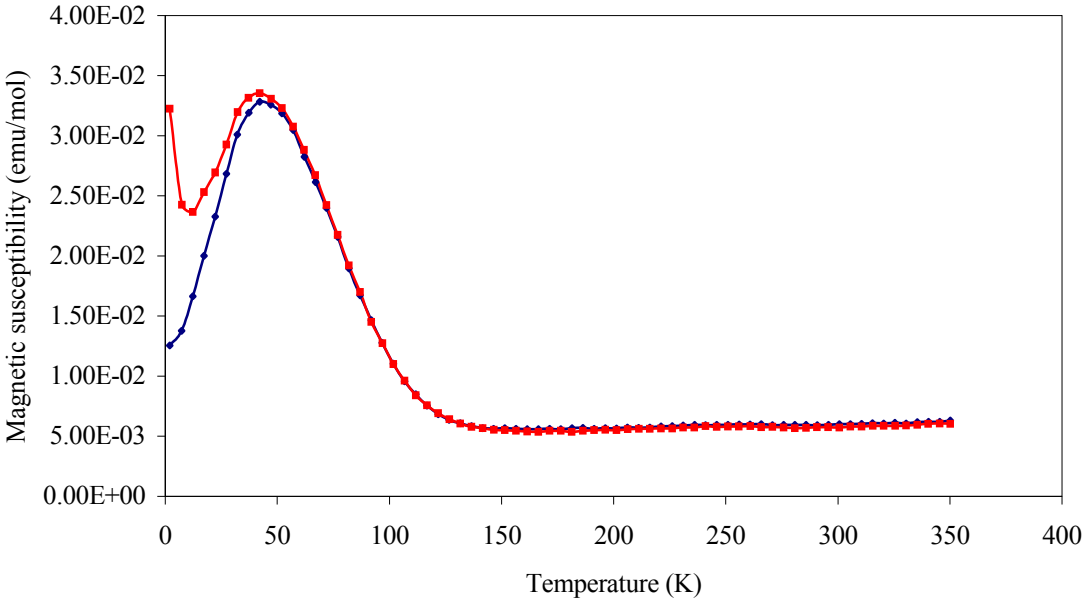

Figure 5.12. Magnetic susceptibility versus temperature plot for $Pb_4Fe_{2.4}Co_{0.6}O_8Cl$ performed in an applied field of 1000 Gauss. Zero-field cooled is shown in blue and field cooled data in red.

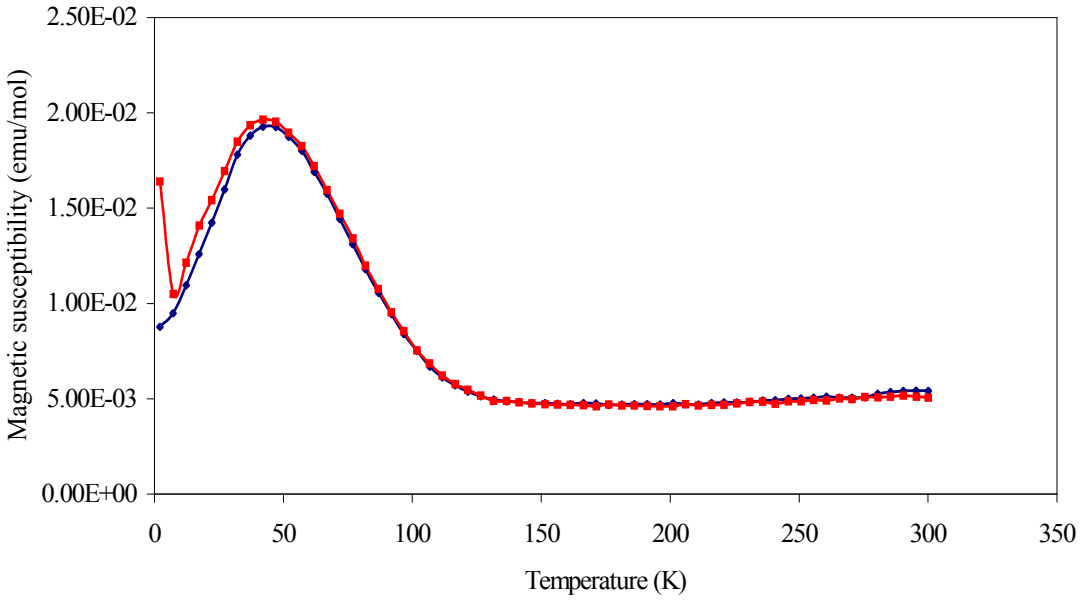

Figure 5.13. Magnetic susceptibility versus temperature plot for $Pb_4Fe_{2.6}Co_{0.4}O_8Cl$ performed in an applied field of 1000 Gauss. Zero-field cooled is shown in blue and field cooled data in red.

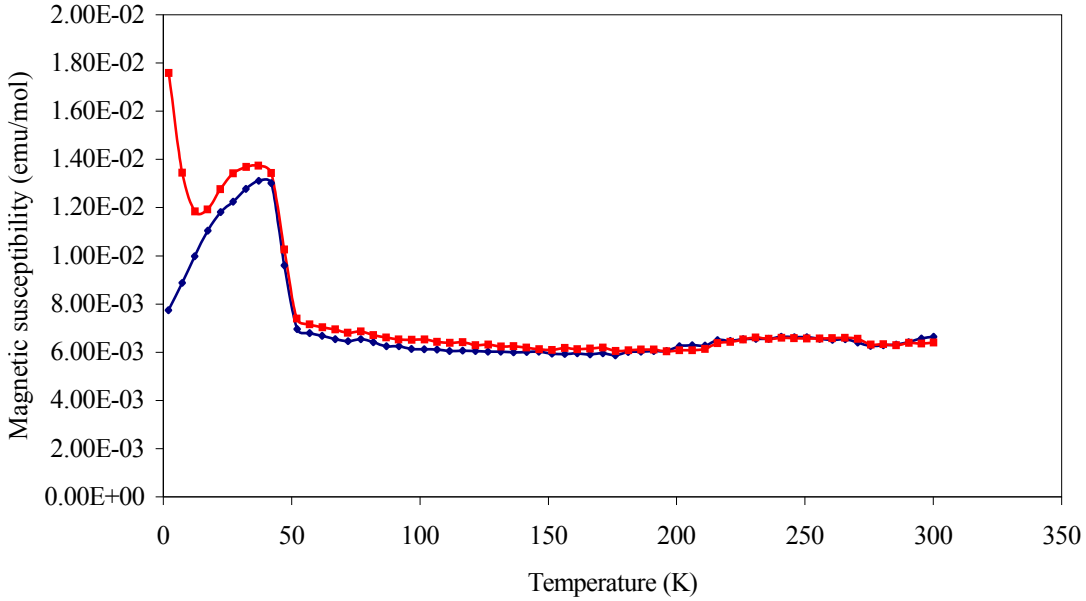

Figure 5.14. Magnetic susceptibility versus temperature plot for $Pb_4Fe_{2.6}Mn_{0.4}O_8Cl$ performed in an applied field of 1000 Gauss. Zero-field cooled is shown in blue and field cooled data in red.

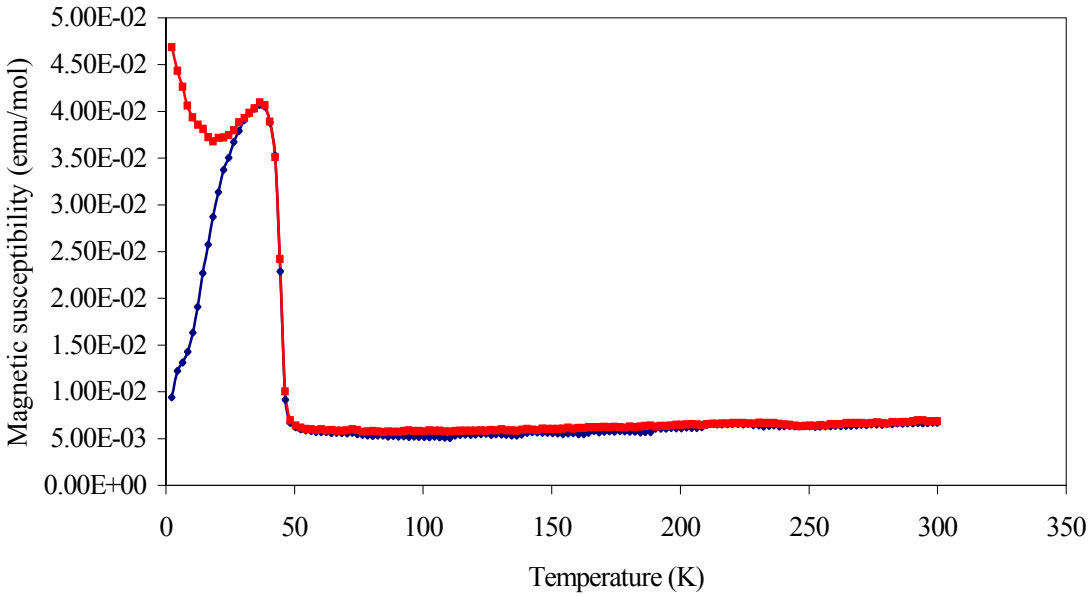

Figure 5.15. Magnetic susceptibility versus temperature plot for $Pb_4Fe_{2.6}Mn_{0.4}O_8Br$ performed in an applied field of 1000 Gauss. Zero-field cooled is shown in blue and field cooled data in red.

Magnetic susceptibility measurements were taken below the antiferromagnetic ordering temperature of the parent material, 610(5)K for $Pb_4Fe_3O_8Cl$ and 600(5)K for $Pb_4Fe_3O_8Br$, so that the predicted maximum in the susceptibility plot due to antiferromagnetic ordering at high temperature is not observed. Plots for all four substituted samples show a maximum in the susceptibility plot at a temperature below the ordering temperature of the parent material as follows: $Pb_4Fe_{2.4}Co_{0.6}O_8Cl$ ~ 42K, $Pb_4Fe_{2.6}Co_{0.4}O_8Cl$ ~ 42K, $Pb_4Fe_{2.6}Mn_{0.4}O_8Cl$ ~ 37K and $Pb_4Fe_{2.6}Mn_{0.4}O_8Cl$ ~ 38K. All susceptibility plots for the substituted samples show a positive gradient above 150K indicating that a second peak in the susceptibility plot is likely at higher temperatures.

Divergence of the field cooled and zero field plots at the low temperature maxima for all four substituted samples suggests a ferromagnetic component to the magnetic ordering, which may occur as a result of canting of the magnetic moments at this second ordering temperature. The magnetic anomaly at ~ 260K for the parent material, *figure 5.11*, may be the evidence of similar magnetic behaviour for the parent material at higher temperature.

5.5 References

[1] R. C. Rouse. *Am. Mineral.,***56**, 625, (1971).

[2] J. Pannetier and P. Batail. *Journal of Solid State Chemistry*, **39**, 15, (1981).

[3]] J. Emery, A. Cereze and F. Varret. *Journal Phys. Chem. Solids,* **41**, 1035, (1980).

[4] C. S. Knee and M. T. Weller. *Journal of Materials Chemistry*, **11**, 2350, (2001).

[5] Rukang Li. *Physica C,* **277**, 252, (1997).

[6] Rukang Li. *Journal of Solid State Chemistry*, **130**, 154, (1997).

[7] R. J. Crooks, C. S. Knee and M. T. Weller. *Chemical Materials*, **10**, 4169, (1998).

[8] A.C. Larson and R.B. Von Dreele. *General Structure Analysis System (GSAS)*, Los Alamos National Laboratory Report LAUR 86-748 (2004).

[9] Q. Huang, P. Karen, V. L. Karen, A. Kjekshus, J. W. Lynn, A. D. Mighell, N. Rosov, A. Santoro. *Physical Review B.* 45, no.**17**, 9611 (1992)

[10] Q. Z. Huang, V. L. Karen, A. Santoro, A. Kjekshus, J. Lindén, T. Pietari and P. Karen. *Journal of Solid State Chemistry.* **172**, 73, (2003).

[11] R. D. Shannon. *Acta Cryst,* **A32**, 751, (1976).

CHAPTER 6

Structural Characterisation of $Pb_8WO_{10}Cl_2$

6.1 Background

Numerous lead oxychloride minerals have been discovered in several locations, worldwide. These include hematophanite ($Pb_4Fe_3O_8Cl$) [1], asisite ($Pb_7SiO_8Cl_2$) [2] and pinalite ($Pb_3WO_5Cl_2$) [3].

Hematophanite, as discussed in Chapter 5, consists of a central FeO_6 octahedron connected to two FeO_5 square pyramids, each of these oxygen deficient triple perovskite units is separated by a $PbCl_2$ layer with CsCl- type structure. This structure can be compared to the high T_c superconductor $YBa_2Cu_3O_{7-\delta,}$ in which a central CuO_4 square plane is connected to two CuO_5 square pyramids, these triple perovskite units are separated by yttrium ions [4, 5]. It was proposed that a hematophanite type material in which Cu^{2+} replaced Fe^{3+}, with W^{6+} to provide charge balance may result in a layered material in which copper has the square pyramidal coordination found in cuprate superconductors. Attempts to synthesis single phase samples of materials such as $Pb_4Fe_{0.33}W_{0.66}Cu_2O_8Cl$ and $Pb_4W_{0.75}Cu_{2.25}O_8Cl$ proved unsuccessful. A second phase, $Pb_8WO_{10}Cl_2$, was identified while attempting to synthesise these copper containing hematophanite materials. A single phase sample of $Pb_8WO_{10}Cl_2$ was subsequently synthesised.

$Pb_8WO_{10}Cl_2$ is one of a series of compounds characterised by Aurivillius [6], of general formulae $7PbO.RO_y.PbX_2$; R= Si, Ge, P, V, As, Mo and W and X = Cl, Br and I. X = I compounds with R= Ge, V, As and W only, were synthesised. Although Aurivillius characterised $Pb_8WO_{10}Cl_2$ by single crystal X-ray diffraction the occupancy of some cation and anion sites remained in doubt. The material was considered to

consist of PbO like blocks separated by Cl^- layers, with W^{6+} located on some of the Pb sites in a disordered arrangement. Refinement of single crystal X-ray diffraction data concluded that the material belonged to space group I4/*mmm,* with lattice parameters a = 3.9871(2)Å and c = 22.536(2)Å. Following density measurements of 8.57g cm^{-3} Aurivillius proposed two models: one in which there is partial occupation of all sites in the unit cell to give an overall occupancy of 0.89 formula units/ unit cell i.e. $Pb_{7.12}W_{0.89}O_{8.9}Cl_{1.78}$/ unit cell; alternatively he proposed that the cell content is $Pb_{7.27}W_{0.91}O_{9.1}Cl_{1.82}$ with the deficiency on the Cl sites filled by Pb cations, resulting in a disordered structure in which some PbO layers replace Cl layers. Although the second model gives a calculated density of 8.73g cm^{-3} and the first model is in agreement with the experimental density measured, it was concluded that the second was the more likely model. The position of one oxygen per unit cell remained unidentified.

The following work uses neutron powder diffraction (NPD) to re-evaluate the structure of this phase.

The structure of lead oxyhalides can be related to two typical subcells corresponding to ideal M_2O_2X and M_4O_4X compositions, as shown in *figure 6.1*. *Figure 6.1a* shows a typical bismuth oxychloride or Sillén's phase, $LiBi_3O_4Cl_2$ which corresponds to M_2O_2X [7] and *Figure 6.1b* shows the structure of the mineral Asisite, $Pb_7SiO_8Cl_2$ which corresponds to M_4O_4X [2].

Figure 6.1a.

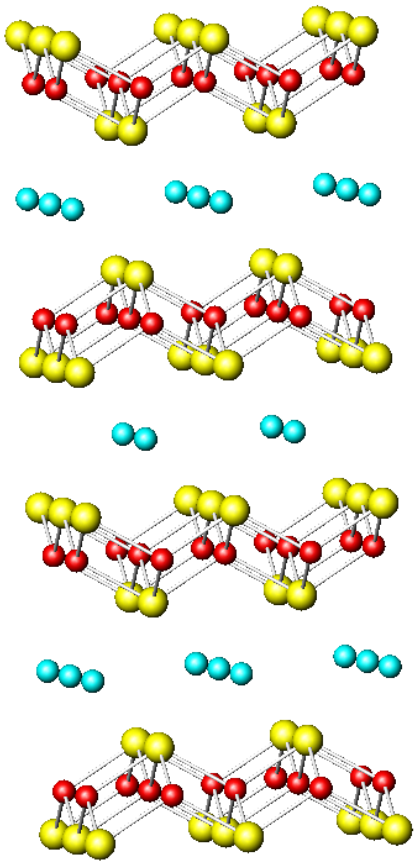

Figure 6.1b.

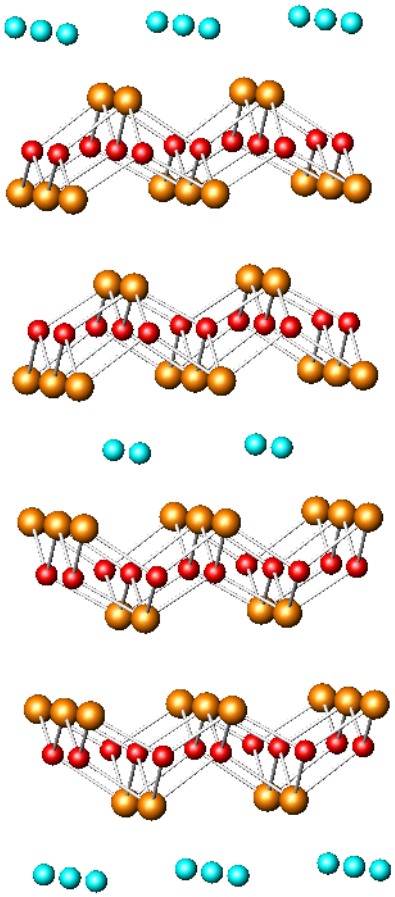

Figure 6.1. Crystallographic structure of a) $LiBi_3O_4Cl_2$, showing Li/ Bi (yellow spheres), O (red spheres) and Cl (turquoise spheres) and b) $Pb_7SiO_8Cl_2$, showing Pb/Si (orange spheres, O (red spheres) and Cl (turquoise spheres).

Sillén investigated a series of oxide halides consisting of fluorite related cationic M_2O_2 layers (M= Bi, Sb, Pb, Cd, Ca, Sr, Ba, Li, Na) separated by halide layers. The number of halide layers separating the metal oxide layers varied from 1-3, and was given the notation X_n (n=1, 2, 3) to indicate the number of halide layers [8]. $BiPbO_2Cl$

[9] is an example of an X_1 type that adopts the same structure as $LiBi_3O_4Cl_2$ shown in *figure 6.1a.*

The X_1 materials $BiMO_2NO_3$ (*M*=Pb, Ca), in which a nitrate group replaces the halide ion, have been characterised by Kodama, who has patented their applications as anion-exchange materials [10]. The oxide nitrates with *M*=Pb/ Ca crystallise in the tetragonal space group I4/*mmm* with two formula units per unit cell; room temperature lattice parameters are a = 3.97144(4) Å, c = 14.8257(2) Å for M = Pb and a = 3.96337(5) Å, c = 14.1283(3) Å for M = Ca. X_1 materials, $BiMO_2NO_3$, with mixed M^{2+} cations (*M*=Pb, Ca, Sr) have been used as precursors in a reliable and reproducible synthetic route for the high T_c superconductor $(Bi, Pb)_2Sr_2Ca_2Cu_3O_{10+\delta}$ (Bi, Pb-2223) [11, 12].

$Pb_3WO_5Cl_2$ [3], $Pb_3WO_5Br_2$ and $Pb_3MoO_5Cl_2$ [13] can be related to the X_1 Sillén structure type; *figure 6.2* shows the structure of $Pb_3WO_5Cl_2$, which is typical for these materials. W/Mo is associated with the 'extra' oxygen to form square pyramidal W/MoO_5. By comparison of *figures 6.1a* and *6.2* it can be seen that the 'extra' oxygen atom protrudes into the halide layer leading to displacement of the chloride ions, leaving little room for the lone pair of the neighbouring lead atom. W-O bonds, at 1.90(1) Å for the equatorial and 1.70(5) Å for the apical bonds, for $Pb_3WO_5Cl_2$ are significantly shorter than Pb-O bonds 2.43(1), 2.46(1), Å [13]. Strain is induced by the protrusion of the 'extra' oxygen into the halide layer, precluding the synthesis of the iodine or bromine analogues of these structures, except $Pb_3WO_5Br_2$. Charkin et al. [13] proposed that a material with a double Pb/W_2O_2 layer, with a structure based on *figure 6.1b*, would be able to accommodate the extra oxygen in the interlayer space and would be less strained.

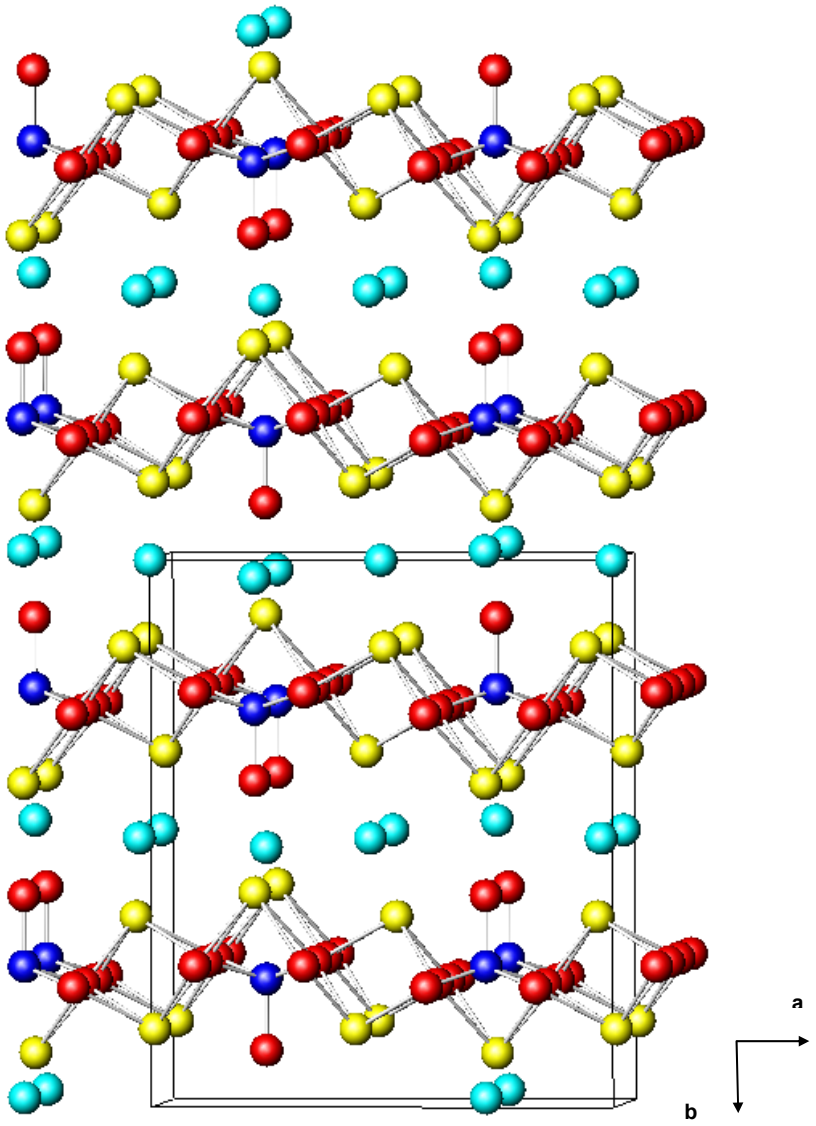

Figure 6.2. Crystallographic structure of $Pb_3WO_5Cl_2$, showing Pb (yellow spheres), O (red spheres) and Cl (turquoise spheres) and W (blue spheres). Space group *Amam*, a = 11.073(2), b = 13.067(3) and c = 5.617(1) Å [3]. Axes of unit cell shown.

Structural characterisation of $Pb_8WO_{10}Cl_2$ by Aurivillius [6] identified a typical lead oxyhalide structure based on that of the mineral assite, $Pb_7SiO_8Cl_2$, as shown in *figure 6.1b* in which a double Pb/W_2O_2 layer is separated by a single chloride layer. The site of the extra oxygen was unidentified.

6.2 Synthesis of $Pb_8WO_{10}Cl_2$

Stoichiometric quantities of PbO, $PbCl_2$ and WO_3 were thoroughly ground and fired at 550°C for 6 hours. The precursor powder was reground and heated to 680°C for 12 hours. Phase purity was obtained following a further two firings to 680°C, with intermediate regrinding. Phase purity was monitored by X-ray powder diffraction (XRPD) (Siemens D5000, PSD, Ge monochromator, $CuK_{\alpha 1}$ radiation).

6.3 Structural Characterisation of $Pb_8WO_{10}Cl_2$

NPD data were collected at ambient temperature on instrument HRPT at the Swiss spallation neutron source, SINQ at PSI. (λ = 1.49423 Å). Diffraction data were analysed using the GSAS suite of programs [14].

Pb atoms, due to their high scattering power and high concentration in this material, dominate the XRPD pattern of $Pb_8WO_{10}Cl_2$. There is a less pronounced difference in the scattering power of the atoms when neutrons are diffracted by the crystal lattice, allowing a more detailed structural determination with respect to the anion sub-lattice.

Refinement of NPD data using the GSAS suite of programs [14] was carried out, using the atomic positions reported by Aurivillius as the starting point [6], it was proposed that the difference in the neutron scattering lengths of W (4.86×10^{-15} m) and Pb (9.405×10^{-15} m) would allow this initial model to be revised providing a more accurate structural determination. Background parameters, lattice parameters, thermal parameters, histogram scale factors, diffractometer zero point, peak shape (pseudo-Voigt) and atomic coordinates were refined. The Rietveld plot is shown in *figure 6.3*, and the related structural parameters are given in *table 6.1*.

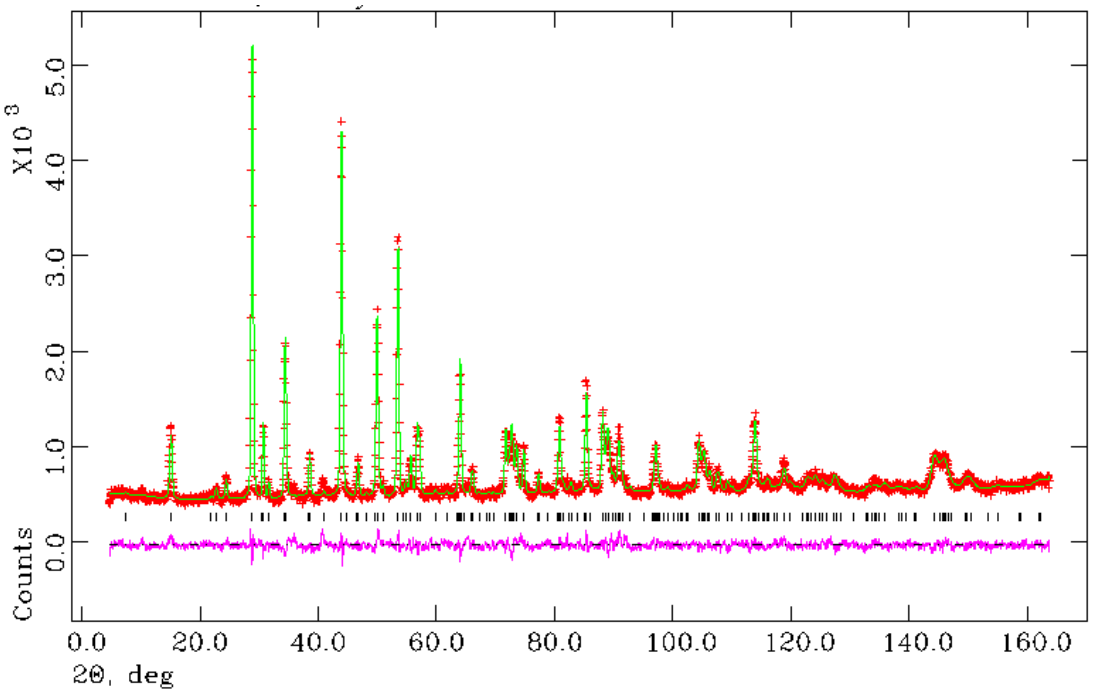

Figure 6.3. Observed (+), calculated (-) and difference (-) profiles from refinement using room temperature NPD data for $Pb_8WO_{10}Cl_2$ in space group I4/*mmm*. χ^2=2.036, R_{wp} =5.47% and R_p = 4.26%.

Table 6.1a. Refinement results from room temperature NPD data for $Pb_8WO_{10}Cl_2$

Atom	Position	x	y	z	U_{iso} x100/ Å^2	Frac.
Pb 1	4*e*	0	0	0.0822(1)	1.54(5)	1
Pb 2	4*e*	0	0	0.3077(2)	1.98(9)*	0.7778
W	4*e*	0	0	0.3213(2)	1.98(9)*	0.2222
Cl	2*b*	0	0	0.5	2.35(9)	0.8889
O 1	8*g*	0.5	0	0.1415(2)	2.69(8)*	1
O 2	4*e*	0	0	0.2463(9)	2.69(8)*	0.2222

Space group I4/*mmm*; *a* = 3.9846(2) Å; *c* = 22.690(2) Å. χ^2 =2.036, R_{wp} = 5.47 % and R_p = 4.26%

* constrained to be equal to avoid correlation effects.

*Table 6.1b.*Selected bond lengths for $Pb_8WO_{10}Cl_2$.

Pb/W-O bond lengths,	**Å**	**BVS**
Pb1- O1 (x4)	2.404(2)	1.95
Pb2- O1 (x4)	2.302(3)	2.39
W – O1 (x4)	2.16(1)	3.85
W – O2 (x1)	1.70(4)	
Pb1 – Cl (x8)	3.379(1)	

Table 6.1c. Selected bond angles for $Pb_8WO_{10}Cl_2$

Pb/W – O angles,	**degrees**
O1 – Pb1- O1 (x4)	71.75(9)
O1 – Pb2- O1 (x4)	75.5(1)
O1 - W – O1 (x4)	81.2(6)
O1 - W – O2 (x4)	113.0(8)

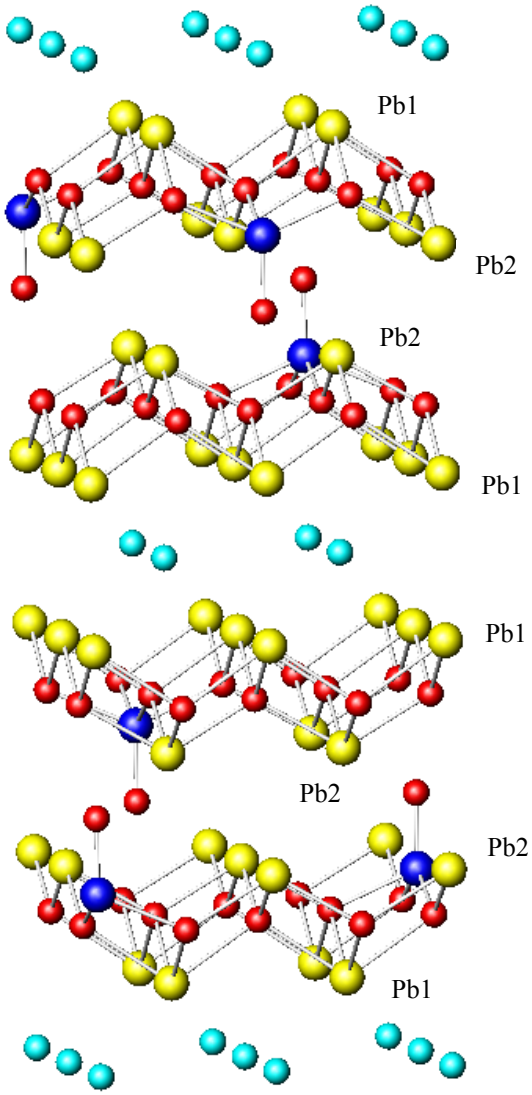

Figure 6.4. Crystallographic structure of $Pb_8WO_{10}Cl_2$, showing Pb (yellow spheres), O (red spheres) and Cl (turquoise spheres) and W (blue spheres). Space group I4/*mmm*, a = 3.9846(2) and c = 22.690(2)Å .

Rietveld refinement of NPD data, in the body-centred tetragonal space group I4/*mmm,* converged to $\chi^2 = 2.036$.

Following refinement of single crystal x-ray diffraction data, Aurivillius identified the following sites; Pb1 (0, 0, ~0.1), Pb2 (0, 0, ~0.3), O (0.5, 0, ~0.15) and Cl

(0, 0, 0.5) , the oxygen site is an eight fold position leaving the site of one oxygen ion unidentified. Aurivillius assumed that tungsten occupied the lead positions in a disordered arrangement.

Initial refinement indicated that W occupied only the Pb2 site within the Pb_2O_2 blocks and away from the Cl layer. Allowing an additional oxygen atom, which provides tungsten with an apical bond, made further improvements to the refinement. The agreement between calculated and experimental profiles was also improved by allowing the tungsten site to be refined independently to the lead site. The results of this refinement shows that W-O bonds (2.16(1) and 1.70(4) Å) are significantly shorter than Pb-O bonds (2.404(1) and 2.302(3) Å), as shown in *figure 6.5*, which results in a movement of tungsten into the $(Pb/W)_2O_2$ layer. Tungsten was found to occupy a site within the Pb2 layer only, in a disordered arrangement.

The 'extra' oxygen was initially positioned to allow coordination to tungsten, refinement of this oxygen position further improved the fit between calculated and observed profiles, resulting in a cation layer occupied by 4-coordinate Pb^{2+}, with a geometry based on a square pyramid having Pb at its apex, and by 5-coordinate square pyramidal W^{6+}. *Figure 6.5* shows the coordination around tungsten in detail. Although square pyramidal co-ordination is unusual for tungsten, it is found in $Pb_3WO_5Cl_2$ [3] and $Pb_3WO_5Br_2$ [13]. Short W- O bond lengths, for example 1.90(1) Å equatorial and 1.70(5) Å apical compared to Pb- O bond lengths of 2.43(1) and 2.46(1) for $Pb_3WO_5Cl_2$, were also evident for these materials

The structure of $Pb_8WO_{10}Cl_2$ is typical of the lead oxyhalides and is similar to that of the mineral assite ($Pb_7SiO_8Cl_2$) as shown by comparison of *figures 6.1b and 6.4.* The 'extra' oxygen of $Pb_8WO_{10}Cl_2$ is situated between the $(Pb/W)_2O_2$ blocks directed

away from the halide layer thus avoiding the strain identified in $Pb_3WO_5Cl_2$, $Pb_3WO_5Br_2$ and $Pb_3MoO_5Cl_2$ [13], which is induced as the halide ions are displaced away from the oxygen.

The density of $Pb_8WO_{10}Cl_2$ measured by Aurivillius is 8.57g cm^{-3} , the density of this model is 8.49g cm^{-3}, a difference of only 0.9%. The model proposed in this thesis is structurally sensible and consistent with related structures such as $Pb_3WO_5Cl_2$. There is full occupancy of all of the cation sites and a slight deficiency in the chlorine site.

The stoichiometric formula of $Pb_8WO_{10}Cl_2$ results in 8/9 occupancy of the chloride site, whereas the stoichiometric formula $Pb_7WO_9Cl_2$ would, in theory, allow full occupancy of all atom sites. Attempts to synthesise $Pb_7WO_9Cl_2$, however, resulted in a second phase, identified as Pb_2WO_5. Attempts by Aurivillius [6] to synthesise both materials also resulted in fewer impurities for $Pb_8WO_{10}Cl_2$.

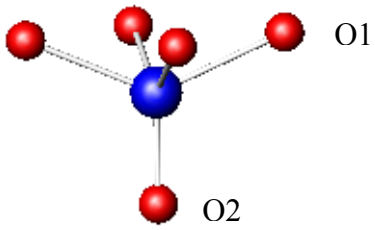

Figure 6.5. The W^{6+} (blue sphere) coordination showing bonds to O1, 2.16(1) Å and an apical bond to O2, 1.70(4) Å.

Bond valence sum calculations [15, 16], as shown in *table 6.1b*, for Pb1 give a value of 1.95, which is close to the expected value of 2. Pb2 with a value of 2.39

valence units has a higher than optimum value, while W with a value of 3.85 units is lower that the expected valency of 6. Discrepancy between expected values and calculated values is anticipated for Pb2 and W, since sites within the Pb2 layer are occupied by tungsten or lead in a disordered fashion. The Pb2-O1 and W-O1 bond distances are average values; locally within the structure actual Pb2-O1 bond distances will be greater than those recorded in *table 6.1* and W-O1 distances will be less than those recorded.

6.4 References

[1] C. S. Knee and M. T. Weller, *Journal of Materials Chemistry,* **11**, 2350, (2001).

[2] R. C. Rouse, D. R. Peacor, P. J. Dunn, A. J. Criddle, C. J. Stanley and J. Innes, *American Mineralogist*, **73**, 643, (1988).

[3] J. D. Grice and P. J. Dunn, *American Mineralogist*, **85**, 806, (2000).

[4] M. K. Wu, J. R. Ashburn, C. J. Torng, R. L. Meng, L. Gao, Z. J. Huang, Y. Q. Wang and C. W. Chu, *Phys. Rev. Lett.* **58**, 909, (1987).

[5] A. W. Sleight *Science* Vol. **242**. no. 4885, 1519, (1988).

[6] B. Aurivillius, *Chemica Scripta*, **19**, 97, (1982).

[7] L. G. Sillén, *Die Naturwissenschaften,* **22**, 318, (1942).

[8] P. Ziegler, I. Grigoraviciute, K. Gibson, J. Glaser, Aivaras Kareiva and H. -Jürgen Meyer, *Journal of Solid State Chemistry,***177**, Issue 10, 3610, (2004).

[9] J. Ketterer and V. Krämer. *Material Research Bulletin* **20**, 1031, (1985).

[10] H. Kodama, in: A. Dyer, M.J. Hudson, P.A. Williams (Eds.), Progress in Ion Exchange, The Royal Society of Chemistry **196**, 39, (1997).

[11] K. Gibson, P. Ziegler and H.-J. Meyer. *Superconductor Science and Technology* **17,** p. 786, (2004).

[12] K. Gibson, P. Ziegler and H.-J. Meyer. *Physica C* **403,** p.1, (2004).

[13] D. O. Charkin and P. Lightfoot, *American Mineralogist*, **91**, p.1918 (2006)

[14] A. C. Larson, R. B. Von Dreele, General Structure Analysis System, Los Alamos National Laboratory, Los Alamos, NM, 1994.

[15] I. D. Brown and D. Altermatt. *Acta Cryst.,* **B41**, p.244-247,(1985).

[16] N. E. Brese and M. O'Keeffe. *Acta Cryst.,* **B47**, p.192-197, (1991).

CHAPTER 7

Conclusions and Further Work

7.1 Structural and Magnetic Characterisation of $YSr_3Mn_{4-x}Ga_xO_{10.5}$

The material $YSr_3Mn_{4-x}Ga_xO_{10.5}$ has been synthesised with gallium contents in the range $0.9 \leq x \leq 1.77$. The upper value of the gallium content may be limited by the need to maintain manganese in the 'tetrahedral site' where it coordinates to a partially occupied oxygen site, resulting in a Jahn Teller distorted square pyramid. Mn^{3+} is frequently found with square pyramidal coordination in oxide environments. Earlier work on the material $Y_{0.8}Sr_{2.2}Mn_2GaO_8$ ($Y_{1.07}Sr_{2.93}Mn_{2.67}Ga_{1.33}O_{7.8}$) identified a magnetic peak which could not be fitted to the antiferromagnetically ordered model of the material [1 ,2]. The 'extra' magnetic peak was also evident for two of the samples synthesised in this work, $YSr_3Mn_{3.1}Ga_{0.9}O_{10.4}$ and $YSr_3Mn_{2.67}Ga_{1.33}O_{10.5,}$ it was concluded that this extra peak was actually due to a small MnO impurity, for which the intensity of the nuclear diffraction was not sufficient to show in the room temperature profiles.

Oxidation of samples with various Mn:Ga ratios resulted in the oxidation of Mn^{3+} to Mn^{4+} with a concurrent increase in the coordination on the former 'tetrahedral' site. Low temperature NPD revealed extra peaks due to magnetic scattering for $YSr_3Mn_{3.1}Ga_{0.9}O_{10.4}$ only. The magnetic ordering of this oxidised sample differed from the reduced sample, with AFM ordering in all directions of the unit cell, compared to FM ordering in the [001] direction and AFM ordering in the [100] and [010] directions for the parent material. It was proposed that contraction of the Mn^{4+} *d* orbitals would lead to poorer overlap with the O^{2-} *p* orbitals and so suppress magnetic ordering in the samples with higher gallium content.

Following fluorination, the AFM ordering of the samples remained as for the parent material. Magnetic susceptibility studies suggested a ferromagnetic component to the magnetic properties for many of these samples. Fluorination was only achieved up to a maximum of 0.3 formula units, for$YSr_3Mn_{3.1}Ga_{0.9}O_{10.4}F_{0.3}$. Fluorination results in mixed valence Mn^{3+}/ Mn^{4+} cations, but future work aimed at increasing the proportion of fluorine and investigating the effects of mixed valency manganese on the transport properties of the material may be of interest.

7.2 Structural and Magnetic Characterisation of Chemically Modified Hematophanite.

$Pb_4Fe_3O_8Cl$, hematophanite, and its analogue $Pb_4Fe_3O_8Br$ were modified by the substitution of Fe^{3+} by Co^{3+} or Mn^{3+}. It was only possible to partially substitute Fe^{3+}, to give a maximum Co level of $Pb_4Fe_{2.4}Co_{0.6}O_8Cl$ and a maximum Mn level of $Pb_4Fe_{2.6}Mn_{0.4}O_8Cl$/ Br. Magnetic susceptibility measurements and NPD suggest AFM ordering, with an ordering temperature above room temperature, as observed in the parent material [3]. A low temperature maxima in the susceptibility plots suggests a ferromagnetic component to the magnetic ordering at ~ 40K for all of the substituted samples.

It appears to be difficult to substitute Fe^{3+} with other magnetic cations, future work could investigate the reasons for this difficulty and identify other cations that may be able to substitute for Fe^{3+}.

7.3 Structural Characterisation of $Pb_8WO_{10}Cl_2$

NPD of polycrystalline samples has allowed a detailed characterisation of $Pb_8WO_{10}Cl_2$, following on from the earlier characterisation as a result of single crystal X-ray diffraction by Aurivillius [4]. The model proposed in this work matches density

measurements more closely than the earlier model. The site of an 'extra' oxygen atom that could not be located by Aurivillius was identified and a separate site for tungsten was identified which allows coordination to the 'extra' oxygen atom. The model proposed in this work allows full occupancy of the cation sites with a slight deficiency in the chlorine site compared to the original model that proposed under occupancy on all sites. Aurivillius [4] also characterised the Molybdenum analogue, $Pb_8MoO_{10}Cl_2$, the study had the same limitations as his work on $Pb_8WO_{10}Cl_2$. A more detailed structural analysis of $Pb_8MoO_{10}Cl_2$ would be of interest.

Aurivillius suggests that it is possible to synthesise single phase samples of the bromine analogue with stoichiometric formula $Pb_7WO_9Br_2$, in which all of the atom sites would be fully occupied, although the site of one oxygen also remained unidentified for this material in his original paper. A full structural characterisation of the bromine analogue would be of interest in the future. Interestingly Aurivillius discovered that single phase samples of the iodine analogue could only be synthesised with stoichiometric formula $Pb_8WO_{10}I_2$.

7.4 References

[1] L. J. Gillie, PhD University of Birmingham 2003.

[2] L. J. Gillie, H. M. Palmer, A. J. Wright, J. Hadermann, G. Van Tendeloo, C Greaves. *Journal of Physics and Chemistry of Solids* 65, 87-93, (2004).

[3] C. S. Knee and M. T. Weller. *Journal of Materials Chemistry*, **11**, 2350-2357, (2001).

[4] B. Aurivillius, *Chemica Scripta*, **19**, p.97 (1982).